Modelling turbulence and transport of buoyant material in the ocean surface mixed layer

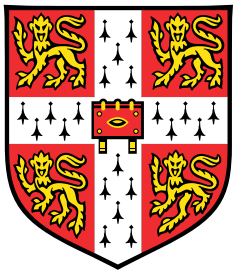

Jennifer Alice Dingwall

Supervisor: Prof. John R. Taylor

Department of Applied Mathematics and Theoretical Physics
University of Cambridge

This dissertation is submitted for the degree of
Doctor of Philosophy

Pembroke College

March 2024

Declaration

This thesis is a result of my own work and includes nothing which is the outcome of work done in collaboration except as stated below and specified in the text. It is not substantially the same as any work that has already been submitted for any degree or other qualification at the University of Cambridge, or any other university or similar institution except as declared below and specified in the text. I further state that no substantial part of my dissertation has already been submitted, or is being concurrently submitted for any such degree, diploma or other qualification at the University of Cambridge or any other University or similar institutions except as declared below and specified in the text. This thesis does not exceed 65,000 words including appendices, bibliography, footnotes, tables and equations, and has fewer than 150 figures.

Jennifer Alice Dingwall
March 2024

Abstract

The ocean mixed layer (OML) is a significant and dynamically active part of the ocean which plays an important role in climate variability. Here, atmospheric processes such as winds, heat fluxes or density differences drive the generation of small-scale, three-dimensional turbulence and mixing of oceanic waters. These turbulent flows govern the distribution of buoyant materials including oil droplets and microplastics, which have significant implications for marine life and safety. However, turbulent flow structures are often too small to be resolved by global or regional circulation models, and observations at these scales remain limited. The focus of this thesis is to use numerical simulations to improve our understanding of the small-scale, three-dimensional turbulent processes in the OML and examine their role on transporting and accumulating buoyant material.

We use high resolution large eddy simulations (LES) and direct numerical simulations (DNS), and model non-inertial, buoyant particles using a combination of buoyant tracers and three-dimensional Lagrangian particles. Surface cooling drives convection, and under this regime persistent convective vortices form which trap and accumulate buoyant particles. We test the resilience of convective vortices under the additional presence of wind, and find that in weak winds, convective vortices survive but are less effective at trapping buoyant material. With sufficiently strong wind forcing, convective vortices are no longer visible, but some clustering occurs in downwelling regions associated with longitudinal wind rolls.

Despite their small size, the convective vortices exhibit a bias towards cyclonic vorticity which has not been reported previously. We independently vary the Coriolis acceleration and surface buoyancy flux, and using Lagrangian particles, we find that the large convective vortices develop through the merger of many small unbiased convective vortices. We propose a statistical theory to predict the cyclonic bias of large convective vortices and test the theory using LES results. We apply the theory to typical convective conditions and find that convective vortices in OML are expected to exhibit a bias, but convective vortices in the terrestrial and Martian atmospheres are expected to be largely unbiased.

Finally, motivated by accumulation of buoyant material observed at surface fronts in the SUNRISE field campaign in the Gulf of Mexico, we run simulations of a highly idealised front under geostrophic adjustment. By varying the balanced Rossby number, we show that

strong fronts develop a three-dimensional instability which generates turbulence near the top and bottom boundaries. We describe the physical mechanisms at play and the energy pathways as the front evolves over time. In the case of the most turbulent dynamics, we additionally model the movement of buoyant particles. Shear instabilities drive turbulence which enhances mixing, and strongly buoyant particles are carried out of the front during the first inertial period, which segregates the particles and leaves a large void in the centre of the front. In contrast, weakly buoyant particles are quickly subducted into the interior, and subsequently move according to the inertial oscillations of the front.

"You have brains in your head. You have feet in your shoes.
You can steer yourself any direction you choose."
– Dr Seuss

Acknowledgements

First, I would like to thank my supervisor, John Taylor, who has guided me so positively for the last four years. I am grateful for the knowledge, expertise and experience he has patiently passed on to me, and for the exciting opportunities he shared along the way.

I would also like to thank the Atmosphere-Ocean Dynamics group, members of DAMTP and the SUNRISE team for their camaraderie, and their helpful suggestions on my work. I extend thanks to my friends from Oxford and beyond for their continued support and encouragement.

Thanks to Jonny, who understood the challenges of a PhD and tried his best to make my journey smoother than his own. He has been my motivator, my soundboard, my proof-reader, and above all, my closest companion. Thanks for seeing me through the ups and downs, and for always putting things into perspective.

Finally, I would like to thank my parents, my brother, and my sister, without whom I would not have reached this point. I am grateful for the upbringing, education and opportunities afforded to me, which have taught me to be strong and independent. Most of all, thanks for the care, support and humour that keeps me grounded. I dedicate this thesis to you.

Table of contents

1 Introduction **1**

1.1 Motivation . . . 1

1.2 Physical background . . . 3

1.2.1 Small-scale turbulent processes . . . 5

1.2.2 Convective vortices . . . 7

1.2.3 Submesoscale fronts . . . 9

1.3 Modelling the ocean mixed layer . . . 12

1.3.1 Direct numerical simulations . . . 14

1.3.2 Large eddy simulations . . . 15

1.4 Material transport . . . 17

1.4.1 Particle equations of motion . . . 17

1.4.2 Eulerian approach . . . 20

1.4.3 Lagrangian approach . . . 21

1.4.4 Accumulation of buoyant material . . . 22

1.5 Thesis outline . . . 26

2 Lagrangian Particle Tracking Model **29**

2.1 Introduction . . . 29

2.2 Interpolation . . . 29

2.2.1 Horizontal interpolation . . . 30

2.2.2 Vertical interpolation . . . 32

2.3 Parallel Computing . . . 33

2.3.1 Parallelisation of particles . . . 33

2.3.2 Ghost cells . . . 37

2.4 Implementation . . . 37

3 LES of buoyant material in wind-driven and convective turbulence **41**

3.1 Introduction . . . 41

3.2 Setup and numerical methods . . . 43
3.3 Results . . . 48
3.3.1 Qualitative description of the flow and the distribution of buoyant material . . . 49
3.3.2 Convective vortices . . . 53
3.3.3 Clustering of buoyant material . . . 62
3.4 Conclusions and discussion . . . 69
Appendix 3.A . . . 72
Appendix 3.B . . . 73

4 A model for the cyclonic bias of convective vortices in a rotating system 75
4.1 Introduction . . . 75
4.2 Setup and numerical methods . . . 76
4.3 Results . . . 78
4.3.1 Large eddy simulations . . . 78
4.3.2 Statistical theory for vorticity bias . . . 81
4.4 Conclusions and discussion . . . 89
Appendix 4.A . . . 92
Appendix 4.B . . . 94
Appendix 4.C . . . 94
Appendix 4.D . . . 96

5 DNS of a geostrophically adjusting front 99
5.1 Introduction . . . 99
5.2 Setup and numerical methods . . . 101
5.3 Results . . . 105
5.3.1 Qualitative description of the flow . . . 105
5.3.2 Adjustment energetics . . . 109
5.3.3 Estimating the mixing efficiency . . . 112
5.4 Conclusions and discussion . . . 116
Appendix 5.A . . . 117
Appendix 5.B . . . 118

6 LES of buoyant particles in a geostrophically adjusting front 123
6.1 Introduction . . . 123
6.2 Setup and numerical methods . . . 124
6.3 Results . . . 127

6.3.1 Qualitative description of the flow and the distribution of buoyant particles 128
6.3.2 Movement of particles between fluid of different densities 136
6.4 Conclusions and discussion 140
Appendix 6.A 142

7 Conclusions **145**
7.1 Conclusions 145
7.2 Future directions 149

References **153**

Chapter 1

Introduction

1.1 Motivation

The upper ocean separates the atmosphere from the deep ocean and plays a crucial role in the climate system. In this layer, interactions with the atmosphere drive large-scale currents and small-scale three-dimensional turbulence. These turbulent flows influence the air-sea exchange of carbon, momentum and heat fluxes, and are an essential component in the Earth's climate system (Belcher et al., 2012; Caldwell and Mourn, 1995; D'Asaro, 2014). Turbulence also determines the transport, dispersion, and accumulation of materials such as dissolved gases, nutrients, phytoplankton cells and pollutants. These play a key role in the marine ecosystem (Denman and Gargett, 1995; Mendelssohn et al., 2012; Worm et al., 2017) and biogeochemistry. The turbulent flow moves material in ways that are difficult to predict or model, often causing irregular distributions and much remains unknown about how turbulent processes affect material transport and mixing in the upper ocean.

Consider as an example the case of microplastics, which are now widespread in the world oceans and represent a major source of marine pollution (Borrelle et al., 2020). Large plastics are deposited as waste and fragmented into microplastics through UV radiation, chemical degradation and mechanical abrasion (Ward and Reddy, 2020). Microplastics tend to be less dense than seawater (Geyer et al., 2017) with an average density of 965 kg/m^3 compared to the average density of 1027 kg/m^3 for seawater (Morét-Ferguson et al., 2010), and hence microplastics generally remain close to the surface. Observations suggest that there are up to 51 trillion pieces of microplastic at the surface of the ocean, corresponding to a mass of up to 236 thousand metric tonnes (Sebille et al., 2015). This is significantly less than the 20 million metric tonnes deposited each year (Borrelle et al., 2020), and has led scientists to investigate the so-called 'missing plastic' quandary, to which the lack of understanding of fluid dynamical processes is a major contributor (Sutherland et al., 2023). Plastics degrade

very slowly and can be ingested by marine life, often at the surface of the ocean (Compa et al., 2019; Wilcox et al., 2015) which poses a threat to marine life and safety. The development of removal strategies for microplastics and the design of marine protected areas require detailed knowledge of the transport and distribution of microplastics in the ocean.

There are a wealth of ocean processes that contribute to the transport of microplastics which are summarised in figure 1.1. More generally, these processes influence any passive, buoyant material. At the mesoscale ($\sim$ 100 kilometres), wind-driven ocean gyres transport buoyant material. This is well supported by global circulation models and observations operational since the 20th century (Kubota, 1994). In particular, the breadth of observations from the Global Drifter Program since the late 1970s means that transport on this largest scale is relatively well understood (Elipot et al., 2016) and is not the focus of this thesis.

At the smallest scales, material is subject to much smaller, fully three-dimensional processes including wind transport, surface waves and convective plumes (C-G in figure 1.1) which have typical time-scales of seconds to minutes and length-scales of down to a few centimeters. Field observations of small-scale processes are challenging and few (D'Asaro et al., 2018) and transport scales are much too small to be investigated with global circulation models. Progress has been made using more localised numerical models but face the ongoing challenge of simultaneously simulating very small vertical scales and larger horizontal scales (Chamecki et al., 2019).

More recently, increased attention has been brought to oceanographic processes on scales between the mesoscale and small-scale turbulence. These processes contribute to inter-scale coupling (McWilliams, 2016) and the transfer of energy through scales. The ocean submesoscales (B in figure 1.1) range from 0.1 kilometres to 10 kilometres with time-scales on the order of hours to days. Although often visible from high-resolution satellite imagery (Kudryavtsev et al., 2012), observations of submesoscale flow features remain limited due to their rapid evolution (D'Asaro, 2014).

Observational challenges have led scientists to rely more strongly on numerical methods which have significantly advanced our understanding of oceanic processes over the last few years. However there are still obstacles to overcome in the computational world. Numerical simulations on the global scale are too coarse to capture small-scale flow features that may influence the transport of material (Haine et al., 2021; Hewitt et al., 2022) including dynamics at the submesoscale and below. Instead, these processes are parameterised in global ocean models to account for their effects (Dauhajre et al., 2017; Uchiyama et al., 2017). The parameterisations are informed by a combination of observations, laboratory experiments, theory and idealised high resolution numerical simulations (Chor et al., 2021; de Lavergne et al., 2020). Here, we take the approach of running small-domain *numerical experiments*

of isolated physical phenomena on the small-scale turbulent and submesoscale level, where the role of fluid dynamics on particle motion is most pronounced. Note that our attention is confined to physical processes in the open-ocean and hence we do not address processes (H-K) in figure 1.2 in this thesis.

Below I present an overview of the physics and modelling needed to study the diverse field of material transport. In section 1.2, I provide a detailed discussion of the physical and theoretical background pertaining to the upper-ocean, with a particular focus on those addressed in chapters 2-5 of the thesis (convective vortices in section 1.2.2 and adjusting fronts in section 1.2.3). I then guide the reader through different approaches used to model upper-ocean processes in section 1.3, before outlining how we model buoyant material and reviewing the existing literature surrounding buoyant material transport in section 1.4. Finally, in section 1.5, I give an outline of the following chapters.

1.2 Physical background

The surface ocean mixed layer (OML) is the uppermost layer of the ocean where turbulence driven by atmospheric forcing acts to maintain weak density stratification (McWilliams, 2006; Pedlosky, 1987) and vertically mixes water properties to depths of roughly 10 to 100 metres. The OML is bounded from below by a strong buoyancy interface which takes the form of a layer with a sharp vertical decrease in temperature (the seasonal thermocline) or a sharp vertical increase in salinity (halocline), or both. In all cases, this layer (called a pycnocline) is stably stratified, and here turbulence is damped, suppressing vertical motions below it. The OML also admits a variety of submesoscale processes due to the abundance of lateral density gradients, vertical shear and weak stratification. These provide ideal conditions for the formation of sharp density fronts. Larger submesoscale currents act to increase the stratification of the upper ocean (Bachman and Taylor, 2016; Callies and Ferrari, 2018; Fox-Kemper et al., 2008; Mahadevan et al., 2012) which limits the depth to which atmospheric-driven small-scale turbulent processes can penetrate downwards and reduces the depth of the OML (Taylor, 2016; Taylor and Ferrari, 2011).

Despite being small in volume, the OML plays a vital role in the climate system. For example, the OML regulates sea-surface temperature dynamics (Deser et al., 2010) and boundary conditions for air-sea fluxes (Frankignoul and Hasselmann, 1977; Kraus and Turner, 1967) and controls global ocean circulation (Hanawa and Talley, 2001) thus impacting climate change (Belcher et al., 2012; D'Asaro, 2014; Gargett and Wells, 2007; Li et al., 2017). A significant fraction of the ocean's primary production occurs in the sunlit OML, while the ocean contributes roughly half of the global primary production (Falkowski et al., 1998).

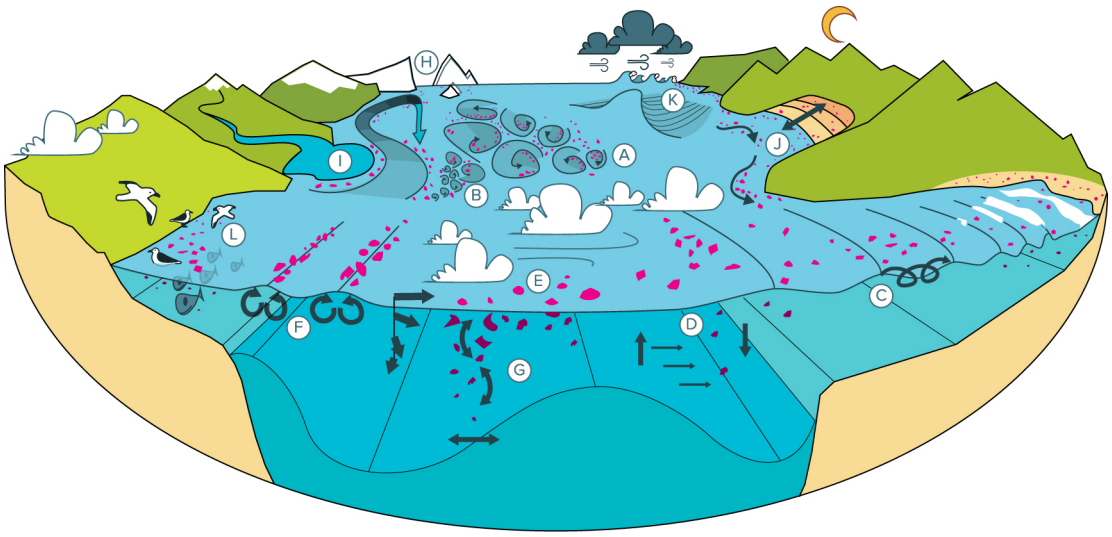

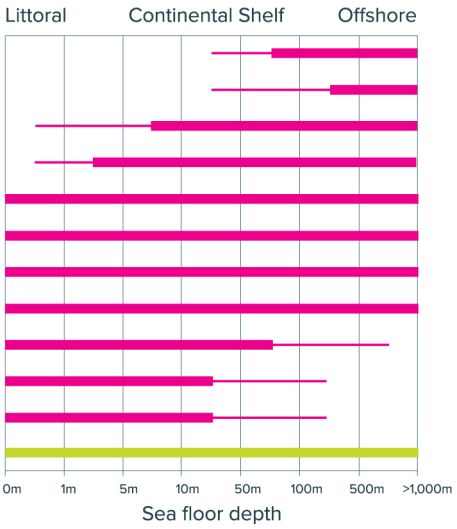

	PHYSICAL PROCESSES
A	Large-scale open ocean processes
B	Submesoscale open ocean processes
C	Open ocean Stokes drift
D	Internal tides
E	Direct wind transport (windage)
F	Langmuir circulation
G	Vertical mixing
H	Ice formation, melting and drift
I	River plumes and coastal fronts
J	Coastal currents, surface waves and beaching
K	Extreme events
L	*Transport by biology*

Fig. 1.1 A schematic showing the physical processes in the ocean which affect transport of plastic (depicted in pink), accompanied by a table quantifying the relative importance of each process. Thick pink lines indicate a highly important physical process and thin pink lines indicate physical processes of lesser importance. Green lines indicate transport by organisms. Reprinted with permission from Sebille et al. (2020).

Most human interactions with the ocean are confined to the OML making it an important region for the mixing and transport of pollutants. Although the atmospheric boundary layer (ABL) has some striking similarities to the OML (such as the stratification profile), the constantly changing mobile sea surface modifies turbulent dynamics in the OML resulting in unique flows that have no atmospheric counterparts.

1.2.1 Small-scale turbulent processes

The turbulence which characterises the OML is primarily driven by atmospheric processes at the upper boundary, although at the bottom boundary, large turbulent eddies can entrain denser fluid from below into the OML. Figure 1.2 provides an overview of the physical processes relevant to material transport in the OML. Within this, there are three main forcings that account for the majority of the turbulence in the OML (Belcher et al., 2012): buoyancy fluxes at the surface (associated with shortwave and longwave radiation entering and leaving the ocean and evaporation and precipitation), wind shear (with an Ekman spiral in the presence of rotation), and waves (breaking and non-breaking).

Buoyancy fluxes occur whenever there is a change in water density at the ocean surface, either via incoming and outgoing heat fluxes, or salinity fluxes driven by precipitation or evaporation. Here, we use the convention that a positive buoyancy flux is associated with an input of buoyancy at the sea surface which increases the density stratification and reduces the mixed layer depth. These conditions are usually associated with solar insolation during daylight hours, or precipitation. In contrast, night-time cooling of the ocean surface causes a negative buoyancy flux which drives turbulence and helps to deepen the OML (McWilliams, 2006). In this case, surface waters become more dense than the subsurface waters and down-well as convective plumes which creates small-scale three-dimensional turbulence with large vertical motions throughout the OML. This convective regime is often characterised by a regular pattern of narrow and intense convergent plumes surrounding large, weak areas of diverging fluid (Busse, 1978; Mason, 1989). Once surface cooling begins to wane at the start of day, convection quickly ceases and a diurnal cycle of restratification and deepening is borne out. The diurnal heating cycle which drives convection is one of the aforementioned similarities between the OML and ABL.

Secondly, wind blowing over the surface of the ocean induces a tangential stress (wind stress) at the interface which generates a vertical flux of horizontal momentum. When the OML is neutrally or stably stratified, the momentum flux is large at the surface and decreases as depth increases. Viscous forces between the moving surface water and the relatively stationary water below drive a vertical shear and when the shear is sufficiently strong, turbulence is generated. There are a number of pathways through which the energy

input from the wind is dissipated (Wunsch and Ferrari, 2004). Wind-driven turbulence transfers energy to small-scales where it can be removed via molecular friction. Turbulent kinetic energy can also be used to mix the stable density profile, increasing the potential energy at the expense of kinetic energy. In addition, low frequency (near-inertial) internal waves carry momentum and energy into the ocean interior. Over timescales of about a day, the Coriolis acceleration deflects the wind-driven currents and an Ekman spiral forms. In the Northern Hemisphere, the surface layer transport points to the right of the wind stress and convergence and divergence of surface flow associated with variable wind forcing drives vertical motion in subsurface waters.

Winds also generate surface waves. Surface waves drive an orbital motion which directly contributes to the surface circulation. The depth dependence of the amplitude of the orbital motion induces a mean Lagrangian velocity profile in the direction of wave propagation, commonly referred to as Stokes drift (McWilliams et al., 1997; Stokes, 1847; Thorpe, 2004). The interaction between the Stokes drift and turbulence, known as the Craik-Leibovich interaction generates the well-known Langmuir circulations (Craik and Leibovich, 1976) characterised by large, coherent, counter-rotating vortices in the upper ocean which align with the direction of surface wind (Leibovich, 1983). When neighbouring vortices rotate away from each other, a divergent zone of upwelling is created between cells and when they rotate towards each other, a convergent zone of downwelling is created. The alternating regions of divergence and convergence can concentrate material in long windrows parallel to the wind direction which was first quantitatively observed by Langmuir (1938).

Breaking waves release momentum input by the wind into the water column in localised intermittent impulses, producing bubbles and sea spray. This dissipates energy and produces turbulence near the surface, which contributes to mixing. However, the intensity of turbulence is generally confined to a depth comparable to the breaking wave's amplitude, which is usually much smaller than the depth of the OML (Melville, 1996).

Finally, we note that compared to large-scale motion, the effect of the Earth's planetary rotation at small-scales is usually assumed to be negligible (Klinger and Marshall, 1995; Morton, 1966). The Rossby number characterises the relative importance of the Coriolis acceleration and the fluid inertia and is defined as $Ro \equiv U/(fL)$ where U and L are the characteristic scales of horizontal velocity and length, and f is the Coriolis parameter. When $Ro \gg 1$, flows are in a non-rotating regime with dynamics dominated by advection and diffusion. Horizontal scales smaller than a few hundred metres are characterised by a large Rossby number ($Ro \gg 1$), so rotational effects are generally assumed to be weak for small-scale, turbulent processes in the OML described above. Indeed, rotation is largely neglected

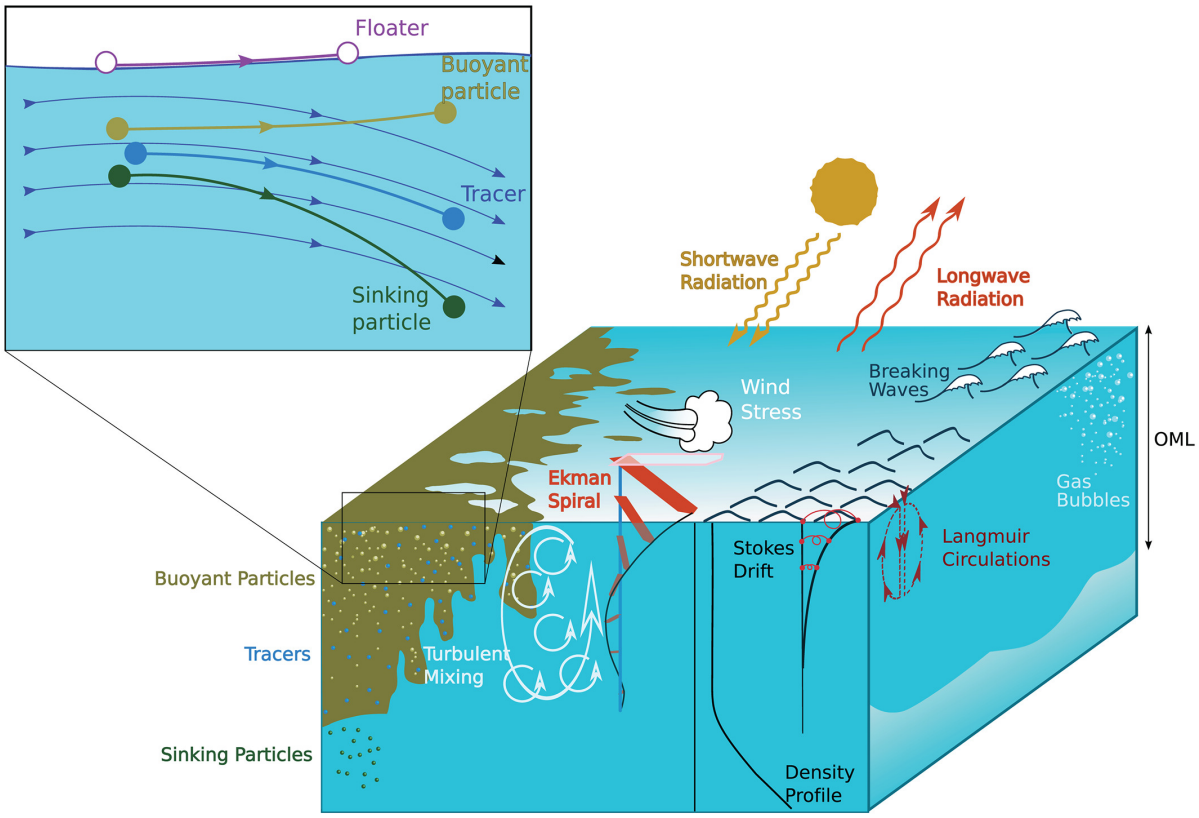

Fig. 1.2 Schematic of relevant processes for the transport of material in the OML including wind shear (which induces an Ekman spiral in the presence of rotation), buoyancy fluxes (driven by longwave and shortwave radiation) and breaking waves. The inset shows four different particle trajectories compared to flow streamlines: a surface floater (which we refer to as surface drifters), a buoyant particle, a neutral fluid tracer (or a neutrally buoyant particle - note that we use the term 'tracer' to describe a continuous Eulerian concentration field) and a sinking particle (negatively buoyant particle). Reprinted with permission from Chamecki et al. (2019).

in most studies of the OML (Chor et al., 2018a) and ABL (Stubley and Riopelle, 1988). The work presented in this thesis challenges this assumption.

1.2.2 Convective vortices

Before proceeding to larger scales, we provide a more extended discussion on features in buoyancy driven flows which constitutes a major aspect of chapters 3 and 4 in this thesis. In convective fluids, small 'convective vortices' with a vertical axis of rotation develop, particularly in the vertices joining two or more convective cells. Despite having been studied in the ABL for more than a century (Baddeley, 1860), only recently have oceanic simulations uncovered the presence of convective vortices akin to those observed in the atmosphere

(Chor et al., 2018a). Although this thesis predominantly focuses on oceanic applications, here we discuss convective vortices more generally to better contextualise and introduce this interesting phenomenon.

The most widely documented convective vortices occur in the terrestrial atmosphere. These are often made visible by entrained dust, sand and soil and for this reason, are commonly referred to as dust devils. Atmospheric convective vortices can also take the form of water spouts if they form over a body of water, or can occur in the absence of any visible tracers leading scientists to believe they are much more common than originally thought (Kanak, 2006). The upward moving, spiraling flow, as in figure 1.3a, is typically caused by insolation-induced heating of near-surface air. Wind speeds of dust devils are not high enough to significantly endanger humans, but their ability to lift mineral dust and aerosols makes them an important component of the climate system. For example, the transport of dust from the surface to the atmosphere is thought to be several orders of magnitude higher than the background dust flux when a dust devil is present (Renno et al., 2004). Consequently, dust devils have been considered in the global dust budget (Gillette and Sinclair, 1990; Han et al., 2016; Metzger et al., 2011; Tang et al., 2018), global radiation budget and the water and carbon cycle (Shao et al., 2011), and could be hazardous to low flying aircraft (Lorenz, 2012; Lorenz and Myers, 2005). The contribution of dust devils compared to boundary layer winds in the dust cycle is still under debate (Jemmett-Smith et al., 2015; Koch and Renno, 2005) and apart from in some arid regions, dust devils are thought to be only 'nuisance level' phenomena.

More recently, several landed spacecraft (e.g. VO, MPF-IMP) have observed convective vortices in the Martian atmosphere (Balme and Greeley, 2006; Ellehoj et al., 2010; Kahanpää et al., 2016; Metzger et al., 1999), an example of which can be seen in figure 1.3b. Although the structure of a Martian dust devil is similar to its terrestrial counter-part (Balme and Greeley, 2006; Metzger et al., 1999), they can be up to an order of magnitude larger and thus have a higher dust load which could pose challenges to future exploration of Mars (Balme and Greeley, 2006). As in the terrestrial case, they play an important role in the climate, surface-atmosphere interaction and dust cycle on Mars (Greeley et al., 2003; Toigo et al., 2003).

Convective vortices in the OML have only been reported in simulations within the last few years (Chor et al., 2018a) and, to our knowledge, have not yet been observed in the ocean. Chor et al. (2018a) suggests that oceanic convective vortices are resilient and coherent features of the flow (figure 1.3d) with a much longer persistence time than other surface flow structures. Additionally, convective vortices can advect buoyant particles such as microplastics and oil droplets, trapping them in small clusters at the surface (Chor et al.,

2018a) which could have strong implications for marine life (Compa et al., 2019; Wilcox et al., 2015).

Although some properties may differ between convective vortices in different settings, there are several similarities worth noting. Similar to Rayleigh-Benard convection, atmospheric and oceanic convection is often characterised by a regular, hexagonal-like (Busse, 1978; Mason, 1989) pattern with narrow and intense convergent plumes surrounding large, weak areas of diverging fluid. It is within the narrow, convergent regions where the convective vortices are most frequently found, particularly in the vertices joining two or more convective cells (Chor et al., 2018a; Raasch and Franke, 2011). The centre of a convective vortex is marked by a local maximum of vorticity, a minimum of pressure and a change in the direction of horizontal velocity (Sinclair, 1969). An example of the instantaneous three-dimensional structure of a simulated convective vortex is visualised in figure 1.3c, which uses Lagrangian particles, analogous to dust particles in dust devils, advected with the velocity field and reveals the inwards spiraling, tube-like flow pattern. Efforts to understand the formation mechanism of convective vortices remain inconclusive, with favoured theories being the so-called 'hairpin' mechanism (Kanak, 2006; Renno et al., 2004), or the concentration of vertical vorticity by general flow convergence. Difficulties arise in explaining why they form in the absence of mean winds or surface inhomogeneities, and why vortices preferentially appear at the vertices between convective cells. Finally, whether convective vortices have a preferred sense of rotation is a long-debated topic (Durward, 1931; Sinclair, 1965). It is often assumed that planetary rotation does not have a direct influence on convection in boundary layers in the atmosphere and ocean (Klinger and Marshall, 1995; Morton, 1966; Stubley and Riopelle, 1988). The general consensus in the atmosphere is that there is no rotational bias (Raasch and Franke, 2011), which agrees well with the conventional view that convective vortices are too small to be affected by planetary rotation (Morton, 1966).

1.2.3 Submesoscale fronts

Submesoscale dynamics fall between the small-scale, turbulent processes and the rotationally-dominated, geostrophically-balanced large-scale motions and develop in a regime of weak stratification such as the OML (Thomas et al., 2008). Flows at the submesoscale level are usually visible as smaller eddies at the periphery of mesoscale eddies, or along temperature or salinity fronts and filaments. Typically characterised by $Ro \sim 1$, Earth's rotation is important but does not constrain motion as strongly as at the larger scales, allowing for some three-dimensional motion. This enables flows at the submesoscale level to develop strong horizontally convergent surface currents and strong vertical velocities (Mahadevan and Tandon, 2006) which could stimulate the subduction of surface waters to the interior

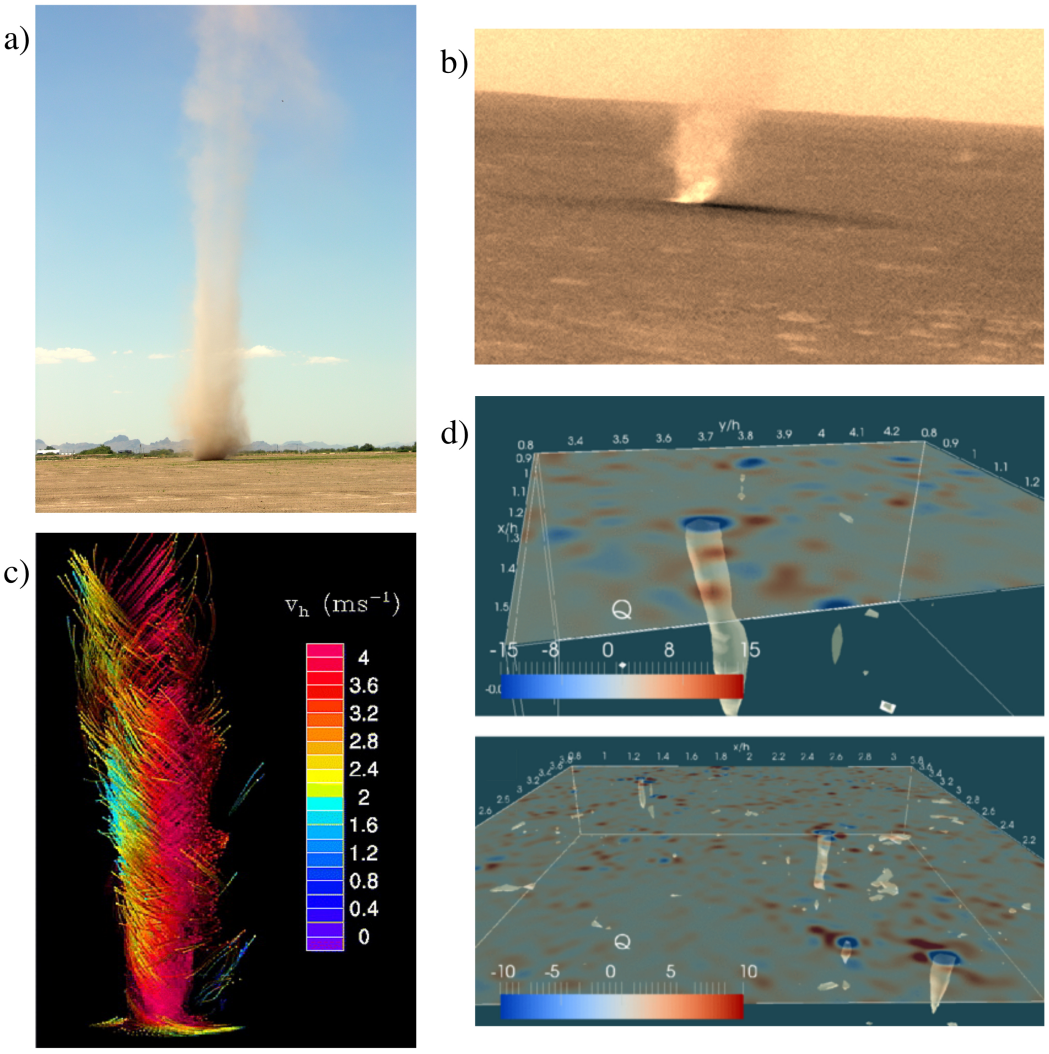

Fig. 1.3 (a) A dust devil in the Arizona desert on June 10, 2005 (NASA); (b) a dust devil on Mars photographed by the Spirit rover on the 486th day of the Martian year (NASA); (c) flow visualisation of a convective vortex in the atmosphere using trajectories of particles moving passively with the flow (reproduced with permission from Raasch and Franke (2011)); (d) visualisation of several vertical vortices in a small region of an oceanic convection simulation with colour contours of the 2D Okubo parameter at the top surface (reproduced with permission from Chor et al. (2018a)).

(Capet et al., 2008; Lévy et al., 2012; Thomas et al., 2008), or enhance nutrient supply and the exchange of dissolved gases with the atmosphere. In contrast to the well-studied large and small-scale processes in the OML, research on the impacts of submesoscales are limited to the last two decades and much remains unknown.

Submesoscales arise in the upper ocean through a variety of mechanisms including unforced instabilities, such as the ageostrophic baroclinic instability (Boccaletti et al., 2007; Molemaker et al., 2005), forced instabilities, for example through surface winds, waves or heat fluxes at the boundaries (Tandon and Garrett, 1994) or frontal sharpening (frontogenesis). Due to the relative importance of rotation, inertia and stratification, submesoscales are associated with a dual energy cascade transferring energy both up-scale and down-scale (Capet et al., 2008; Molemaker et al., 2010). Firstly, energy can move up scales due to an inverse 2D cascade or via geostrophic turbulence (Salmon, 1980). More interestingly, submesoscales play a key role in the forward energy cascade, which has been an ongoing conundrum in geophysical fluid dynamics (McWilliams et al., 2001). The instabilities associated with submesoscale dynamics draw their energy from kinetic and potential energy reservoirs stored in mesoscale features and transfer it to smaller scales where it can be dissipated through secondary instabilities and three-dimensional processes (Boccaletti et al., 2007; Capet et al., 2008; Klein et al., 2008).

A front is an elongated region of fluid with an abrupt change in density in one horizontal direction, typically known as the 'cross-front' direction, but a weak density gradient in the perpendicular direction (the 'along front' direction) (Hoskins, 1982). Although fronts are commonplace in both larger (e.g. western boundary currents or the Antarctic Circumpolar Current) and smaller scales (e.g. shelf break and tidal fronts), the $\mathcal{O}(1)$ Rossby number at the submesoscale level rapidly intensifies submesoscale fronts making them amongst the strongest in the OML (McWilliams, 2016; Shakespeare and Taylor, 2014). Submesoscale fronts are associated with large vertical velocities which act to increase the transport of tracers (e.g. heat, carbon dioxide, nutrients, pollutants) into the ocean interior. The enhanced communication between the atmosphere and ocean (Taylor and Thompson, 2023) means that submesoscales are often hotspots for biological activity (Ferrari, 2011; Thomas et al., 2008).

Submesoscale fronts tend to exist as relatively stable and long-lived features of the ocean that can last for several days. The density gradient across the front is associated with a pressure gradient which can be partly balanced by the Coriolis acceleration, arising due to the rotation of the Earth. If the pressure gradient and Coriolis acceleration are in exact geostrophic balance, we observe flow along the front. When the pressure field is also in hydrostatic balance, flow is often said to be in thermal wind balance (originally derived in the atmospheric framework).

Geostrophic balance can be disrupted by background flows (such as eddies) or external forcing (such as buoyancy fluxes or wind stress). The process by which an unbalanced flow tends to evolve back towards geostrophic balance is known as geostrophic adjustment, also commonly referred to as Rossby adjustment. This was first introduced by Rossby (1937) who considered a wind-driven momentum imbalance and found that for a relatively weak imbalance, a secondary, ageostrophic circulation is generated about the front that restores the flow back to a balanced geostrophic state by tilting the isopycnals toward the horizontal, bringing light fluid over the top of dense fluid. Later studies (Tandon and Garrett, 1994) showed that a change in the buoyancy of a fluid layer (which could be driven by insolation, precipitation or a storm) leads to a pressure imbalance and also stimulates geostrophic adjustment and a corresponding secondary circulation.

In 1984, Ou (1984) used a Lagrangian framework to study the geostrophically adjusted state of an initially motionless fluid with non-constant buoyancy gradients. Ou's results demonstrated that the secondary circulations associated with geostrophic adjustment can produce regions of strong convergence where pre-existing density gradients are steepened. When the initial density gradient is sufficiently sharp, Ou's analysis revealed the possibility for the formation of singularities in the inviscid equations at the region of strong convergence and in this case, a geostrophically adjusted state does not exist. Blumen and Wu (1995) extended Ou's work by putting the above formulation into the Eliassen (1962) momentum co-ordinate framework to determine the solution for the adjusted steady state in the case of uniform potential vorticity flow. Even still, questions about the larger imbalance case remain (Plougonven and Zeitlin, 2005). In chapters 5 and 6, we use numerical simulations to study geostrophic adjustment and use these to compare and contrast the geostrophically balanced state with Ou (1984) for weak imbalances, and explore the very sharp density gradients that arise during frontogenesis for larger imbalances.

1.3 Modelling the ocean mixed layer

Observing small-scale, turbulent processes in the OML is very difficult due to the rapid evolution and small length-scale of these features. They are often masked by larger, non-turbulent motions such as surface and internal waves which are present across the entire layer and cannot be easily separated from the turbulent motions of interest (D'Asaro, 2014). It is difficult to take measurements since velocities generated by a moving ship (or similar platform) are much larger than the turbulent velocities of interest at the surface. Some success has been achieved with instruments such as Lagrangian floats (D'Asaro, 2003; D'Asaro et al., 1996), multibeam acoustic Doppler current profilers (Gargett and Wells, 2007; Thomson et al.,

2009) and fast-response sensors on vertical or horizontal profiling instruments (Gregg, 1998) but it remains challenging to assess the effects of a single ocean process under controlled conditions. Partly due to these difficulties, computational methods are an important tool in understanding OML dynamics.

Like most computational fluid dynamics problems, we begin with the classical Navier–Stokes equations. For an incompressible fluid under the Boussinesq approximation (where we assume that changes in density are small compared with the mean density of the fluid for buoyancy-driven flows), the equations for velocity $\mathbf{u} = (u,\ v,\ w)$, pressure p and buoyancy b are:

$$\nabla \cdot \mathbf{u} = 0, \tag{1.1}$$

$$\frac{\mathrm{D}\mathbf{u}}{\mathrm{D}t} + \mathbf{f} \times \mathbf{u} = -\frac{1}{\rho_0}\nabla p + \nu \nabla^2 \mathbf{u} + b\,\widehat{\mathbf{z}} + \mathbf{F}(x,y), \tag{1.2}$$

$$\frac{\mathrm{D}b}{\mathrm{D}t} = \kappa_b \nabla^2 b \ . \tag{1.3}$$

In equation (1.2), $\mathbf{f}$ is the Coriolis force, ν is the molecular viscosity, ρ_0 is the reference density, $\mathbf{F}(x,y)$ is a spatially-varying body force, $\nabla = (\partial/\partial x, \partial/\partial y, \partial/\partial z)$, $\widehat{\mathbf{z}} = (0,0,1)$ is the basis vector in the positive z direction, and $\mathrm{D}/\mathrm{D}t = \partial/\partial t + \mathbf{u} \cdot \nabla$ is the material derivative. In equation (1.3), κ_b is the molecular diffusivity for buoyancy. To solve this system of equations numerically, two different discretisations are required; we need to approximate the flow field on a discrete set of spatial points and we need to advance the equation in time using discrete time-steps. An ongoing challenge of the numerical approach is how to best choose the number of spatial points and time-steps; too few points or time-steps can result in an inaccurate, unstable simulation but too many can be prohibitively computationally expensive. Depending on the length and time-scale of the process being modelled, we have to find a practical balance.

To model the roughly nine orders of magnitude difference in scales in the OML would require a very large domain to capture the largest scales, but a very fine grid discretisation to ensure that the smallest scales are also resolved. The computational power required for this is so large that a simulation which truly captures the full range of processes is unfeasible for the foreseeable future (Pope, 2001). To overcome this obstacle, studies typically use one of two approaches, which prioritise either the large-scale or small-scale motions. The first approach consists of running large-domain, global or regional models and parameterising the small-scale processes. The difficulty of observing OML phenomena means that many such parameterisations have been adapted from the ABL (Large et al., 1994) which sometimes leads to incorrect modelling or omission of processes that are unique to the ocean. For

example, studies have expressed a need for parameterising mixing generated in Langmuir turbulence (McWilliams and Sullivan, 2000; McWilliams et al., 1997) which is missed in an ABL parameterisation. Large domain models are the most applicable to studies of mesoscale processes and the associated material transport at this level (Dauhajre et al., 2017; Uchiyama et al., 2017). The second approach targets small-scale processes by focusing on a small domain and disregarding the larger-scale phenomena. In this setup, it is common to isolate one or two small-scale processes, for example simulating either Langmuir dominated regimes or convective dominated regimes. Although it may be challenging to obtain a full picture of how different processes interact, the controlled, systematic approach allows us to explore each process in detail and fully understand the physics and its effects. This can in turn inform the larger-scale models which parameterise the effects of small-scale processes.

Throughout this thesis, we take the latter approach and run numerical experiments with horizontal scale $\mathcal{O}(100\text{ m})$. Even still, challenges remain in choosing the spatial and temporal resolution small enough to be computationally efficient, but large enough to capture enough information about the desired system. Consider as an example the case of convective vortices. Since convective vortices are not isolated phenomena but are part of a convective system, we need to resolve scales of the whole convective layer as well as capturing the much smaller convective vortices. This limits the resolution of a convective vortex to only a couple of grid points (Chor et al., 2018a; Giersch et al., 2019). Below, we outline two of the main numerical methods used to tackle such problems.

1.3.1 Direct numerical simulations

A direct numerical simulation (DNS) is a technique that solves the governing equations (1.1)-(1.3) 'exactly' without any turbulence model. This minimises numerical artefacts that could be introduced and unwittingly interact with the physical phenomena we want to study. To ensure the equations are solved accurately, we need to make the spatial and temporal resolution to be small enough to capture the very smallest and fastest evolving features. We can estimate the smallest scale of turbulence using the Kolmogorov scale, η_K, defined as

$$\eta_K \sim \left(\frac{\nu^3}{\varepsilon}\right)^{1/4}, \tag{1.4}$$

where ν is the molecular viscosity and ε is the viscous dissipation of kinetic energy (Kolmogorov, 1962, 1991). The fastest time-scale of turbulence is estimated as

$$t_\eta \sim \left(\frac{\nu}{\varepsilon}\right)^{1/2}. \tag{1.5}$$

For flows with a wide range of scales, it quickly becomes difficult to resolve a simulation down to the Kolmogorov scale in every direction. One way to circumvent this is to choose an artificially high value of viscosity which forces the Kolmogorov scale to be more attainable. However, ν is then much larger than the true molecular value which somewhat clouds the interpretation of the simulations. We can view these simulations in two ways. Firstly, we can simply interpret them as low Reynolds number simulations. Secondly, we can view the larger value of viscosity as an eddy viscosity which is associated with unresolved turbulence in the mixed layer. In chapter 5, we use DNS and take the latter approach. Even still, the high computational expense associated with DNS limits the parameter space and domain size that we can feasibly consider.

1.3.2 Large eddy simulations

Oftentimes DNS is still prohibitively computationally expensive simply because we do not have enough computational resources to resolve down to the Kolmogorov scale. In the past few decades, large eddy simulations (LES) have been adopted in ocean modelling (McWilliams et al., 1997; Skyllingstad and Denbo, 1995) which have enabled high-fidelity simulations that capture three-dimensional turbulence with a good level of accuracy. Coupled with the recent progress in parallel computing, LES can tackle problems with a wider range of scales than DNS, such as those associated with OML turbulence.

Whilst DNS resolves all scales of motion, LES only resolve scales larger than a prescribed length-scale (usually termed the filter width) set by the grid spacing, and model the influence of any smaller scales using a parameterisation scheme. Comprehensive reviews of LES can be found in Lesieur and Metais (1996), Meneveau and Katz (2000), and Sagaut (2006). This modelling approach lies in between DNS and the less accurate Reynolds averaged Navier Stokes (RANS) approach, where all turbulence is parameterised. We use the LES approach in chapters 3, 4 and 6.

In an LES, the Navier-Stokes equations are filtered in space modifying equations (1.1 -1.3) to:

$$\nabla \cdot \overline{\mathbf{u}} = 0 \,, \tag{1.6}$$

$$\frac{\mathrm{D}\overline{\mathbf{u}}}{\mathrm{D}t} + \mathbf{f} \times \overline{\mathbf{u}} = -\frac{1}{\rho_0}\nabla \overline{p} + \nu \nabla^2 \overline{\mathbf{u}} + \overline{b}\,\widehat{\mathbf{z}} + \mathbf{F}(x,y) - \nabla \cdot \boldsymbol{\tau} \,, \tag{1.7}$$

$$\frac{\mathrm{D}\overline{b}}{\mathrm{D}t} = \kappa_b \nabla^2 \overline{b} - \nabla \cdot \boldsymbol{\lambda} \,, \tag{1.8}$$

where $\overline{\mathbf{u}}$ indicates the filtered velocity, more formally defined as $\mathbf{u} = \overline{\mathbf{u}} + \mathbf{u}_{SGS}$ where $\mathbf{u}_{SGS}$ is the sub-grid scale (SGS) velocity. The pressure and buoyancy fields are decomposed

similarly as $b = \overline{b} + b_{SGS}$ and $p = \overline{p} + p_{SGS}$. LES solve for $\overline{\mathbf{u}}$ on a discretised grid and model contributions of $\mathbf{u}_{SGS}$. In particular, $\boldsymbol{\tau}$ in equation (1.7) and $\boldsymbol{\lambda}$ in equation (1.8) represent the effect of the sub-filter scales on the filtered velocity and buoyancy. By only resolving the filtered velocity, the number of grid points is significantly smaller which reduces the overall computational cost of the simulation.

There are many possible choices of models for $\boldsymbol{\tau}$ and $\boldsymbol{\lambda}$. Studies of OML turbulence often use an eddy-viscosity model (Smagorinsky, 1963) where $\boldsymbol{\tau} = -2\nu_{SGS}|\mathbf{S}|$ for the resolved strain-rate tensor, $\mathbf{S}$, and $\boldsymbol{\lambda} = -\kappa_{SGS}\nabla b$. Under this configuration, the aim is to develop a model for the SGS viscosity, ν_{SGS}, and the SGS scalar diffusivity, κ_{SGS}. Typically, models assume that the SGS Prandtl number $Pr_{SGS} = \nu_{SGS}/\kappa_{SGS} = 1$, so we only need to model ν_{SGS}. Common choices often include the Smagorinsky model (Smagorinsky, 1963), dynamic Smagorinsky model (Germano et al., 1991) or Deardorff 1.5 closure (Deardorff, 1973), which we review briefly below. The choice of SGS model is important; although the mean fields are fairly insensitive to the SGS model, second-order statistics and behaviour near the boundaries are more significantly affected (see as an example the comparison between McWilliams et al. (1997) and Yang et al. (2015) for a Langmuir turbulent regime). In the ABL, the effects of different SGS models have been compared at length (Bou-Zeid et al., 2005; Mirocha et al., 2014) and given the importance of small-scale turbulence near the surface of the ocean, a similar comparison for the OML remains a desirable topic of research, although not one addressed here.

The constant Smagorinsky model is one of the oldest and most frequently used SGS models (Smagorinsky, 1963). Here, the SGS viscosity is $\nu_{SGS} = (C_s\Delta)^2|\mathbf{S}|$ where Δ is the filter width and C_s is the Smagorinksy constant (usually taken as $C_s = 0.13$ as suggested by Deardorff (1970)). However, the constant Smagorinsky model typically performs poorly in laminar flows where the SGS energy is very small. To address this, the dynamic Smagroinksy model was derived by Germano et al. (1991), which calculates the SGS viscosity in the same way as the Smagorinsky model, but allows the coefficient C_s to vary in space and time. The dynamic coefficient is estimated by a comparison of scales between a test case filter and the original LES filter width. This model performs better in laminar flows, but is highly computationally expensive and can be numerically unstable. More recently, the anisotropic minimum dissipation (AMD) model has been developed by Rozema et al. (2015) following Abkar et al. (2016). This model seeks to minimise the eddy viscosity required to dissipate the SGS energy, whilst also maintaining separation between large and small scales of motion. Specifically, ν_{SGS} depends on invariants of the resolved rate of strain and rate of rotation tensors, whose full expression is given in Vreugdenhil and Taylor (2018). In chapter 3 and 4, we use the AMD model to ensure energy is not overly dissipated in wind-driven flows. In

contrast, chapter 6 employs the constant Smagorinsky model for ease of comparison with the DNS presented in chapter 5, and to reduce numerical noise near the surface. Further specifics about the SGS model choice are presented in appendix 6.A.

All simulations conducted as part of this thesis use the numerical solver DIABLO, originally developed by Taylor (2008) and Bewley (2019). MPI parallelisation enhances computational efficiency, horizontal derivatives are computed using pseudospectral methods and fast Fourier transforms (FFT) in the horizontal directions and centred second-order finite difference in the vertical direction, and time-stepping is achieved through a combination of the explicit third-order Runge–Kutta method and Crank–Nicolson method.

1.4 Material transport

The challenges in modelling the OML also have repercussions on the study of material transport, of which there are again limited observations due to the short time-scales and small length-scales involved. We broadly define material to include solid particles, liquid droplets (in a gas), and gas bubbles (in a liquid). Material that is small enough to be treated as a point particle (i.e. the geometry doesn't matter) is termed a particle. Particles that are less dense than sea water are positively buoyant, and tend to remain close to the surface of the ocean (e.g. microplastics, oil droplets, sargassum, some phytoplankton cells). We refer to buoyant particles that stay on the surface and never move off as surface particles, sometimes also known as surface drifters or floaters. Neutrally buoyant particles have the same density as sea water and their motion tracks that of fluid particles. Particles which have a density greater than seawater are termed sinking particles (e.g. suspended sediments), and self-propelled particles which can produce their own motion are known as active particles (e.g. swimming plankton). A summary of this is given in the inset of figure 1.2 where the only distinction is that 'tracer' is used to describe a neutrally buoyant particle. In this thesis, our attention is primarily devoted to buoyant particles, examples of which include microplastics, oil droplets and some phytoplankta.

1.4.1 Particle equations of motion

Similar to the Navier-Stokes equations for a fluid, we need an equation of motion to model the movement of particles. We begin by describing some further details about properties of particles before introducing the relevant equations below. The difference between the particle velocity, w_p and the vertical fluid velocity, w is called the slip velocity, $w_s = w_p - w$, also known as the terminal rise velocity or free-fall velocity. This characterises how positively

or negatively buoyant a particle is. For buoyant particles which are our primary focus, w_s is positive. If the slip velocity exceeds the local downwards vertical velocity, that is $w_s + w > 0$, the particle moves upwards. Similarly, if $w_s + w < 0$ then the particle moves downwards. Examples of typical values of the slip velocity are $w_s \simeq 5 - 25$ mm/s for microplastics (Kukulka et al., 2012), $w_s \simeq 8 - 300$ mm/s for oil droplets (Chor et al., 2018a) and $w_s \simeq 0.27$ mm/s for the marine species Noctiluca scintillans (Tiselius and Kiørboe, 1998). Contrast this with an estimate of the vertical velocity in the OML such as Langmuir circulations which have an average vertical velocity of about $10 - 200$ mm/s (Harcourt and D'Asaro, 2008; Leibovich, 1983; Weller and Price, 1988), breaking waves which have an average vertical velocity of about 50 mm/s (Sullivan et al., 2007) or submesoscales which have a vertical velocity of about 10 mm/s (D'Asaro et al., 2018; Taylor, 2018). Overall, we estimate the root mean square vertical velocity in the OML to be $w_{rms} = \simeq 1 - 100$ mm/s which places the particle slip velocity in the middle of the typical range of the vertical velocity. To simplify modelling, most studies hold w_s constant (D'Asaro, 2008; Lande and Wood, 1987; Ruiz, 1996) which is equivalent to assuming the particle has constant size and density. In reality there are many factors including biofouling, chemical degradation or mechanical abrasion which change w_s and can even turn buoyant particles into sinking particles (Kooi et al., 2017; Long et al., 2015), although on much longer time-scales than we consider here.

In most practical applications, the volume fraction and mass loading of particles is small. Here, we assume it is sufficiently small that we can neglect both interactions between the particles and neglect the effect of particles on the flow. This approach is often referred to as one way coupling (Balachandar and Eaton, 2010), or a passive dispersed phase. Note this means that although the particles themselves may be buoyant, they do not affect the fluid buoyancy.

The motion of small, inertial, spherical particles immersed in a turbulent flow field is described by the Maxey-Riley equation (Maxey and Riley, 1983). The starting point for most studies is a somewhat simplified version of the particle equation (Balkovsky et al., 2001; Chamecki et al., 2019) where the Faxen correction, Basset history force and lift force are neglected on the basis that the radius of the particle is much smaller than the scales over which the fluid velocity changes (i.e. particle radius is much smaller than the Kolmogorov scale). Brownian motion is also neglected since the focus is on sufficiently large scales that this factor is unimportant. Under these assumptions, the particle velocity, $\mathbf{v}_p$, satisfies the following equation:

$$\frac{\mathrm{d}\mathbf{v_p}}{\mathrm{d}t} = -\frac{\mathbf{v_p} - \mathbf{u}}{\tau_p} + \frac{w_s}{\tau_p}\widehat{\mathbf{z}} + \left(1 + \frac{w_s}{\tau_p g}\right)\frac{\mathrm{D}\mathbf{u}}{\mathrm{D}t}, \tag{1.9}$$

where $\mathbf{u}$ is the fluid velocity, τ_p is the particle response time and w_s is the terminal slip velocity. Even still, solving this equation requires evolving a complicated set of differential equations and further simplification is not only desirable but often necessary for modelling purposes. Similar to other studies of particles in OML turbulence (Chamecki et al., 2019; Yang et al., 2014), we make three further assumptions outlined below.

Firstly, we consider the particle Reynolds number, $Re_p = |\mathbf{v}_p - \mathbf{u}|d_p/\nu$ (where d_p is the particle diameter) which characterises the relative importance of viscous drag and fluid inertia on a particle. When $Re_p \ll 1$, particles are described as being in the Stokes regime. Under this regime, the drag force and buoyancy force on a small spherical particle are given by (Balachandar and Eaton, 2010; Yang et al., 2016):

$$F_D = \frac{1}{8}\rho_f|\mathbf{v}_p - \mathbf{u}|^2\pi d_p^2 C_d \ , \tag{1.10}$$

$$F_B = \frac{1}{6}(\rho_f - \rho_p)g\pi d_p^3 \ . \tag{1.11}$$

Here, ρ_f is the fluid density, ρ_p is the particle density and $C_d = 24Re_p^{-1}$ is the Stokes drag coefficient. We assume that there is an exact balance between the drag and buoyancy and no other forces contribute. Equality between equation (1.10) and equation (1.11) yields an expression for the particle response time, τ_p, and terminal slip velocity, w_s, which can be written as:

$$\tau_p = \frac{(\rho_p + \rho_f/2)d_p^2}{18\mu_f} \ , \tag{1.12}$$

$$w_s = \frac{(\rho_p - \rho_f)gd_p^2}{18\mu_f} \ , \tag{1.13}$$

where μ_f is the dynamic viscosity of the fluid. Since the particles under consideration move passively with the flow, we assume that the timescale for particle acceleration is much longer than the particle response time to the fluid, i.e. $|\mathrm{d}\mathbf{v}_p/\mathrm{d}t| \ll |\mathbf{v}_p/\tau_p|$. Then the first term in equation (1.9) is negligible and our governing equation becomes,

$$\mathbf{v}_p = \mathbf{u} + w_s\widehat{\mathbf{z}} + \left(\tau_p + \frac{w_s}{g}\right)\frac{\mathrm{D}\mathbf{u}}{\mathrm{D}t}. \tag{1.14}$$

Secondly, we consider the Stokes number, which characterises the tendency of a particle to move with the fluid velocity. The Stokes number is defined as the ratio between the particle response time and the turbulence timescale (the shortest fluid timescale of interest), $St \equiv \tau_p/\tau_t$. A very small Stokes number indicates that the particle motion is strongly influenced by the fluid flow whilst a large Stokes number indicates that the particle moves

independently of the fluid. The Stokes number for microplastics has been estimated to be between $\mathscr{O}(10^{-3})$ and $\mathscr{O}(10^{-2})$ at the surface (Chamecki et al., 2019; Kukulka et al., 2012) which corresponds to a particle size of about 1cm or less (Poulain et al., 2018). In the limit where $St \ll 1$, $|\mathrm{D}\mathbf{u}/\mathrm{D}t| \ll |\mathbf{u}/\tau_p|$ and equation (1.14) can be further approximated as (Ferry and Balachandar, 2001; Sutherland et al., 2023; Yang et al., 2016):

$$\mathbf{v}_p = \mathbf{u} + w_s\widehat{\mathbf{z}} + \frac{w_s}{g}\frac{\mathrm{D}\mathbf{u}}{\mathrm{D}t} \,. \tag{1.15}$$

The last term on the right-hand side is the leading-order inertial effect. Similarly to Chor et al. (2018a), we are interested in flows for which fluid acceleration is small compared to gravity, i.e. $g^{-1}\mathrm{D}\mathbf{u}/\mathrm{D}t \ll 1$. This gives our final particle motion equation as

$$\mathbf{v}_p = \mathbf{u} + w_s\widehat{\mathbf{z}}, \tag{1.16}$$

which describes the motion of particles for which inertial effects are negligible compared to flow advection and buoyancy effects.

In some scenarios, the applicability of this simplified equation is limited. For example, the lift force and Basset history force terms are not always negligible (Fraga and Stoesser, 2016; Guseva et al., 2016), and inertial effects may play a role near the surface of the OML when wave breaking occurs. If particles are nonspherical, reassessment of the form of F_D and F_B is required, which will depend on the particle geometry, roughness and orientation in the flow (Bagheri and Bonadonna, 2016; Loth, 2008). In most cases, the additional effects of neglected terms would severely increase computational cost and only have a very small impact on results (Yang et al., 2014), so we proceed using the simplified equation (1.16) to model particle motion throughout this thesis.

1.4.2 Eulerian approach

In the Eulerian approach, the concentration of buoyant particles is modelled via a continuum approximation which considers the behaviour of the whole concentration of particles rather than the behaviour of each individual particle. We use the term tracer to describe such a concentration field, which has previously been used to model microplastics (Kukulka and Brunner, 2015), oil droplets (Yang et al., 2014) and phytoplankton cells (Smith et al., 2016). A continuous version of equation (1.16) is given by:

$$\frac{\mathrm{D}c}{\mathrm{D}t} + w_s\frac{\partial c}{\partial z} = \kappa_c\nabla^2 c \,, \tag{1.17}$$

where c is the tracer field and κ_c is the tracer diffusivity. For LES, the equation includes an additional sub-grid scale term:

$$\frac{\mathrm{D}\overline{c}}{\mathrm{D}t} + w_s \frac{\partial \overline{c}}{\partial z} = \nabla \cdot ((\kappa_c + \kappa_{sgs}) \nabla \overline{c}), \tag{1.18}$$

where κ_{sgs} is the sub-grid scale diffusivity. One advantage of this approach is that the equation for the tracer can be solved alongside the velocity and buoyancy field equations of motion (Yang et al., 2014). Additionally, the SGS term can be handled as an extension to the SGS models used for the buoyancy (or temperature/salinity) field. Some studies also include a particle feedback term by adding a Boussinesq-approximated buoyancy force onto equation (1.17) which extends the applicability to two-way coupled materials (Liang et al., 2012; Yang et al., 2015).

However, this approach does not come without disadvantages. Although the total tracer concentration is conserved, a small number of negative concentration values can occur due to Gibbs ringing at the grid-scale and the meaning of negative concentrations is entirely nonphysical. For large values of w_s, the buoyant tracer strongly accumulates near the surface, leading to difficulties in resolving vertical gradients.

1.4.3 Lagrangian approach

Alternatively, we can solve equation (1.16) directly for a set of individual particles and track the position of each one, which is known as the Lagrangian approach. The flow is seeded with a large number of particles whose position, $\mathbf{x}_p$, evolves according to the time-stepped version of equation (1.16),

$$\mathbf{x}_p(t+dt) = \mathbf{x}_p(t) + \mathbf{u}(\mathbf{x}_p, t)dt + w_s dt\, \widehat{\mathbf{z}}\,. \tag{1.19}$$

In LES, the effects of SGS terms can be accounted for by including an additional SGS modelling term:

$$\mathbf{x}_p(t+dt) = \mathbf{x}_p(t) + \overline{\mathbf{u}}(\mathbf{x}_p, t)dt + w_s dt\, \widehat{\mathbf{z}} + \mathbf{x}_{sgs}(\mathbf{x}_p, t)\,, \tag{1.20}$$

where the random displacement model for $\mathbf{x}_{sgs}$ can be chosen circumstantially. For example, in the ABL, a Lagrangian stochastic model (LSM) has been used for $\mathbf{x}_{sgs}$ (Weil et al., 2004). In the OML, consideration of the SGS term has been largely neglected without much justification (Noh et al., 2006). However recently, introduction of a random displacement model (Liang et al., 2018) and an ocean based LSM (Kukulka and Veron, 2019) have shown

the importance of the SGS component on particle trajectories and the necessity for their inclusion. We implement a random displacement model following Liang et al. (2018) which we describe in chapter 2.

The earliest papers which investigate material transport in the OML were somewhat limited by computational requirements forcing the use of two-dimensional surface particles. These are often interpreted as the limit of extremely buoyant particles when $w_s \gg |w|$. Confining the particles to the surface allows easy visualisation of distinct flow features such as surface convergence or patterns of accumulation. For example, long, narrow windrows which constitute one of the most recognisable characteristics of Langmuir turbulence were originally illustrated using surface particles (McWilliams and Sullivan, 2000; McWilliams et al., 1997; Skyllingstad, 2000; Skyllingstad and Denbo, 1995). It is only in the last few decades that studies have progressed beyond surface particles and have started to investigate the behaviour of buoyant (Kukulka et al., 2012) and sinking (Noh et al., 2006) three-dimensional particles. Surface particles remain a useful tool which we make use of in chapters 3 and 4, before using three-dimensional buoyant particles in chapter 6.

There are some clear advantages of the Lagrangian approach. Tracking the position, velocity and other properties of a large number of individual particles gives a wealth of data about how particles are transported within a turbulent fluid system. This approach also provides a different perspective of the flow compared to the Eulerian framework which the velocity and buoyancy fields are solved in, allowing us to look at complicated physical phenomena in more than one way. Since all particles are advected independently, it is easily parallelisable and straightforward to implement (Liang et al., 2011). Compared to the Eulerian approach, we aren't limited by numerical noise for large values of w_s. However, issues arise when the number of particles to be simulated is very large, which is sometimes needed to ensure that results are statistically converged. This is particularly problematic when particles cover the whole three-dimensional space.

1.4.4 Accumulation of buoyant material

Buoyant material is generally not uniformly distributed in the OML but instead accumulates near the surface in regions of strong convergence. On the global scale, convergent wind-driven currents cause microplastics to accumulate in mid-ocean gyres (Cole et al., 2011; Eriksen et al., 2017) leading to well-known 'garbage patches'. At the submesoscale, strongly convergent flow causes oil and surface particles to accumulate in narrow (10-100m) density fronts (D'Asaro et al., 2018; Taylor, 2018). Finally, at the small, turbulent scales, wind and buoyancy-driven turbulence drive buoyant particles to accumulate in ephemeral patches and

streaks. Again, we focus on accumulation at the submesoscale level and below, sequentially providing examples of accumulation in some of the most common oceanic conditions.

One of the most widely observed and striking examples of accumulation at the smallest scales are the narrow, streak-like pattern of particles in the convergent regions of Langmuir cells. Figure 1.4a shows the effect of an oil spill from a deep-water blowout interacting with Langmuir turbulence. Here, the patches of oil are confined to the characteristic Langmuir windrows. Early LES with surface particles captured this in numerical models (McWilliams and Sullivan, 2000; McWilliams et al., 1997; Skyllingstad, 2000), an example of which can be seen in the second panel of figure 1.4b (Skyllingstad and Denbo, 1995) where the velocity has transported most of the surface particles into thin, distinct lines. More recent simulations have revealed that behaviour is similar for three-dimensional buoyant particles under Langmuir turbulence (Kukulka et al., 2012; Liang et al., 2012), although the degree of particle accumulation in the windrows is heavily impacted by the particle buoyancy (Yang et al., 2014), with the more buoyant tracer being more strongly clustered. The relatively strong vertical velocities associated with Langmuir circulations can also submerge buoyant particles deep into the OML (Kukulka and Brunner, 2015; Kukulka et al., 2016).

Particles accumulate in convergent regions associated with other small-scale turbulent processes, although with somewhat less striking patterns. In contrast to the relatively straight accumulation lines in the second panel of figure 1.4b, the first panel shows more random, less aligned accumulation of surface drifters under a combination of wind shear and convective forcing from early LES (Skyllingstad and Denbo, 1995). Under these conditions, there is a distinguishable flow transition from convective cells to longitudinal wind rolls as wind forcing is added to a convective regime, with three distinct flow patterns being observed under weak, moderate and strong wind forcing (Heitmann and Backhaus, 2005). Mensa et al. (2015) produced similar patterns of accumulation using low-resolution RANS. They found that under pure convection, buoyant tracer accumulates in convergent regions of convective cells and with the additional presence of weak wind forcing, tracer accumulates in downwelling regions of distorted convection cells. In the absence of convective forcing, Kukulka et al. (2012) used observations and a one-dimensional column model to study wind-driven vertical mixing of plastic debris and showed that surface measurements may underestimate the prevalence of buoyant plastics. Similarly, in the absence of wind stress, Kukulka et al. (2016) used observations and numerical simulations to show that turbulence generated by convection can deeply submerge buoyant particles.

More recently, high resolution simulations of pure convection have revealed that in addition to buoyant particles accumulating in convergent regions of convective cells, the presence of convective vortices in the vertices between some cells act to additionally cluster

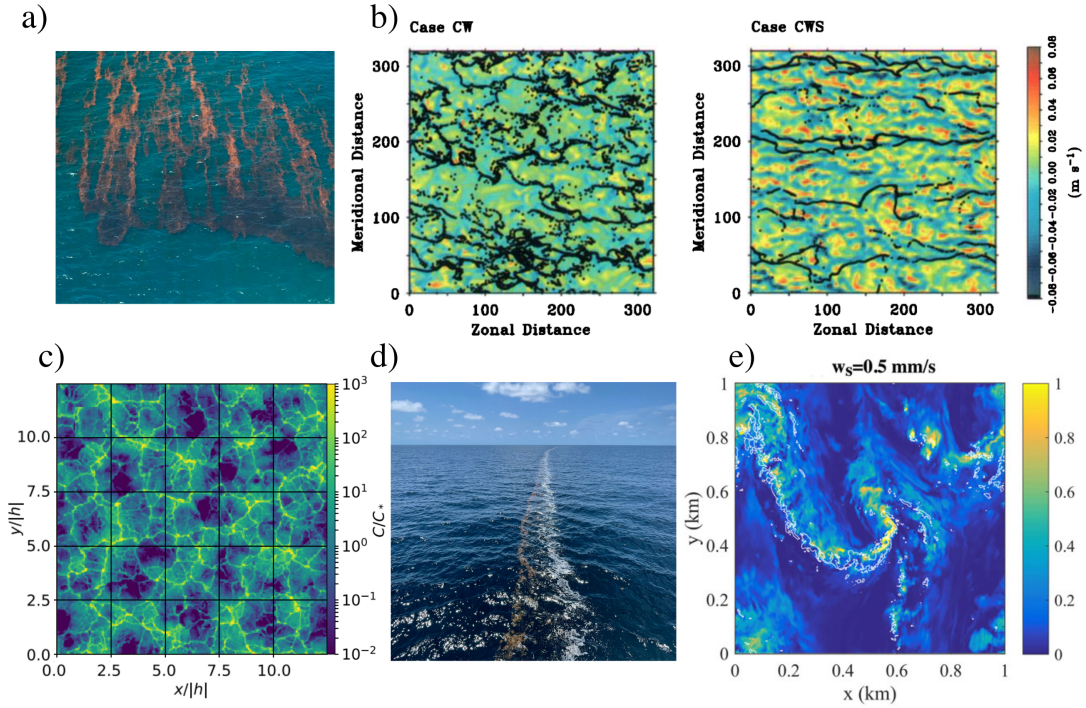

Fig. 1.4 (a) Field images of surface oil slicks from an underwater blowout (U.S. Air Force photo/Tech.Sgt.Adrian Cadiz); (b) Position of floaters 1 hour after uniform release (black dots) in a simulation driven by wind shear and surface cooling (left panel) and Langmuir turbulence (right panel). Vertical velocity is shown 5 m below the surface (colour) and distances in both axes are indicated in metres (reproduced with permission from Skyllingstad and Denbo (1995)); (c) Normalised surface concentration of a positively buoyant tracer field in a simulation of pure convection in the OML (reproduced with permission from Chor et al. (2018a)); (d) Field images of bubbles and sargassum along a submesoscale front in the Gulf of Mexico (photo credited to SUNRISE 2023); (e) Horizontal slices of positively buoyant tracer concentration at $z = -25$ m and $t = 3.3$ days in a submesoscale eddy. White contours indicate regions of strong downwelling with $w = 0.005$ m/s (reproduced with permission from Taylor (2018)).

the most buoyant particles (Chor et al., 2018a). Figure 1.4c shows a horizontal slice of the buoyant tracer concentration at the surface in a convectively-driven flow when $w_s = 7.77$ mm/s. Here, we again see that the tracer accumulates in the convergent regions of convective cells, but surprisingly there is a significantly higher concentration at the nodes between cells. This pattern becomes even more extreme for higher values of w_s with almost all tracer inside the nodes. The highly buoyant tracer is advected into and trapped inside resilient convective vortices. Each convective vortex continuously collects more and more tracer, concentrating it in a significantly smaller area than the convergent regions of convective cells. Eventually, the vortices weaken and are broken up by the flow, leaving behind small clusters of buoyant tracer. The relatively recent discovery of oceanic convective vortices leaves this accumulation mechanism one of the lesser explored areas which we address in chapters 3 and 4.

Finally, we turn to submesoscale fronts. These are often associated with a strongly convergent zone between two water masses of differing density, salinity or temperature which creates potential for strong particle accumulation. Often, the particles, foams and debris that accumulate in the convergent regions make fronts visible on the surface. For example, figure 1.4d shows sargassum and bubbles accumulating in a submesoscale front captured on the Submesoscales Under Near Resonant Inertial Shear Experiment (SUNRISE) campaign in 2023 in the Gulf of Mexico. Here, a rich field of submesoscale fronts and eddies are generated by the interactions between the output from the Mississippi-Atchafalaya river plume and the salty, more dense, off-shore coastal water. A striking feature of this image is the offset between the sargassum (on the salty side) and the bubbles (on the fresh side) along the relatively two-dimensional, straight front which inspired the work in chapters 5 and 6. The downwelling associated with such a front could transport buoyant particles downwards, potentially sinking them to the ocean interior (Omand et al., 2015).

Also in the Gulf of Mexico, D'Asaro et al. (2018) illustrated the strong convergence mechanism at play in a cyclonic, submesoscale eddy using 200 satellite-tracked surface drifters in the CARTHE field campaign. They found that over half of the floating drifters concentrated in a region 10^4 times smaller than the initial separation between drifters, a stark difference to the dispersive effect that was predicted. Taylor (2018) used LES to demonstrate that buoyant tracers accumulate at the surface along a submesoscale density front, and are subsequently subducted down into the water column. Even in the presence of additional convective forcing, the frontal downwelling associated with the front enhances the vertical velocities enough to distinctly concentrate the tracer. Figure 1.4e shows the horizontal slice of a buoyant tracer ($w_s = 0.5$ mm/s) at a depth -25 m below the surface overlain with contours of strong downwelling. The highest concentration of tracer occurs near the front coincident with the regions of strong downwelling and strong convergence. More work is needed to

explain the complicated transport mechanisms associated with submesoscale fronts such as those visible in figure 1.4d.

1.5 Thesis outline

Our understanding of the oceanic processes that govern the distribution of buoyant materials at the submesoscale level and smaller is far from complete. Challenges remain in designing numerical simulations which can accurately capture small-scale processes, with the additional hurdle of how to best include a computationally affordable particle tracking model. This thesis aims to push the limits of numerical modelling in some of the less explored oceanic flows at the small-scale turbulent and the submesoscale level, utilising Lagrangian and Eulerian buoyant material.

In chapter 2, we introduce a three-dimensional Lagrangian particle model which was written and implemented into the existing channel flow solver (DIABLO) as part of this thesis. In particular, we highlight the interpolation method employed and details of how the code is parallelised.

In chapter 3, we consider the accumulation of buoyant material in the newly discovered oceanic convective vortices. We build on the work by Chor et al. (2018a) and use high resolution LES to test the resilience of convective vortices under combined wind and convective forcing. We model non-inertial buoyant particles using both buoyant tracers and Lagrangian surface particles, which allows us to explore a wide range of particle buoyancies. Despite their small size, we show that the convective vortices exhibit an unexpected bias towards cyclonic vorticity which has not been reported previously. Analysis of the Lagrangian trajectories allows us to partially explain the bias based on the average time that a particle spends inside a convective vortex. The addition of wind forcing reveals three distinct flow patterns under weak, moderate, and strong wind forcing. We characterise the convective vortices in each of these regimes, and quantify the degree of particle clustering.

Chapter 4 continues in a similar vein to chapter 3, delving deeper into the cyclonic bias of oceanic convective vortices and applying a predictive analysis to atmospheric convective vortices on Earth and on Mars. We use even higher resolution LES compared to those in chapter 3 under pure convective forcing and uncover a new class of small convective vortices. Using Lagrangian particles, we find that the small convective vortices play a significant role in setting the bias of the larger convective vortices. We propose a scaling theory to predict the cyclonic bias of convective vortices under different convective conditions and test the theory using highly idealised LES of a simplified circulation cell. We then apply the scaling to typical convective conditions in the ocean and the terrestrial and Martian atmospheres.

In chapter 5, we turn our focus to submesoscale fronts. We use DNS and study the frontal dynamics, instabilities, and three-dimensional turbulence associated with geostrophic adjustment. We consider an isolated, finite-width front comprising a frontal region with horizontally-varying and time evolving buoyancy gradients, initialised with motionless fluid with a lateral density gradient analogous to Ou (1984). To our knowledge, this is the first time that DNS has been applied to this problem. By varying the initial frontal strength, Γ_0, we find that strong fronts develop a buoyancy jump which generates three-dimensional turbulence near the top and bottom boundary. We analyse and quantify the energy pathways and mixing dynamics as the front evolves over time.

In chapter 6, we extend our simulations to investigate the movement of three-dimensional, buoyant material in a geostrophically adjusting front. We use LES of the strongest front simulated in chapter 5 ($\Gamma_0 = 16$), and include three-dimensional buoyant Lagrangian particles with several classes of particle buoyancy. We identify several different accumulation mechanisms based on the particle buoyancy and connect this to the frontal dynamics investigated in chapter 5.

Finally in chapter 7, we conclude with a discussion of the overall findings of this thesis and consider the future directions this research field could take.

Chapter 2

Lagrangian Particle Tracking Model

2.1 Introduction

Throughout this thesis, we perform LES using the open-source computational fluid dynamics (CFD) solver, DIABLO, designed by Bewley (2019) and extended by Taylor (2008) to allow for the consideration of geophysical problems, channel flows and scalar advection. An in-depth description of the numerical solver, including details of the parallel computing and algorithm structure, can be found in chapter 6 of Taylor (2008). As part of this thesis, a new three-dimensional Lagrangian particle tracking model has been developed and implemented alongside the main numerical solver. In this chapter, we discuss the intricacies of the model including the interpolation scheme, parallelisation and details of how to implement the model.

2.2 Interpolation

To model particles in the Lagrangian framework, we need to solve equation (1.16) for each individual particle. In particular, recall that $\mathbf{u}(\mathbf{x}_p)$ is the velocity field at the particle location. In the main numerical solver, the velocity field is solved on a discretised grid and is not readily available at the location of particles, which are not confined to grid points. Thus to find $\mathbf{u}(\mathbf{x}_p)$, interpolation is required. However, interpolation can be time consuming, requires large amounts of memory and is generally the most computationally expensive aspect of particle advection. Hence, we aim to choose an interpolation method that is both highly accurate and computationally efficient. Like many CFD solvers, DIABLO treats periodic horizontal directions using pseudo-spectral methods, where fast Fourier transforms (FFTs) are used to transform data between real space and Fourier space. FFTs computationally expensive, so to minimise the computational cost of the particle model, we aim to minimise the number

of FFTs in the interpolation step. Several studies have already investigated interpolation for spectral codes (Balachandar and Maxey, 1989; Hinsberg et al., 2012; Yeung and Pope, 1988) and we closely follow the work of Hinsberg et al. (2012) and use B-spline interpolation in the horizontal. DIABLO uses second-order finite differences to calculate derivatives in the vertical (wall-bounded) direction, so another interpolation scheme is required for the vertical direction. Here, we use second-order accurate linear interpolation in the vertical (to match the order of accuracy for vertical derivatives). To combine horizontal and vertical interpolation schemes, we first interpolate horizontally, and then interpolate vertically.

2.2.1 Horizontal interpolation

In the last few decades, B-spline interpolation has been used to remedy shortcomings of other interpolation methods and to take advantage of spectral codes. For example, Hermite interpolation requires several additional FFTs, making it computationally expensive. B-splines require only one additional FFT, have a small interpolation error, and the interpolated field has a high order of continuity. A detailed discussion of the comparison and implementation of linear, Hermite and B-spline methods can be found in Hinsberg et al. (2012), while here we provide relevant details of how we incorporate the B-spline method into our particle tracking model.

In the numerical solver, $\mathbf{u}$ is discretised on a uniform grid in the horizontal directions with N_x and N_y grid points in the x and y directions respectively. We aim to create an interpolated approximation to $\mathbf{u}$ that is as smooth as possible which we do by expressing the velocity field in terms of the B-spline basis functions. Below, we first outline the interpolation of a one-dimensional function, which we then extend to the two horizontal directions needed in our model. Without loss of generality, we work in the x direction with periodicity of $\mathbf{u}$ on the interval $x \in [0, N_x - 1]$ (where the variable x denotes position along the grid). Additionally, we consider a singular component of the velocity field, u, and generalise to the full velocity field, $\mathbf{u}$, afterwards.

The uniform B-spline basis function with degree n is defined recurrently as:

$$B_n(x) = (B_{n-1} * B_1)(x), \tag{2.1}$$

$$B_1(x) = \begin{cases} 1 & \text{if } -0.5 \leq x < 0.5, \\ 0 & \text{elsewhere,} \end{cases} \tag{2.2}$$

where $*$ represents the convolution product defined by

$$(f*g)(x) = \int_{-\infty}^{\infty} f(y)g(x-y)\mathrm{d}y \; . \tag{2.3}$$

The nth function is of degree $n-1$, and is $(n-2)$ times differentiable with a continuous $(n-2)$th derivative (i.e. C^{n-2}), and has local support length n. In our interpolation scheme, we use cubic B-splines (where $n=4$). Hinsberg et al. (2012) shows that this will give a high enough degree of accuracy without being too computationally expensive (as described later, higher order accuracy would require more horizontal ghost cells in a parallel run which adds adversely to the computational cost). The functions can also be written in matrix form, with the $n=4$ case written as:

$$B_4(x) = \sum_{i=1}^{4} B_{4,i}(x) \; , \tag{2.4}$$

$$B_{4,i}(x+2-i) = \begin{cases} \sum_{j=1}^{4} M_{ij}\, x^{j-1} & \text{if } 0 \le x < 1 \; , \\ 0 & \text{elsewhere,} \end{cases} \tag{2.5}$$

$$M = \frac{1}{3!} \begin{pmatrix} 1 & -3 & 3 & -1 \\ 4 & 0 & -6 & -3 \\ 1 & 3 & 3 & -3 \\ 0 & 0 & 0 & 1 \end{pmatrix} . \tag{2.6}$$

We ensure periodicity of the B-spline concurrent with boundary conditions in the horizontal directions by defining,

$$B_D(x) = \begin{cases} B_4(x) & \text{if } x < N_x/2 \; , \\ B_4(x-N_x) & \text{if } x \ge N_x/2 \end{cases} \qquad x \in [0,\, N_x - 1]. \tag{2.7}$$

The discrete function u can be expressed in terms of the B-spline basis functions using the relation $u = u_B *_D B_D$, where u_B are coefficients of the B-spline functions and $*_D$ is the circular discrete convolution:

$$(f *_D g)(x) = \sum_{y=0}^{m} f(y)g((x-y) \bmod (m)), \qquad x = 0, 1, ..., m-1, \tag{2.8}$$

for a periodic function g with period m (where $m = N_x$ in this work). In principle, we know both u and B_D, so it remains to find u_B. This can be done by computing the inverse, $u_B = u *_D B_D^{-1}$ where B_D^{-1} is defined such that $B_D *_D B_D^{-1} = \delta_i$ and δ_i is the discrete Kronecker delta function. This inverse convolution is an expensive step in physical space, but relatively

inexpensive in Fourier space. The velocity field is already readily available in Fourier space after solving for the updated velocity field, so we perform the inverse operation as:

$$\widehat{u_B}(k) = \widehat{(u *_D B_D^{-1})}(k) = \widehat{u}(k)\,\widehat{B_D^{-1}}(k) = \frac{\widehat{u}(k)}{\widehat{B_D}(k)}, \tag{2.9}$$

where $\widehat{.}$ denotes a variable in the Fourier space. The coefficients $\widehat{B_D}(k)$ only need to be calculated once which can be done at the start of the code. After evaluating $\widehat{u_B}$, we use a single inverse FFT to return to physical space and find u_B.

The cubic B-spline functions have support length 4, and we make use of this to further reduce computations in constructing the interpolant. Given a particle position x_p at which to interpolate, we only need to evaluate at the four nearest grid points, x_1, x_2, x_3 and x_4 (two to the right of x_p and two to the left). The interpolated approximation to u, denoted $\tilde{u}$, is then:

$$\tilde{u}(x_p) = \sum_{i=1}^{4} u_B(x_i)\, B_4(x_p - x_i). \tag{2.10}$$

Finally, we can easily extend this to two dimensions with the basis coefficients given by

$$\widehat{u_B}(\mathbf{k}) = \frac{\widehat{u}(\mathbf{k})}{\widehat{B_D}(k_x) \times \widehat{B_D}(k_y)}\,, \tag{2.11}$$

where $\mathbf{k} = (k_x, k_y)$, and equation (2.10) is evaluated as a double sum (in the x direction and the y direction). This can be done for each component of the velocity field, $\mathbf{u} = (u, v, w)$.

2.2.2 Vertical interpolation

In DIABLO, variable grid spacing is used in the vertical direction. This allows us to capture the turbulence near the surface using a fine grid, but also save on computational cost at a greater depth where motions have a larger scale. In the vertical direction, calculations in the main code have errors which are second-order accurate (Taylor, 2008) (e.g. finite difference method, grid interpolation, vertical derivatives) and so we choose to implement linear interpolation in the vertical direction, which is also second-order accurate, (i.e. the error in the interpolant is $\mathscr{O}(\Delta z^2)$ where Δz is the vertical grid spacing). Higher order schemes would involve communicating additional 'ghost cells' on the vertical grid (see section 2.3.2) which would be computationally expensive and difficult to implement. For a particle located

at z_p, the linear interpolant is

$$u(z_p) = \frac{u(z_0)(z_1 - z_p) + u(z_1)(z_p - z_0)}{z_1 - z_0}\,, \tag{2.12}$$

where z_0 is the closest grid point below z_p and z_1 is the closest grid point above z_p.

In many geophysical problems, the flow is bounded above and below with the vertical velocity set to zero on the boundary. To avoid particles becoming trapped on either boundary, we include a small buffer at the top and bottom into which the particles cannot move. If the particle position exceeds the buffer boundary at the top, we return it to the buffer boundary for the next time-step (and similarly at the bottom). Wave-breaking often submerges particles a few metres deeper than the surface, but wave breaking is not captured in our simulations, which have a flat ocean. The buffer zone can be viewed as simple way to represent missing transport processes like wave breaking. To implement a surface particle model, particles are vertically fixed at the first grid point below the surface (as in chapters 3 and 4).

2.3 Parallel Computing

Parallel computing enables large, expensive fluid dynamics problems to be solved more efficiently by using several computers (or several processors within one computer). Parallelisation has been implemented in DIABLO using the standardised Message Passing Interface (MPI) library. It uses a two-dimensional parallelisation in one horizontal direction (x-direction in Fourier space and y-direction in physical space) and in the vertical direction, z. The grid in the z direction is split into sub-grids for each processor which each contain ghost points at either end. The scheme relies upon communication of variables at these ghost points between two neighbouring processes.

In the Lagrangian particle framework, each individual particle trajectory is determined independently and we need the interpolated velocity for every single particle. We often require a very large number of particles to achieve convergence of statistical properties, which means the particle model can be time consuming and memory demanding. In developing the particle tracking model, we take advantage of the existing parallelisation and implement some new strategies to increase computational efficiency.

2.3.1 Parallelisation of particles

The goal of parallelisation is to split the work of a simulation as equally as possible between different processors. For this reason, we divide particles equally between the processors

so that each processor has a specific set of particle positions which it tracks throughout the whole simulation. We call the processor which stores an individual particle's position the particle processor. This is not necessarily the same as the processor which the particle is spatially located on, which we call the spatial processor. This ensures that in a convergent flow such as those investigated in this thesis, information about particle position does not all end up on one processor when the particles spatially cluster together. However, by doing this, we create additional communication challenges when finding the interpolated particle velocity, because the particle processor does not store the velocity local to the particle.

To overcome this hurdle, we employ several stages of communication between the particle processor and the spatial processor. The number of processors used in a simulation is determined by the main DIABLO code, we do not add any processors to deal only with particles. We initialise each processor with N particles which it retains throughout the simulation (no exchanges of particles or change in number of particles). The particle processor stores the particle location and any other statistics we choose to save along particle paths (e.g. velocity, vorticity, pressure). The initial conditions, time update, application of boundary conditions and saving statistics are all completed on the particle processor. The only step which is carried out on the spatial processor is the interpolation. To do this, we need to communicate information between the particle and spatial processors at every time-step.

For each of the N particles on a given particle processor, we first find the associated spatial processor. The horizontal grid is uniform and easily defined between processors, but the vertical grid is not uniform and we need to communicate the end-points of the z-subgrid between processors before finding the vertical processor associated with the particle location. Since the grid does not change throughout the simulation, this can be done once at the start. Once we have determined the spatial processor for each particle, we count how many of the N particles are on each spatial processor which tells us how large the communication will be. We communicate this number between a particle processor and a spatial processor. Since each processor acts as both a particle and spatial processor, we use two-way communication, so as well as sending a particle count to another processor, each particle processor also receives a particle count. Once the size of communication is known, we send and receive a vector of particle positions between processors. The particles received have a spatial location within the grid limits of the processor by which they are received and the interpolation can be carried out at each particle position. After interpolation, we send a vector of interpolated particle velocities back to the processor on which they are stored (the original particle processor), and receive back a vector of particle velocities from another processor (since we are using two-way communication). These velocities can then be used to update the particle position on the particle processor. Communication is done between all pairs of processors in a circular

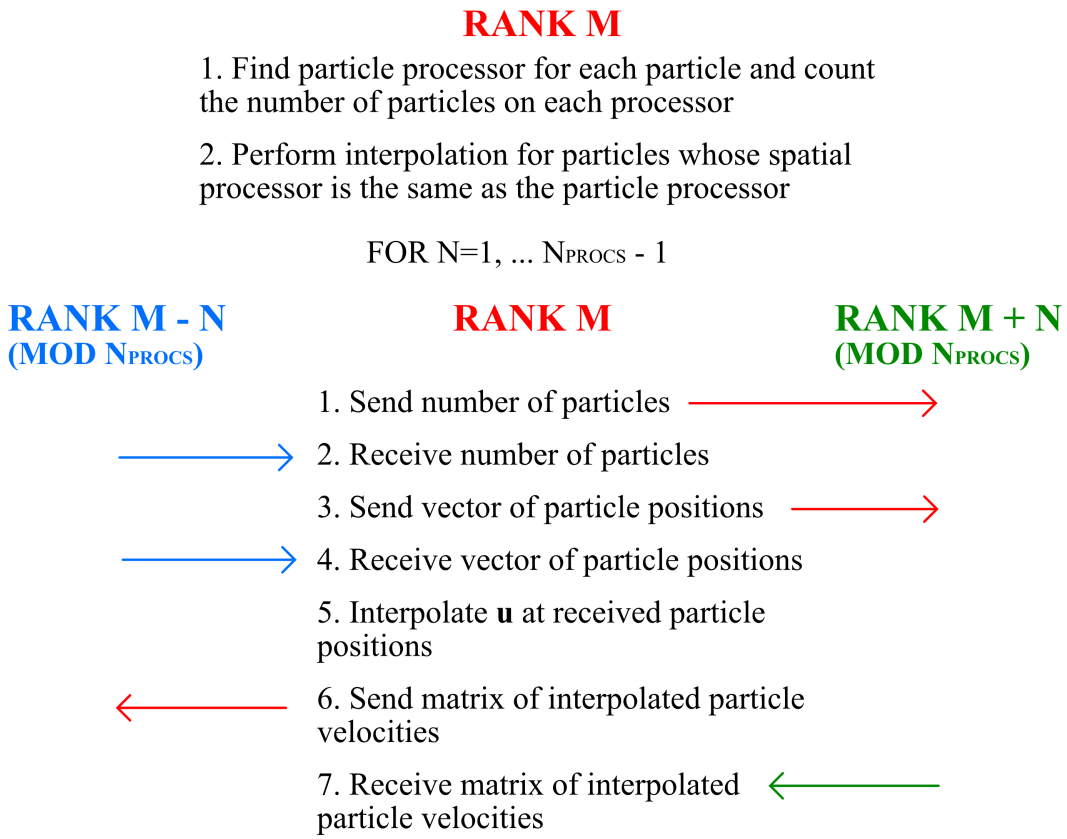

Fig. 2.1 Illustration of communication between different processors during the interpolation of particle velocities with reduced wait-times using a circular approach. Here, N_{PROCS} is the number of processors which we run on, RANK is the current processor, and arrows indicate passage of information.

fashion to avoid idle processors. A summary of this communication can be seen in figure 2.1 and an example of the code can be seen in figure 2.2.

Although the interpolation step needs to be performed for each velocity component $(u,\ v,\ w)$, we can communicate the particle positions once at the start of each time-step and carry out all interpolations before sending the interpolated quantities back. If any additional statistics are saved, we must additionally communicate the particle position at the end of the time-step and interpolate again.

```
! Now find particle velocity for particles with position on
! non-local process
      DO M=1,NPROCS-1
! Loop through the processes
       RANK_SEND=MODULO(RANK+M,NPROCS)
       RANK_RECV=MODULO(RANK-M,NPROCS)

! Create send buffer array XP_SEND
      i=1
      DO N=1,NP
! Loop over the number of particles
        IF (RANK_SEND.eq.RANK_PARTICLE(N)) THEN
          XP_SEND(i,1)=XP(N)
          XP_SEND(i,2)=YP(N)
          XP_SEND(i,3)=ZP(N)
          XP_INDEX(i)=N
          i=i+1
        END IF
      END DO

! Determine how many particles to send and receive

      CALL MPI_SEND(NUM_SEND(RANK_SEND),1,MPI_INTEGER
     &   ,RANK_SEND,1,MPI_COMM_WORLD,IERROR)
      CALL MPI_RECV(NUM_RECV,1,MPI_INTEGER
     &   ,RANK_RECV,1,MPI_COMM_WORLD,STATUS,IERROR)

! Send this rank the particle position
      IF (NUM_SEND(RANK_SEND).GT.0) THEN
      CALL MPI_SEND(XP_SEND(1:NUM_SEND(RANK_SEND),1:3)
     &  ,3*NUM_SEND(RANK_SEND),MPI_DOUBLE,RANK_SEND
     &     ,1,MPI_COMM_WORLD,IERROR)
      END IF
! Receive particle position
      IF (NUM_RECV.GT.0) THEN
      CALL MPI_RECV(XP_RECV(1:NUM_RECV,1:3),3*NUM_RECV,
     &      MPI_DOUBLE, RANK_RECV,1,MPI_COMM_WORLD,STATUS,IERROR)
```

```
! Interpolate the velocity to the particle position in XP_RECV
! Returns the velocity in VP_SEND
      CALL INTERPOLATION_3D(BU1,NUM_RECV,XP_RECV,V1P_SEND)
      CALL INTERPOLATION_3D(BU2,NUM_RECV,XP_RECV,V2P_SEND)
      CALL INTERPOLATION_3D(BU3,NUM_RECV,XP_RECV,V3P_SEND)

! Pack into an array to send back to the original process
      DO N=1,NUM_RECV
      VP_SEND(N,1)=V1P_SEND(N,1)
      VP_SEND(N,2)=V2P_SEND(N,1)
      VP_SEND(N,3)=V3P_SEND(N,1)
      END DO

! Send the velocity back to the original process
      CALL MPI_SEND(VP_SEND(1:NUM_RECV,1:3),3*NUM_RECV,MPI_DOUBLE
     &    ,RANK_RECV,1,MPI_COMM_WORLD,IERROR)
      END IF

      IF (NUM_SEND(RANK_SEND).GT.0) THEN
      CALL MPI_RECV(VP_RECV(1:NUM_SEND(RANK_SEND),1:3)
     &  ,3*NUM_SEND(RANK_SEND),MPI_DOUBLE,RANK_SEND
     &     ,1,MPI_COMM_WORLD,STATUS,IERROR)

! Save the velocity corresponding to each particle
      DO i=1,NUM_SEND(RANK_SEND)
        U1P(XP_index(i))=VP_RECV(i,1)
        U2P(XP_index(i))=VP_RECV(i,2)
        U3P(XP_index(i))=VP_RECV(i,3)
      END DO
      END IF
```

Fig. 2.2 Source code from DIABLO subroutine ‘particles.f’ illustrating the communication of particle velocity between a particle processor and a spatial processor. Note that in the code, the y and z directions are transposed.

2.3.2 Ghost cells

The interpolation step requires knowledge of the basis coefficients and B-spline function for a 4×4 grid of points in the horizontal, and knowledge of the interpolating field for 2 points in the vertical. We update the position of particles in physical space, where the horizontal grid is parallelised in the y direction and the vertical grid is also parallelised. If a particle is located near the edge of either a y or z subgrid, the processor may not contain all the information required to construct the interpolant. To overcome this, we add extra cells beyond the edge of the domain called 'ghost cells' which store information from a neighbouring processor. However, this information must be communicated between processors at each time-step.

The vertical grid already has ghost cells at either end, so we do not need to additionally communicate anything in this direction. The x direction is not parallelised in physical space, so we also do not need to communicate in this direction. However, in the y direction, there may be particles close to the boundaries which require information from grid points on a different horizontal processor which the main DIABLO code does not communicate. The B-spline function can be easily defined on all processors and so we do not need to communicated anything about B-splines. However, a subset of the basis coefficients, $\mathbf{u}_B$, are stored on each processor, so we must add some ghost cells in the horizontal direction to allow for interpolation near the boundaries. Each horizontal processor has N_{yp} grid points indexed $0, 1, ..., N_{yp} - 1$, and on a given spatial processor, the particle position (which is not bound to grid cells) can vary from the 0th grid cell (inclusive) to the N_{yp}th grid cell (exclusive).

For a field u, a matrix of the basis coefficients for the local grid points, u_B, is calculated on each processor by first finding $\widehat{u_B}$ (in Fourier space) and then performing an inverse FFT. Given that we need the coefficients at two points either side of the particle position in equation (2.10), we create one ghost cell below the 0th point for interpolation of particles between the 0th and 1st grid points and two ghost cells above the $(N_{yp} - 1)$th grid point for interpolation of particles between the $(N_{yp} - 2)$th and N_{yp}th grid points. Each time the matrix is found, we communicate the points from the processor above/below to fill the ghost cells in physical space. Then the matrix contains all the required information for interpolation of points on that processor even if a particle is near the edge. A summary of ghost cell communication is provided in figure 2.3, and an example of the source code is provided in figure 2.4. Again, communication is implemented in a circular manner to avoid idle processors.

2.4 Implementation

We implement the Lagrangian particle tracking model in DIABLO in a carefully ordered way to minimise the number of storage variables and FFTs. In particular, the algorithm is ordered

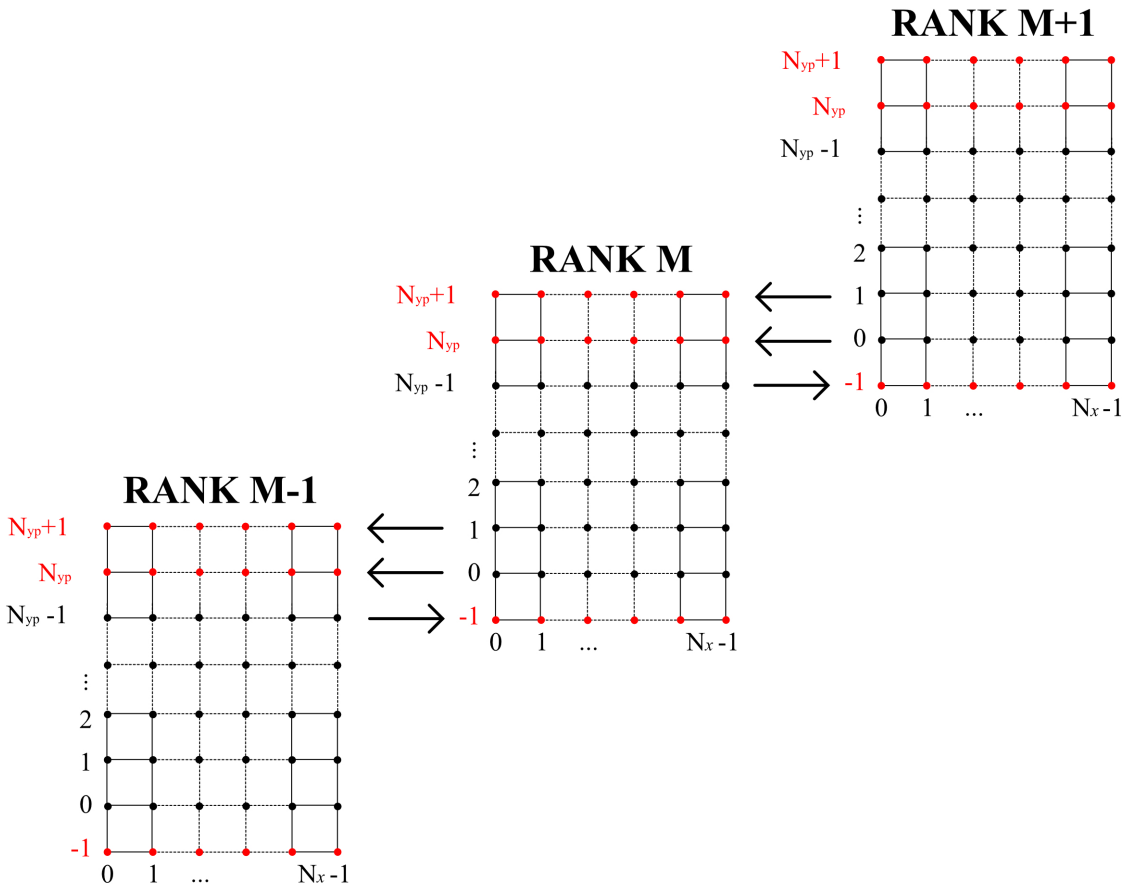

Fig. 2.3 Grid indexing with ghost cell communication of the basis coefficients in the x and y directions. Here, N_{yp} is the number of grid points on each y processor, N_x is the number of grid points in the x direction, and RANK is the current processor. Communication is depicted by arrows, and ghost cells are coloured in red.

```
! The size of T1B is U1B(0:NX+1,0:NZP+1,0:NY+1)
! The size of T1B_FULL is T1B_FULL(0:NX+1,-1:NZP+1,0:NY+1)
! T1B is local in X and split in Z

! Pass the points in the Z direction to add ghost cells
! Pack the data points into an array to send
      DO J=0,NY+1
      DO I=0,NX+1
          TB_SENDDOWN(I,J,1)=T1B(I,0,J)
          TB_SENDDOWN(I,J,2)=T1B(I,1,J)
          TB_SENDUP(I,J)=T1B(I,NZP-1,J)
      END DO
      END DO

! Pass points between 0&1,1&2,2&3 etc...
      IF (MODULO(RANKZ,2).eq.0) THEN
      CALL MPI_SENDRECV(TB_SENDUP,(NX+2)*(NY+2),MPI_DOUBLE,
     &      RANKZ+1,1,TB_RECVDOWN,(NX+2)*(NY+2)*2,MPI_DOUBLE,
     &      RANKZ+1,1,MPI_COMM_Z,STATUS,IERROR)
      ELSE
      CALL MPI_SENDRECV(TB_SENDDOWN,(NX+2)*(NY+2)*2,MPI_DOUBLE,
     &      RANKZ-1,1,TB_RECVUP,(NX+2)*(NY+2),MPI_DOUBLE,
     &      RANKZ-1,1,MPI_COMM_Z,STATUS,IERROR)
      END IF

! Pass points between NPROCZ-1&0,1&2,3&4 etc...
      IF (MODULO(RANKZ,2).eq.0) THEN
      CALL MPI_SENDRECV(TB_SENDDOWN,(NX+2)*(NY+2)*2,MPI_DOUBLE,
     &      MODULO(RANKZ-1,NPROCZ),1, TB_RECVUP,(NX+2)*(NY+2),
     &      MPI_DOUBLE,MODULO(RANKZ-1,NPROCZ),1,MPI_COMM_Z,
     &      STATUS,IERROR)
      ELSE
      CALL MPI_SENDRECV(TB_SENDUP,(NX+2)*(NY+2),MPI_DOUBLE,
     &      MODULO(RANKZ+1,NPROCZ),1,TB_RECVDOWN,(NX+2)*(NY+2)*2,
     &      MPI_DOUBLE,MODULO(RANKZ+1,NPROCZ),1,MPI_COMM_Z,
     &      STATUS,IERROR)
      END IF

! Unpack data
      DO J=0,NY+1
      DO I=0,NX+1
          T1B_FULL(I,-1,J)=TB_RECVUP(I,J)
          T1B_FULL(I,NZP,J)=TB_RECVDOWN(I,J,1)
          T1B_FULL(I,NZP+1,J)=TB_RECVDOWN(I,J,2)
      END DO
      END DO
```

Fig. 2.4 Source code from DIABLO subroutine 'particles.f' illustrating the communication of endpoints on the basis matrix between adjacent processors. Note that in the code, the y and z directions are transposed. Here T1B is a storage variable of basis coefficients, TB_SENDDOWN and TB_SENDUP are packing variables used in the communication step.

so that the physical and Fourier space arrays can occupy the same location in memory. A full algorithm of the velocity-solver in DIABLO can be found in Taylor (2008). Execution of the particle model takes place after the velocity and pressure fields have been updated, but before the start of the next time-step.

The boundary conditions for the particles can be easily altered depending on the physical requirements of a specific problem, but in our work, we implement periodic boundary conditions in the x and y directions. As mentioned previously, we apply vertical buffers bounding the particles in the z direction. The size of the buffer is a variable that can be set in the input file. Additionally, the particle slip velocity, w_s, and the number of particles per processor, N, can be set in the input file.

Time-stepping is accomplished with a low storage third-order Runge-Kutta (R-K) method with time-marching at each R-K substep determined in the main code. We ensure this scheme is storage efficient by only using two storage variables per particle velocity component.

In conjunction with the main DIABLO code, any output statistics along particle paths are saved in the HDF5 data format for I/O. This is a highly effective data storage method which allows for easier post-processing.

For completeness, we also include details of a random motion model which partially accounts for Brownian motion and makes use of the SGS viscosity in the main code of an LES run. This can be optionally included in the full particle model and is easily switched on or off. Recall that equations for the motion of non-inertial particles are:

$$\mathbf{x}_p(t+dt) = \mathbf{x}_p(t) + \overline{\mathbf{u}}(\mathbf{x}_p,t)dt + w_s dt\widehat{\mathbf{z}} + \mathbf{x}_{sgs}(\mathbf{x}_p,t), \tag{2.13}$$

where $\mathbf{x}_{sgs}$ models the influence of SGS effects. We follow the approach in Liang et al. (2018) and implement a random displacement model. In particular, we have

$$x_{sgs,i} = \frac{\partial \nu_{sgs}}{\partial x_i}(\mathbf{x}_p,t)\,dt + (2(\nu_{sgs}(\mathbf{x}_p,t))_+)^{\frac{1}{2}} d\xi_i, \tag{2.14}$$

where $\mathbf{u}$ is the resolved velocity interpolated at the particle position and $\mathbf{x}_{sgs}$ is the displacement due to sub-grid scale motion. In equation (2.14), the subscript i indicates the spatial dimension, ν_{sgs} is the sub-grid scale viscosity (which is readily available in the main code) interpolated at the particle position, $d\xi_i$ is Gaussian white noise with variance dt, and $(\cdot)_+ = \max(\cdot, 0)$. Note that inclusion of the SGS model requires interpolating four additional variables (ν_{SGS} and its three horizontal derivatives). Interpolation is implemented in the same way and at the same time as particle velocity interpolation to minimise communication between processors.

Chapter 3

Large eddy simulations of the accumulation of buoyant material in oceanic wind-driven and convective turbulence

This chapter is a slightly modified version of the work published in Dingwall, J., Chor, T., and Taylor, J. R. (2023). Large eddy simulations of the accumulation of buoyant material in oceanic wind-driven and convective turbulence. *Journal of Fluid Mechanics*, 954:A27.

3.1 Introduction

In the ocean mixed layer (OML), buoyant material is subject to a variety of processes including convective plumes, Langmuir and wind-driven turbulence, submesoscale eddies, Ekman flow and Stokes drift. Due to their low density, buoyant materials such as microplastics tend to remain in the OML and accumulate near the ocean surface in regions with convergent surface currents. In this chapter, our focus is on the smaller scales where buoyant material accumulates in ephemeral patches and streaks.

In the absence of Stokes drift, the small-scale structure of the ocean mixed layer is governed by processes such as convection forced from night-time cooling and shear stress generated by surface winds. Kukulka et al. (2016) showed that convective turbulence can submerge buoyant particles into the water column, while Kukulka et al. (2012) revealed that wind-driven mixing can vertically distribute buoyant particles in the OML. Skyllingstad and Denbo (1995) showed that under a combination of wind and convective forcing, the

horizontal distribution of particles at the ocean surface coincides with regions of convergence. Mensa et al. (2015) used a relatively low-resolution model to demonstrate that under pure convection, tracer accumulates in convergent regions of Rayleigh-Benard cells. With the additional presence of weak wind forcing, they found that convection cells were distorted but tracer continued to accumulate in downwelling regions. Chor et al. (2018a) expanded on this using higher resolution numerical simulations in a purely convective regime and a range of buoyancies for the tracer field. They found that, in addition to buoyant particles accumulating in convergent regions of the Rayleigh-Benard cells, the presence of convective vortices in the vertices between some cells acted to additionally cluster the most buoyant particles. It remains unclear to what extent convective vortices and the associated accumulation of buoyant particles persist in the presence of wind forcing.

In this chapter, we extend previous work by studying the formation and persistence of convective vortices under the combined effects of wind and convective forcing and their influence on buoyant material. In the atmosphere it has been noted that the number and strength of convective vortices (e.g. dust devils) that form depend strongly on wind conditions (Raasch and Franke, 2011).

We study these processes using a series of LES under idealised conditions where turbulence is generated by imposing a constant surface heat flux and shear stress. LES is a useful tool for studying the accumulation of buoyant particles because they resolve the largest turbulent motions responsible for particle accumulation and vertical transport. LES has also been used to study convective vortices in the atmosphere (Raasch and Franke, 2011) and the ocean (Chor et al., 2018a).

We model buoyant material using a combination of buoyant tracers and Lagrangian surface particles (advected with the surface velocity). The upwards slip velocity causes buoyant tracers to concentrate near the surface of the ocean and is opposed by turbulence and diffusion which transports the tracer downwards. For a buoyant tracer to be effectively trapped at the surface, the slip velocity must exceed the maximum vertical velocity of the fluid. Due to numerical constraints, there is a limit to the slip velocity that can be added to a tracer field. Here, we additionally use Lagrangian particles at the surface which allows us to investigate the limit where the slip velocity is much larger than the fluid vertical velocity.

Whilst Chor et al. (2018a) provides an extensive study of convective vortices in a purely convective regime, we focus on the extent to which convective vortices persist in the presence of a surface wind stress, and how this affects particle clustering inside convective vortices. Unlike our simulations, Chor et al. (2018a) did not include the Coriolis acceleration due to the Earth's rotation and hence they did not observe the bias towards cyclonic convective vortices that we observe. Additionally, Chor et al. (2018a) only used a tracer field to investigate

clustering of buoyant material and did not look at the limit of extremely buoyant material with Lagrangian particles.

Below, in section 3.2, we introduce the problem configuration and numerical methods. In section 3.3, we present our results. Section 3.3.1 includes a qualitative description of the flow and the buoyant particles, section 3.3.2 describes convective vortices with and without wind forcing, and section 3.3.3 includes a quantification of the accumulation of buoyant particles. A summary of the study and discussion of the key results is given in section 3.4.

3.2 Setup and numerical methods

Here, we use large eddy simulations to solve a low-pass filtered version of the non-hydrostatic incompressible Boussinesq Navier-Stokes equations (3.1) and (3.2) in terms of the low-pass filtered velocity $\mathbf{u} = (u, v, w)$, low-pass filtered pressure p, and buoyancy b,

$$\frac{\partial \mathbf{u}}{\partial t} + \mathbf{u} \cdot \nabla \mathbf{u} + \mathbf{f} \times \mathbf{u} = -\frac{1}{\rho_0} \nabla p + \nu \nabla^2 \mathbf{u} - \nabla \cdot \boldsymbol{\tau} + b\widehat{\mathbf{z}} \,, \tag{3.1}$$

$$\frac{\partial b}{\partial t} + \mathbf{u} \cdot \nabla b = \kappa_b \nabla^2 b - \nabla \cdot \boldsymbol{\lambda} \,. \tag{3.2}$$

The buoyancy is treated as a single scalar variable under the assumption of a linear equation of state and neglecting double diffusive effects. In the momentum equation, $\mathbf{f} = (0, 0, f)$ is the Coriolis parameter under the 'traditional' approximation. The sub-grid scale stress tensor, $\boldsymbol{\tau}$, and sub-grid scale scalar flux, $\boldsymbol{\lambda}$, are both calculated using the anisotropic minimum dissipation model (Abkar et al., 2016; Vreugdenhil and Taylor, 2018) which is described below.

The computational domain is 500 m in each horizontal direction and 120 m in the vertical direction. A constant buoyancy loss (equivalent to cooling the surface of the ocean) is applied at the surface to drive convection. Various values of the imposed surface buoyancy flux are used, ranging from 0 to -4.24×10^{-8} m^2/s^3, but the surface buoyancy flux is constant in each simulation. Using a thermal expansion coefficient of $\alpha = 1.65 \times 10^{-4}$ C^{-1} and a heat capacity of 4×10^3 J kg C^{-1}, a surface buoyancy flux of -4.24×10^{-8} m^2/s^3 corresponds to a heat loss of about 100 Wm^{-2}. Wind is applied using a shear stress at $z = 0$ m which is aligned with the x-axis without loss of generality. Various values of the wind stress are considered, ranging from 0 to 0.1 Nm^{-2}, but again this value is constant for each simulation. At the bottom of the computational domain, a no stress boundary condition is applied in both horizontal directions and a sponge layer is applied to prevent reflections. Planetary rotation is included with a Coriolis parameter of $f = 10^{-4}$ s^{-1}. At $t = 0$ hours, the

buoyancy is initialised with a mixed layer with depth 80m overlying a region with stable stratification. Specifically, $\partial b/\partial z = 0$ s^{-2} for -80 m $< z < 0$ and $\partial b/\partial z = 9 \times 10^{-6}$ s^{-2} for $z < -80$ m. This stratification is in the range of values observed by Brainerd and Gregg (1993) in the diurnal thermocline and is equivalent to a potential temperature gradient of $\partial\theta/\partial z = 0.01^{\circ}$Cm^{-1} for $z < -80$ m.

The vertical velocity is set to zero at the top and bottom of the domain. We also do not include the Craik-Leibovich vortex force. Hence, although we run simulations for about 24 hours to allow wind and convective turbulence to fully develop, we do not consider the development of surface waves or Langmuir circulation. This can be viewed as an approximation to calm conditions (e.g. at the start of a wind event before waves have had time develop), but our primary motivation is to simplify the physical processes and isolate the influence of wind-driven shear on convective vortices. Periodic boundary conditions are applied in both horizontal directions. The velocity is initialised as random white noise with an amplitude of 10^{-4} m/s. The molecular viscosity is $\nu = 10^{-6}$ m^2/s and the molecular diffusivity is $\kappa_b = 10^{-6}$ m^2/s, although both are small compared to the sub-grid scale terms and do not directly influence the model results.

The resolved fields are discretised on a grid with 512 points in each horizontal direction and 65 points in the vertical direction. This gives a horizontal grid spacing of 0.98 m and a variable vertical grid spacing between 0.95 m and 2.57 m with higher resolution near $z = 0$ m. Derivatives in the horizontal directions are calculated using a pseudospectral method, whilst vertical derivatives are approximated using second-order finite differences. The equations are time-stepped using an implicit Crank-Nicolson method for the viscous and diffusive terms and a third-order Runge-Kutta method for all other terms. Further details of the numerics can be found in Taylor (2008).

The sub-grid scale terms are modeled with the anisotropic minimum dissipation (AMD) model (Abkar et al., 2016; Rozema et al., 2015; Vreugdenhil and Taylor, 2018). In developing our simulations, we also tested the constant Smagorinsky model but found that the AMD model converged more rapidly as the resolution was increased. With the AMD model, the dynamics under pure convection are relatively insensitive to grid spacing. In the wind forced case, the root mean square vertical velocity and pressure near the surface increase as the resolution increases. This is likely due to additional small-scale turbulence near $z = 0$ m being resolved in higher resolution runs. However, at a depth of -30 m, close to the depth where the rms vertical velocity reaches its maximum, the vertical velocity is only weakly dependent on the resolution under both convection and wind forcing. A detailed discussion of the resolution convergence can be found in appendix 3.A.

Buoyant material is modelled using two approaches: an Eulerian tracer concentration field and Lagrangian surface particles. The setup for the Eulerian tracer concentration field is similar to Taylor (2018) and Chor et al. (2018a). The tracer is modelled as a continuous concentration of non-interacting particles. Each particle moves with the local fluid velocity plus a constant upwards slip velocity. This is equivalent to considering small, buoyant particles of a fixed size and density. We assume low tracer concentrations, so although the tracers themselves are buoyant, they do not affect fluid buoyancy. The equation for the concentration of buoyant material is given by:

$$\frac{\partial c}{\partial t} + \mathbf{u} \cdot \nabla c + w_s \frac{\partial c}{\partial z} = \nabla \cdot ((\kappa_{SGS} + \kappa_c) \nabla c) \tag{3.3}$$

where w_s is the constant slip velocity and κ_{SGS} is the sub-grid scale diffusivity. We set $\kappa_c = \kappa_b = 10^{-6}$ m^2/s, although this value is very small compared with κ_{SGS} and does not influence the tracer concentration. The buoyant tracer concentration is updated using the same numerical method as the main LES code. A small number of negative values of the tracer concentration occur due to Gibbs ringing at the grid-scale, but the total tracer concentration is conserved by the numerical scheme. The initial condition of the tracer is exponential in depth, specifically $c(x,y,z,t=0) = e^{z/10\text{m}}$. In this study, three tracers are considered with slip velocities of $w_s = 0.001$, 0.005, 0.01 m/s. Experiments on a sample of microplastics from the North Atlantic Subtropical Gyre estimate the slip velocity to be between 0.005 and 0.025 m/s (Kooi et al., 2016) which coincides with the two most buoyant tracers in our simulations. Above a value of 0.01 m/s the continuous tracer field exhibits significant numerical noise which prevents us from further increasing the slip velocity.

To investigate buoyant material with higher slip velocities, we turn to Lagrangian particles. We implement a two-dimensional particle model at the surface of the domain, which can be interpreted as the limit of extremely buoyant particles where $w_s \gg |w|$. The movement of small inertial particles for which inertial effects are negligible compared to flow advection and buoyancy effects is governed by a simplified version of the Maxey-Riley equations (Maxey and Riley, 1983), which we outlined in chapter 1. To model the influence of unresolved turbulence on particle motion, a random displacement is included following the approach in Liang et al. (2018). This gives the equations for the motion of two-dimensional non-inertial particles as the following:

$$\mathbf{x}_p(t+dt) = \mathbf{x}_p(t) + \mathbf{u}(\mathbf{x}_p,t)dt + \mathbf{x}_{sgs}(\mathbf{x}_p,t) \ , \tag{3.4}$$

$$x_{sgs,i} = \frac{\partial \nu_{sgs}}{\partial x_i}(\mathbf{x}_p,t)\,dt + (2(\nu_{sgs}(\mathbf{x}_p,t))_+)^{\frac{1}{2}} d\xi_i \ . \tag{3.5}$$

In equation (3.4), $\mathbf{u}$ is the resolved velocity interpolated at the particle position and $\mathbf{x}_{sgs}$ is the displacement due to sub-grid scale motion. In equation (3.5), the subscript i indicates the spatial dimension, ν_{sgs} is the sub-grid scale viscosity interpolated at the particle position, $d\xi_i$ is Gaussian white noise with variance dt, and $(\cdot)_+ = \max(\cdot, 0)$.

Interpolated quantities are calculated using cubic B-splines following Hinsberg et al. (2012). This method was chosen due to its low computational cost and high accuracy (outlined in chapter 2). The particle evolution equations are time-stepped using the third-order Runge-Kutta method alongside the main LES code. We simulate the motion of 4000 particles which are initially randomly distributed. In appendix 3.A, we discuss the sensitivity of particle clustering to the resolution of the LES and find that in the cases with pure convective forcing, the results are not very sensitive to resolution. In the wind forced case increasing the resolution slightly reduces the tendency for the particles to cluster.

Here, we report seven simulations with different values of the surface buoyancy flux and wind stress. The parameter space can be interpreted in terms of the friction velocity u^* and the convective velocity w^* (Deardorff, 1970) which characterise the velocity scales of wind-driven turbulence and convection, respectively. These are defined as:

$$u^* = \left(\frac{\tau}{\rho_0}\right)^{\frac{1}{2}}, \tag{3.6}$$

$$w^* = (|B_0|H)^{\frac{1}{3}}. \tag{3.7}$$

Here, τ is the surface wind stress, ρ_0 is the constant reference seawater density, B_0 is the surface buoyancy flux and H is the initial mixed layer depth. The ratio between u^* and w^* measures the relative importance of wind and convection.

There is some disagreement in the literature as to the ratio of u^* and w^* that marks a transition from convective turbulence to stress-driven turbulence. For example, early numerical studies using LES estimated that a value of $u^*/w^* = 0.65$ marks the change from convective cells to convective rolls in the atmospheric boundary layer (Moeng and Sullivan, 1994), whilst for convection between flat plates the estimated transitional value is $u^*/w^* = 0.35$ (Sykes and Henn, 1989). In the ocean, Heitmann and Backhaus (2005) found a change in flow behaviour for $u^*/w^* = 0.4 - 0.7$. Regardless of the transition value, we expect wind-driven turbulence to dominate when $u^*/w^* \gg 1$ and convection to dominate when $u^*/w^* \ll 1$. For intermediate values, both wind and convective forcing likely both influence the dynamics to some degree. In the context of vertical mixing of buoyant materials, Chor et al. (2018b) introduced a generalised turbulence velocity scale, W, and in the absence

Simulation name	$B_0 \times 10^8$ (m^2/s^3)	τ (Nm^{-2})	w^*(m/s)	u^* (m/s)	$\frac{u^*}{w^*}$
I	−4.24	0	0.015	0	0
	−4.24	0.01	0.015	0.003	0.21
	−4.24	0.05	0.015	0.007	0.46
II	−4.24	0.1	0.015	0.01	0.66
	−0.424	0.1	0.0070	0.01	1.41
	−0.0424	0.1	0.0032	0.01	3.05
III	0	0.1	0	0.01	∞

Table 3.1 Simulation parameters

of Langmuir turbulence this is given by:

$$W^3 = u^{*3}\kappa^3 + A_c^3 w^{*3} \,, \tag{3.8}$$

where $\kappa = 0.41$ is the von Kármán constant and A_c represents the contribution of convective turbulence to W which Chor et al. (2018b) estimated to be $A_c = 1.170$. The larger convective coefficient suggests that vertical mixing is influenced more strongly by convective turbulence than wind shear when $u^* = w^*$. The Monin-Obukhov length-scale also characterises the importance of convective forcing and wind forcing, and is defined as

$$L = \frac{-u^{*3}}{\kappa B_0} \,, \tag{3.9}$$

where κ is the von Kármán constant as above, and B_0 is the surface buoyancy flux. In case II defined below ($u^* = w^*$), we find $L = 58$ m which predicts that wind forcing is important throughout the upper part of the mixed layer.

Our simulations can be arranged into two series, each independently varying the strength of the wind or the convective forcing. This includes one simulation with pure convection and one simulation with pure wind forcing, which act as control simulations. The first series is run with a surface buoyancy flux held constant at -4.24×10^{-8} m^2/s^3 and the wind stress varying between 0 and 0.1 Nm^{-2}, which is equivalent to wind velocities at 10 m ranging between 0 and 8.1 m/s (calculated using a drag coefficient $C_D = 0.0013$). The second series is run with wind stress held constant at 0.1 Nm^{-2} and the surface buoyancy flux varying between 0 and -4.24×10^{-8} m^2/s^3. This allows us to see the effect of increasing wind and convection independently and ensures that we cover a wide range of flow behaviour without applying unrealistic wind or convection forcing. Each simulation has a different value of u^*/w^*. The parameters of the simulations are listed in table 3.1, and the parameter space can be visualised in figure 3.1.

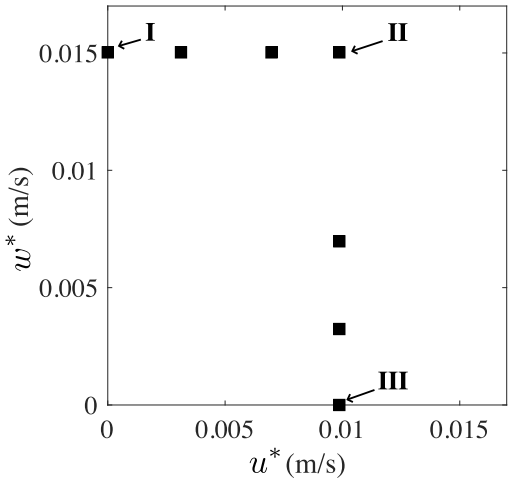

Fig. 3.1 u^* and w^* parameter space for simulations. Case I, II and III are labelled for reference.

3.3 Results

Here, we primarily focus on three simulations that illustrate the three main flow regimes: pure convection (case I), combined wind and convection (case II) and pure wind forcing (case III). In case I, $w^* = 0.01$ m/s and $u^* = 0$ m/s, in case II, $w^* = u^* = 0.01$ m/s, and in case III, $w^* = 0$ m/s and $u^* = 0.01$ m/s. This allows us to directly examine convection and wind forcing of similar strengths. The remaining simulations exhibit qualitative features that are represented in one of these three cases. In all analysis below, we neglect transient effects by considering horizontal slices at $t = 12$ hours and calculating time averages over one inertial period from $6 - 23.5$ hours. This ensures that the simulated flow has reached a fully developed turbulent condition before the start of the time average. In cases I and II, quasi-steady convection is established by approximately 4 hours. This suggests that our results might be consistent with at least part of the diurnal cycle when night-time convection becomes fully developed.

The results are organised into three subsections: in section 3.3.1, we present a qualitative description of the flow, buoyant tracers and surface particles; in section 3.3.2, we investigate the formation of convective vortices and the influence of wind forcing on the vortices; in section 3.3.3, we look at the accumulation of buoyant tracer and surface particles.

3.3.1 Qualitative description of the flow and the distribution of buoyant material

In this section, we start by describing the qualitative features of the turbulence and the distribution of buoyant tracers and particles in cases I, II, and III. Figure 3.2 shows horizontal slices of the vertical velocity, tracer concentration and surface particle positions. The vertical velocity field is shown 5 m below the surface. The tracer concentration and particles are shown at the surface ($z = 0$ m). We show the tracer with $w_s = 0.005$ m/s, which is the intermediate buoyancy used in our simulations. A smaller value of w_s gives a more uniformly distributed tracer field, whilst a larger value of w_s gives a more strongly clustered tracer field (shown below). In all of the cases, the average vertical fluid velocity is zero due to the boundary conditions at the surface. The regions of downwelling appear to occupy a smaller area (particularly in I and II) but are larger in magnitude.

In case I, distinct convection cells are visible. Convective cells are characterised by large areas of weak upwelling surrounded by narrow regions of strong downwelling. The downwelling regions between neighbouring convective cells meet at convective 'nodes'. As in Chor et al. (2018a), the horizontal scale of the convective cells is typically about 1-2 times the depth of the mixed layer (recall that the mixed layer depth is 80 m). The buoyant tracer concentration is elevated in locations of downwelling between convective cells with the highest concentrations in the nodes. The particles, which unlike the tracer are confined to the surface, have a more extreme distribution and are located almost exclusively in the nodes.

In case II with convective and wind forcing, the convection cells are replaced by distinct larger-scale downwelling streaks. The tracer accumulates in the streaks with the strongest downwelling. This is mirrored in the distribution of surface particles. In case III with pure wind forcing, the vertical velocity exhibits horizontal streaks on a smaller scale compared to case II and the tracer concentration also exhibits streaks. In section 3.3.3, we show that the tracer accumulates in streaks of high speed. The average tracer concentration is noticeably higher at the surface for the same slip velocity (discussed below). The surface particles appear to be less organised than the tracer in this case, although this might be due to the small size of the wind-driven turbulent streaks and the limited number of particles. Inherent differences between Eulerian and Lagrangian dynamics and statistics are interesting, but we are not able to comment on this directly since the tracers and particles sample different depths in our simulations. Still, some areas exhibit elevated particle concentrations and the particles are not uniformly distributed.

As the slip velocity of the tracer increases, the surface tracer concentration increases and the tracer becomes more clustered. Figure 3.3 shows the tracer distribution at the surface with increasing slip velocity (left to right) in case II. The least buoyant tracer concentration

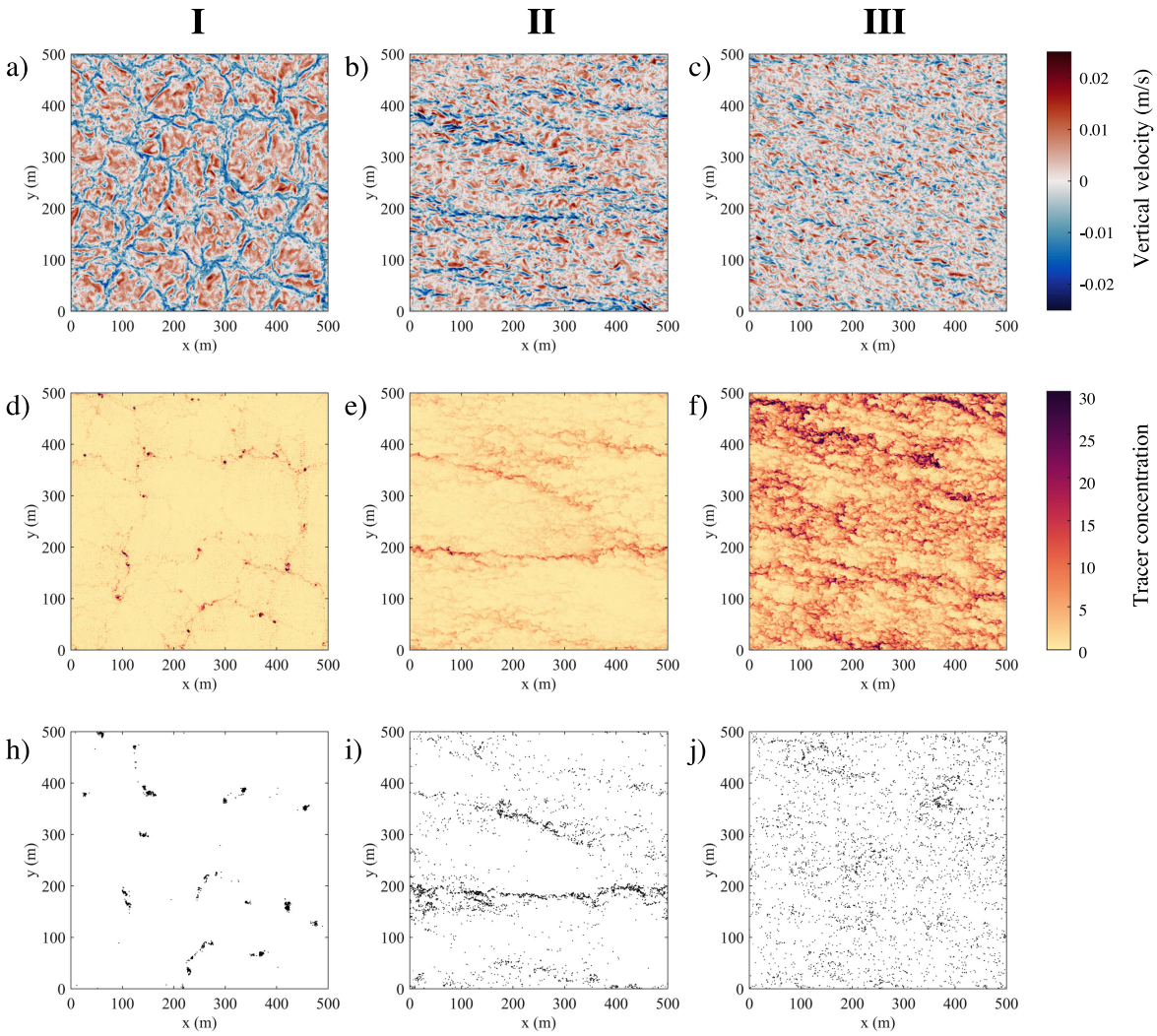

Fig. 3.2 Horizontal cross sections of the vertical velocity at $z = -5$ m (a,b,c), tracer concentration with slip velocity 0.005 m/s at $z = 0$ m (d,e,f) and particle position at $z = 0$ m (h,i,j).

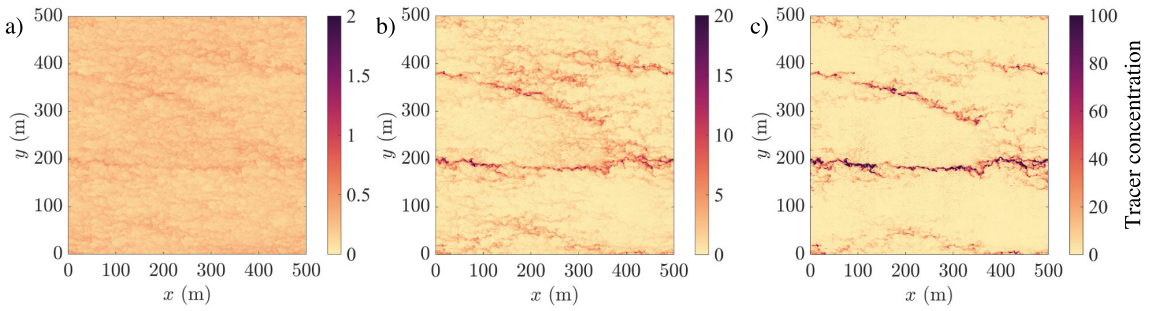

Fig. 3.3 Horizontal cross section at $z = 0$ m of tracer with $w_s = 0.001$ m/s (a), $w_s = 0.005$ m/s (b), $w_s = 0.01$ m/s (c) in case II.

(left) exhibits horizontal streaks but with smaller variations (note the difference in colour axis scale for the three horizontal slices). The most buoyant tracer (right) is more strongly clustered; it has wide expanses of low concentration as well as a few large-scale horizontal streaks with very high tracer concentration, up to fifty times higher than the least buoyant tracer. The distribution of surface particles (see figure 3.2i) exhibits the same patterns as the most buoyant tracer. Note that the mean surface tracer concentration is also significantly higher for the more buoyant tracers, and this is discussed further below.

The influence of the slip velocity on the tracer distribution can be explained in terms of the ability of the vertical fluid velocity to overcome the slip velocity. For all three tracers, the slip velocity is smaller than the maximum vertical velocity (approximately 0.02 m/s). Tracer accumulates in regions of horizontal flow convergence, and at the surface this coincides with downwelling regions of the flow where tracer can be transported below the surface. A less buoyant tracer is more easily submerged and may then resurface in an upwelling (horizontally divergent) region giving a more uniform distribution. Very buoyant tracers are only subducted in regions of strong downwelling and the tracer then quickly rises back to the surface. As a result, very buoyant tracers remain close to regions of strong horizontal convergence and downwelling. It is worth noting, however, that not all downwelling regions exhibit high tracer concentrations. In case I the buoyant tracer and surface particles are strongly clustered in a subset of the convective nodes. As we will see in the next section, these regions are occupied by convective vortices.

Figure 3.4 shows vertical profiles of the mean tracer concentration (horizontally and time averaged) under different wind and convection forcing conditions. In all cases, the mean tracer concentration is surface intensified and the concentration at $z = 0$ m is highest for the most buoyant tracer. As noted from visualisations of the buoyant tracer (figure 3.2), the mean tracer concentration is noticeably higher at the surface in case III compared to

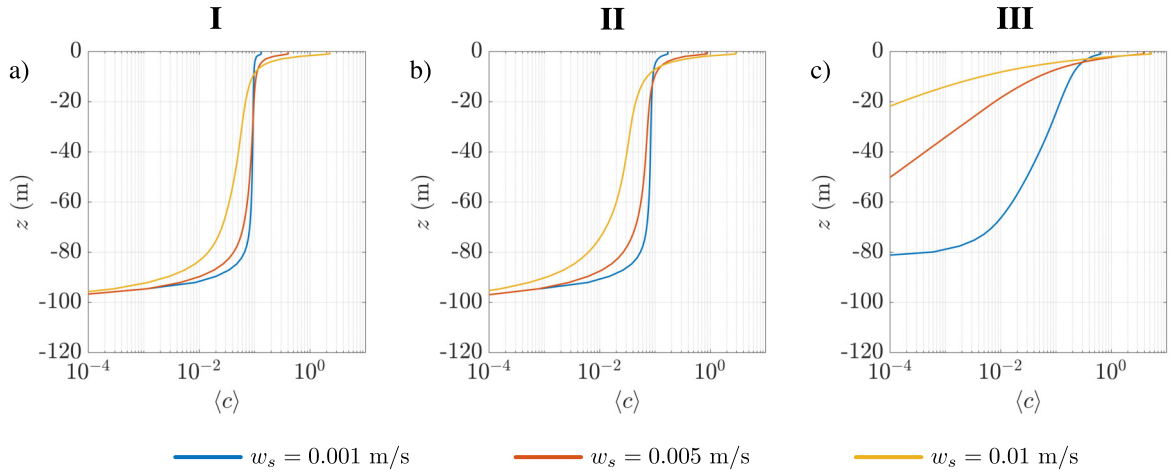

Fig. 3.4 Vertical profile of mean tracer concentrations.

cases I and II. This is confirmed in figure 3.4, which shows that in case III, the vertical distribution of the mean tracer concentration is significantly different from I and II. For all slip velocities in case III, the tracer concentration at the bottom of the mixed layer ($z = -80$ m) is small compared to the surface concentration ($z = 0$ m). In comparison, the mean tracer concentration profiles in I and II are quite similar. In both cases the weakly buoyant tracers are relatively homogeneous in the middle of the mixed layer (i.e. -60 m $< z < -20$ m). These vertical profiles closely resemble those in Chor et al. (2018b) and suggest that vertical mixing by convection is fast enough to overcome the effects of tracer buoyancy with or without wind forcing. The turbulence velocity scale, W (see equation (3.8)), predicts that convective forcing contributes to vertical mixing more than wind shear when $u^* = w^*$, and explains why the vertical distribution of the buoyant tracers in case II is more similar to case I than case III.

Although the mean tracer concentration is relatively constant in the vertical direction in cases I and II, the tracer concentration within the mixed layer is not uniform. Figure 3.5 shows the tracer concentration on horizontal slices at $z = -30$ m. By comparing with figure 3.2, it is evident that regions with high tracer concentration at $z = -30$ m generally coincide with regions with high concentration at $z = 0$ m. This suggests that regions with elevated tracer concentration are vertically coherent in cases I and II. There are also small areas of very high concentration, particularly visible in case I. These are generally co-located with the surface particles and in the next section we will show that these correspond to convective vortices. In case III, there are a few small spots with elevated tracer concentration, but the concentration is generally quite small at this depth.

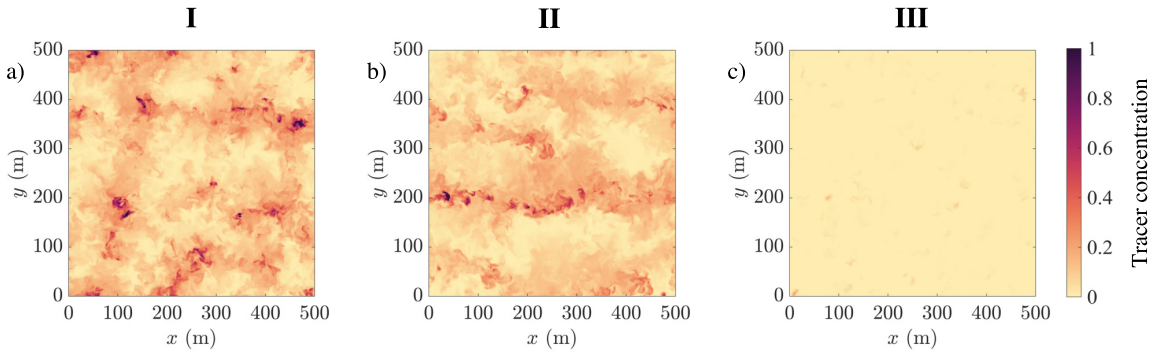

Fig. 3.5 Horizontal cross section at $z = -30$ m of buoyant tracer ($w_s = 0.005$ m/s).

3.3.2 Convective vortices

In this section, we examine the convective vortices in more detail, focusing in particular on the influence of wind forcing on the convective vortices. There are several ways to identify convective vortices. Chor et al. (2018a) characterised convective vortices using the two-dimensional Okubo parameter. Here, we apply a similar method as developed in Raasch and Franke (2011) who identified dust devils in a convective boundary layer using pressure and vorticity. Whilst vorticity is an obvious measure, small-scale turbulence also contributes to vorticity, making it difficult to identify coherent convective vortices. We eliminate some of this small-scale noise by applying a Gaussian filter to the vorticity field before using it to identify convective vortices. In addition, structures such as regions of high shear can have large values of vorticity, and so we use the pressure field in conjunction with vorticity to exclude such structures. The physical reasoning behind using the pressure field is that the centrifugal force created by the fluid rotating inside the vortex causes the pressure to be lower than the surrounding fluid (Hussain and Jeong, 1995). We have verified that pressure and the Okubo parameter yield qualitatively similar results (see appendix 3.B).

Vortices are identified using the local minima of the departure from the hydrostatic pressure and local maxima of the filtered absolute vorticity field, where local minimum/maximum means that the values are smaller/larger than the adjacent 224 grid points (forming a 15×15 grid). This grid size has been determined empirically to avoid detection of multiple vortex centres within one convective vortex. We use the pressure and vorticity fields evaluated at $z = -1$ m to match the depth of the surface particles. We require the pressure minimum to be located within two horizontal grid points of the filtered absolute vorticity maximum, which we define as the vortex centre. We use a threshold value of 5 times the standard deviation of filtered absolute vorticity ($5\sigma_{\tilde{\zeta}}$, where $\tilde{\zeta}$ denotes the Gaussian filtered vorticity) and 5

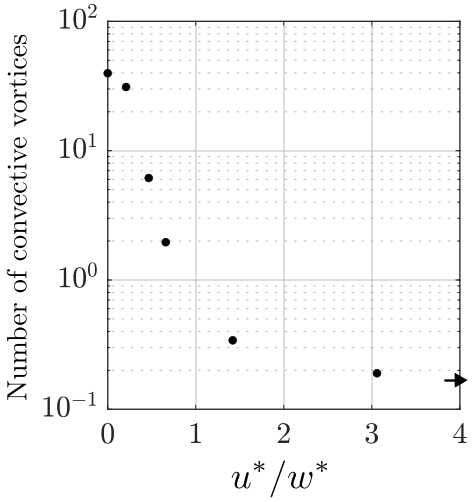

Fig. 3.6 Ratio of u^* and w^* against the number of vortices detected at any given time averaged over one inertial period in the full domain (500 m $\times$ 500 m). The arrow indicates the number when u^*/w^* is infinite.

times the standard deviation of perturbation pressure ($5\sigma_p$) at $z = -1$ m which is similar to the applied thresholds in other vortex detection algorithms (Giersch et al., 2019; Nishizawa et al., 2016b). This threshold aims to eliminate as much non-coherent turbulence as possible, whilst still capturing sufficient information for analysis. The magnitude of the threshold value depends on the strength of wind forcing and convective forcing of each simulation.

More convective vortices are identified under strong convective conditions, and the number of convective vortices decreases with increasing wind strength. To quantify this in all simulations, we count the number of vortices detected using our criterion at each time-step and average over one inertial period. Figure 3.6 shows that the total number of vortices decreases as u^*/w^* increases. In case I, there are approximately 2 vortices per 100 m^2 (40 vortices in the 500 m^2 domain). When $u^* \simeq w^*$ (case II), the number decreases by about two orders of magnitude compared to when $u^* = 0$ m/s (case I). For higher values of u^*/w^*, less than one vortex is detected in the domain at any given time. Note that the number of convective vortices is not exactly equal to zero when $w^* = 0$ m/s. We interpret this as rare regions of intense turbulence that happen to meet our criterion rather than as convective vortices.

To visualise the convective vortices in cases I, II and III, we use the pressure field. Figure 3.7 shows pressure isosurfaces in the upper panel and pressure contours at $z = -1$ m (black) and particle position (red) in the lower panel. In cases I and II, we observe coherent convective vortices which typically occur in the regions of strong downwelling and extend down from the surface into the mixed layer. Note, however, by comparison with figure 3.2

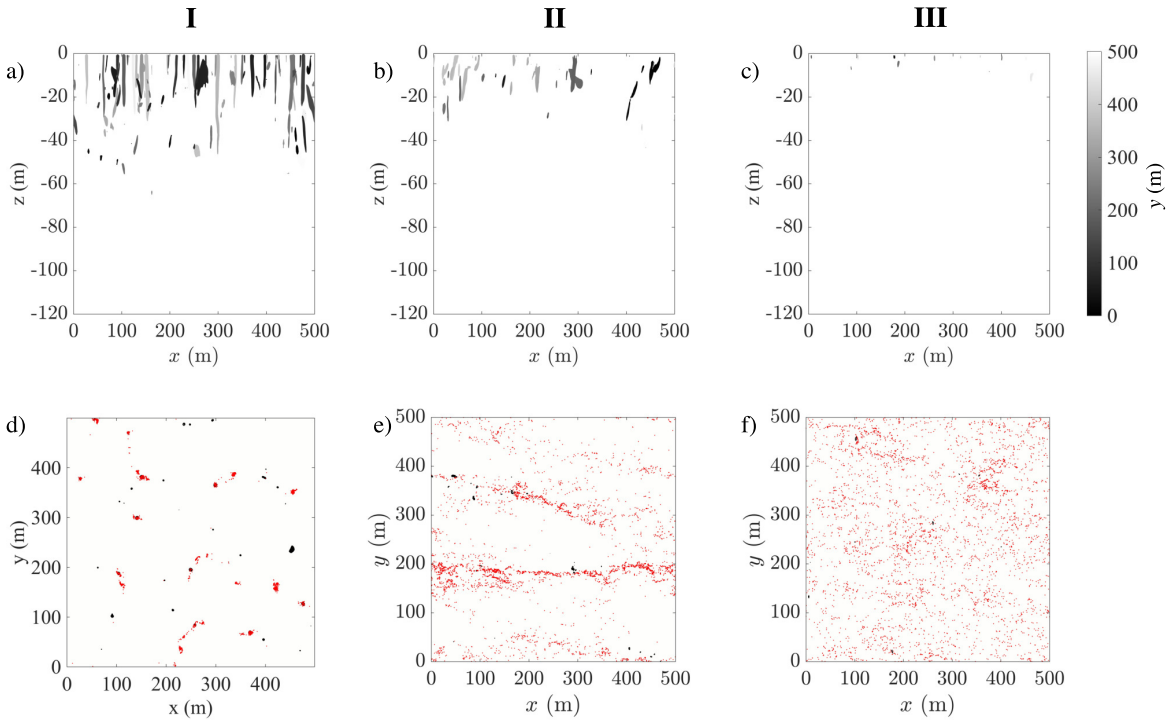

Fig. 3.7 (a,b,c) Spanwise view of pressure isosurfaces where the departure from the hydrostatic pressure is $\delta p = -5 \times \sigma_p$ Pa, taken at $t = 12$ hours. All regions with $\delta p < -5 \times \sigma_p$ Pa are visible in this view. (d,e,f) Horizontal cross section of the pressure contour at $z = -1$ m (black) with surface particle position superimposed (red), taken at $t = 12$ hours.

that not all locations with strong downwelling contain a convective vortex. In case I, the convective vortices occur in the nodes where downwelling regions join together and there is coincident particle clustering inside the convective vortices. In case II, the convective vortices preferentially occur in the coherent downwelling streaks and are tilted in the direction of wind forcing. Surface particles cluster in the larger downwelling streaks and are less confined to convective vortices than in case I. In case III, coherent vortices are not visible and there is relatively little particle clustering. In all cases, the convective vortices detected have a relatively small diameter of a few metres. This implies that simulations need a high resolution for convective vortices to be visible and observations in the ocean would require measurements at small-scales.

To further characterise the surface flow, we look at the relationship between vertical velocity and pressure. This allows us to identify regions of downwelling and convective vortices, both of which have a role in clustering buoyant material. The joint probability distribution function of vertical velocity and pressure is shown in figure 3.8 under different wind and convective forcing at $z = -1$ m. In all cases, points which have values of vertical velocity and pressure near zero are much more common than points with extreme values. In case I, the distribution of points is highly skewed, with a long tail of values with negative pressure. The contour at probability density level 10^{-4} demonstrates that there are more points with negative pressure and negative vertical velocity. This indicates that convective vortices experience a bias towards downwelling circulation, which is consistent with the visualisations (figure 3.7d).

With wind forcing (cases II and III), the shape of the joint probability density function becomes more isotropic, in particular in the distribution of pressure points between positive and negative values. The range in vertical velocity is larger in case II and III compared to case I (note the change in axis limits). Case II has more points with low pressure than case III, consistent with the visualisation showing well-defined convective vortices in case II but not case III, and the very small number of vortices detected (figure 3.6).

We can analyse the mean structure of the convective vortices by superposing many convective vortices and averaging their properties. For each time-step, we identify convective vortices using the detection method described above and average the field centred at the vortex centre over all of the vortex centres found during one inertial period.

Figure 3.9 shows horizontal (a) and vertical (b) slices of the vertical velocity for the averaged convective vortex in case I. The horizontal cross sections are taken at $z = -1$ m whilst the vertical cross sections are taken through the centre of the averaged convective vortex. The threshold pressure contour (red) is included along with the vectors of velocity (black).

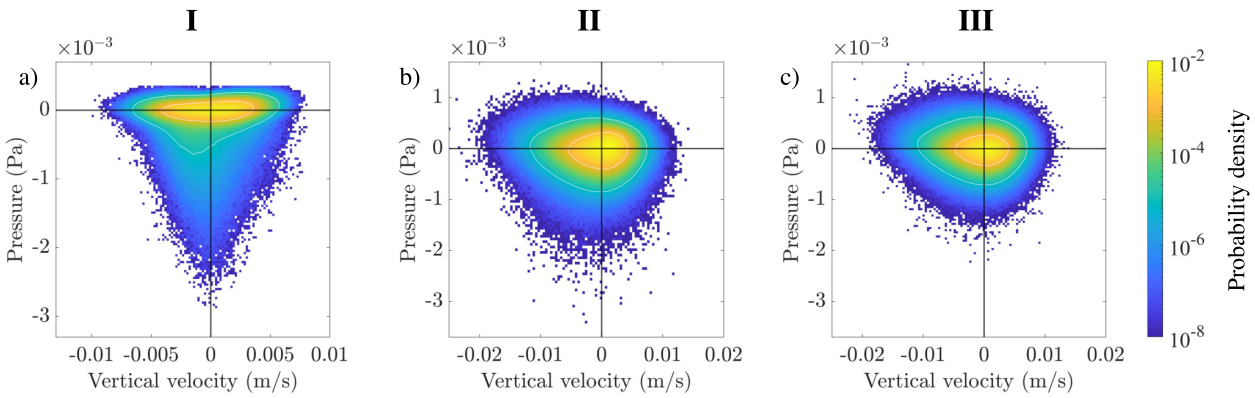

Fig. 3.8 Joint probability density function of vertical velocity and pressure perturbation (δp) at $z = -1$ m. White contours show where the PDF is 10^{-2} and 10^{-4}.

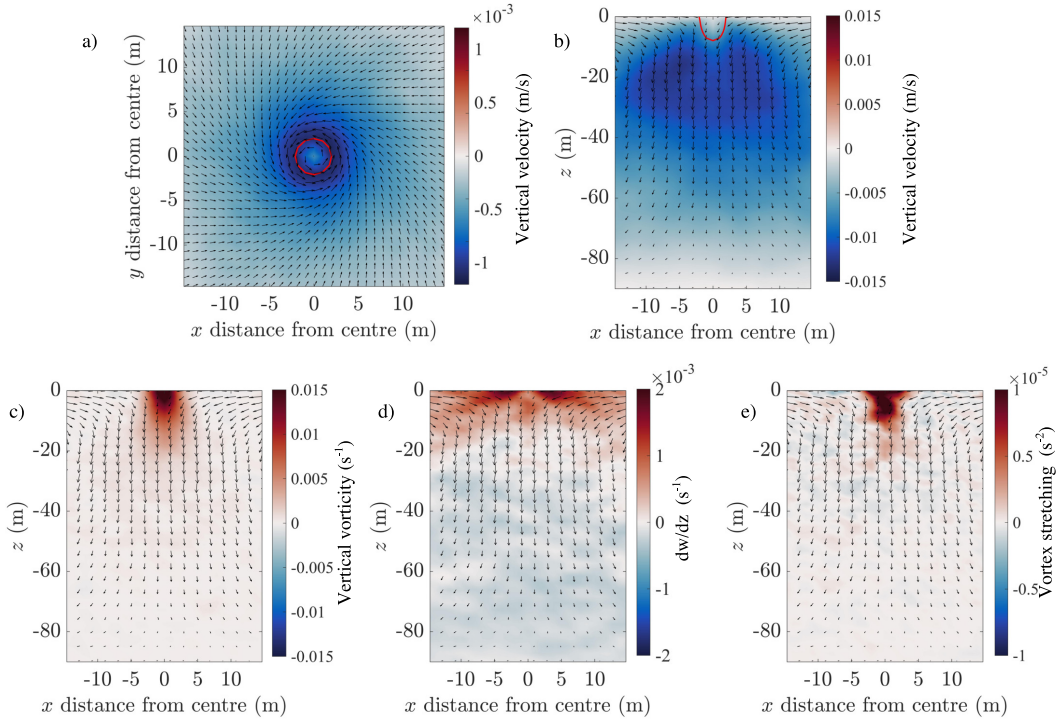

Fig. 3.9 Horizontal cross section of vertical velocity at $z = -1$ m (a) and vertical cross sections of vertical velocity (b), vertical vorticity (c), $\partial w/\partial z$ (d) and vertical vortex stretching (e) for the averaged vortex in case I with vectors of horizontal velocity (black) and the threshold pressure contour (red).

The averaged convective vortex is symmetric about its centre. Although the mean vortex diameter is about 5 m based on the pressure threshold, enhanced subduction extends about 15 m from the vortex centre. Since the vortex diameter is only a few times larger than the model grid spacing, it is possible that the vortex diameter would be even smaller in higher resolution simulations. The mean flow spirals inwards to the centre of the convective vortex with cyclonic (counter-clockwise) rotation. The peak vertical velocity occurs on the periphery of the convective vortex and encircles a local minimum in the centre. This is consistent with simulations of dust devils in the atmosphere (Giersch and Raasch, 2021; Raasch and Franke, 2011) which speculate that the decrease in vertical velocity in the central core of an averaged vortex could indicate stagnation points or flow reversal inside dust devils, shown schematically in Balme and Greeley (2006). Such features may be observable in instantaneous data with higher resolution, but this is outside the scope of the current study. Below 30 m the downwelling broadens and becomes weaker in the bottom half of the mixed layer.

The convective vortices are maintained by vortex stretching. The vertical component of the vortex stretching term is $\boldsymbol{\omega} \cdot \nabla w$ where $\boldsymbol{\omega} = \nabla \times \mathbf{u}$ is the vorticity and w is the vertical velocity. Figure 3.9c-e shows the vertical component of vorticity, ζ, $\partial w/\partial z$, and $\zeta \partial w/\partial z$ all averaged over the ensemble of convective vortices. The term $\boldsymbol{\omega} \cdot \nabla w$ is dominated by stretching of vertical vorticity ($\zeta \partial w/\partial z$), whilst the vortex twisting term ($\zeta_x \partial w/\partial x + \zeta_y \partial w/\partial y$) is one order of magnitude smaller and shows little coherence. The ensemble mean is characterised by large vertical vorticity near the surface which decreases with depth. Interestingly, the average vorticity is positive, which indicates a bias towards cyclonic rotation as explored further below. The vertical component of the vortex stretching term is positive in the core of the mean vortex, indicating a source of positive vertical vorticity. Below 30 m, $\partial w/\partial z$ changes sign and there is little coherence in the vortex stretching field. The relatively small positive vorticity below 30 m is likely maintained by advection or diffusion.

The structure of the convective vortex changes as the wind stress increases. Figure 3.10 shows horizontal (a-d) and vertical (e-h) cross sections of the vertical vorticity averaged over the ensemble of convective vortices for $\tau = 0$ (case I) , 0.01, 0.05, 0.1 Nm^{-2} (case II), with the buoyancy flux remaining constant ($B_0 = -4.24 \times 10^{-8}$ $\mathrm{m}^2/\mathrm{s}^3$). The remaining simulations do not have a sufficiently large number of convective vortices to provide a robust average (see figure 3.6) and are not shown. As wind forcing increases, the horizontal vortex structure becomes less symmetric and we observe a streak of increased vorticity which extends from the vortex centre in the direction of wind forcing. Under these higher wind strengths, the vortex tilts and is confined to shallower depths which is consistent with the shearing of the convective vortices seen in figure 3.7. Interestingly, the magnitude of vorticity

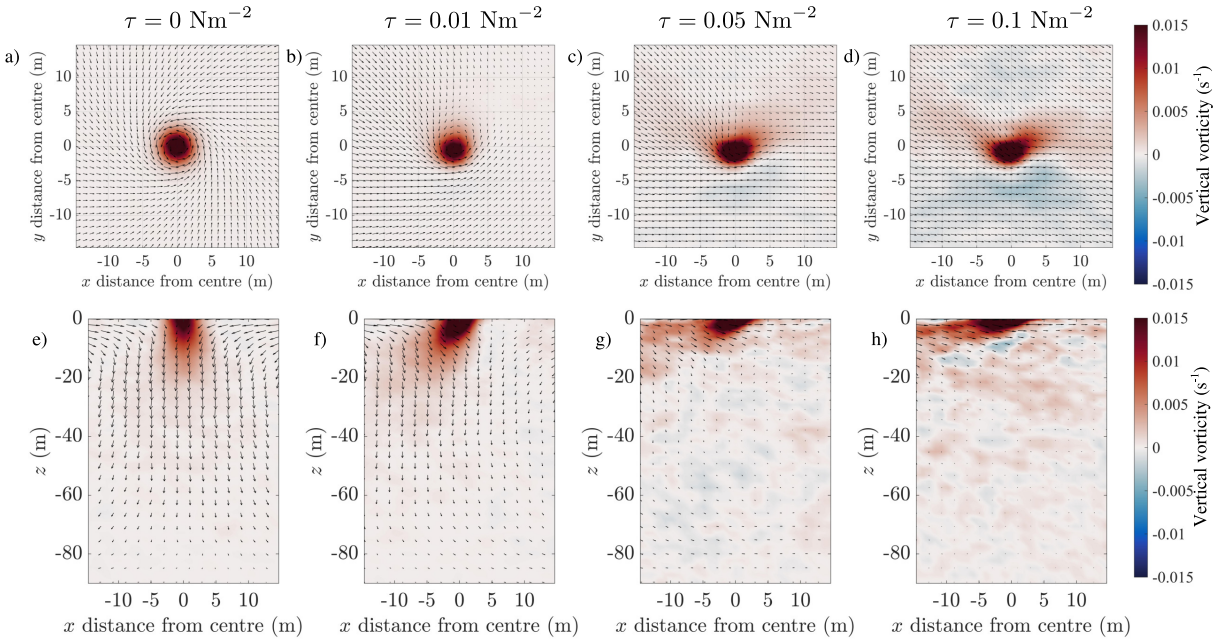

Fig. 3.10 Horizontal (a-d) and vertical (e-h) cross sections of vertical vorticity for the averaged vortex for $\tau = 0, 0.01, 0.05, 0.1$ Nm^{-2} with vectors of horizontal velocity superimposed.

inside the convective vortex is not strongly dependent on the strength of the wind forcing, and the bias towards positive vorticity also persists.

Despite their small size, the convective vortices in our simulations exhibit a strong bias towards cyclonic (counter-clockwise in the northern hemisphere) rotation, suggesting an influence from the Coriolis acceleration. The relative importance of the Coriolis acceleration is typically quantified using the Rossby number, $Ro \equiv U/(fL) \sim \zeta/f$. It is generally assumed that the planetary rotation is unimportant for processes that are characterised by $Ro \gg 1$. Here, $\zeta/f > 100$ within the convective vortices in case I, and hence the bias towards cyclonic rotation is surprising. Although there has been some debate, observations and simulations of dust devils in the atmosphere appear to indicate that cyclonic and anticyclonic vortices form in roughly equal number (Balme and Greeley, 2006; Sinclair, 1965). In the oceanic case, Chor et al. (2018a) set $f = 0$ s^{-1} and hence did not explore the possibility of a cyclone/anticyclone asymmetry. Similar observations of a rotational bias within a high Rossby regime have been recorded in experiments and simulations of convective plumes in a rotating environment (Frank et al., 2017; Sutherland et al., 2021).

Figure 3.11 shows the probability density function (PDF) of the vertical vorticity at $z = 0$ m for points associated with convective vortices (left) and for all points in the domain (right) over one inertial period. To remove turbulent fluctuations, the vorticity at each point is

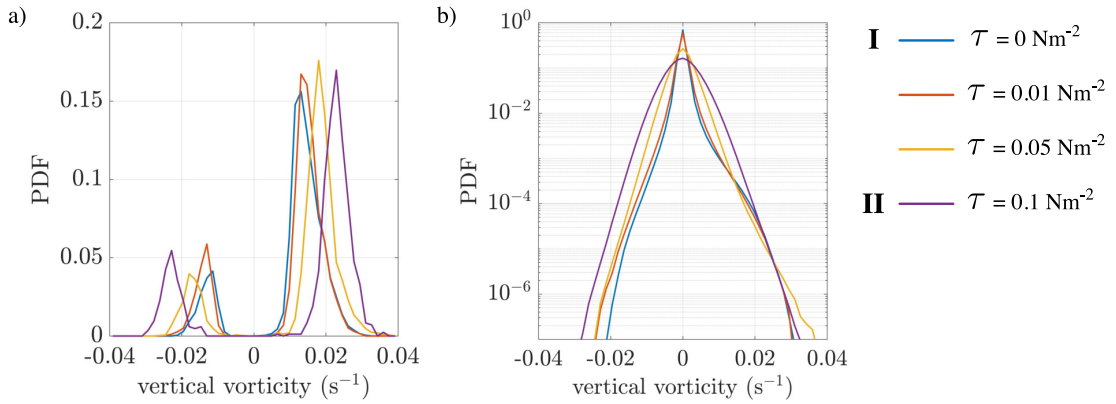

Fig. 3.11 Probability density function of vertical vorticity at $z = 0$ m for points identified as convective vortices (a) and all points in the domain (b).

averaged over a box measuring approximately 5 m×5 m, which is a similar length-scale to the diameter of a convective vortex. In addition to cases I ($\tau = 0$ Nm^{-2}) and II ($\tau = 0.1$ Nm^{-2}), we show the vorticity distribution for the two simulations with intermediate wind stress $\tau = 0.01$ Nm^{-2} and $\tau = 0.05$ Nm^{-2}, with the buoyancy flux remaining the same ($B_0 = -4.24 \times 10^{-8}$ m^2/s^3).

In case I, the PDF shows a distinct peak at $\zeta \simeq \pm 0.015$ s^{-1} which agrees with the ensemble mean shown in figure 3.10. All cases show a bias towards cyclonic vorticity, and for $\tau = 0$ Nm^{-2} and $\tau = 0.01$ Nm^{-2}, there is a noticeable bias in the distribution of vorticity for all points in the domain. As the wind stress increases, the peak in vorticity has a larger magnitude. This is likely due to the increased standard deviation of filtered vorticity in the stronger wind cases, leading to a larger threshold value used to identify convective vortices.

To explain the cyclonic bias, it is useful to examine the evolution of vorticity along the trajectory of surface particles. In the absence of friction, the vertical component of the vorticity evaluated along the paths of Lagrangian particles at $z = 0$ m satisfies

$$\frac{d\zeta}{dt} = (\zeta + f)\frac{\partial w}{\partial z}, \tag{3.10}$$

where ζ is the vertical component of the vorticity vector and f is the constant Coriolis parameter.

We can obtain a useful approximation if we use a constant value for $\partial w/\partial z$ to characterise the flow within a convective vortex. In the limit when $|\zeta| \ll |f|$ (corresponding to early times

when particle vorticity is very small), equation (3.10) then yields

$$\zeta = \zeta_0 + f\frac{\partial w}{\partial z}t, \tag{3.11}$$

where ζ_0 can be interpreted as the vorticity when the particle first encounters the convective vortex.

Sutherland et al. (2021) used a similar argument, along with a scaling for $\partial w/\partial z$, to explain the unexpected influence of rotation on high Rossby number plumes in a rotating environment observed in lab experiments reported earlier in Frank et al. (2017). Following their arguments, we can estimate the timescale needed for a particle that initially has no vorticity to reach a state with $|\zeta| \simeq |f|$. Using $\partial w/\partial z \simeq 2\times 10^{-3}\mathrm{s}^{-1}$ (figure 3.9d) gives a timescale of about 8 minutes. In section 3.3, we quantify the time a particle spends inside a convective vortex using particle statistics and find that in case I, particles remain within a convective vortex for an average of 47 minutes. This suggests that particles spend enough time within convective vortices for the planetary rotation to become important even if a particle enters a vortex with no relative vorticity.

The argument above holds when $|\zeta| \ll |f|$. However, the mean vorticity within convective vortices greatly exceeds f (figure 3.10). Returning to equation (3.10) and taking $|\zeta| \gg |f|$ while again using a constant value for $\partial w/\partial z$ yields solutions with exponentially increasing vorticity:

$$\zeta = \zeta_0 e^{\frac{\partial w}{\partial z}t}. \tag{3.12}$$

To examine the applicability of the linear and exponential solutions for vorticity, we evaluate the vorticity along trajectories of surface particles. For each particle, the pressure and vertical vorticity are interpolated at every time-step using cubic B-splines. We identify the time when each particle enters a convective vortex as the time when the particle pressure falls below $5\sigma_p$ and the particle filtered vorticity falls below $5\sigma_{\tilde{\zeta}}$ (the same criterion as used to identify convective vortices) and remains below this threshold for 30 minutes when $\tau = 0$ Nm^{-2} (case I) and 10 minutes when $\tau = 0.05$ Nm^{-2}. We then average the vorticity sampled along each particle path as a function of time referenced to the time when the particle entered the convective vortex (labelled $t = 0$ mins). Figure 3.12 shows the timeseries of the average vorticity sampled along the surface particle paths for $\tau = 0$ Nm^{-2} and $\tau = 0.05$ Nm^{-2}, where we also show the linear and exponential growth solutions using $\partial w/\partial z = 2\times 10^{-3}$ s^{-1}. We have verified that for $\tau = 0.01$ Nm^{-2}, the timeseries of the average vorticity is similar to case I, whilst for $\tau = 0.1$ Nm^{-2}, the particles do not enter enough convective vortices to provide a meaningful average.

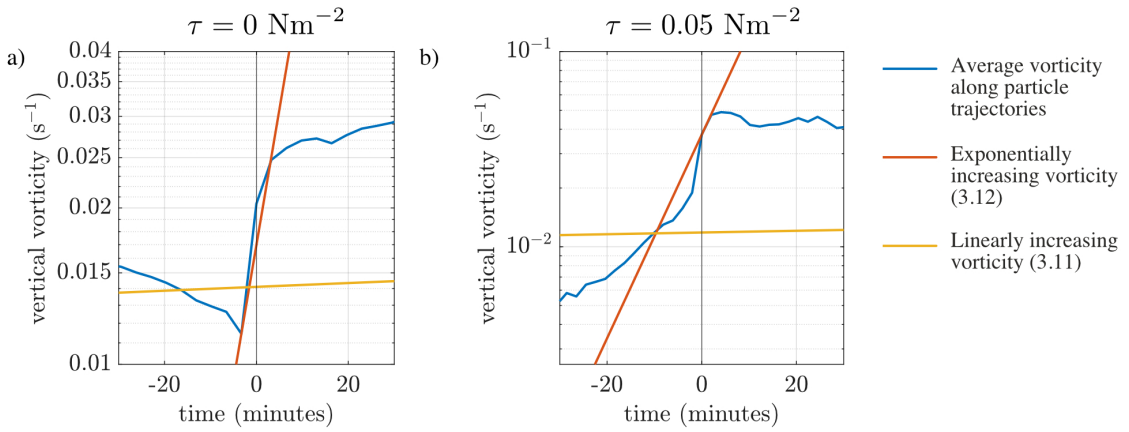

Fig. 3.12 Average trajectory of ζ along a surface particle path against the time spent inside a convective vortex (blue) with the exponential (red) and linear (yellow) vorticity solutions superimposed. Time $t = 0$ minutes corresponds to the time at which the particle enters a convective vortex.

In both cases, the sudden increase in vertical vorticity just before the particle enters a convective vortex is consistent with an exponential increase in vorticity at a rate set by the value of $\partial w/\partial z$ given above. Even before entering a convective vortex, particles are biased towards cyclonic vorticity from vortex stretching acting on the planetary vorticity (equation (3.11)). During each vortex encounter, the vorticity sampled along particle paths exponentially increases due to vortex stretching. Shortly after the particles enter the convective vortices, the vertical vorticity saturates. It is likely that frictional dissipation (which we neglected in equation (3.10)) competes with vortex stretching to prevent the relative vorticity from increasing further. A full exploration of the dynamics of convective vortices including frictional effects is left for a future study.

3.3.3 Clustering of buoyant material

In this section, we analyse the influence of convective vortices on the accumulation of buoyant material. We start by looking at the distribution of a buoyant tracer in the flow and then analyse the trajectories of surface particles. Finally, we introduce a measure to quantify buoyant material clustering and give an overview of clustering for all simulations.

Figure 3.13 shows the horizontal and vertical slices of the tracer concentration averaged over the ensemble of convective vortices for $\tau = 0,\ 0.01,\ 0.05,\ 0.1$ Nm^{-2}. In case I, the concentration of the buoyant tracer is highest at the surface and inside the convective vortex, and the tracer concentration decreases with distance from the vortex centre. Interestingly,

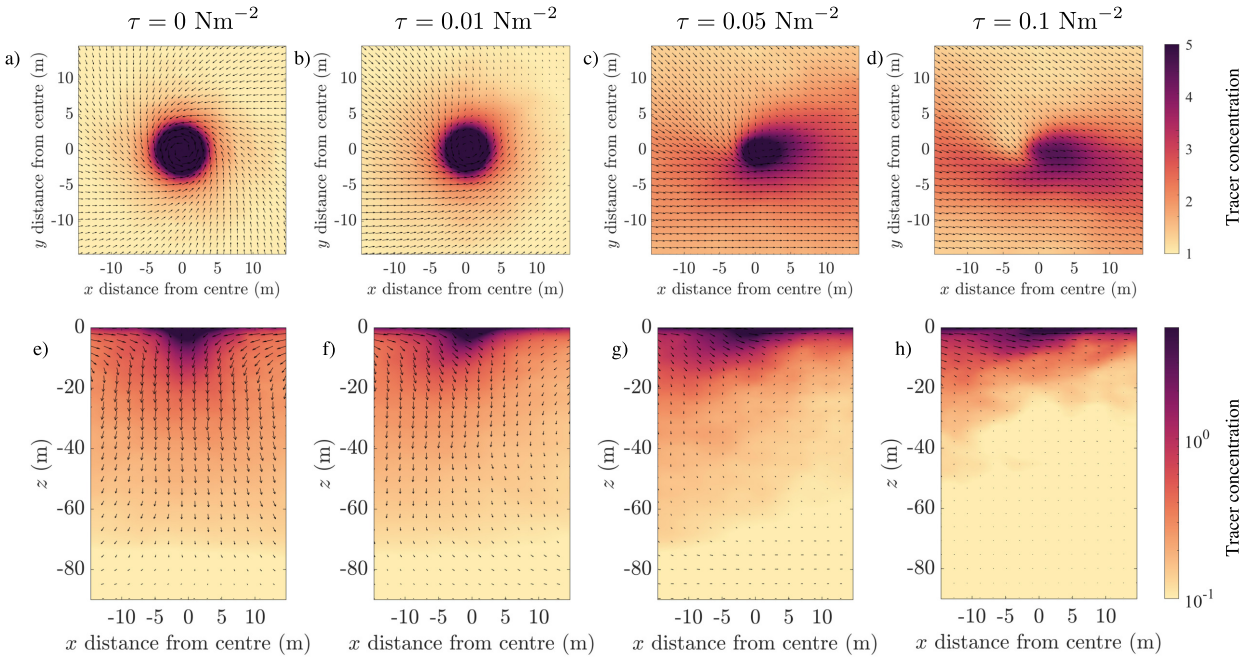

Fig. 3.13 Horizontal (a-d) and vertical (e-h) cross sections of tracer concentration ($w_s = 0.005$ m/s) for the averaged vortex for $\tau = 0, 0.01, 0.05, 0.1$ Nm^{-2} with vectors of horizontal velocity superimposed.

the maximum buoyant tracer concentration does not coincide with the region of maximum downwelling (figure 3.9a,b) but with the maximum vorticity. The reason for this is not clear, but we explore the relation between vertical velocity, pressure and tracer concentration further below. Under strong wind forcing, the maximum tracer concentration occurs upstream of the vortex centre and tracer accumulates in a horizontal streak oriented in the direction of wind forcing. We observe vertical shearing of the vortex similar to the vorticity field (figure 3.10) and there is less tracer at depth under stronger wind forcing.

The cyclonic convective vortices are more effective at accumulating buoyant particles than the anticyclonic vortices. To quantify this, we count the number of particles inside each convective vortex identified using our vortex detection criterion, where a particle is counted as being inside a vortex if it is located within a 15×15 grid (corresponding to 14.25 m $\times$ 14.25 m grid) centred at the vortex centre. We find that in case I, the average number of particles inside a cyclonic vortex is 23, whilst the average number of particles inside an anticyclonic vortex is 6. This bias continues up to $\tau = 0.01$ Nm^{-2} with the buoyancy flux remaining constant ($B_0 = -4.24 \times 10^{-8}$ m^2/s^3). Beyond this, we do not observe enough particles accumulating inside the convective vortex to give a statistically significant result. We see a similar pattern with the tracer field. Although the average tracer concentration

($w_s = 0.005$ m/s) is qualitatively similar in cyclonic and anticyclonic convective vortices, the tracer concentration is much higher inside the cyclonic vortices (maximum surface tracer concentration in the averaged cyclonic vortex is three times higher than in the averaged anticyclonic vortex for case I).

In convective dominated simulations, we observe buoyant material accumulating inside convective vortices rather than downwelling regions (figure 3.2d, figure 3.13). Figure 3.14 shows the concentration of buoyant tracer with $w_s = 0.005$ m/s at $z = 0$ m, averaged in bins based on the vertical velocity and pressure at $z = -1$ m. In case I, the buoyant tracer has a strong tendency to accumulate in regions with negative pressure which characterise convective vortices. This effect is dominant over the preference for particles to accumulate in regions with negative vertical velocity. This result is in line with the findings from Chor et al. (2018a). The large variability of tracer concentration at the edge of the distribution is associated with averaging over a small number of points (see figure 3.8). Outside the convective vortices, the regions with positive vertical velocity (above 0.002 m/s) have a very low tracer concentration, which is consistent with the visualisation in figure 3.2d.

When wind forcing is present (cases II and III), the tracer is more uniformly distributed across pressure and vertical velocity and there are fewer extremes in the tracer concentration (note the difference in colour axis for these panels). In both cases there is a distinct minimum in the tracer concentration in regions with positive vertical velocity. When convection and wind are both present (case II), the tracer concentration is large in regions of strong downwelling and low pressure. The notable difference in the tracer distribution in cases I and II shows that although convective vortices are present in case II, they are not as effective at accumulating buoyant tracers compared to the convective vortices in case I.

Although the buoyant tracer does not accumulate as effectively inside the convective vortices under strong wind forcing, we see accumulation inside streaks of high speed. Figure 3.15a-c shows the concentration of the buoyant tracer with $w_s = 0.005$ m/s at $z = 0$ m, averaged in bins based on the vertical velocity and squared horizontal speed ($u^2 + v^2$) at $z = -1$ m. In case III, the concentration of buoyant tracer is highest in regions of high speed, even when the vertical velocity is positive. In case II, the tracer is more uniformly distributed (note change in colour axis) but there are still elevated concentrations in regions of high speed. This is consistent with the close resemblance of horizontal distribution of speed (figure 3.15d-f) and buoyant tracer (figure 3.2e,f), both of which show clear streaks with elevated speed/tracer concentration.

When wind forcing is removed (case I), there is a clear difference in tracer distribution amongst speed and vertical velocity points. We see a distinct minimum tracer concentration when vertical velocity is positive (similar to figure 3.14a). There is a small set of points

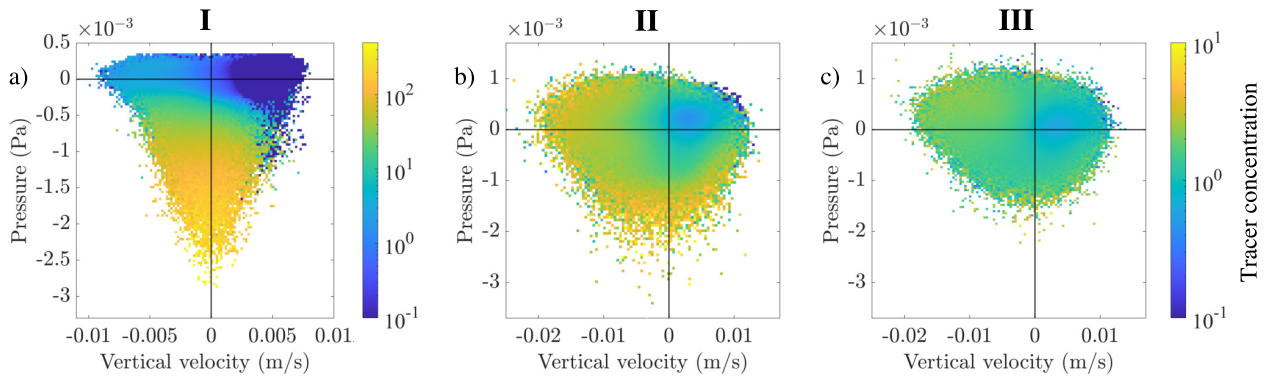

Fig. 3.14 Concentration of buoyant tracer ($w_s = 0.005$ m/s) at $z = 0$ m conditioned to pairs of vertical velocity and pressure perturbation (δp) at $z = -1$ m.

which have high tracer concentration and large values of speed and from figure 3.15d, we see that these correspond to convective vortices which have high speed on the periphery.

We can use the surface particles to describe the statistics of particle encounters with convective vortices. We calculate the time that a particle spends inside a convective vortex based on the time that the pressure sampled along the particle path is below the threshold value ($5\sigma_p$) and the filtered absolute vorticity sampled along the particle path is above the threshold value ($5\sigma_{\tilde{\zeta}}$). We repeat this for 4000 particles over one inertial period. We also measure the distance that each particle is transported by the convective vortices. This is done by calculating the Euclidean distance between the point where the particle first falls below the pressure threshold value and the last point where the particle pressure is below the threshold value before increasing. In a similar way, we calculate the time spent and distance travelled by a particle outside of a convective vortex. This is the period after a particle has just been expelled from a convective vortex (pressure or filtered vorticity are below/above threshold values) until it next enters another convective vortex. Some key statistics from these calculations are given in table 3.2 for each of the three cases.

In case I, particles enter and exit convective vortices frequently. On average, particles enter a convective vortex more than 10 times during one inertial period and particles spend a similar amount of time inside and outside convective vortices. This latter statistic is remarkable considering the relatively small area occupied by convective vortices (see figure 3.2h). The time that particles spend in a convective vortex can be compared with the convective timescale. This is defined as $t_c = H/w^*$ and provides a characteristic timescale for the mean circulation within convective cells. In case I, $t_c \simeq 88$ minutes, which is comparable to the average time that particles spend inside a convective vortex. This suggests that in

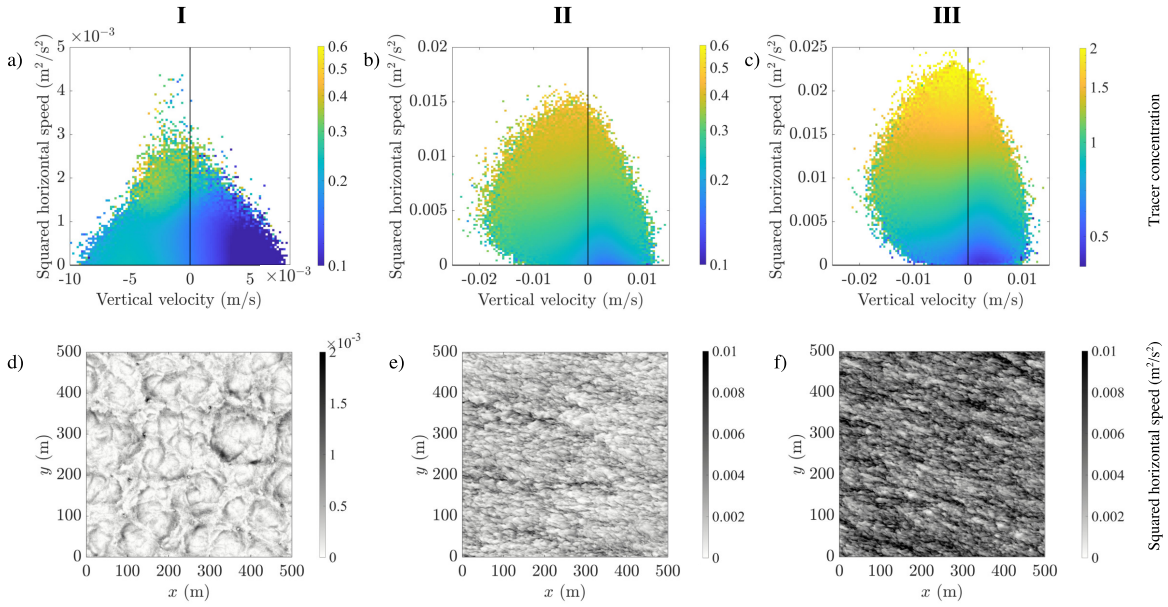

Fig. 3.15 Concentration of buoyant tracer ($w_s = 0.005$ m/s) conditioned to pairs of vertical velocity and squared horizontal speed ($u^2 + v^2$) at $z = -1$ m (a-c). Horizontal cross sections of squared horizontal speed at $z = -1$ m at $t = 12$ hours (d-f).

this case, convective vortices trap particles for a period of time that is significant compared to the convective timescale. In addition, the average distance that particles travel during periods inside and outside of convective vortices is small compared to the $50 - 150$ m size of convective cells (see figure 3.2). This suggests that convective vortices do not travel long distances sweeping up particles as suggested in Chor et al. (2018a), but rather that particles remain close to the convective vortices in the convective nodes.

The addition of wind disrupts the effectiveness of convective vortices at trapping particles, which can be seen by the contrast in statistics in cases II and III. Most particles do not enter a convective vortex at all, and upon entering, particles spend just 2-3 minutes on average inside the convective vortices. This is much smaller than both the average time spent outside convective vortices and the convective timescale, which is also 88 minutes for case II. In cases II and III, particles travel much further outside convective vortices than inside the vortices, and the distance travelled outside is comparable to the scale of the wind streaks. This suggests that the dynamics outside the convective vortex are much more important in determining particle distribution compared to case I.

A physical explanation for the clustering of surface particles inside convective vortices is as follows. Convective vortices preferentially occur in the 'nodes' linking the downwelling

	Case I	Case II	Case III
Number of times 4000 particles enter a vortex	44424	231	5
Mean time spent in a vortex (mins)	47	3	2
Upper centile time spent in a vortex (mins)	118	5	3
Mean distance travelled in a vortex (m)	9	2	1
Upper centile distance travelled in a vortex (m)	17	6	3
Number of times 4000 particles are outside vortex	41984	4555	4022
Mean time spent outside a vortex (mins)	44	951	1070
Upper centile time spent outside a vortex (mins)	115	1084	1080
Mean distance travelled outside a vortex (m)	11	199	225
Upper centile distance travelled outside a vortex (m)	28	301	312

Table 3.2 Statistics from individual surface particle trajectories for time and distance travelled inside (upper half) and outside (lower half) a convective vortex

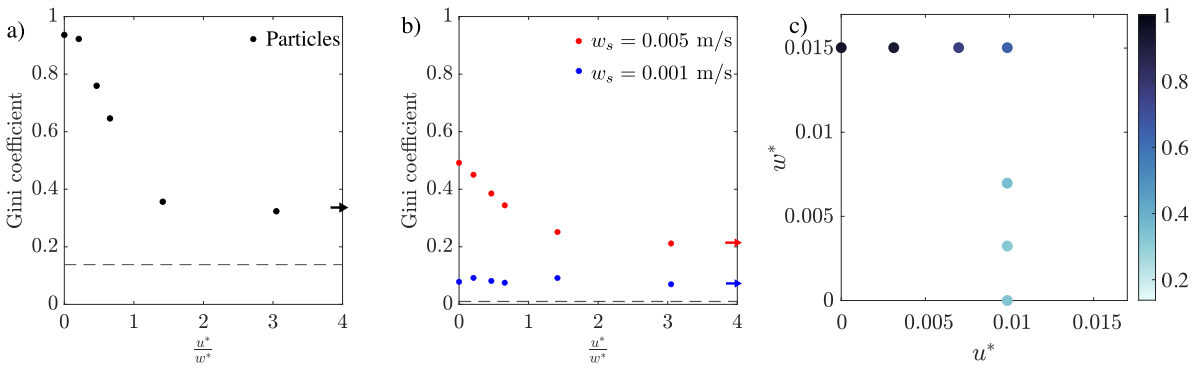

Fig. 3.16 Ratio of u^* and w^* against the Gini coefficient averaged over one inertial period for surface particles (a) and buoyant tracer (b). The dashed line indicates the Gini coefficient for a random distribution. The arrow indicates the Gini coefficient for case III where the ratio is infinite. (c) Parameter space coloured by Gini coefficient for surface particles.

regions of neighbouring convection cells. Particles that are brought into the convection nodes by convergent surface currents are pulled into the centre of the convective vortex by the inwards spiralling flow. In pure convection and under additional weak wind forcing, convective vortices are able to collect many neighbouring particles which, on average, remain trapped inside the vortex for a relatively long time compared to the convective timescale and only travel a short distance inside the vortex. When a convective vortex eventually breaks up, it leaves behind a cluster of particles inside the convective nodes which tend to stay close together since their local flow field is the same. The cluster may then fall into another nearby convective vortex, which attracts additional particles and further increases clustering.

The degree of clustering for buoyant tracers and surface particles can be quantified using the Gini coefficient (Gini, 1912). For a sample of size n where observed values y_i ($i = 1, ..., n$) are in non-decreasing order ($y_i \leq y_{i+1}$), the Gini coefficient is defined as:

$$G = \frac{1}{n}\left(n + 1 - 2\left(\frac{\sum_{i=1}^{n}(n+1-i)\, y_i}{\sum_{i=1}^{n} y_i}\right)\right). \tag{3.13}$$

A Gini coefficient close to 0 indicates a uniform distribution, while a value close to 1 indicates strong clustering. For the surface particles, we calculate the Gini coefficient using the number of particles within boxes formed of 32×32 grid points (or 31.25 m $\times$ 31.25 m) at each time-step, and we average the Gini coefficient over one inertial period. This box size has been chosen because it characterises clustering at a scale which captures the two most extreme behaviours of our simulation: under strong convective forcing, 31.25 m is small enough to distinguish clustering in different vortices, while under strong wind forcing, it captures the larger scale behaviour when there is less clustering.

Figure 3.16a shows that the Gini coefficient for surface particles decreases as the ratio u^*/w^* increases. The limited number of particles in our simulations implies that the particles will not be evenly distributed between the boxes even if the particle distribution is purely random. To quantify this and provide a baseline for comparison, we calculate the Gini coefficient for a set of particles which have been randomly distributed. To do this, we randomly distribute 4000 particles throughout the domain and calculate the Gini coefficient using equation (3.13). We repeat this process 500 times and the dashed line in figure 3.16a indicates the average of the resulting Gini coefficients for random distributions. The particles in the wind dominated regime (III) exhibit more clustering than would be seen for a random distribution of the same number of particles (dashed line), suggesting that some clustering still occurs in the wind-forced case. The ratio of u^* and w^* against the Gini coefficient closely resembles the ratio of u^* and w^* against the instantaneous number of vortices (figure 3.6) and suggests that fewer convective vortices leads to less particle clustering.

For the buoyant tracer, we apply the Gini coefficient to the total tracer concentration within boxes composed of 32×32 grid points (same clustering scale as above) at each time-step and average over one inertial period. For comparison with a random distribution of tracer, we generate a uniformly random concentration at each grid point on the 512×512 grid and calculate the Gini coefficient using equation (3.13), averaged over 500 samples. The slip velocity has a significant impact on tracer clustering as can be seen in figure 3.16b. Under all forcing conditions, the strongly buoyant tracer (red) is more clustered than the weakly buoyant tracer (blue). For the strongly buoyant tracer, the Gini coefficient trend is very similar to that for surface particles: the Gini coefficient decreases as the wind to convection ratio increases. The Gini coefficient for the weakly buoyant tracer is not strongly affected by the strength of wind or convection, but the distribution is still distinct from a random distribution of tracer (dashed line). Even in case I ($u^*/w^* = 0$), the convective vortices that effectively trap surface particles do not cause strong accumulation for the weakly buoyant tracer.

Figure 3.16c shows the particle Gini coefficient as a function of u^* and w^*. This enables us to separate out the behaviour for increasing wind strength and increasing convective forcing. Recall that the simulations are initialised with the same reference density and mixed layer depth, and hence changes in u^* and w^* (calculated with constant $H = 80$ m) reflect changes in the surface wind stress and the surface buoyancy flux, respectively.

In the series of simulations with constant wind stress (vertical line of points in figure 3.16c), increasing the magnitude of surface cooling leads to more clustering and a larger Gini coefficient, while increasing the wind stress for a fixed level of convective forcing (horizontal line of points) results in a decrease in the Gini coefficient. Although it is tempting to draw conclusions about the value of the Gini coefficient on lines of constant u^*/w^*, only a small section of the parameter space has been covered by our simulations. It remains unclear whether the Gini coefficient can be described purely as a function of u^*/w^*.

3.4 Conclusions and discussion

In this chapter, we used idealised large eddy simulations to investigate the distribution of buoyant material in the ocean under combined wind and convection forcing. Convective turbulence was generated using a constant buoyancy flux at the surface and wind forcing was generated using a constant shear stress boundary condition applied at the surface ($z = 0$ m). A series of simulations were conducted with different strengths of wind and convective forcing. We used two approaches to model buoyant particles: a continuous Eulerian tracer field with an upwards slip velocity and Lagrangian particles that were confined to the surface. The

tracer field allowed us to look at the distribution of particles with vertical motion included, whilst the surface particles allowed us to look at the limit where the slip velocity exceeds the maximum flow speed. The flow dynamics and subsequent clustering of buoyant material depend on wind and convection forcing, which we characterised with the ratio of the frictional velocity and convective velocity u^*/w^*.

The horizontal distribution of buoyant material depends strongly on the slip velocity. Weakly buoyant tracers are relatively uniformly distributed at the surface and are advected deeper in the turbulent mixed layer. We used the Gini coefficient to characterise clustering and found that clustering decreases with increasing wind strength, while it increases with increasing convection strength. On the other hand, weakly buoyant tracers remain nearly uniformly distributed regardless of the strength of wind or convection forcing.

In the simulations with strong convection, convective vortices form in the 'nodes' that join regions of downwelling in neighbouring convective cells. In the absence of wind forcing, convective vortices are highly effective at accumulating surface particles and strongly buoyant tracers. Convective vortices also act to transport buoyant tracer deep into the mixed layer. This is consistent with the findings from Chor et al. (2018a) who considered simulations of buoyant tracers in convection without wind forcing.

Although convective vortices survive under strong wind forcing, they become less effective at clustering buoyant material as the wind stress increases. As wind forcing is increased under a convective regime, we observe fewer convective vortices and a transition from clustering inside convective vortices to clustering inside streaks of high speed. When convective forcing is removed, the buoyant tracers remain close to the surface and some clustering occurs due to accumulation in regions of high speed and downwelling regions.

Surprisingly, the convective vortices exhibit a bias towards cyclonic vorticity despite their small size and the fact that they are characterised by very large Rossby numbers. The vorticity sampled along particle paths increases exponentially as the particles enter convective vortices. This is consistent with a simple theory for the vorticity amplification using the vertical divergence ($\partial w/\partial z$) measured near the convective vortices. A similar argument was put forward by Frank et al. (2017) and Sutherland et al. (2021) to explain rotational effects on buoyant plumes from a fixed source. This might help explain how a cyclonic bias first develops, but their assumption that $|\zeta| \ll f$ (small Rossby number) and the predicted linear increase in vorticity are not consistent with our simulations.

The picture that emerges is that surface particles that accumulate in the nodes between convection cells frequently encounter convective vortices. The first time that a particle encounters a convective vortex, the planetary vorticity is amplified, leading to a bias towards cyclonic vorticity. With each subsequent encounter, the relative vorticity is 'ratcheted' up.

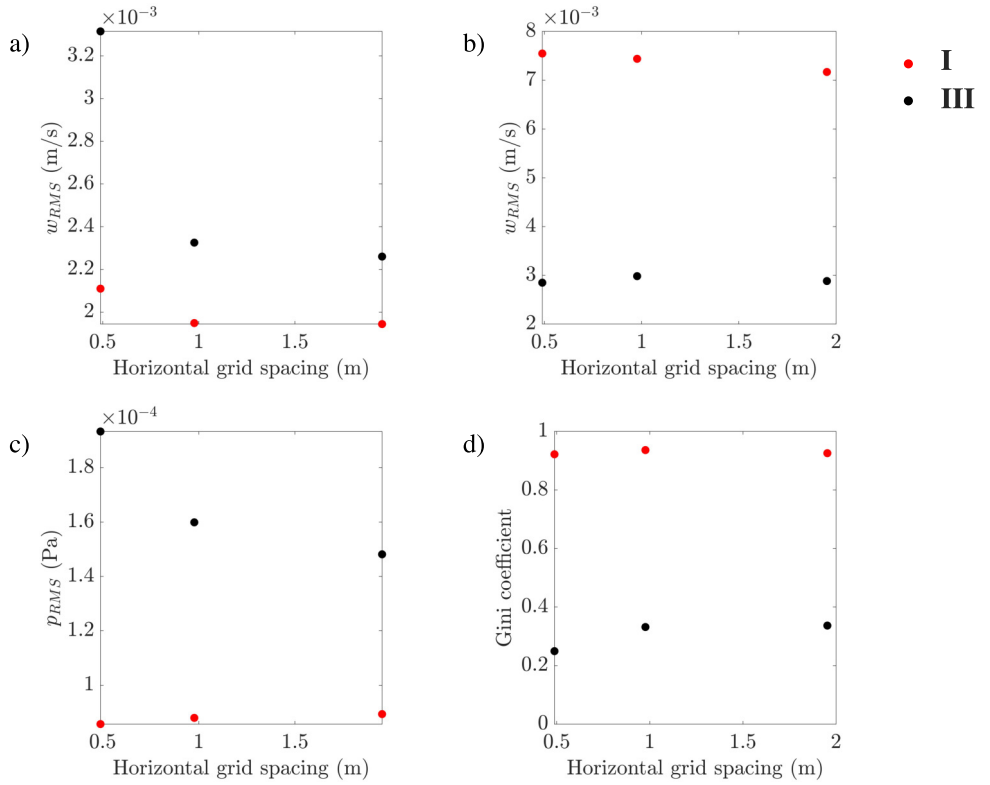

Fig. 3.17 (a) Root mean square vertical velocity at $z = -1$ m, (b) Root mean square vertical velocity at $z = -30$ m, (c) Root mean square pressure at $z = -1$ m, (d) Gini coefficient at $z = 0$ m.

Eventually this increase is balanced by the removal of vorticity through viscosity, although we have not investigated this balance and we leave this for future work.

It is important to keep in mind potential limitations of the current study. In our simulations, we held the surface forcing constant. In the ocean, the surface heat flux and wind stress are often highly variable, and this variability could impact the distribution of buoyant material. Here, we also focused solely on the effects of convection and wind-driven turbulence and neglected many other processes that are active in the upper ocean, notably surface waves and Langmuir circulation, mesoscale and submesoscale eddies, and density fronts. Future work could examine the relative importance of convective vortices in the presence of these processes.

Appendix 3.A

We examine the influence of horizontal grid resolution on the flow dynamics for two simulations: pure convection (case I) and pure wind (case III). The horizontal resolution is varied from 0.5 m $-$ 2 m, whilst all other parameters in the simulations, including vertical resolution, are kept the same. To reach a 0.5 m resolution without the simulation being too computationally expensive, we reduce the domain size to 250 m and use a 512$\times$512 point grid. Since convective cells are approximately $50-150$ m in diameter and wind streaks are even smaller, this is still large enough to capture the flow dynamics. All quantities are averaged over one inertial period.

Figure 3.17 shows the resolution dependence of the root mean square (rms) vertical velocity (a) and pressure (c) at $z=-1$ m for pure wind (black) and pure convection (red). In case I the dependence of the rms vertical velocity on resolution is small.

In case III, increasing the resolution causes a significant increase in rms vertical velocity and rms pressure. Our simulations do not have sufficiently high resolution to capture all turbulent motions that develop close to the boundary at $z=0$ m. For example, near-wall streaks develop in shear-driven turbulent boundary layers with a characteristic wavelength of $\lambda \simeq 100\nu/u^*$ (Smith and Metzler, 1983). For $u^*=0.01$ m/s and $\nu=10^{-6}$ m^2/s, this gives $\lambda \simeq 1$ cm which is far too small to be resolved with our 1 m grid spacing. As the resolution is increased, we anticipate that more of the near-wall turbulent structures will be resolved in the simulations. Here however, we are interested in accumulation at a much larger scale (in section 3.3 we quantify clustering on a 31.25 m scale).

Figure 3.17b shows the dependence of the rms vertical velocity at $z=-30$ m. In both cases I and III, the rms vertical velocity is weakly dependent on grid spacing. This is because the additional small-scale structures which feature under wind forcing only occur near the surface.

The random displacement model that we add to the particle motion equations helps compensate for the unresolved wind-driven turbulence. In section 3.3, we introduce the Gini coefficient to quantify particle clustering and we use the same quantity to check particle convergence, which can be seen in figure 3.17d. In the case of the highest resolution, our domain size is reduced to 250 m and for a comparable particle distribution, we tile four 250m domains together in a 500 m $\times$ 500 m square with 1000 particles on each tile. We find that in case I, the Gini coefficient is insensitive to grid spacing. In case III, the Gini coefficient decreases by 26% for the highest resolution. This is due to either missing larger scale flow structures which are not present in the smaller domain size or additional small-scale structures that are resolved only on the highest resolution grid.

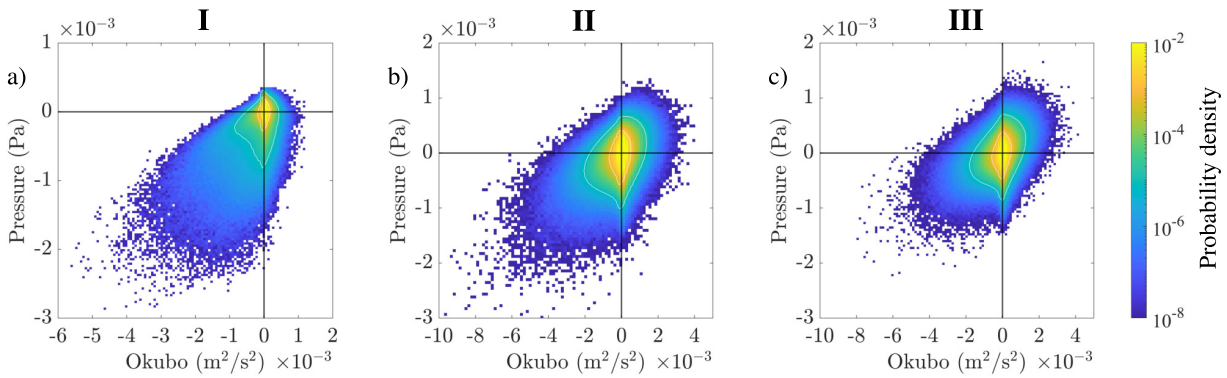

Fig. 3.18 Joint probability density function of the Okubo parameter at $z = 0$ m and pressure perturbation (δp) at $z = -1$ m. White contours show where the PDF is 10^{-2} and 10^{-4}.

Appendix 3.B

The two-dimensional Okubo parameter, Q, is defined as:

$$Q = \left[\left(\frac{\partial u}{\partial x} - \frac{\partial v}{\partial y} \right)^2 + \left(\frac{\partial u}{\partial y} + \frac{\partial v}{\partial x} \right)^2 - \left(\frac{\partial v}{\partial x} - \frac{\partial u}{\partial y} \right)^2 \right]_{z=0} . \tag{3.14}$$

Regions with $Q > 0$ tend to be strain-dominated, whilst regions with $Q < 0$ can be understood as being vorticity-dominated. Chor et al. (2018a) identified convective vortices as regions with extreme negative Q. Figure 3.18 shows the joint probability density function of the Okubo parameter and pressure. In all cases, points with the most negative values of the Okubo parameter also have negative pressure. Under strong wind forcing, there are some points (figure 3.18b,c) which have negative pressure but near-zero Okubo parameter. These may characterise horizontal vortices which form under wind shear and are not classified as vortices by the two-dimensional Okubo parameter.

Chapter 4

A model for the cyclonic bias of convective vortices in a rotating system

This chapter is a slightly modified version of the work published in Dingwall, J. and Taylor, J. R. (2024). Model for the cyclonic bias of convective vortices in a rotating system. *Physical Review Fluids*, 9:033503.

4.1 Introduction

It is often assumed that planetary rotation does not have a direct influence on convection in boundary layers in the atmosphere and ocean (Klinger and Marshall, 1995; Morton, 1966; Stubley and Riopelle, 1988). Surprisingly, in chapter 3 we found that convective vortices in ocean mixed layer convection display a strong bias towards cyclonic vorticity. By diagnosing the evolution of vorticity along particle paths, we found that vortex stretching amplifies the planetary vorticity to generate the observed cyclonic bias in relative vorticity. However, this approach was purely diagnostic. In this chapter, we develop a prediction for the vorticity bias of convective vortices in terms of the bulk parameters of the flow, and extend our prediction to convection in the terrestrial and Martian atmosphere.

Thermal convection can occur when a fluid is heated from below or cooled from above, leading to an unstable density configuration. The relative importance of the nonlinear advection and Coriolis terms in convective flows is set by the convective Rossby number, $Ro^* = |B_0|^{1/2} f^{-3/2} H^{-1}$, where B_0 is the surface buoyancy flux driving convection, f is the Coriolis parameter, and H is the height of the convective layer (Chen et al., 1989; Fernando et al., 1991; Julien et al., 1996; Marshall and Schott, 1999). Laboratory and numerical experiments suggest that rotational effects become important when $Ro^* \lesssim 0.1 - 0.7$ (Coates

et al., 1995; Jones and Marshall, 1993; Maxworthy and Narimousa, 1994). The well-studied problem of turbulent Rayleigh-Benard convection under steady rotation has revealed asymmetric behaviour of cyclones and anticyclones (Favier et al., 2014; Guervilly et al., 2014; Sipp et al., 1999; Vorobieff and Ecke, 2002). However, symmetry-breaking largely arises in the case of rapid rotation and relatively small Rossby numbers ($Ro^* < 1$) whereas flows with larger Ro^* are typically dominated by convective plumes which do not display a bias (Vorobieff and Ecke, 2002). In atmospheric convection for a height of $H = 1-2$ km, $Ro^* \simeq 10$ (Marshall and Schott, 1999), and despite some initial debate (Brooks, 1960; Durward, 1931), the general consensus is that there is no significant rotational bias for dust devils (Balme and Greeley, 2006; Raasch and Franke, 2011; Sinclair, 1965).

In the upper ocean when convection develops in the top $10-100$ m (D'Asaro, 2014) and the heat flux is $\mathscr{O}(100\ \mathrm{Wm}^{-2})$ (Marshall and Schott, 1999), Ro^* typically ranges between 0.5 and 10. In chapter 3, the simulations which revealed a strong bias towards cyclonic convective vortices were characterised by $Ro^* = 2.6$. Similar reports of an unexpected rotational bias exist in other flows. For example, Frank et al. (2017); Sutherland et al. (2021) observed a bias in the rotation of buoyant plumes in experiments with a large Rossy number.

In this chapter, we propose a mechanism to explain the rotational bias of convective vortices and make a prediction for the bias in terms of the bulk parameters of the flow. Throughout this study, we assume $f > 0$. Our analysis is based on large eddy simulations (LES) of free convection in an idealised domain. LES has been used to investigate terrestrial (Giersch and Raasch, 2021; Raasch and Franke, 2011), Martian (Michaels and Rafkin, 2004; Nishizawa et al., 2016a; Spiga et al., 2016) and oceanic (Chor et al., 2018a; Dingwall et al., 2023) convective vortices.

4.2 Setup and numerical methods

We use large eddy simulations to solve a low-pass filtered version of the nonhydrostatic incompressible Boussinesq Navier-Stokes equations (4.1) and (4.2) in terms of the low-pass filtered velocity $\mathbf{u} = (u, v, w)$, low-pass filtered pressure p, and buoyancy b,

$$\frac{\partial \mathbf{u}}{\partial t} + \mathbf{u}\cdot\nabla\mathbf{u} + \mathbf{f}\times\mathbf{u} = -\frac{1}{\rho_0}\nabla p + \nu\nabla^2\mathbf{u} - \nabla\cdot\boldsymbol{\tau} + b\,\widehat{\mathbf{z}}, \tag{4.1}$$

$$\frac{\partial b}{\partial t} + \mathbf{u}\cdot\nabla b = \kappa_b\nabla^2 b - \nabla\cdot\boldsymbol{\lambda}. \tag{4.2}$$

Buoyancy is treated as a single scalar variable under the assumption of a linear equation of state and neglecting double diffusive effects. In equation (4.1), ρ_0 is the reference density,

$\widehat{\mathbf{z}}$ is the unit vector in the vertical direction, ν is the molecular viscosity, $\boldsymbol{\tau}$ is the sub-grid scale stress tensor, and $\mathbf{f} = (0,0,f)$ is the Coriolis force accounting only for the vertical component of the angular velocity vector using the so-called 'traditional approximation'. In reality, the horizontal component of Earth's rotation may have an effect, particularly at low latitudes, but here we neglect the horizontal component to simplify the analysis and focus only on the influence of the vertical component of rotation on convective vortices. In equation (4.2), $\boldsymbol{\lambda}$ is the sub-grid scale scalar flux and κ_b is the molecular diffusivity. Both $\boldsymbol{\tau}$ and $\boldsymbol{\lambda}$ are calculated using the anisotropic minimum dissipation model (Abkar et al., 2016; Vreugdenhil and Taylor, 2018) as in chapter 3.

The simulations are configured to represent an idealised ocean surface boundary layer cooled from the top, and we report dimensional values that are typical of the ocean, but the idealisation of our simulations makes the results more broadly relevant. The domain is 125 m in the horizontal directions with periodic boundary conditions, and 120 m in the vertical. Convection is driven using a constant buoyancy loss at the surface with values ranging between $B_0 = -4.24 \times 10^{-10}$ m^2/s^3 (about 1 Wm^{-2}) and $B_0 = -4.24 \times 10^{-7}$ m^2/s^3 (about 1000 Wm^{-2}), and a zero flux bottom boundary condition for buoyancy. A no-stress boundary condition is applied at the top and bottom of the domain where the vertical velocity is zero. The Coriolis parameter is varied from $f = 10^{-6}$ s^{-1} to $f = 10^{-4}$ s^{-1}. Buoyancy is initialised with a mixed layer of depth 80 m (where $\partial b/\partial z = 0$ s^{-2}) overlying a region with stable stratification ($\partial b/\partial z = 9 \times 10^{-6}$ s^{-2}). Velocity is initialised as random white noise with an amplitude of 10^{-4} m/s. The molecular viscosity is $\nu = 10^{-6}$ m^2/s and the molecular diffusivity is $\kappa_b = 10^{-6}$ m^2/s ($Pr = \nu/\kappa_b = 1$), although both are small compared to the sub-grid scale terms and hence do not have a direct impact on the simulations. The Rayleigh number based on the molecular viscosity and diffusivity varies between $Ra = \mathscr{O}(10^{16})$ and $Ra = \mathscr{O}(10^{18})$. We neglect transient effects by starting our analysis after the simulated flow has reached a fully developed turbulent state (approximately 4 hours). Time averages are calculated over one inertial period, starting after 4 hours which is sufficient time for convection to develop into a statistically steady state.

The numerical code uses a pseudospectral method to calculate derivatives in the horizontal directions and second-order finite differences for the vertical direction. The timestepping algorithm is a mixed implicit/explicit scheme using third-order Runge-Kutta and Crank-Nicolson methods. Further details of the code can be found in Taylor (2008). In all simulations, resolved fields are discretised on a $512 \times 512 \times 65$ grid. This gives a horizontal grid spacing of 0.25 m. The vertical grid spacing is variable between 0.95 m and 2.57 m with higher resolution near the surface. The domain size is large enough to accommodate one at least one convective cell. Although the large-scale convective dynamics may be constrained by

the box size, the focus of this study is on the small-scale vortices, for which we need high resolution. As discussed in appendix 4.A, the number, intensity, and bias of the convective vortices do not change with increasing domain size or resolution.

We also include 16,000 non-inertial Lagrangian surface particles advected with the surface horizontal velocity field and vertically fixed at the first grid point below the surface. These follow the simplified Maxey-Riley equations (Maxey and Riley, 1983) with all terms except for flow advection and Brownian motion neglected (see chapter 1 for more details). The particle equations of motion are given by

$$\mathbf{x}_p(t+dt) = \mathbf{x}_p(t) + \mathbf{u}(\mathbf{x}_p,t)dt + \mathbf{x}_{sgs}(\mathbf{x}_p,t) \ , \tag{4.3}$$

$$x_{sgs,i} = \frac{\partial \nu_{sgs}}{\partial x_i}(\mathbf{x}_p,t)\,dt + (2(\nu_{sgs}(\mathbf{x}_p,t))_+)^{\frac{1}{2}} d\xi_i \ , \tag{4.4}$$

where $\mathbf{u}$ is the resolved velocity interpolated at the particle position and $\mathbf{x}_{sgs}$ is the displacement due to sub-grid scale motion, although this only has a small effect on particle motion. In equation (4.4), the subscript i indicates the spatial dimension, ν_{sgs} is the sub-grid scale viscosity interpolated at the particle position, $d\xi_i$ is Gaussian white noise with variance dt, and $(\cdot)_+ = \max(\,\cdot\,,0)$. Details of particle initialisation are given later in the text when particles are used.

4.3 Results

4.3.1 Large eddy simulations

In figure 4.1a, distinct convective cells are visible where large areas of weak upwelling are surrounded by small areas of strong downwelling in a simulation with $f = 10^{-4}$ s^{-1} and $B_0 = -4.24 \times 10^{-8}$ m^2/s^3 at $t = 16.5$ hours. A two fold structure can be seen with a spoke-like pattern of small convective cells (horizontal scale approximately 25 m) in the upper portion of the convective layer (figure 4.1a), and larger convective cells (horizontal scale approximately 50m) which penetrate deeper into the upper mixed layer (figure 4.1b). This structure is consistent with similar simulations of the ocean (Skyllingstad and Denbo, 1995) and atmosphere (Schmidt and Schumann, 1989).

The pressure field highlights convective vortices as areas with a local pressure minima. The convective vortices can be grouped into two classes. Large convective vortices are found in downwelling bands of large convective cells at the nodes between convective cells, and smaller convective vortices are seen populating the large and small-scale downwelling bands. Similar convective vortices were reported for idealised simulations of a convective

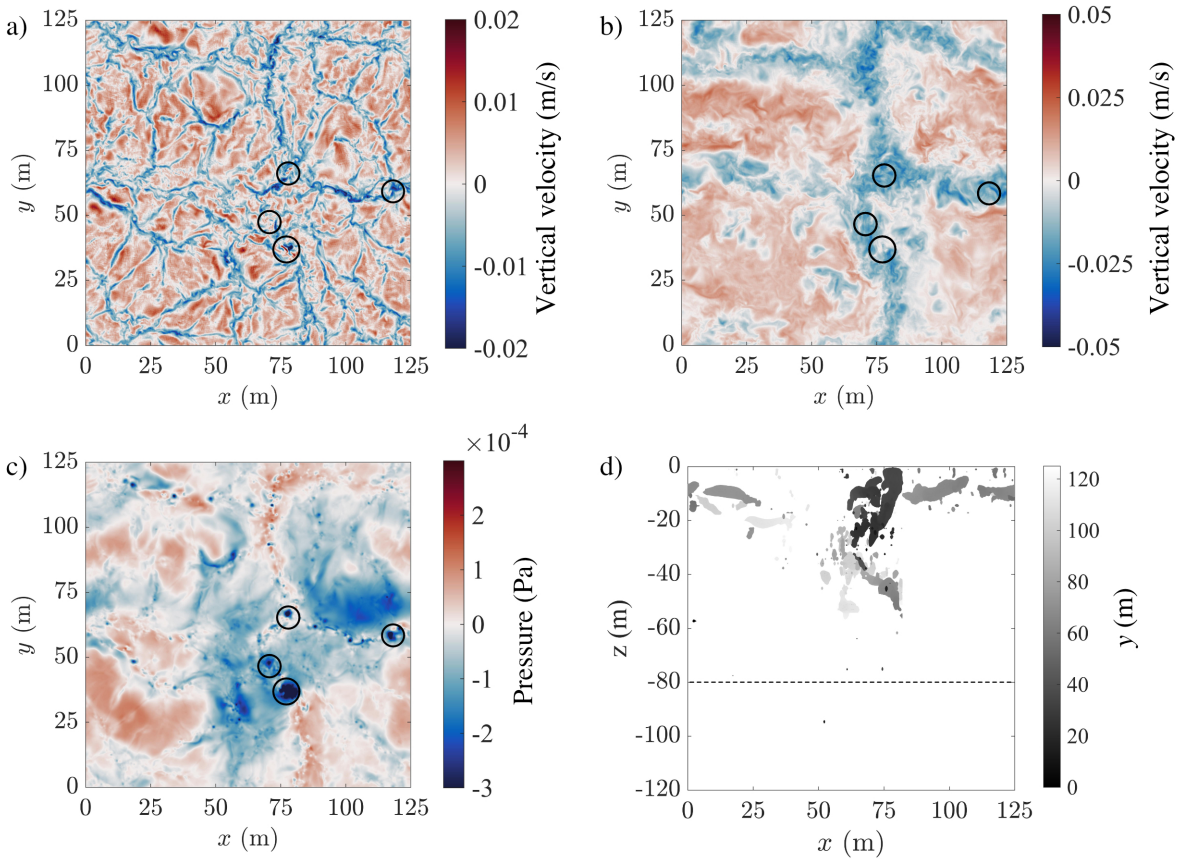

Fig. 4.1 Horizontal cross sections at $t = 16.5$ hours of the vertical velocity at $z = -1$ m (a), vertical velocity at $z = -10$ m (b), pressure at $z = -1$ m (c), and a vertical cross section of pressure isosurfaces for $\delta p < -3 \times \sigma_p$ Pa (d) in a simulation with $B_0 = -4.24 \times 10^{-8}$ m^2/s^3 and $f = 10^{-4}$ s^{-1}. Circles highlight locations of the largest four convective vortices (a,b,c) and the dashed line indicates the bottom of the mixed layer (d).

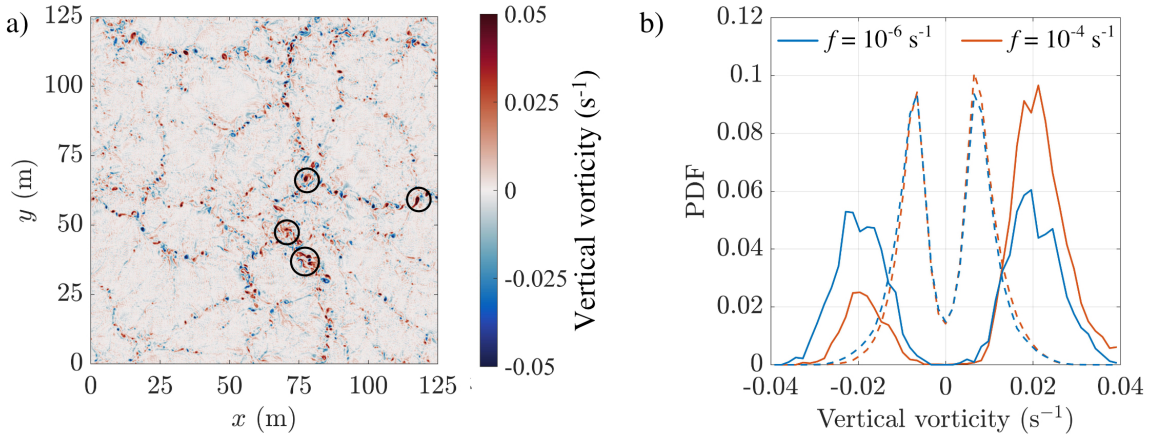

Fig. 4.2 (a) Horizontal cross sections at time $t = 16.5$ hours of the vertical vorticity averaged over the top 5 m in a simulation with $B_0 = -4.24 \times 10^{-8}$ m^2/s^3 and $f = 10^{-4}$ s^{-1}. (b) Probability density function of vertical vorticity at $z = 0$ m for points identified as large (solid) and small (dashed) convective vortices for $B_0 = -4.24 \times 10^{-8}$ m^2/s^3 and $f = 10^{-4}$ s^{-1} (red) and $f = 10^{-6}$ s^{-1} (blue).

atmospheric boundary layer by Raasch and Franke (2011). The small convective vortices are short-lived and extend to a depth of about 5 m, while the large convective vortices are much more persistent and extend up to 40 m which can be seen in figure 4.1d, which shows a vertical cross section of pressure isosurfaces (see appendix 4.B for three-dimensional visualisation).

Figure 4.2a shows the vertical vorticity field, ζ, averaged over the top 5 m (to reduce numerical noise near the surface) for the same B_0, f and t as in figure 4.1. The four convective vortices with the lowest pressure and largest area (circled) are all cyclonic but the small convective vortices show a roughly even mix of positive and negative vorticity.

We identify convective vortices following Dingwall et al. (2023) based on algorithms used to detect dust devils in the atmosphere (Giersch and Raasch, 2021; Raasch and Franke, 2011). Specifically we find the vortex centre by identifying local minima in pressure and local maxima in the magnitude of filtered vorticity (we apply a Gaussian filter to the vorticity field to eliminate small-scale noise and denote the Gaussian filtered vorticity $\tilde{\zeta}$). Here, local minima/maxima are defined as points where the pressure/vertical vorticity is smaller or larger than all points within a stencil of 15×15 neighbouring grid points. This stencil size has been determined empirically to avoid detecting multiple vortex centres within one convective vortex. We use the pressure and vorticity fields evaluated at $z = -1$ m (the first grid cell below the surface) to ensure that the small, shallow vortices are captured. We additionally require the pressure minimum to be located within two horizontal grid points of the filtered

vorticity maximum. The pressure minima must be less than 5 times the standard deviation of pressure ($p_{\min} < -5\sigma_p$) for the large convective vortices and between 0.5 and 5 times the standard deviation of pressure for the small convective vortices ($-5\sigma_p < p_{\min} < -0.5\sigma_p$). Similarly, we require the filtered vorticity extremum to be greater than 5 times the standard deviation of filtered vorticity ($|\tilde{\zeta}_{\max}| > 5\sigma_{\tilde{\zeta}}$) for the large convective vortices and between 2.5 and 5 times the standard deviation of filtered vorticity ($2.5\sigma_{\tilde{\zeta}} < |\tilde{\zeta}_{\max}| < 5\sigma_{\tilde{\zeta}}$) for small convective vortices. Here, the standard deviation for both pressure and filtered vorticity is calculated using horizontal cross sections taken at the analysis height and averaged over one inertial period. This threshold aims to eliminate as much noncoherent turbulence as possible, while still capturing sufficient information for analysis.

Figure 4.2b shows probability density functions (PDF) of ζ for two simulations with the same surface buoyancy flux but different values of f for all large and small convective vortices detected within one inertial period. To remove turbulent fluctuations, the vorticity at each vortex centre is averaged over a 15×15 box (3.75 m$\times$3.75 m) centred at the vortex centre. Both simulations exhibit a distinct peak at $\zeta = \pm 0.02$ s^{-1} for the large convective vortices (solid) and a peak at $\zeta = \pm 0.007$ s^{-1} for the small convective vortices (dashed). When $f = 10^{-4}$ s^{-1} the large convective vortices have a distinct bias towards positive vorticity, but the distribution is relatively symmetric (with a slight positive bias) for the small convective vortices. When $f = 10^{-6}$ s^{-1}, the large convective vortices do not show a clear bias. The PDF for small convective vortices is very similar and nearly symmetric in both cases.

Our simulations reveal that the large convective vortices are composed of a large number of small convective vortices. We seed a collection of Lagrangian surface particles in a 5 m $\times$ 5 m box inside each small convective vortex (both cyclonic and anticyclonic) detected by the algorithm at $t = 5$ hours in a simulation with $B_0 = -4.24 \times 10^{-8}$ m^2/s^3 and $f = 10^{-4}$ s^{-1} (when there is not a large vortex present) and track them until a large vortex forms at $t = 5.5$ hours. Initially, the particles are distributed along the downwelling bands (figure 4.3a,c). The small vortices quickly merge and particles accumulate in a much smaller area within the downwelling bands. As the vortices get closer to the node which joins nearby large-scale cells, they interact nonlinearly and eventually merge into one large vortex (figure 4.3b,d).

4.3.2 Statistical theory for vorticity bias

Here, we propose a statistical theory to quantitatively predict the cyclonic bias of the large convective vortices which is based on the observation above that large convective vortices are formed through the merger of many relatively unbiased small convective vortices. Statistically, the vorticity bias for large convective vortices can be predicted by averaging the absolute vorticity of many unbiased small convective vortices whose relative vorticity is sampled from

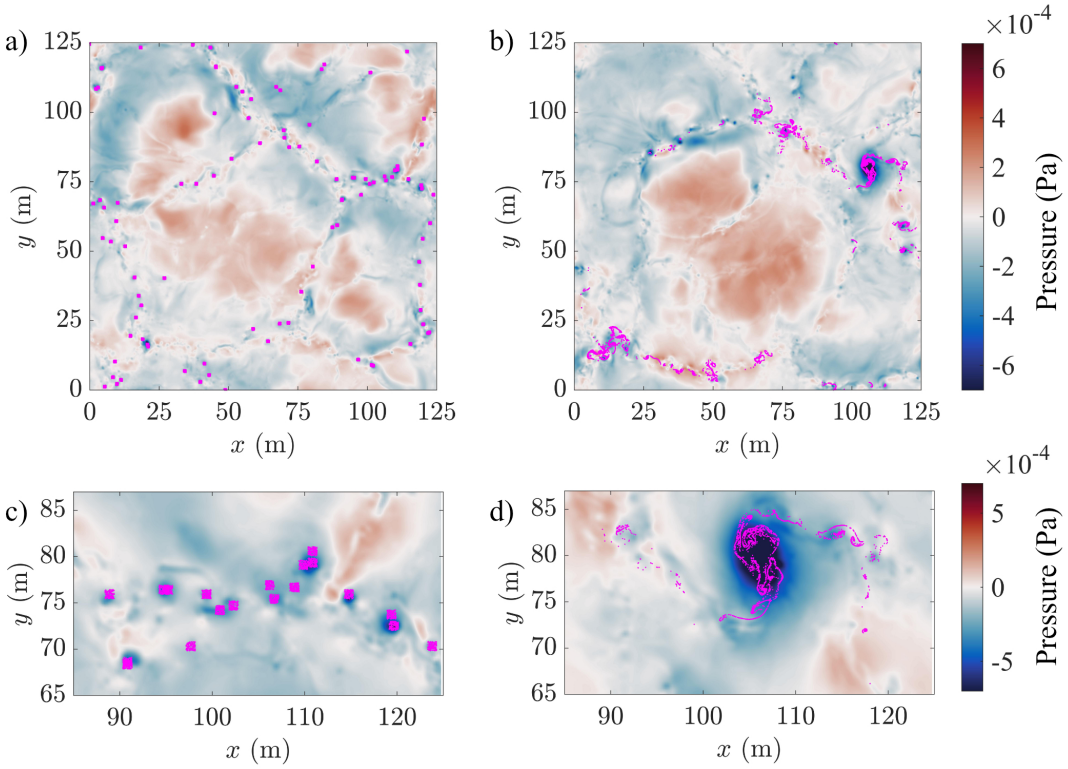

Fig. 4.3 Horizontal slices of pressure at $z = -1$ m with surface particle position (magenta) superimposed for $t = 5$ hours (a) and (c) and $t = 5.5$ hours (b,d). Panels c,d show a zoomed in section of panels a,b containing the large convective vortex.

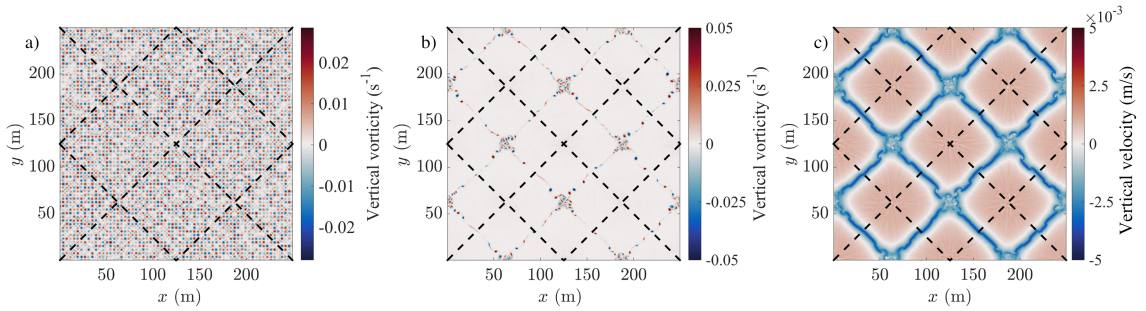

Fig. 4.4 Horizontal slice at $z = -1$ m of vertical vorticity when $t = 0$ hours (a) and $t = 0.8$ hours (b), and of vertical velocity when $t = 0.8$ hours (c) with boundaries of basins of attraction superimposed (black dashed line) for $\xi = 0.025$ m^2/s and $f = 2 \times 10^{-5}$ s^{-1}.

an unbiased uniform distribution. Below, we demonstrate this mechanism using simulations of idealised convective cells seeded with small random vortices. We then describe how to apply this prediction to forced convective flows using a scaling analysis and test it using the LES described above.

To explore the mechanism leading to a bias in the sign of the vorticity of the large convective vortices, we ran a suite of idealised LES, initialised with several overturning circulation cells, superimposed with smaller vortices with random amplitude and an equal probability of cyclonic and anticyclonic vorticity. This simplified initial value problem allows us to control the structures and parameters in the flow much more closely and provides an ideal setting to introduce our mechanism and predictive analysis. The numerical method is the same as above, so here we only note changes and additions to those simulations. The initial vertical velocity is

$$w = w_0 \cos\left(\frac{4\pi x}{LX}\right) \cos\left(\frac{4\pi y}{LY}\right) \times \frac{-(z^2 + H_0\, z)}{H_0}\,, \tag{4.5}$$

in a 250 m $\times$ 250 m $\times$ 120 m domain. This forms eight circulation cells, each of which mimic a convective cell. To model the small convective vortices, we superimpose a streamfunction composed of Gaussian vortices, each with radius $r = 2$ m and depth $d = 15$ m:

$$\psi = \sum_i \sum_j \xi_{ij} \exp\left(-\frac{(x - x_i)^2}{r^2} - \frac{(y - y_j)^2}{r^2}\right)\left(\frac{z + d}{d}\right), \tag{4.6}$$

where x_i and y_j denote the centres of the vortices and ξ_{ij} denotes the vorticity at the centre of a given vortex, which is randomly sampled from a continuous uniform distribution on the interval $[-\xi,\ \xi]$. We systematically vary ξ and the Coriolis parameter, f. Since the

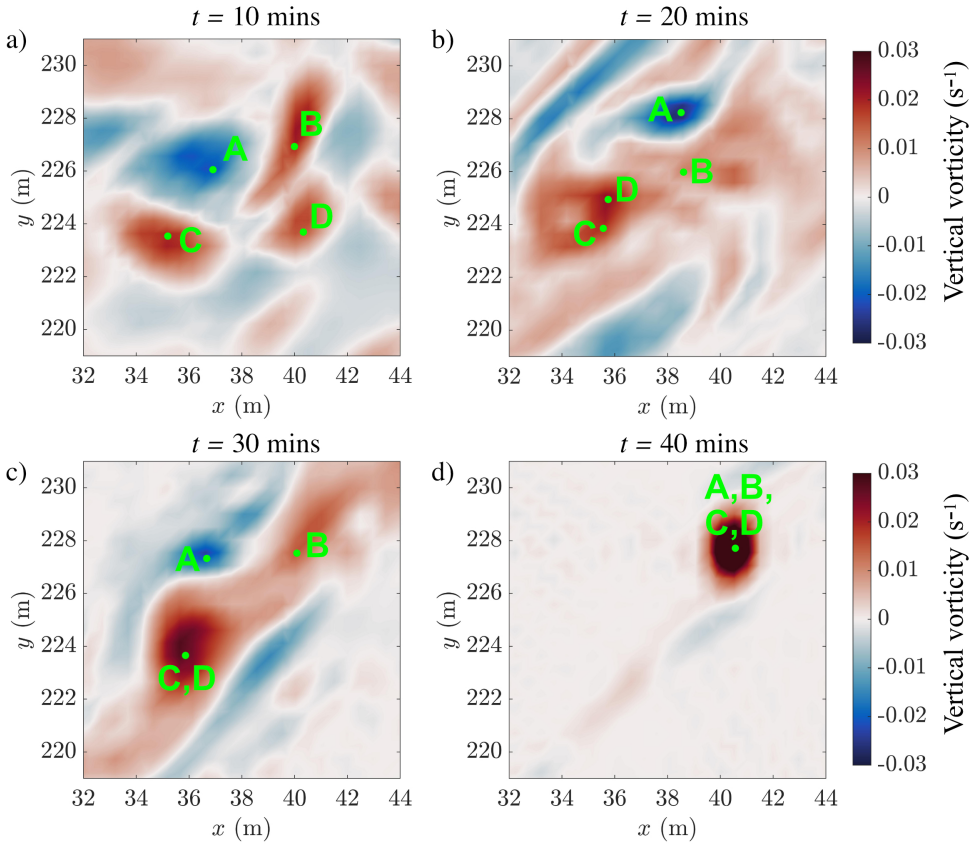

Fig. 4.5 Horizontal slices of vertical vorticity at $z = -1$ m with the position of four surface particles (A,B,C and D) superimposed in a simulation with $\xi = 0.025$ m^2/s and $f = 2 \times 10^{-5}$ s^{-1} at $t = 10$ mins (a), $t = 20$ mins (b), $t = 30$ mins (c) and $t = 40$ mins (d). The sequence shows the interaction and merging of four small vortices of opposing signs into one larger cyclonic vortex. In (c), particles C and D are at the same location and in (d), particles A,B,C and D are all co-located.

convective cells are prescribed in the initial condition, we do not cool the surface and the surface buoyancy flux is $B_0 = 0$ m^2/s^3.

Figure 4.4a shows the initial condition of small vortices with uniformly distributed amplitude when $\xi = 0.025$ m^2/s and $f = 2 \times 10^{-5}$ s^{-1}. After $t = 0.8$ hours, the small vortices have been advected towards the nodes joining neighbouring circulation cells and the small vortices merge to form a large vortex. By design of the circulation cells, each large vortex has a distinct basin of attraction (marked with a dashed black line). We focus on the time period from the start of the simulation until the large vortex forms, at approximately 1 hour. This ensures that the eight convective cells remain distinct and do not merge or interact with one another.

In order to quantify the change in vorticity as the small vortices merge into a large vortex, we seed Lagrangian surface particles at the centre of each small vortex at the start of the simulation, and we track the vorticity along particle paths. The behaviour of merging vortices is illustrated in figure 4.5 which shows zoomed-in snapshots of the vertical vorticity field and tracks the position of four surface particles throughout the merger. Initially the particles are located at the centre of four small Gaussian vortices (see figure 4.4 for the initial condition) of which three are cyclonic (with particles B,C and D) and one anticylonic (with particle A). By $t = 10$ minutes, the vortices begin to interact with one another (figure 4.5a) which results in the three small cyclonic vortices merging into one larger cyclonic vortex. The interaction distorts the anticyclonic vortex and causes it to reduce in size and strength (figure 4.5b,c). Eventually, the cyclonic vortex envelopes the weaker anticyclonic vortex, so that by $t = 40$ minutes, all particles are contained inside a single, cyclonic vortex. This vortex is advected towards the node of the circulation cell, and may undergo subsequent merging events.

At the stress-free upper surface ($z = 0$ m), the vertical component of the absolute vorticity $(\zeta + f)$ satisfies:

$$\frac{\mathrm{D}(\zeta + f)}{\mathrm{D}t} = (\zeta + f)\frac{\partial w}{\partial z} + \underbrace{\nu \nabla^2 \zeta}_{\zeta_{\mathrm{diff}}}, \tag{4.7}$$

where $\mathrm{D}/\mathrm{D}t$ is the material derivative, w is the vertical velocity and ν is the molecular diffusivity. The right-hand side comprises vortex stretching and diffusion. Hence, if diffusion is negligible and there are no vortex merging events, then the sign of the absolute vorticity is preserved along the particle paths. In the absence of vortex stretching, we might expect the vorticity of the large vortices to be small since the large vortices are formed through the merger of many small vortices with opposing sign. For example, in figure 4.5, the three cyclones and one anticyclone will still merge, but the resulting cyclonic vortex will be broader and weaker. Without vortex stretching, the vorticity would not increase in magnitude following the merger. Similarly in a merger of three anticyclones and one cyclone (which is equally likely given our initial conditions), we could expect a broad and weak anticyclone to form. Because f does not play a role when there is no vortex stretching, the distribution of cyclones and anticyclones would be symmetric.

In our convective regime, the sign of $\partial w/\partial z$ can be both positive and negative, but it is positive in the downwelling regions where the large convective vortices are found. When $\partial w/\partial z > 0$, vortex stretching increases the magnitude of $\zeta + f$, leading to strong large vortices whose sign (after merging) is preserved. This effect can be seen in figure 4.5. The resultant cyclonic vortex contracts and its strength steadily increases between 20 and 40 minutes (at $t = 40$ minutes, the maximum vorticity is 0.08 s^{-1}). In the absence of any further mergers, this vortex remains cyclonic (since the sign of absolute vorticity is

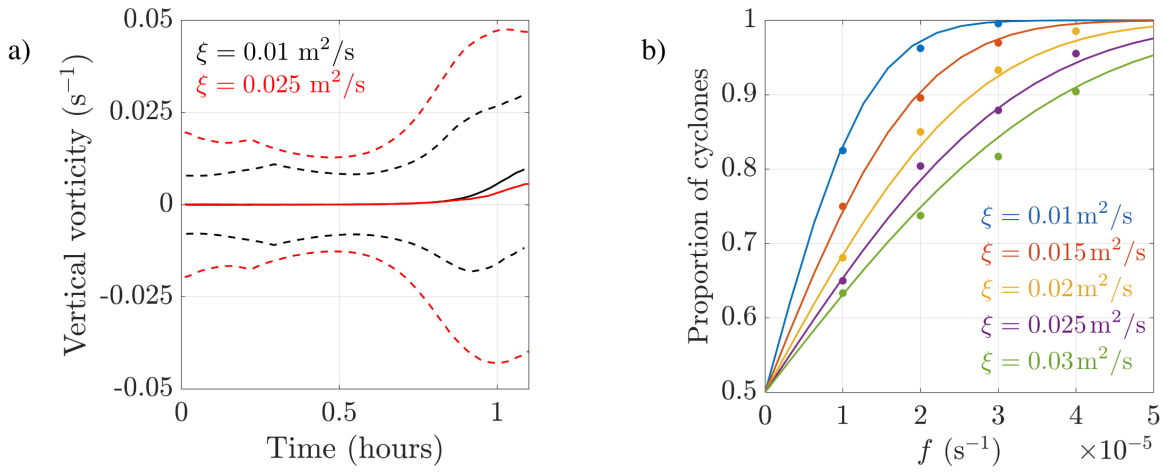

Fig. 4.6 (a) Median (solid) and 25th/75th percentile (upper/lower dashed) particle vorticity when $\xi = 0.01$ m^2/s (black) and $\xi = 0.025$ m^2/s (red) for $f = 2 \times 10^{-5}$ s^{-1}. (b) The predicted proportion of cyclones versus f for different values of ξ (lines) and observed proportion of cyclones in simulations (points).

preserved) and vortex stretching continues to amplify its magnitude. Eventually, diffusion balances vortex stretching after the large vortex has formed. In a comparable merger between three anticyclones and one cyclone, the resultant vortex would initially have weak, negative vorticity. The magnitude of $\zeta + f$ would be smaller than the cyclonic case (since f is positive and ζ is negative) and so vortex stretching would be less effective at amplifying the vortex. If ζ were negative but very small (for example if a larger number of small vortices merge), then $\zeta + f$ could be positive and amplification of $\zeta + f$ through vortex stretching could lead to a large cyclone, despite the vortex being composed of more anticyclones than cyclones.

Figure 4.6a shows statistics of the vorticity sampled along Lagrangian particle paths as a function of time for two cases with $\xi = 0.01$ m^2/s and $\xi = 0.025$ m^2/s. The upper (and lower) quartile curves highlight the three stages by which small vortices merge into a large convective vortex: amplification of small vortices by vortex stretching (initial increase), nonlinear interactions between small vortices (slight decrease) followed by the amplification of the large vortex by vortex stretching (large increase). For both $\xi = 0.01$ m^2/s and $\xi = 0.025$ m^2/s the maximum positive vorticity of the 75th percentile is higher than the minimum negative 25th percentile due to the the rotational bias of convective vortices (where particles are preferentially located), and the bias is larger for $\xi = 0.01$ m^2/s. The small vortices begin to merge at about 0.6 hours after which there is a significant cyclonic bias (median line in figure 4.6a). The cyclonic bias is weaker when the amplitude of the small vortices, ξ, is larger.

In our idealised simulations, the number of convective vortices that merge into a single large vortex is fixed by the initial condition, but we vary f and the amplitude of the small convective vortices (which we control using the parameter ξ). Since the sign of the absolute vorticity is conserved following particle paths (neglecting diffusion), we expect the sign of the absolute vorticity of the large vortex to be determined by the sign of the mean absolute vorticity of all small convective vortices from which it is composed. In our idealised simulations, we can calculate this by averaging the absolute vorticity over each basin of attraction at the start of the simulation. Since the relative vorticity of the small convective vortices is random and unbiased and since there are many small convective vortices in each basin of attraction, the mean absolute vorticity has a relatively small magnitude. However, vortex stretching amplifies the magnitude of the relative vorticity, and the simulations show that the relative vorticity of the large convective vortices is several orders of magnitude larger than the planetary vorticity, f. Hence the relative vorticity dominates the absolute vorticity of the large convective vortices, and the sense of rotation of the large convective vortices will be set by the sign of the mean absolute vorticity in each basin of attraction.

To test this hypothesis, we calculate the vorticity of large convective vortices in simulations for 18 different combinations of f and ξ. For each value of f and ξ, we run 30 simulations (which each have eight basins of attraction/large vortices) to ensure averaged results are statistically converged. In each case, we calculate the number of basins of attraction with cyclonic mean absolute vorticity and compare this with the number of large convective vortices with cyclonic rotation that develop in the simulation. Below, we outline the model for predicting the proportion of cyclones versus f based only on the initial condition, similar to that shown in figure 4.4a. Further details of the calculation are described in appendix 4.C.

For a given ξ, the distribution of initial mean absolute vorticity in a basin of attraction is well approximated by a Gaussian (since the initial vorticity distribution is a collection of Gaussian vortices). The amplitude of each vortex is uniformly distributed on the interval $[-\xi,\ \xi]$, so the mean of the distribution of initial mean vorticity in a basin of attraction is $\mu = 0$, and hence the mean of the absolute vorticity distribution is $\mu = -f$. The standard deviation of the Gaussian distribution is $\sigma = 0.98 \times 10^{-3}\mathrm{m}^{-2} \times \xi$, where the constant has been determined empirically from numerical simulations. We expect the sign of the vorticity of the large convective vortex that forms to be determined by the sign of the mean absolute vorticity in the basin of attraction. Therefore, the predicted bias is equivalent to the bias of the Gaussian distribution. For a given f and ξ, the bias of the Gaussian is $P(Z > -f/\sigma)$, where Z is the standard normal distribution and σ is as above. In terms of the probability density function of the Gaussian, this is

$$\text{bias}(\mu,\sigma) = \frac{1}{2\pi\sigma}\int_0^\infty \exp\left\{\frac{-(x-\mu)^2}{2\sigma^2}\right\}dx, \tag{4.8}$$

or substituting in μ and σ, this can be written in terms of f and ξ as

$$\text{bias}(f,\xi) = \frac{1}{1.96\pi\times10^{-3}\times\xi}\int_0^\infty \exp\left\{\frac{-(x+f)^2}{2(0.98\times10^{-3}\times\xi)^2}\right\}dx. \tag{4.9}$$

Varying f for a given ξ yields the lines of a predicted bias, as depicted in figure 4.6b.

The predictive lines are based solely on the initial condition. To test whether the prediction is accurate, we compare the predicted lines to the observed proportion of cyclones after running the simulation (which gives the points in figure 4.6b). Specifically in each test simulation (recall we run 30 simulations for 18 different combinations of f and ξ), we determine whether a large cyclone or anticyclone has formed at the centre of each basin of attraction once the small convective vortices have merged, shown in figure 4.4b. We find the sign of the vertical vorticity field within radius 5 m of the centre of the basin of attraction, averaged over a time interval $t = 0.875 - 0.925$ hours (after the large vortex has formed but before dissipation of the large vortex ensues). If this is positive, then we judge that a cyclone has formed. Performing this numerical calculation for each basin of attraction yields an observed bias of cyclones.

The predicted proportion of cyclones (figure 4.6b, lines) agrees very well with the proportion of cyclones observed (points) for different values of f and ξ. The predicted and simulated cyclonic bias is more prominent for larger values of f and smaller values of ξ. When f is small or ξ is large, the width of the probability distribution for the absolute vorticity averaged in each basin of attraction will be large compared to f, resulting in a weaker cyclonic bias. Due to nonlinear interactions between vortices, vortex stretching, and dissipation, not all individual regions preserve the sign of the mean absolute vorticity, but the close agreement between our prediction and simulations in figure 4.6b suggests that statistically, our prediction works very well.

The addition of many small convective vortices with a small bias in the absolute vorticity leads to a much more significant bias for the large convective vortices. Under this mechanism, the parameters which determine the bias are f, the vorticity of the small convective vortices and the number of small convective vortices that make up each large convective vortex. Changing f or the vorticity amplitude changes the initial the bias of the small convective vortices. Equally, the more small convective vortices that merge into a large vortex, the stronger we expect the bias to be.

This theoretical framework and the idealised LES can be used to predict the bias of convective vortices in the more realistic LES analysed in the previous section. The bias of the large convective vortices is determined by the amplitude of the small vortices, ξ, the number of small vortices contributing to each large vortex, and the Coriolis parameter, f. In the more realistic simulations, the number of small vortices feeding each large vortex is no longer fixed, and the vorticity of the small vortices is not controlled. We use scaling theory to relate these quantities to the bulk properties of the flow and apply the statistical theory described above.

The vorticity of the small convective vortices scales with B_0 and the depth of the convective layer, H, such that $\zeta \sim w^*/H$ where $w^* = (|B_0|H)^{1/3}$ is the convective velocity (Deardorff, 1972) (see appendix 4.D). When $|B_0|$ is large or H is small, the vorticity distribution has more extreme vorticity values so that $\zeta + f$ is less biased (equivalent to when ξ is large). To set the maximum amplitude of the small convective vortices, ξ, we use the upper limit set in our vortex detection algorithm, $\xi = 5\mathrm{m}^2 \times \sigma_\zeta$. Empirically, we then find that $\xi = 260\mathrm{m}^2 \times |B_0|^{1/3} H^{-2/3}$.

Based on the total number of small and large convective vortices detected from the LES, we find that on average there are 40 small vortices for every large convective vortex. Since the detection algorithm only identifies a small vortex when the vorticity is half of the maximum threshold, this is equivalent to 80 vortices with an amplitude that is randomly sampled from a uniform vorticity distribution. Here, we model the statistics of the large convective vortices by averaging the vorticity of 80 small convective vortices, each randomly sampled from an unbiased uniform distribution with amplitude ξ. Applying this approach, we find that the vorticity distribution of the large convective vortices is well approximated by a Gaussian with mean $\mu = 0$ and standard deviation $\sigma = 3.4 \times 10^{-3}\mathrm{m}^{-2} \times \xi$, where ξ is the maximum vorticity of the small convective vortices. The sense of rotation of the large convective vortices is then set by the sign of the mean absolute vorticity of the 80 small vortices.

Figure 4.7 shows the proportion of large cyclonic convective vortices, with a convective layer depth of 80 m (typical of oceanic convection), for the theory (lines) and the LES (dots). The convective vortices show the largest bias for large f and small B_0, a trend supported by both the simulations and theory. The mean-squared error of the points and lines in figure 4.7 is MSE $= 0.0054$.

4.4 Conclusions and discussion

Here, we built on the work in chapter 3 which showed that convective vortices can exhibit a significant rotational bias, even when Ro^* is large. In particular, we used large eddy

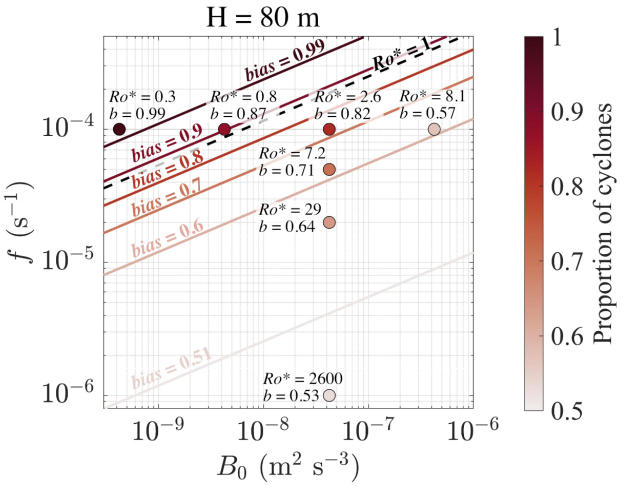

Fig. 4.7 Predicted probability contours (coloured lines) and $Ro^* = 1$ line (black dashed) for constant H. We include Ro^* and the observed bias for simulations (points).

simulations seeded with Lagrangian particles to analyse the development of a cyclonic bias in convective vortices. The convective vortices can be categorised into two types: small convective vortices which are approximately equally distributed between cyclones and anticyclones, and large convective vortices which exhibit a clear cyclonic bias. Our Lagrangian analysis shows that the large convective vortices develop through the merger of many small convective vortices. We developed a statistical theory to predict the bias in the large convective vortices as a function of the bulk parameters of the flow.

We can apply the statistical theory to predict the bias in other settings. Figure 4.8 shows the approximate parameter space for convection in the terrestrial and Martian atmospheres and for shallow and deep ocean convection. In all cases we take $f = 7 \times 10^{-5}$ s^{-1}, although this is the lower end of f values for deep ocean convection which generally occurs in higher-latitude polar oceans. Below, we provide further justification of the approximate ranges that B_0 and H take in the different convective regimes, which we summarise in table 4.1.

Observations and measurements of deep ocean convection are extensive and well-reported. A cohesive review of typical deep ocean convective conditions is given in Marshall and Schott (1999), and here we summarise the key values relevant to this study. Sites of deep ocean convection include the Labrador Sea, Greenland Sea, Mediterranean Sea and the Weddell Sea where the mixed layer depth, H, ranges from about 1000 m$-$4000 m. Typical values of the surface buoyancy flux range from $|B_0| = 10^{-6} - 10^{-8}$ m^2/s^3 where the corresponding heat loss can be between $Q = 100 - 1500$ Wm^{-2}. For example, in the Mediterranean Sea, $H = 2000$ m, $f = 10^{-4}$ s^{-1} and $B_0 = -4 \times 10^{-8}$ m^2/s^3, giving $Ro^* = 0.3$. More generally, we can expect $Ro^* \sim 0.01 - 1$ in a deep convective regime.

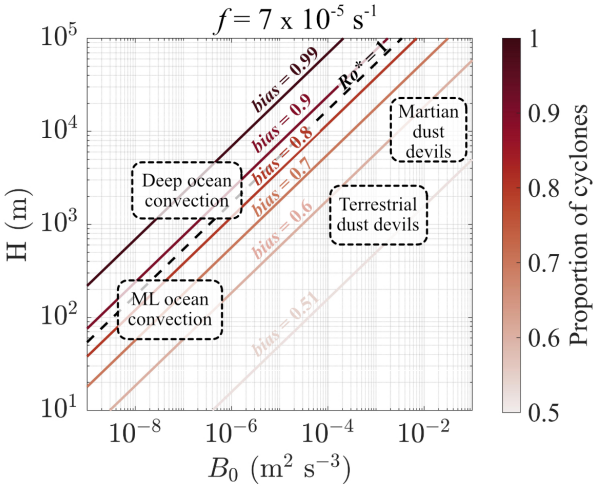

Fig. 4.8 Predicted probability contours (coloured lines) and $Ro^* = 1$ line (black dashed) for constant f. We highlight the approximate parameter spaces for convective vortex regimes.

Shallow mixed layer convection is typically characterised by a much smaller H and a smaller B_0. For example, Chor et al. (2018a) used $H = 80$ m and a surface heat flux of $Q = 150$ Wm^{-2}, while Mensa et al. (2015) used $H = 50$ m and $Q = 1000$ Wm^{-2} to model convection in the ocean surface boundary layer. In this case, we estimate $Ro^* \sim 0.5 - 10$.

Heat fluxes in the terrestrial atmosphere are similar to those in oceanic convection because heat loss to the atmosphere drives convection in the ocean, but they have very different buoyancy fluxes. The ratio of the buoyancy fluxes in the ocean, B_{ocean}, and atmosphere, B_{atmos} is written in Marshall and Schott (1999) as:

$$\frac{B_{atmos}}{B_{ocean}} = \frac{\rho_w c_w}{\rho_a \alpha c_a b_a} \approx 10^5 \,, \tag{4.10}$$

where ρ is the density, c is the specific heat, α is the thermal expansion over water and b is the typical air temperature. Subscript w denotes water and a denotes terrestrial air. An estimate of the ratio is determined using typical meteorological values which suggests that the atmospheric buoyancy fluxes are about 10^5 times larger than oceanic buoyancy fluxes. This is consistent with Caughey (1982) who estimate that $B_0 \approx 5 \times 10^{-3}$ m^2/s^3 in atmospheric boundary layer convection. The mixed layer depth in the terrestrial atmosphere is typically $H = 1000 - 2000$ m. Such parameters yield $Ro^* \sim 10 - 250$ in the terrestrial atmosphere.

Finally, Martian convection is similar to atmospheric convection but characterised by a larger H and larger B_0. We can write

$$\frac{B_{mars}}{B_{atmos}} = \frac{\rho_a c_a b_a g_m}{\rho_m c_m b_m g_a} \approx 50 \,, \tag{4.11}$$

Type of convection	B_0 (m^2/s^3)	H (m)	Ro^*
Deep ocean convection	$10^{-7} - 5\times10^{-7}$	$1000 - 5000$	$0.01 - 1$
Mixed layer ocean convection	$10^{-8} - 10^{-7}$	$50 - 150$	$0.5 - 10$
Terrestrial atmosphere	$10^{-3} - 5\times10^{-2}$	$1000 - 2000$	$10 - 250$
Martian atmosphere	$5\times10^{-3} - 10^{-1}$	$5000 - 10000$	$5 - 100$

Table 4.1 Typical parameters in different convective regimes

where subscript m denotes Martian air and g is gravity. Again, the ratio is determined from typical Martian (Thomas and Gierasch, 1985) and terrestrial (Marshall and Schott, 1999) values. On Mars, the convective boundary layer can be up to 10000 m (Balme and Greeley, 2006), giving a similar range of Ro^* as in the atmosphere, $Ro^* \sim 5 - 100$.

Figure 4.8 shows that ocean mixed layer (ML) convection is expected to usually exhibit a cyclonic bias, consistent with Dingwall et al. (2023), while deep oceanic convection is highly biased. Our theory predicts that most atmospheric regimes will be unbiased, with a slight rotational bias in Martian dust devils. This is consistent with observations and simulations of terrestrial dust devils (Balme and Greeley, 2006; Raasch and Franke, 2011), but Martian dust devil data are not yet extensive enough to test this prediction.

Finally, note that convective conditions often have additional sources of vorticity other than buoyancy flux which may influence the derived scaling law. Examples include wind forcing (Dingwall et al., 2023), or bottom friction in the atmosphere, both of which have potential to increase vorticity fluctuations and inhibit the cyclonic bias. The rotational bias of convective vortices under more realistic conditions should be explored in future work.

Appendix 4.A

The bias of convective vortices is independent of the simulation's horizontal resolution, Δx, vertical resolution, Δz, and horizontal domain size, L. To verify this, we run simulations varying L keeping $\Delta x = 1$ m and $\Delta z = 0.95 - 2.57$ m fixed (recall we use variable grid spacing in the z direction). Subsequently, we vary Δx and Δz keeping $L = 125$ m fixed. The additional simulations each have $B_0 = -4.24\times10^{-8}$ m^2/s^3, $f = 10^{-4}$ s^{-1} and $H = 80$ m. To compare the vorticity distributions, we plot the vertical vorticity PDF at $z = -1$ m for points associated with convective vortices (using the vortex detection algorithm) and for all points in the domain. Note that the vortex detection algorithm applied here uses a larger detection radius than in the main text (5 m as opposed to 3.5 m in the main text) to ensure that vortices are captured in low-resolution, large domain simulations. A more detailed description of the method can be found in Dingwall et al. (2023). To remove turbulent fluctuations in the

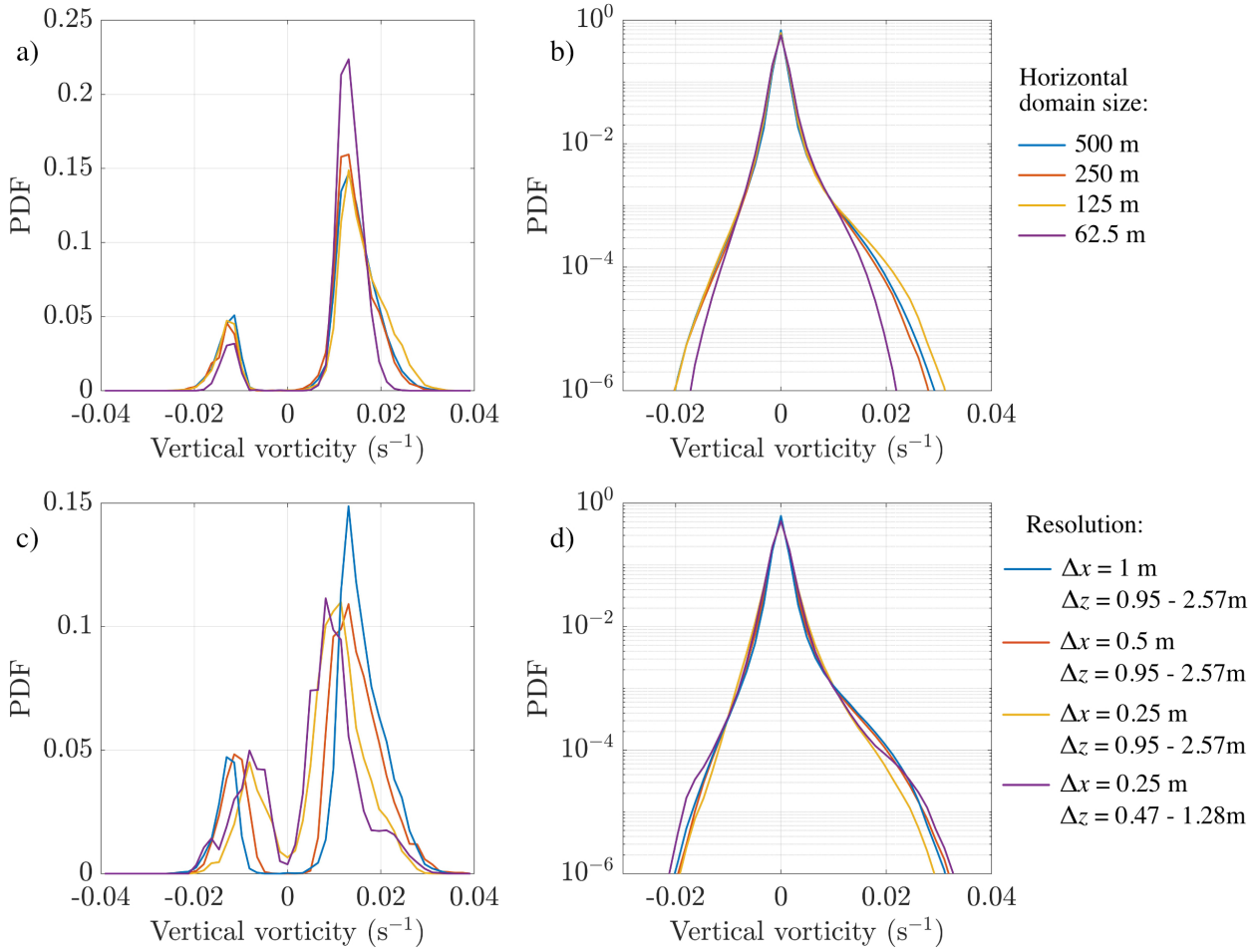

Fig. 4.9 Probability density function of vertical vorticity at $z = 0$ m for points identified as convective vortices (a,c) and all points in the domain (b,d) as the domain size (a,b) and resolution (c,d) are varied.

distribution for all points, the vorticity at each point is averaged over a box measuring 5 m $\times$5 m.

Figure 4.9a,b shows the effect of varying the domain size (with $\Delta x = 1$ m and $\Delta z = 0.95 - 2.57$ m). For points associated with convective vortices (a), the peak remains at $\zeta \simeq \pm 0.015$ s^{-1} as the domain size decreases. The proportion of cyclones and anticyclones stays approximately the same with the most noticeable difference when $L = 62.5$ m. This is reflected in the distribution for all points, with again the most noticeable discrepancy between distributions when $L = 62.5$ m. For this reason, we choose to use a domain $L = 125$ m. At this size, there are only one or two large convective vortices at any given snapshot. However, we aim to resolve the small-scale motions as much as possible without adversely affecting the bias of convective vortices and we run simulations for a long enough period of time for statistical quantities to converge.

Now with $L = 125$ m fixed, figure 4.9c,d shows the effect of increasing the horizontal resolution, Δx, and the vertical resolution, Δz. Again, the proportion of cyclones and the distribution for all points remain similar even for the highest resolution simulations. We choose to use the highest computationally feasible resolution, $\Delta x = 0.25$ m and $\Delta z = 0.95 - 2.57$ m to capture the small-scale convective vortices described in this study. When $\Delta x = 0.25$ m, the vortex detection algorithm detects more convective vortices with a near-zero vorticity. In the main text, we use a smaller detection radius in the algorithm to avoid this.

Appendix 4.B

Figure 4.10 depicts a more detailed visualisation of the small and large convective vortices from a simulation with $B_0 = -4.24 \times 10^{-8}$ m^2/s^3, $H = 80$ m and $f = 10^{-4}$s^{-1} at time $t = 10$ hours. The small vortices are coherent structures which occur regularly throughout the domain and we observe a roughly equal number of cyclones and anticyclones. The small vortices extend to a depth of between $5 - 10$ m while the large vortex in figure 4.10b (and highlighted in the white box in figure 4.10a) extends to a depth of about 40 m, and in this case is cyclonic.

Appendix 4.C

Here, we describe the specifics of the calculations used to predict the number of basins of attraction with cyclonic mean absolute vorticity and the number of large convective vortices with cyclonic rotation that develop in the idealised simulations, which are compared in figure 4.6.

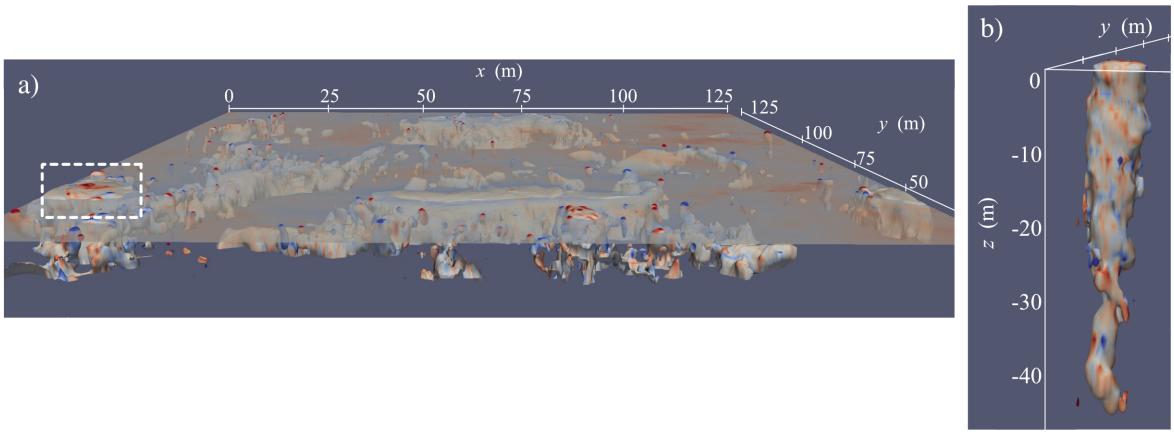

Fig. 4.10 Three-dimensional visualisation of small (a) and large (b) convective vortices in a simulation with $B_0 = -4.24 \times 10^{-8}$ m^2/s^3 and $f = 10^{-4}$ s^{-1}. (a) shows the contour of perturbation pressure at $\delta p = -\sigma_p$ up to a depth $z = -7$ m coloured by vertical vorticity with a horizontal pressure slice overlain. (b) shows the contour of perturbation pressure at $\delta p = -5\sigma_p$ coloured by vertical vorticity for the large vortex highlighted in the white box in (a).

Firstly, for any ξ and f, we calculate the mean vorticity within a single basin of attraction at $t = 0$ hours (dashed square boxes in figure 4.4), $\overline{\zeta_b}$, where overline denotes mean and subscript b denotes a quantity in an individual basin. Since the initial amplitude of the small vortices is uniformly distributed, several have a very small amplitude and we expect these to be quickly dissipated. We neglect such vortices by only considering points whose vorticity magnitude exceeds 20% of the vorticity standard deviation. Computing $\overline{\zeta_b}$ for each basin in each simulation, we find that the distribution of $\overline{\zeta_b}$ is well approximated by a Gaussian. An example of this approximation can be seen in figure 4.11 which shows the PDF of the initial mean basin vorticity, $\overline{\zeta_b}$, for all simulations with $\xi = 0.025$ m^2/s. The distribution is very Gaussian (blacked dash line shows a Gaussian with $\mu = 0$, $\sigma = 2.4 \times 10^{-5}$ s^{-1}). The Gaussian is symmetric about $\overline{\zeta_b} = 0$ by construction of uniformly distributed small vortices. Computing the standard deviation for all values of ξ and f, we find that the standard deviation linearly increases with ξ, with $\sigma = 0.978 \times 10^{-3}m^{-2} \times \xi$, where the constant is determined empirically.

While the distribution of initial relative vorticity, ζ, is symmetric about 0, the distribution of absolute vorticity, $\zeta + f$ is not. Accordingly, the distribution of $\overline{\zeta_b} + f$ is not symmetric about 0. To calculate the extent of the bias, we use the Gaussian approximation of $\overline{\zeta_b}$ and calculate the proportion of the distribution larger than $-f$ (the upper tail to the right of $-f$). This describes the probability of a basin of attraction initially having positive mean absolute

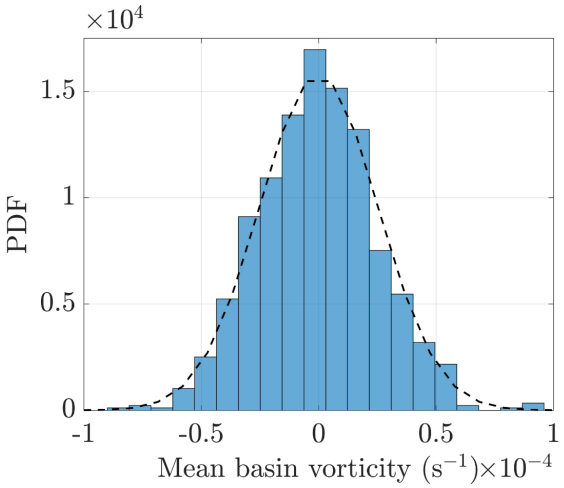

Fig. 4.11 PDF of initial mean basin vorticity for $\xi = 0.025$ m^2/s and Gaussian with $\mu = 0$, $\sigma = 2.4 \times 10^{-5}$ s^{-1} (black dashed line)

vorticity, which we expect to determine whether a cyclone or anticyclone eventually forms. More specifically, we compute $P(Z > -f/\sigma)$ where Z is the standard normal distribution.

Secondly, in each test simulation, we determine whether a large cyclone or anticyclone has formed at the centre of each basin of attraction later in the simulation once the small convective vortices have merged. We find the sign of the vertical vorticity field within radius 5 m of the centre of the basin of attraction, averaged over a time interval $t = 0.875 - 0.925$ hours (after the large vortex has formed but before dissipation of the large vortex ensues). If this is positive, then we judge that a cyclone has formed.

Appendix 4.D

Empirically, the vorticity scales with B_0 and the depth of the convective layer, H, such that $\zeta \sim w^*/H$ where $w^* = (|B_0|H)^{1/3}$. This scaling also holds in the shallow convective cells ($\zeta \sim w^*/h$) where h is the depth of the shallow convective cells. Typically, w^* characterises the velocity scale in the upwelling region for a convectively driven flow. The area of the downwelling and upwelling regions is very asymmetric (figure 4.1), and hence we expect a similar asymmetry between the upwelling and downwelling velocities. We can write this as $w_u = cw_d$ where subscript u denotes upwelling, d denotes downwelling and c is a constant of asymmetry. Since the small convective cells are contained within the upwelling of large convective cells, there must be a point at the base of the small cell where the large-scale upwelling velocity balances the small-scale downwelling velocity, i.e. $W_u = w_u/c$ $(= w_d)$. Rewriting this in terms of the relevant convective velocities gives $(|B_0|H)^{1/3} = (|B_0|h)^{1/3}/c$

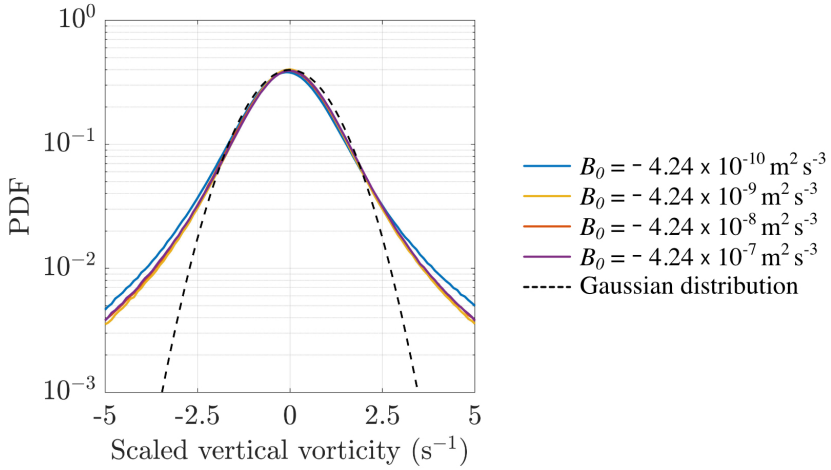

Fig. 4.12 Scaled probability density function of vertical vorticity in large-scale upwelling regions for simulations with $f = 10^{-4}$ s^{-1} with a Gaussian approximation to the scaled curve (dashed line) at $z = -1$ m.

and rearrangement yields $h/H = c^3$, i.e. the ratio of the depth of small and large convective cells is constant. To estimate the vorticity fluctuations in the small convective cells (and large-scale upwelling) which contain the small vortices, we use the relation $\zeta_u \sim |B_0|^{1/3} H^{-2/3}$. Finally, note that the convective Rossby number can be rewritten in terms of ζ with a scaling constant, C, as $Ro^* = C(\zeta/f)^{3/2}$.

Figure 4.12 shows the scaled vertical vorticity pdf in the large-scale upwelling regions, i.e. $H^{2/3}\zeta_u |B_0|^{-1/3}$, for simulations with different values of B_0 but the same value of $f = 10^{-4}$ s^{-1} and $H = 80$ m, and the distributions collapse onto one another. The scaled distribution is relatively Gaussian for small vorticity values, but has much wider tails. Studies of the non-Gaussian distribution of vorticity have previously suggested that the development of wide tails might be associated with vortex stretching of strong vortices (Pope, 2001; Wilczek and Friedrich, 2009), which in our case most likely relates to stretching of the large convective vortices.

Chapter 5

Direct numerical simulations of a geostrophically adjusting front

5.1 Introduction

In this chapter, we change tack and consider the role of density fronts in the ocean surface mixed layer. Here, we define a front to be a region of fluid with a very sharp density gradient in one horizontal direction (the 'cross front' direction), but a weak density gradient in the perpendicular direction (the 'along front' direction) (Hoskins, 1982). This work is broadly motivated by submesoscale fronts observed during the SUNRISE campaign in the Gulf of Mexico. The dramatic density contrast between plumes of freshwater from the Mississippi-Atchafalaya river and salty offshore water creates extremely sharp and energetic fronts. These are associated with strong convergence (visible as surface slicks or accumulated sargassum or bubbles, see figure 1.4), and strong vertical motion. The focus of this chapter is to use numerical experiments to understand the physics and energy pathways of an idealised density front, with a view to applying our findings to the transport of buoyant material in a front in chapter 6.

Density fronts are ubiquitous features of the upper ocean (Boccaletti et al., 2007; Callies et al., 2016; Fox-Kemper et al., 2008; Taylor and Ferrari, 2009; Thomas et al., 2008) and can be established in a variety of situations across several different scales. On the global scale, surface forcing such as wind stresses and buoyancy fluxes drive persistent frontal systems such as the Gulf Stream and Kuroshio, and the Antarctic Circumpolar Current. These currents are barotropically and baroclinically unstable which leads to the generation of mesoscale eddies. The horizontal strain and shear associated with mesoscale and submesoscale eddies leads to frontal sharpening, or frontogenesis (Brannigan et al., 2017). Small-scale fronts

can also be generated through localised buoyancy sources such as river outflows. Fronts are associated with large vertical velocities which act to increase the transport of tracers (e.g. heat, carbon dioxide, nutrients, pollutants) into the ocean interior and high biological productivity (Ferrari, 2011). In global and even regional models, sharp fronts are often spatially and temporally unresolved (Boccaletti et al., 2007) and it is important that their dynamics are well understood (Ferrari, 2011).

The density gradient at a front is associated with a hydrostatic pressure gradient. In the absence of rotation, gravity drives dense waters to sink below light waters leading to tilting of density surfaces towards the horizontal. When density gradients are not constant, regions with a large density gradient tilt faster than regions with a small density gradient and we observe frontogenesis of gravity currents, which has been studied using a combination of mathematical and laboratory models (Simpson and Linden, 1989). When rotation is present, the density gradient at a front can be partly balanced by the Coriolis acceleration, arising due to rotation of Earth. A state of geostrophic and hydrostatic balance is associated with a vertically-sheared 'thermal wind' flow directed along the front. Often, geostrophic balance is disrupted by background flows (such as eddies) or external forcing (such as buoyancy fluxes or wind stress). The process by which an unbalanced flow evolves back towards geostrophic balance is known as geostrophic adjustment.

Geostrophic adjustment has laid the foundation for many analytical studies of density fronts (Blumen and Wu, 1995; Ou, 1984; Rossby, 1937; Tandon and Garrett, 1994) which have the overarching goal of solving a highly idealised model for the final equilibrium steady state. Tandon and Garrett (1994) studied an idealised representation of the response of a front to a mixing event (e.g the passage of a storm). They considered a fluid between two rigid horizontal planes. Their initial condition consisted of a uniform horizontal buoyancy gradient and no vertical buoyancy gradient, and a vertical shear that was partially or fully mixed relative to a state of thermal wind balance. As the front adjusts to this unbalanced initial state, an ageostrophic secondary circulation develops which carries light fluid over the top of dense fluid and flattens the density surfaces (or isopycnals).

In 1984, Ou (1984) used a Lagrangian framework to provide a solution for an initially motionless, isolated, two-dimensional front with a lateral density gradient. They found that the ageostrophic secondary ciruclation can produce regions of convergence and steepen density gradients. For sufficiently large initial density gradients, singularities form in convergent regions and the equilibrium state does not exist. It remains uncertain what prevents the development of a singularity in the full three-dimensional, viscous system, and this is the focus of this work.

A geostrophically adjusting front is associated with reservoirs of potential and kinetic energy. Some gravitational potential energy present in the initially unbalanced front is converted into kinetic energy of the geostrophic current during adjustment, but even in the equilibrium state, there is considerable potential energy that is not released (Gill, 1976). A range of instabilities extract their energy from these reservoirs (Barth, 1989; Haine and Marshall, 1998; Samelson, 1993; Samelson and Chapman, 1995).

Until now, the problem of geostrophic adjustment has largely been studied using analytical models in one or two dimensions (Blumen and Wu, 1995; Ou, 1984; Tandon and Garrett, 1994). Here, we use direct numerical simulations (DNS) to study the frontal dynamics, instabilities, and three-dimensional turbulence associated with geostrophic adjustment. Specifically, we consider an isolated, finite-width front comprising a frontal region with horizontally-varying and time evolving buoyancy gradients, initialised with motionless fluid with a localised horizontal density gradient, analogous to Ou (1984). This allows us to compare and contrast the geostrophically balanced state with Ou (1984) for weak imbalances, and explore the very sharp density gradients that arise during frontogenesis for larger imbalances. To our knowledge, this is the first time that DNS has been applied to this problem.

We begin in section 5.2 by describing the problem set-up and the DNS. In section 5.3, we provide a qualitative and quantitative analysis of the geostrophically adjusting flow for a range of parameters, with an emphasis on the energy budget and instabilities that arise during frontogenesis. Finally, a summary of the study and discussion of the key results is given in section 5.4.

5.2 Setup and numerical methods

Here, we use direct numerical simulations (DNS) to model an idealised representation of a geostrophically adjusting front confined to the ocean mixed layer, following the setup of Ou (1984). Specifically, the initial state of the frontal region consists of incompressible flow initially at rest with a horizontal across-front buoyancy gradient with finite lateral extent. Without loss of generality, the initial frontal gradient is aligned with the x-direction and buoyancy is homogeneous in the along-front (y) direction and the vertical. In dimensional variables, the initial condition is

$$b|_{t=0} = M_0^2 \, L_0 \tanh\left(\frac{x}{L_0}\right), \qquad \mathbf{u}|_{t=0} = \mathbf{0}, \tag{5.1}$$

where L_0 is the characteristic width of the front and M_0^2 is the maximum initial horizontal buoyancy gradient. The bottom and top boundaries are located at $z = 0$ and $z = -H$ (where

H is the depth of the fluid). We neglect boundary effects such as wind forcing, buoyancy fluxes and entrainment from the bottom of the thermocline, which have previously been studied in Taylor and Ferrari (2009, 2010).

We non-dimensionalise the system following Wienkers et al. (2021a,b) using the so-called 'geostrophic units', where the maximum thermal wind shear at the centre of the front and the depth of the fluid are scaled to be unity. Specifically, the dimensionless (*) variables are defined as:

$$\mathbf{u}^* \equiv \mathbf{u}\frac{f}{HM_0^2}; \quad b^* \equiv b\frac{f^2}{HM_0^4}; \quad \mathbf{x}^* \equiv \mathbf{x}\frac{1}{H}; \quad t^* \equiv t\frac{M_0^2}{f}\ , \tag{5.2}$$

where $(0,0,f)$ is the Coriolis force under the 'traditional approximation' where we only retain the vertical component of the angular velocity vector. We further assume that the Coriolis parameter, f, is constant.

Our DNS solves the incompressible Navier-Stokes momentum equations under the Boussinesq approximation. In terms of the dimensionless velocity field $\mathbf{u}^* = (u^*, v^*, w^*)$, the equations are:

$$\frac{\mathrm{D}\mathbf{u}^*}{\mathrm{D}t^*} = -\nabla^*\Pi^* - \frac{1}{\Gamma_0}\widehat{\mathbf{z}}\times\mathbf{u}^* + \frac{Ek}{\Gamma_0}\nabla^{*2}\mathbf{u}^* + b^*\widehat{\mathbf{z}}, \tag{5.3}$$

$$\nabla^*\cdot\mathbf{u}^* = 0, \tag{5.4}$$

where $\nabla^* \equiv H\nabla$ and $\nabla^*\Pi^*$ is the dimensionless pressure head acceleration. In dimensionless variables, the initial state of the frontal region is

$$b^*|_{t^*=0} = \frac{\delta_0}{\Gamma_0}\tanh\left(\frac{x^*}{\delta_0}\right), \quad \mathbf{u}^*|_{t^*=0} = \mathbf{0}. \tag{5.5}$$

This system is associated with four dimensionless parameters which fully describe the initial frontal region,

$$\Gamma_0 \equiv \frac{M_0^2}{f^2}; \quad \delta_0 \equiv \frac{L_0}{H}; \quad Ek \equiv \frac{\nu}{H^2 f}; \quad Pr \equiv \frac{\nu}{\kappa}, \tag{5.6}$$

where a subscript 0 indicates the initial value of a time evolving quantity. Here, ν is the viscosity and κ is the diffusivity.

We apply periodic boundary conditions to $\mathbf{u}^*$ in both horizontal directions. At the top and bottom of our domain ($z = 0$ and $z = -1$), we apply free slip boundary conditions. We decompose the total buoyancy, b^*, into a constant background gradient, Δb^*, and departures from this gradient, $b^{*\dagger}$,

$$b^* = b^{*\dagger} + \frac{\Delta b^*}{L_x^*}x^*, \tag{5.7}$$

where $\Delta b^* = 2\delta_0/\Gamma_0$ and L_x^* is the dimensionless cross-frontal domain size. Under this decomposition, the linear equation of state solved by the DNS is:

$$\frac{\mathrm{D}b^{*\dagger}}{\mathrm{D}t^*} + u^* \frac{\Delta b^*}{L_x^*} = \frac{Ek}{\Gamma_0 Pr} \nabla^{*2} b^{*\dagger}. \tag{5.8}$$

We then apply periodic boundary conditions to $b^{*\dagger}$ in the horizontal directions which ensures that the buoyancy difference across the domain remains constant. This approach has been used in several other studies of submesoscale flows (Taylor, 2016, 2018; Taylor and Ferrari, 2010; Taylor et al., 2020; Thomas et al., 2016). In all that follows, we drop the asterisks for notational simplicity.

Physically, we interpret $\Gamma_0 = M_0^2/f^2$ as a measure of the strength of the front, and $\delta_0 = L_0/H$ as a measure of the aspect ratio of the front. Both Γ and δ vary widely between different locations and evolve over time as the front develops and adjusts (Crowe and Taylor, 2018). For example, in the Gulf Stream, $\Gamma \approx 50$, while in the Gulf of Mexico where $\Gamma \approx 500$ (Jinadasa et al., 2016), and open ocean fronts can have $\Gamma \lessapprox 1$ (Thompson et al., 2016). The balanced Rossby number, which characterises the relative importance of the vertical vorticity, ζ, compared to the planetary vorticity, f, can be defined in terms of Γ_0 as:

$$Ro_0 \equiv \frac{\zeta_f}{f} = \frac{HM_0^2}{f} \cdot \frac{1}{L_0} \cdot \frac{1}{f} = \frac{\Gamma_0}{\delta_0}, \tag{5.9}$$

where ζ_f is the vertical vorticity of the balanced front. We can interpret the inverse Rossby number ($\delta_0/\Gamma_0 = L_0 f^2/(HM_0^2)$) as the front width in units of the deformation length-scale, $L_d = HM_0^2/f^2$. Since Γ and δ vary widely across different regions, fronts take a wide range of Ro_0 in the ocean.

The Rossby number also controls the magnitude of the initial density gradient (see equation (5.5)). Ou (1984) found that analytical solutions for the equilibrium state break down for $Ro_0 > Ro_c$, where $Ro_c = 3.5$ (which is equivalent to $\beta = 2.6$ using Ou's non-dimensionalisation). Beyond this point, the theory predicts that a discontinuity forms. Figure 5.1 shows the initial condition (black dashed line) and Ou's solution of the geostrophically adjusted state (red solid line) in the case $Ro_0 = 1$, which is smaller than the critical value.

We design a set of numerical experiments to investigate the effects of varying the Rossby number, Ro_0, on the geostrophically adjusting front. DNS is a highly computationally expensive approach that requires us to accurately capture all scales of motion. This limits the values of Γ_0, Ek, and Pr that we can feasibly consider. We hold three out of four dimensionless parameters defined in equation (5.6) constant. Specifically, we fix $Ek =$

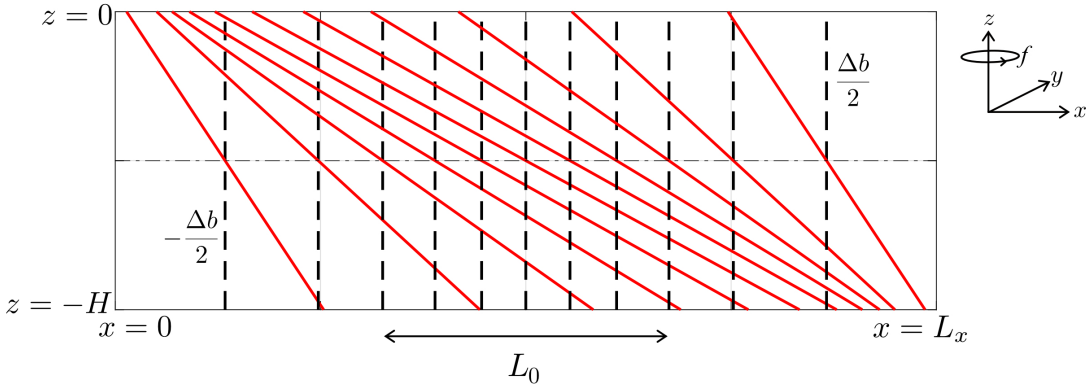

Fig. 5.1 The initial condition and solution for $Ro_0 = 1$ from Ou (1984). Dashed black lines are the buoyancy contours in the initial state, and solid red lines are the buoyancy contours in the adjusted state, and Δb is the buoyancy difference across the domain.

2.5×10^{-3}, $Pr = 1$ and $\delta_0 = 1$ across all of the simulations. Hence, we only vary Γ_0 and in particular, since $\delta_0 = 1$, it follows that $\Gamma_0 = Ro_0$.

The largest Γ_0 is associated with the most energetic turbulence, the largest deformation length-scale and the largest unstable baroclinic mode and is thus the hardest case to resolve. In this study, the largest value we consider is $\Gamma_0 = Ro_0 = 16$. This requires a computational domain with $L_x = 20$ to accommodate the fully adjusted front across the domain in the x direction and $L_y = 25$ to capture the largest unstable baroclinic mode in the y direction. The spatial resolution is then chosen so that the most energetic turbulence is resolved down to the Kolmogorov scale. To resolve boundary-enhanced turbulence during frontogenesis, we use a non-uniform grid in the z direction with 65 grid points which increases the near boundary resolution, giving a vertical resolution of between 0.009 and 0.02. In the horizontal directions, we use 512 uniformly spaced grid points which gives a horizontal resolution of 0.04 in the x direction and 0.05 in the y direction. The horizontal grid spacing is $1/50$ of the initial frontal width, which allows significant frontogenesis. In the cases where $Ro > Ro_c$, there is a short period of time when the front collapses to the grid scale and our simulation is not fully resolved. However, based on resolution sensitivity tests, we have found that this does not influence the turbulence statistics (e.g. energy budget terms or mixing terms). For a full discussion of resolution tests, refer to appendix 5.A.

We run seven simulations with $\Gamma_0 = Ro_0 = 0.25, 0.5, 1, 2, 4, 8, 16$. The domain size and resolution is kept the same for each simulation. After initialising the momentum field with random noise at a dimensionless amplitude 10^{-1}, we evolve each simulation for five inertial periods $T = 10\pi\Gamma_0$.

In the numerical code, derivatives in the horizontal directions are calculated using a pseudospectral method, whilst vertical derivatives are calculated using second-order finite differences. The equations are time-stepped using an implicit Crank–Nicolson method for the viscous and diffusive terms and a third-order Runge–Kutta method for all other terms. Further details of the numerics can be found in Taylor (2008).

5.3 Results

Here, we primarily focus on simulations with $Ro_0 > Ro_c$ for which Ou (1984) predicts formation of a singularity or front. We include some discussion and analysis of the remaining simulations, but they exhibit qualitatively similar features to one another and do not show signs of frontogenesis, which is the main focus of this study. We begin with a qualitative description of the flow in section 5.3.1 and discuss the instabilities that arise. We then compare and analyse the energetics and diagnose contributing terms in the energy budget equation in section 5.3.2. Finally in section 5.3.3, we quantify the mixing efficiency during frontal collapse and discuss the implications.

5.3.1 Qualitative description of the flow

Visualisations of the buoyancy are shown in figure 5.2 for the simulation with the largest Rossby number ($Ro_0 = 16$). At the start of the simulation, the initially unbalanced front slumps outwards and the buoyancy gradients increase near the top and bottom boundaries. The circulation becomes narrower and more intense as it is squeezed inwards, producing regions of horizontal convergence. By $tf = 1.8$, an abrupt density jump (the analogue of the frontal singularity predicted by Ou (1984) in the inviscid equations) has formed in the convergent region at the top and bottom boundary (figure 5.2a). In our simulations, the velocity is initialised with a significant random perturbation with dimensionless magnitude 10^{-1}, but this is still not large enough to prevent the formation of a buoyancy jump. Frontogenesis leads to intense velocity gradients and turbulence along the front, which is visible in figure 5.2b at $tf = 2.8$ (the time of peak turbulent kinetic energy, see figure 5.4).

The frontal collapse is associated with the development of three dimensional turbulence. At $tf = 1.8$, a horizontal cross section of the buoyancy field at the surface shows some fine scale structures visible along the front (figure 5.2d). By $tf = 2.8$, the structures have grown and the front is very turbulent. After several inertial periods the flow settles down into a non-turbulent state with inertial oscillations about the equilibrium state. A vertical slice reveals a slumped, relatively laminar front (figure 5.2c at $tf = 44$). The equilibrium state is

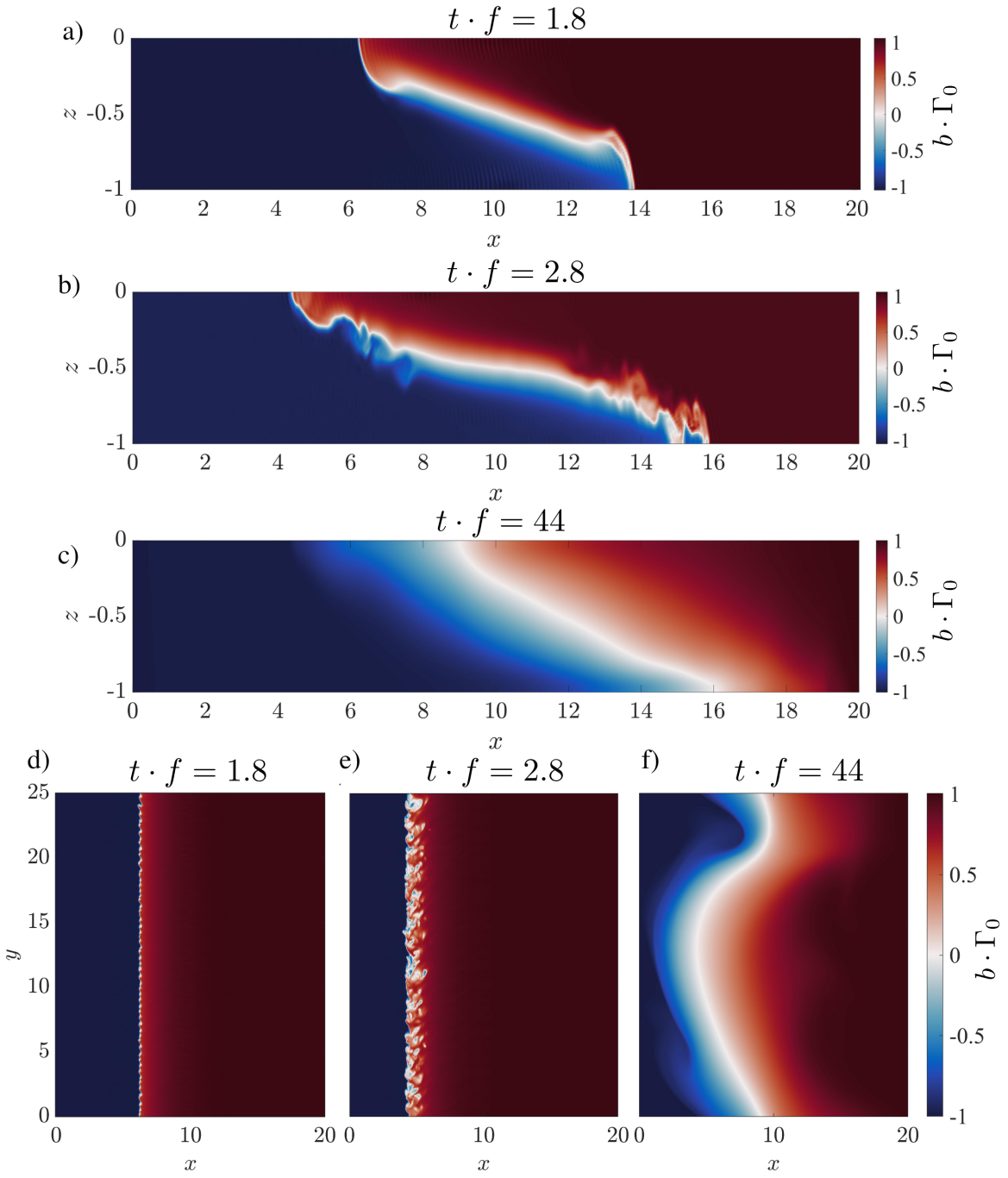

Fig. 5.2 Vertical slice at $y = 0$ (a,b,c) and horizontal slice at $z = 0$ (d,e,f) of the buoyancy field, b, for a simulation with $Ro_0 = 16$ at $tf = 1.8$, $tf = 2.8$ and $tf = 44$.

unstable to baroclinic instability, and the distortions of the front from the growing baroclinic mode can be seen in a horizontal cross section in figure 5.2f.

In contrast, the smaller Ro_0 cases initially have relatively weak, broad buoyancy gradients. At the start of the simulation, the front slumps outwards but to a smaller distance than the high Rossby number cases (note that the deformation scale, L_d, decreases as Ro_0 decreases). Thus, a smaller Rossby number implies that the front remains comparatively upright during adjustment. Below the critical Rossby number, the front does not collapse, but oscillates inertially about the steady equilibrium state. Waves are visible as bands of intensified vertical flow, propagating outward from the edges of the front into the surrounding weakly stratified fluid (not shown). After a period of adjustment, the fluid becomes baroclinically unstable and baroclinic eddies develop. As the Rossby number decreases, the wavelength of the most unstable baroclinic mode decreases.

In order to study the development of frontal instabilities and turbulence, we introduce a turbulent-mean decomposition where the mean fields, denoted $\overline{g}(x,z,t)$, are averaged along the y direction. The three-dimensional fluctuating component is then

$$g'(x,y,z,t) = g(x,y,z,t) - \overline{g}(x,z,t), \tag{5.10}$$

and the turbulent kinetic energy (TKE) is

$$\text{TKE} = \frac{1}{2}(u'^2 + v'^2 + w'^2). \tag{5.11}$$

Figure 5.3 shows along-front averaged buoyancy contours at $z = 0$ in colour and the along-front averaged TKE in grayscale at $z = 0$ for $Ro_0 = 2, 4, 8, 16$ (the smallest of which is below Ro_c). The speed and extent of collapse is greatest for $Ro_0 = 16$, for which we also observe the highest level of turbulence between $tf = 2$ and $tf = 4$. Interestingly, a patch of elevated TKE remains on the dense (left) side of the front, even after the front retreats. The second inertial oscillation is again associated with elevated TKE at $tf = 10$, but to a much lesser extent than the first oscillation.

When Ro_0 decreases but remains above the critical value, the buoyancy contours show a less extreme frontal collapse and less TKE. The front does not slump as far, so oscillations in the buoyancy contours are less abrupt and less extensive. One feature of interest is the spike in TKE at $x = 10$, $tf = 8$ in the simulation with $Ro_0 = 8$. Analysis of this time period (not shown) reveals convective boils where more buoyant fluid rises over the less buoyant fluid. Below the critical Rossby number (i.e. when $Ro_0 = 2$ in figure 5.3a), there is no sign of frontal collapse and no significant increase in TKE. The simulations with an even smaller Rossby behave qualitatively similarly with a decreasing oscillation amplitude.

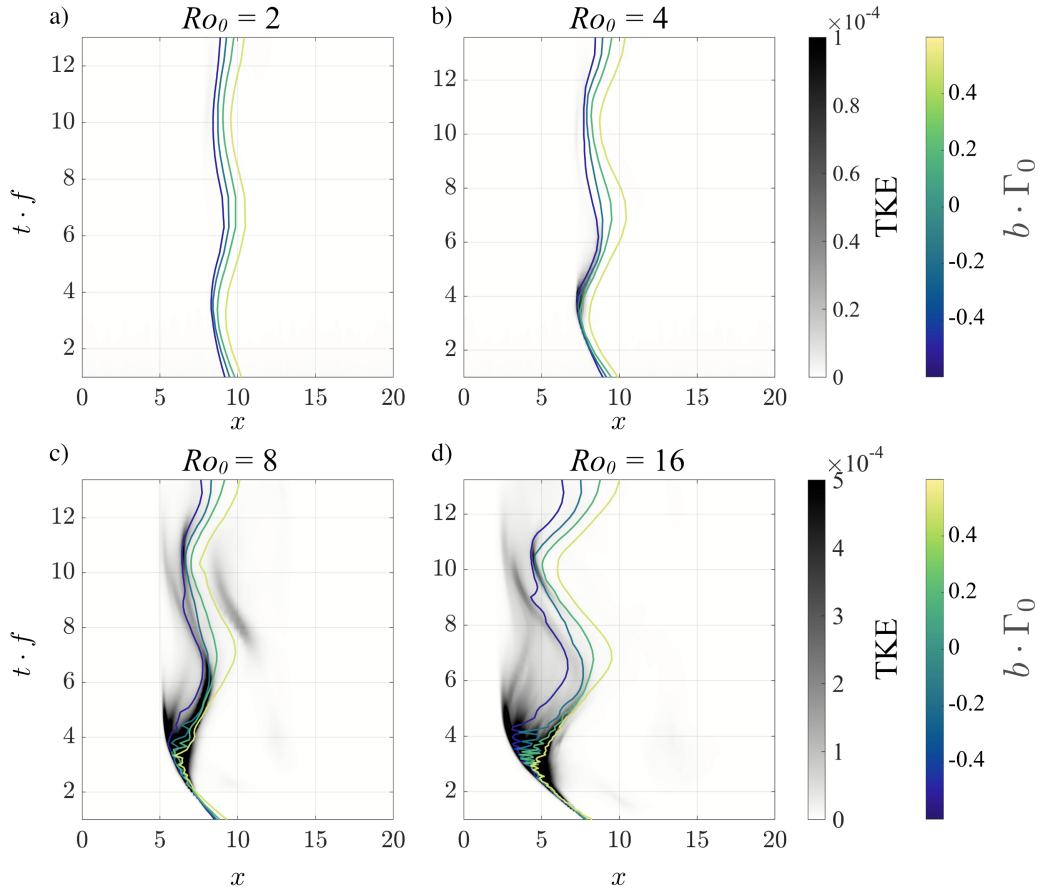

Fig. 5.3 Along-front averaged TKE (black) plotted over cross-front position, x, and time, t, overlain with the time-varying position of buoyancy contours at $z = 0$ for simulations with $Ro_0 = 2, 4, 8, 16$.

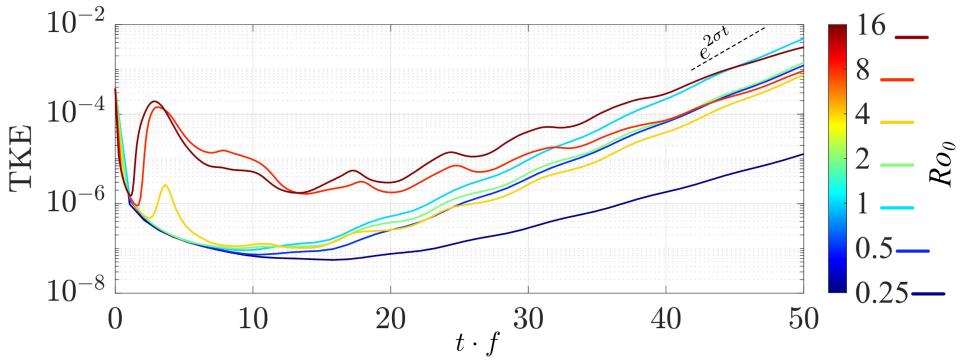

Fig. 5.4 Volume averaged TKE over time for simulations with varying Ro_0. The growth rate predicted by Fox-Kemper et al. (2008); Stone (1966) with $Ri = 1$ is shown with the dotted line.

5.3.2 Adjustment energetics

Figure 5.4 shows the volume averaged TKE as a function of time for each simulation using a logarithmic scale. At early times, there is a large spike in TKE for all simulations with $Ro_0 > Ro_c$ which is associated with turbulence generated during frontal collapse. The TKE reaches a comparable maximum for $Ro_0 = 8$ and $Ro_0 = 16$. When $Ro_0 = 4$, the early maximum in the TKE is smaller, and quickly decreases to a value similar to the smaller Ro_0 cases. The larger values of Ro exhibit larger inertial oscillations in the TKE as the larger Ro cases have larger amplitude inertial oscillations and are more nonlinear.

A second period of TKE growth begins at about $tf = 12$ whose rate is fairly consistent across the simulations. The exponential increase in TKE during this second growth phase is characteristic of baroclinic instability. For a uniform front in thermal wind balance (the Eady model), Stone (1966) found that the largest unstable baroclinic mode grows according to TKE $\sim \exp(2\sigma t)$ where

$$\sigma = \sqrt{\frac{5}{54}} \frac{|f|}{\sqrt{1+Ri}}. \tag{5.12}$$

where $Ri = N^2 f^2 / M^4$ is the balanced Richardson number and $N^2 = |\partial b/\partial z|$ is the buoyancy frequency. The geostrophically adjusted front oscillates about a state with $Ri \simeq 1$ (Fox-Kemper et al., 2008; Tandon and Garrett, 1994). In particular, we find that $Ri \approx 1-6$ when $Ro_0 = 4, 8, 16$ after turbulence from the initial collapse has died down. The dashed line in figure 5.4 shows the growth rate when $Ri = 1$ and confirms that the order of magnitude estimate works relatively well despite the different basic state employed in our work compared to Fox-Kemper et al. (2008); Stone (1966). When $Ro_0 = 0.25$, the growth rate is noticeably slower, and it is not clear why this is the case. We speculate that the slower growth may be due to non-hydrostatic or viscous effects.

Since our simulations apply free-slip and adiabatic boundary conditions at the top and bottom of the domain, there are no boundary forcing terms in the TKE budget. The volume averaged, $\langle\cdot\rangle_V$, TKE evolves according to

$$\frac{\mathrm{d}\langle \mathrm{TKE}\rangle_V}{\mathrm{d}t} = \underbrace{\left\langle -\overline{u_i'u_j'}\frac{\partial \overline{u}_i}{\partial x_j}\right\rangle_V}_{P} + \underbrace{\langle w'b'\rangle_V}_{B} - \underbrace{\frac{Ek}{\Gamma_0}\left\langle \frac{\partial u_i'}{\partial x_j}\frac{\partial u_i'}{\partial x_j}\right\rangle_V}_{\varepsilon_t}. \tag{5.13}$$

There are three significant sources (or sinks, depending on sign) of TKE in this system: the buoyancy flux, production and dissipation. Here, B is the buoyancy flux, which represents the transfer of energy from PE to TKE, ε_t is the volume-averaged TKE dissipation rate, and P is the production, which converts energy from the mean flow into TKE. The production, P, can be expanded into the vertical shear production component (P_v), horizontal shear production component (P_h), and strain production component (P_s):

$$\begin{aligned} P = &\underbrace{\left\langle -\overline{u'w'}\frac{\partial \overline{u}}{\partial z}\right\rangle_V + \left\langle -\overline{v'w'}\frac{\partial \overline{v}}{\partial z}\right\rangle_V}_{P_v} + \underbrace{\left\langle -\overline{v'u'}\frac{\partial \overline{v}}{\partial x}\right\rangle_V + \left\langle -\overline{w'u'}\frac{\partial \overline{w}}{\partial x}\right\rangle_V}_{P_h} \\ &+ \underbrace{\left\langle -\overline{u'u'}\frac{\partial \overline{u}}{\partial x}\right\rangle_V + \left\langle -\overline{w'w'}\frac{\partial \overline{w}}{\partial z}\right\rangle_V}_{P_s}. \end{aligned} \tag{5.14}$$

Figure 5.5 shows the temporal evolution of the volume averaged horizontal shear, strain, and buoyancy production terms for cases with $Ro_0 > Ro_c$. When $Ro_0 = 8$ and $Ro_0 = 16$, we observe a peak in the horizontal shear production, closely followed by a peak in the vertical shear production of a comparable magnitude. The non-uniform cross-frontal structure prompts a fast and energetic transition into three-dimensional turbulence. Interestingly, the onset of horizontal shear production is slightly earlier and takes place over a longer period of time when $Ro_0 = 16$ compared to $Ro_0 = 8$, but the latter case shows a larger maximum value. Strain production is a significant contributor at early times and is similar in magnitude to the horizontal shear production. However, its contribution begins to wane once the vertical shear production reaches comparable values, and its maximum remains much smaller than both shear production terms. There are also times with a positive buoyancy flux, indicative of some convection, closely followed by negative buoyancy flux indicative of mixing of stratified waters. When $Ro_0 = 4$, there is only a small increase in horizontal shear production which does not trigger any vertical shear production. As previously observed, this case is associated with weak turbulence.

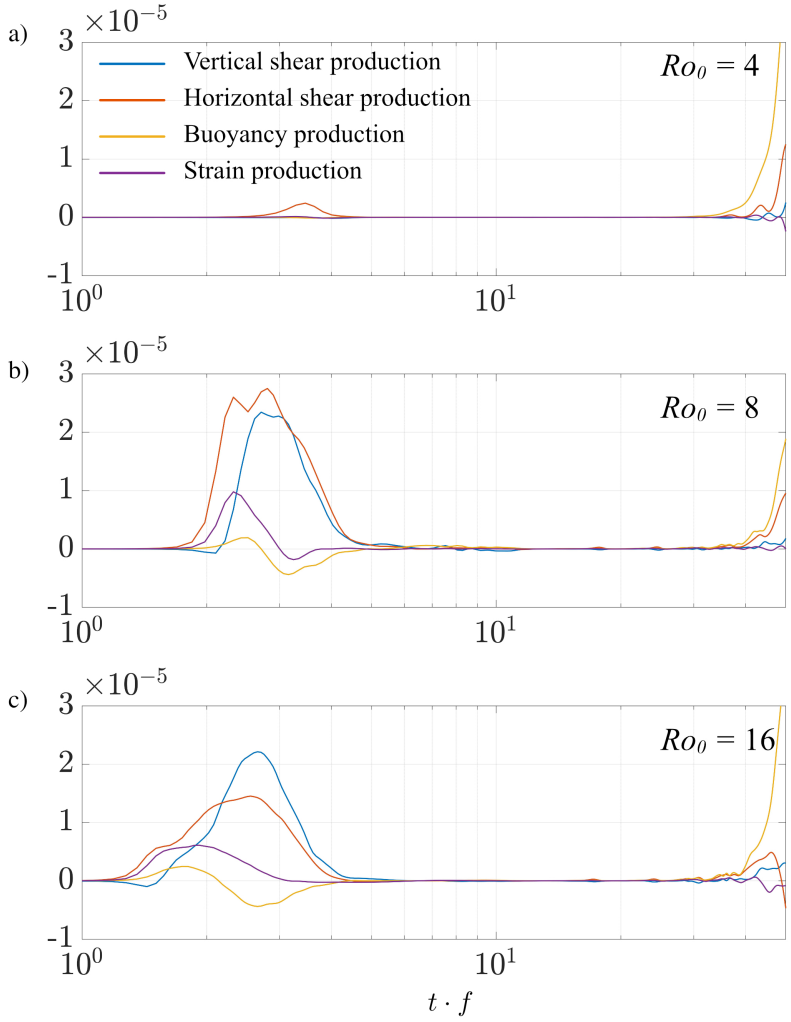

Fig. 5.5 Volume averaged vertical shear production, horizontal shear production, buoyancy production and shear production against logarithmic time for $Ro_0 = 4$ (a), $Ro_0 = 8$ (b) and $Ro_0 = 16$ (c).

Following the peak in horizontal and shear production, there is a period with little activity when the front is adjusting about the equilibrium state. The buoyancy flux exhibits inertial oscillations from around $tf = 6$ to $tf = 30$, but these are difficult to see since their amplitude is very small. Finally, a large increase in the buoyancy flux is consistent with baroclinic instability.

5.3.3 Estimating the mixing efficiency

The two major small-scale energy sinks in the system are TKE dissipation and mixing. Dissipated kinetic energy is entirely lost from the system, while mixing increases the potential energy at the expense of kinetic energy. In a region with constant background buoyancy gradient, N^2, the perturbation potential energy (PPE) is $b'^2/(2N^2)$ and its associated dissipation rate is

$$\chi \equiv \frac{Ek\,|\nabla b' \cdot \nabla b'|}{\Gamma_0\, Pr\, N^2}. \tag{5.15}$$

The TKE dissipation rate is

$$\varepsilon \equiv \frac{Ek}{\Gamma_0} \frac{\partial u_i'}{\partial x_j} \frac{\partial u_i'}{\partial x_j}. \tag{5.16}$$

An instantaneous, local mixing efficiency η can then be defined as

$$\eta \equiv \frac{\chi}{\chi + \varepsilon}, \tag{5.17}$$

which describes the proportion of energy lost by turbulence that leads to irreversible mixing.

Figure 5.6 shows that the region of the frontal collapse is associated with strong dissipation of TKE and PPE (again, the vertical slice is shown at time of peak TKE as in figure 5.2). At the edges of the front where ε is largest, the mixing efficiency is $\eta \sim 0.2 - 0.3$, which is comparable to the typical value $\eta \sim 0.2$ often reported based on observations in the ocean (Gregg et al., 2018). In contrast, the interior of the front is associated with much larger η values which approach 1. Here, ε is much smaller because the interior of the front is non-turbulent at this time, but χ remains large because the convergent flow associated with frontogenesis amplifies the pre-existing buoyancy gradients throughout the whole front.

Over time, χ remains relatively large but ε significantly decreases after the first inertial oscillation. Figure 5.7a (dashed lines) shows the volume integrated (over the whole domain) TKE dissipation rate, ε_V, and volume integrated PPE dissipation rate, χ_V, over the first two inertial periods for $Ro_0 = 16$. Until $tf = 5$, the TKE and PPE dissipation rates are comparable in magnitude with a slightly larger peak in TKE compared to PPE. We define the volume

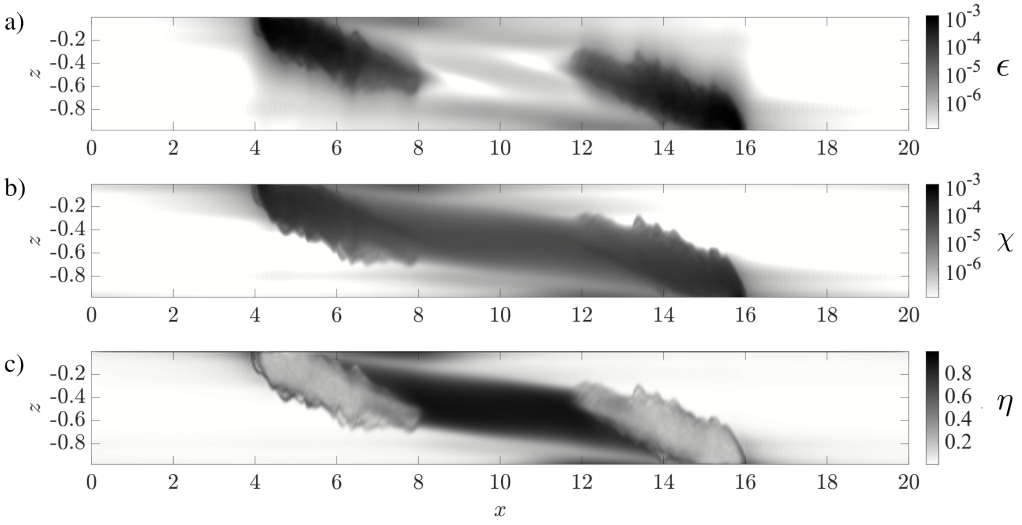

Fig. 5.6 Cross-front, vertical slices of along-front averaged turbulent kinetic energy (TKE) dissipation, ε (a), perturbation potential energy (PPE) dissipation, χ (b), and the mixing efficiency, η (c), at $tf = 2.8$ (time of peak TKE) for a simulation with $Ro_0 = 16$.

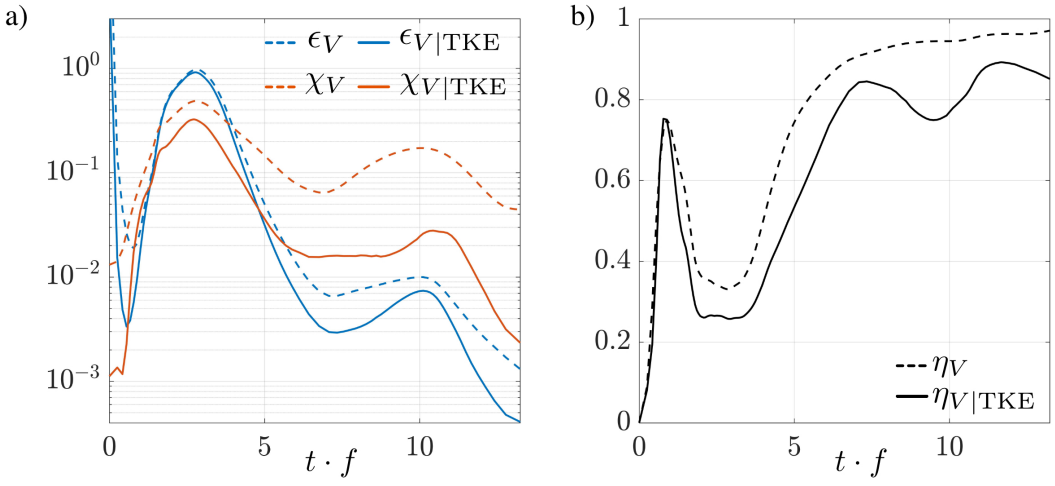

Fig. 5.7 (a) Time evolution of the volume integrated TKE dissipation rate, ε_V, and PPE dissipation rate, χ_V, in dashed lines, and the conditioned volume integrated TKE, $\varepsilon_{V|\mathrm{TKE}}$, and PPE dissipation, $\chi_{V|\mathrm{TKE}}$, in solid lines. (b) Mixing efficiency, η_V, in dashed lines and conditioned mixing efficiency, $\eta_{V|\mathrm{TKE}}$, in solid lines during the first two inertial periods for a simulation with $Ro_0 = 16$.

integrated mixing efficiency as

$$\eta_V \equiv \frac{\chi_V}{\chi_V + \varepsilon_V}. \tag{5.18}$$

Figure 5.7b shows a minimum in the mixing efficiency of $\eta_V = 0.33$, associated with the time when the TKE and PPE are maximum. Following this minimum, η_V, steadily increases to 1. The minimum value of η_V is larger than the instantaneous values of η that occur at the edge of the front because the interior (where χ is large) contributes to the volume integral and increases it.

To account for this, we define a second volume integral which aims to capture the turbulent part of the front only. We condition on the TKE, calculating the integral of ε and χ for all points whose TKE is above the 90th percentile, which we denote $\varepsilon_{V|\mathrm{TKE}}$ and $\chi_{V|\mathrm{TKE}}$. Similarly, the conditioned volume integrated mixing efficiency can be defined as

$$\eta_{V|\mathrm{TKE}} \equiv \frac{\chi_{V|\mathrm{TKE}}}{\chi_{V|\mathrm{TKE}} + \varepsilon_{V|\mathrm{TKE}}}. \tag{5.19}$$

The time evolution of these quantities is shown in solid lines in figure 5.7. When the flow is turbulent (e.g. between $tf = 2-4$), $\varepsilon_V \simeq \varepsilon_{V|\mathrm{TKE}}$ because the overall dissipation is dominated by the turbulent regions inside the front (see figure 5.6a). Most points outside the front have very small values of ε and contribute little to ε_V. In contrast, the PPE dissipation becomes smaller with the conditioned volume average because the interior of the front, which is characterised by values of χ comparable to those at the edges, are excluded from χ_V. This leads to a reduction in $\eta_{V|\mathrm{TKE}}$ which now has a minimum of 0.26, consistent with the local values of η inside the front (see figure 5.6c).

Soon after reaching a maximum during the first inertial period ($tf < 2\pi$), ε_V rapidly decreases. There is a second peak during the second inertial period, but this is much smaller than the first. In contrast, χ_V does not decrease nearly as dramatically during the second inertial period. The second inertial period is associated with less turbulence (and lower ε) but strong buoyancy gradients (so high χ) as the front adjusts. Although ε_V and $\varepsilon_{V|TKE}$ are relatively similar, χ_V and $\chi_{V|TKE}$ show a larger discrepancy, with much smaller values for $\chi_{V|TKE}$. Similar to at early times, this is because strong buoyancy gradients persist in the interior of the front during adjustment. Unlike η_V, $\eta_{V|\mathrm{TKE}}$ exhibits a minimum during the second inertial period with a value close to 0.78. This is significantly higher than the minimum in the first inertial cycle, consistent with the reduction in TKE but relatively strong buoyancy gradients.

We can define the time and volume integrated mixing efficiency, η^*, and the time and TKE-conditioned volume integrated mixing efficiency, η^*_{TKE}, as

$$\eta^* \equiv \frac{\widetilde{\chi_V}^t}{\widetilde{\chi_V}^t + \widetilde{\varepsilon_V}^t}, \quad \eta^*_{\mathrm{TKE}} \equiv \frac{\widetilde{\chi_{V|\mathrm{TKE}}}^t}{\widetilde{\chi_{V|\mathrm{TKE}}}^t + \widetilde{\varepsilon_{V|\mathrm{TKE}}}^t}, \tag{5.20}$$

where $\widetilde{\cdot}^t$ denotes a time average over the first two inertial periods. When $Ro_0 = 16$, we find that $\eta^* = 0.44$ and $\eta^*_{\mathrm{TKE}} = 0.30$. At lower Rossby numbers, $\eta^* = 0.61$ and $\eta^*_{\mathrm{TKE}} = 0.45$ when $Ro_0 = 8$, and $\eta^* = 0.83$ and $\eta^*_{\mathrm{TKE}} = 0.69$ when $Ro_0 = 4$. In all cases $\eta^* > \eta^*_{\mathrm{TKE}}$ because the TKE-conditioned volume integral removes the influence of the central part of the front (where η is large, see figure 5.6). As the Rossby number decreases, the flow is less turbulent, and ε decreases, yielding larger values of η^* and η^*_{TKE}.

Figure 5.8 shows a joint probability density function (PDF) of along-front averaged ε and χ for three values of Rossby number. Here, the PDF of the along-front averaged ε and χ is calculated for all points during the first two inertial periods. For $Ro_0 = 16$, values of η are relatively constrained, with the peak largely remaining between 0.15 and 0.25 for large values of ε (figure 5.8). The highest density lies along $\eta = 0.25$ which matches the minimum of $\varepsilon_{V|\mathrm{TKE}}$. There is also a region of high density for small values of ε with $0.5 < \eta < 0.75$, which could be associated with mixing in the second inertial period, although η is smaller than the second minimum observed in figure 5.7. As Ro_0 decreases, the front is associated with less turbulence and so ε decreases, but χ remains relatively large (the PDF shifts rightwards and upwards). This leads to an increase in η, whose peak lies between 0.25 and 0.5 when $Ro_0 = 8$. Finally, the $Ro_0 = 4$ case is associated with even lower TKE dissipation rates and higher mixing efficiencies, but inhabits a less clear-cut region of the ε and χ parameter space.

We can partially explain the nearly constant η values in the $Ro_0 = 16$ case by evaluating the Froude number, $Fr = U/NL$ where U, L are, respectively, the characteristic velocity and the integral scale of the fluid. Studies suggest that at low Fr, η should asymptote to a constant with values between $0.3 - 0.5$ (Gregg et al., 2018; Maffioli et al., 2016). In our simulations, we find that $Fr = \mathscr{O}(10^{-1})$ in the frontal region for all simulations with $Ro_0 = 8, 16$. These low values are attainable because even though ε is relatively large in the regions of frontal collapse, N^2 is also large since stratification is maintained by the advection of light water over dense water. For $Ro_0 = 8$ and $Ro_0 = 16$, the values of η for large ε are consistent with low Fr stratified turbulence. For $Ro_0 = 4$, we find $Fr = \mathscr{O}(1)$, and the mixing efficiency is higher than expected. This may be due to either the higher Froude number, or small values of the buoyancy Reynolds number which lie around $Re_b \approx 10$. This is consistent with Maffioli

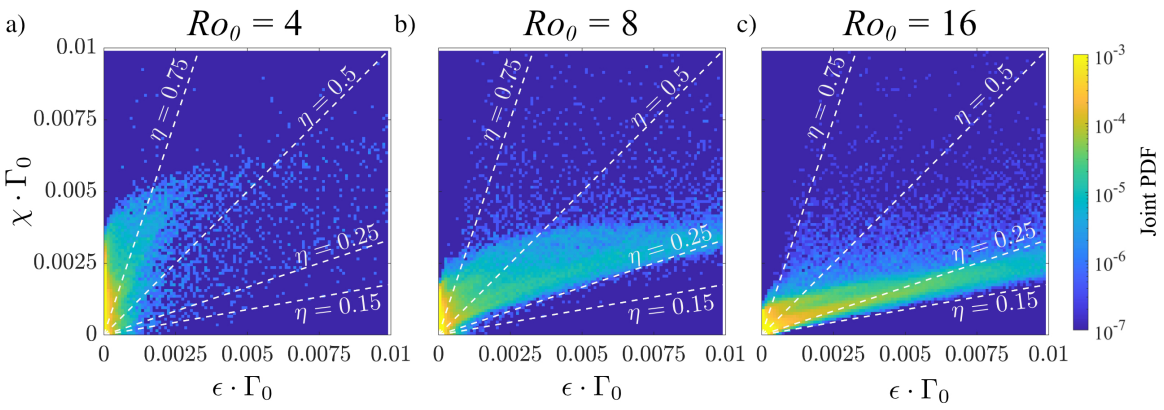

Fig. 5.8 Joint PDF of along-front averaged TKE dissipation, ε, and PPE dissipation, χ, for all points during the first two inertial periods for $Ro_0 = 4$ (a), $Ro_0 = 8$ (b) and $Ro_0 = 16$ (c). Dashed white lines show contours of constant η values.

et al. (2016) which suggests that the mixing coefficient only reaches constant values when $Re_b > 10$.

5.4 Conclusions and discussion

In this chapter, we used DNS to investigate a geostrophically adjusting front using an idealised initial condition similar to Ou (1984). The front is characterised by the dimensionless strength of the initial horizontal buoyancy gradient, $\Gamma_0 = M_0^2/f^2$, which we use to vary the balanced Rossby number, $Ro_0 = \zeta/f = \Gamma_0/\delta_0$. Besides allowing a more detailed analysis of the three-dimensional buoyancy and flow field, the DNS enabled us to investigate the important physical processes at play when a front collapses.

In accordance with Ou's critical value ($\beta_c = 2.6$) we find that when $Ro_0 > Ro_c$, a sharp buoyancy jump forms near the surface and bottom boundary. Turbulence is generated by shear instabilities at the sharpened front. TKE is generated first by horizontal shear production, closely followed by vertical shear production, with strain production and buoyancy production (convection) playing smaller roles. Thus the turbulence is three-dimensional and would not be captured by the more commonly used two-dimensional models of geostrophic adjustment (Ou, 1984; Tandon and Garrett, 1994).

We additionally showed that the mixing efficiency, η, can reach surprisingly large values when the TKE dissipation is small, but is constrained to a smaller, almost constant value when TKE dissipation is large in the region of frontal collapse. As the strength of the front decreases, so too does the TKE dissipation, yielding higher values of η (which are significantly higher than the commonly used 0.2 value). For $Ro_0 < Ro_c$, the initially unbalanced front undergoes

a period of geostrophic adjustment, but the front does not collapse and turbulence does not develop.

After several inertial periods, the evolution of the front is similar in the cases with different Ro_0. In particular, inertial oscillations are followed by baroclinic instability. During this period, the TKE grows exponentially in a manner consistent to the growth rate predicted in Fox-Kemper et al. (2008); Stone (1966).

It is important to keep in mind potential limitations of the current study. In particular, we used a highly idealised model which lacked any buoyancy flux or wind forcing. In the ocean, the surface heat flux and wind stress are often highly variable, and this variability could impact the frontal structure. We also assumed that there were no bottom boundary effects by employing a free-slip condition. In shallow seas, bottom stress and bottom roughness could generate turbulence even when $Ro_0 < Ro_c$. Future work could examine the geostrophically adjusting front and instabilities in the presence of these additional processes.

Appendix 5.A

We examine the influence of the horizontal grid resolution on flow dynamics for the most unstable front ($Ro_0 = 16$) where the density jump is greatest. The horizontal resolution, Δx, is varied from 0.04 to 0.01 while all other parameters in the simulations, including vertical resolution and across-front domain size, are kept the same. To achieve $\Delta x = 0.01$ without the simulation becoming prohibitively expensive, we reduce the along-front (y) domain size to dimensionless length $L_y = 1$. However, this is too small to capture all of the baroclinic modes which results in more erratic behaviour of statistics (since the along-front averages are computed over a much smaller region). To account for this, we compare statistics for simulations with a larger along-front length ($L_y = 7.5$), and along-front length $L_y = 1$ using an intermediary resolution, $\Delta x = 0.02$. In changing the along-front domain size, we also change the number of along-front grid points to ensure comparability.

The front collapses to the grid scale in all simulations except for the very highest resolution ($\Delta x = 0.01$). We compare the statistics in the energy budget for the highest resolution to a lower resolution case with $\Delta x = 0.02$ in which the front is not fully resolved. Both simulations have an along-front dimensionless length of $L_y = 1$ and all other parameters the same. Figure 5.9 shows the time-evolving, volume-averaged TKE and energy budget terms during the first two inertial periods, which are qualitatively and quantitatively similar for both resolutions. In particular, the maximum TKE lies just above 10^{-4}, and the magnitude of all production terms (including peak values) are comparable, despite the differences in oscillations caused by the small along-front length.

We next consider varying the resolution in simulations with a larger along-front domain size. In particular, we compare $\Delta x = 0.02$ (same as the lower resolution case above) with $L_y = 7.5$, with $\Delta x = 0.04$ with $L_y = 25$ (which we use throughout this study). Again, we use statistics in the energy budget as a point of comparison, which can be seen in figure 5.10. The horizontal resolution has little dependence on the statistics, apart from a slight discrepancy in the minimum value and decay of TKE, which is likely due to the smaller along-front length for $\Delta x = 0.02$ (see the even more drastic decay in figure 5.9).

Combining these two resolution tests, we ascertain that a resolution of $\Delta x = 0.04$ is high enough to capture the aspects of frontogenesis that we are interested in, whilst also allowing for baroclinic instability to develop. The $\Delta x = 0.04$ case is comparable to $\Delta x = 0.02$ when the along front length is large. When the along front length is reduced, the $\Delta x = 0.02$ case is comparable to $\Delta x = 0.01$ (in which the front is fully resolved).

Finally, figure 5.11 shows the ratio of the length-scale of the maximum buoyancy jump at the surface (calculated using $\min(\Delta b/b_x)$) and the cross-front grid spacing, Δx. Here, Δb is the change in buoyancy and $b_x = \partial b/\partial x$ is the cross-front buoyancy gradient. This statistic evaluates the number of grid points in the sharpest part of the surface front. The minimum number of grid points in the front increases by a factor of about 1.5 each time Δx doubles. When $\Delta x = 0.04$, there are only three grid points across the front at its sharpest point, but this is only for a very short period of time. Aside from the time of frontal collapse, the dynamics are sufficiently resolved throughout the simulation.

Appendix 5.B

Here, we outline the theory of geostrophic balance that motivates the choice of non-dimensionalisation using so-called 'geostrophic units' introduced in equation (5.2) which leads to the form of the Rossby number given in equation (5.9).

As in most adjustment models (Ou, 1984; Rossby, 1937; Tandon and Garrett, 1994), we assume that adjustment is achieved sufficiently rapidly that the process is considered inviscid and adiabatic. In the steady adjusted state, transverse motion is not allowed and we negelect the non-linear advective term in the horizontal momentum equations. This gives the typical geostrophic balance momentum equations as:

$$u_G = -\frac{1}{f}\frac{\partial p}{\partial y}, \tag{5.21}$$

$$v_G = \frac{1}{f}\frac{\partial p}{\partial x}. \tag{5.22}$$

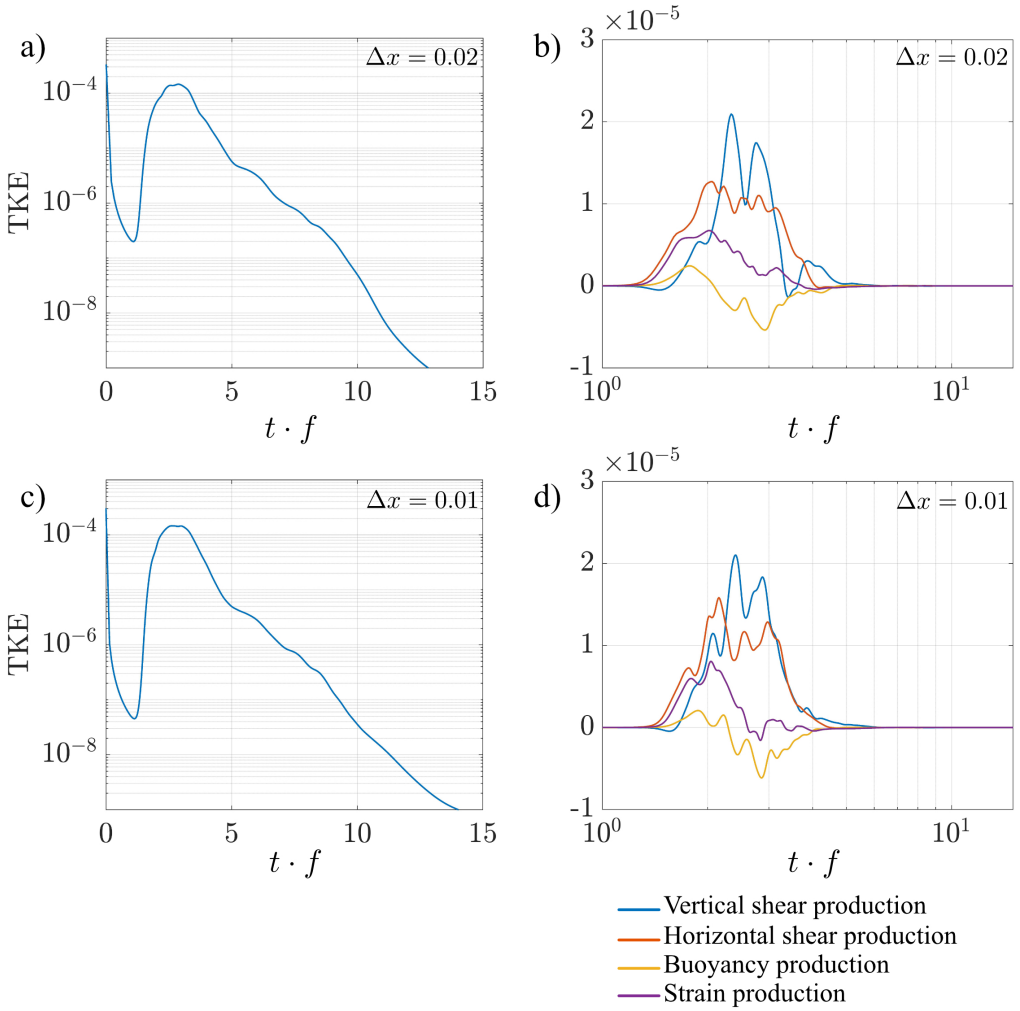

Fig. 5.9 Comparison of TKE (a,c) and energy production terms (b,d) for simulations with horizontal resolution $\Delta x = 0.02$ (a,b) and $\Delta x = 0.01$ (c,d). Both simulations have along-front length $L_y = 1$.

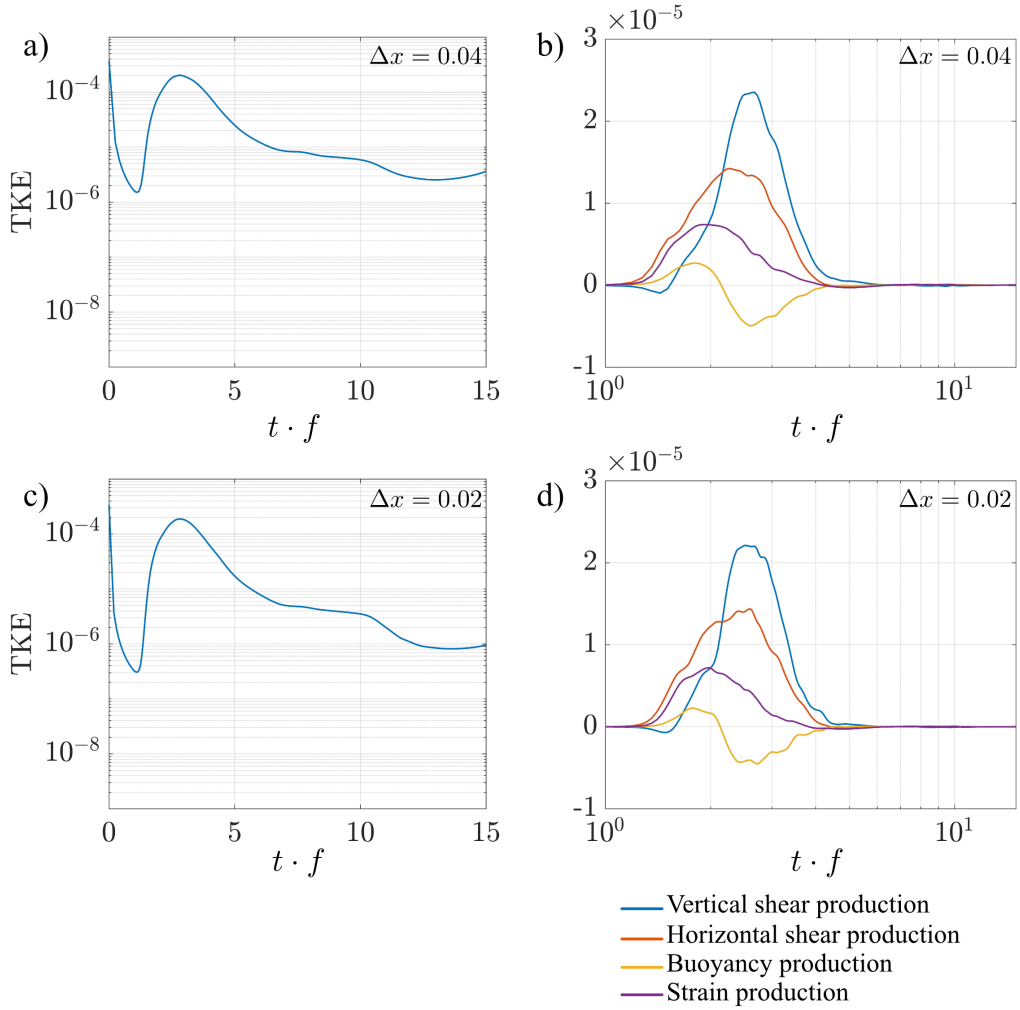

Fig. 5.10 Comparison of TKE (a,c) and energy production terms (b,d) for simulations with $\Delta x = 0.04$, $L_y = 25$ (a,b) and $\Delta x = 0.02$, $L_y = 7.5$ (c,d).

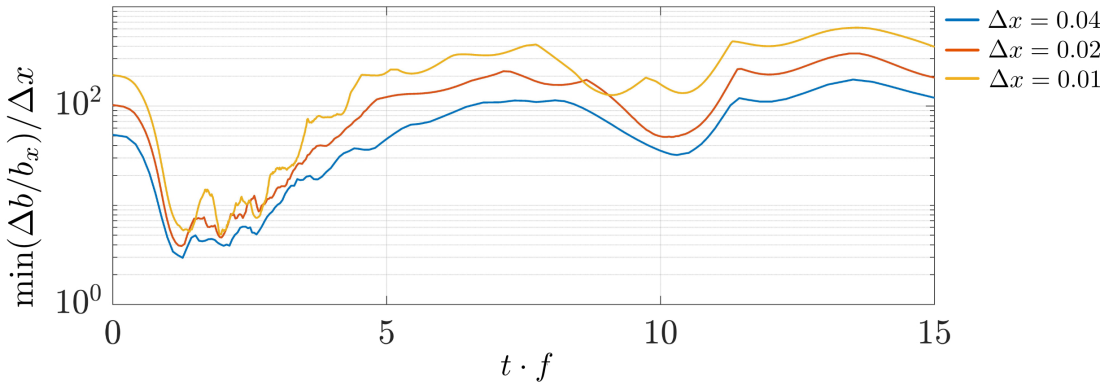

Fig. 5.11 Ratio characterising the number of grid points in the sharpest part of the surface front over time for varying Δx. Here, Δb is the change in buoyancy and $b_x = \partial b/\partial x$ is the cross-front buoyancy gradient.

Additionally, we employ the hydrostatic approximation where vertical accelerations are assumed to be negligible. This results in the vertical momentum equation simplifying to

$$\frac{\partial p}{\partial z} = b. \tag{5.23}$$

Combining the geostrophic and hydrostatic approximations results in thermal wind balance,

$$\frac{\partial u_G}{\partial z} = -\frac{1}{f}\frac{\partial b}{\partial y}, \tag{5.24}$$

$$\frac{\partial v_G}{\partial z} = \frac{1}{f}\frac{\partial b}{\partial x}. \tag{5.25}$$

The initial state of our frontal region is given in equation (5.5), where the characteristic width of the front is L_0 and the maximum initial horizontal buoyancy gradient is M_0^2. Inside the front, $\frac{\partial b}{\partial x} = M_0^2$ and $\frac{\partial b}{\partial y} = 0$. Substituting this into the equations describing the thermal wind balance and integrating results in the characteristic thermal wind velocity, where H is the depth of the fluid,

$$v_G = \frac{M_0^2}{f}\left(z - \frac{H}{2}\right) \tag{5.26}$$

We choose to non-dimensionalise our system such that the thermal wind velocity is unity, i.e. $[\mathbf{u}] = \frac{M_0^2 H}{f}$. Under this configuration, the Rossby number which is defined as $Ro_0 = \zeta/f$, can be rewritten as,

$$Ro_0 = \frac{\zeta}{f} = \frac{v_G/L_0}{f} = \frac{M_0^2 H}{L_0 f^2}. \tag{5.27}$$

Finally, combining this with the dimensionless parameters given in equation (5.6) yields $Ro_0 = \Gamma_0/\delta_0$.

It is worth noting that the model investigated by Ou (1984) uses a different non-dimensionalisation to that described above, whereby the horizontal length scales with the internal radius of deformation $\lambda = (\Delta bH)^{1/2}/f$ and the velocity scales with $f\lambda$. Ou (1984) varies a free parameter β which measures the steepness of the initial density transition. Re-dimensionalising their system and equating the two yields $Ro_0 = \beta^2/2$.

Chapter 6

Large eddy simulations of buoyant particles in a geostrophically adjusting front

6.1 Introduction

In chapter 5, we used direct numerical simulations (DNS) of an isolated front with a lateral density gradient (under the same configuration as Ou (1984)) to investigate frontogenesis in geostrophic adjustment, broadly motivated by the sharp density fronts observed in SUNRISE fieldwork. In this chapter, we consider the effect that density fronts have on the transport and accumulation of buoyant particles.

We continue in a similar vein to chapter 5, and use the geostrophic adjustment framework to model a highly idealised density front with a lateral density gradient, analagous to Ou (1984). The flow is initially unbalanced, which prompts a frontal circulation to develop and drive flow back to a geostrophically balanced state. The frontal circulation is typically characterised by upwelling in light waters and downwelling in dense waters. During periods of frontal intensification, downwelling is much stronger than the upwelling near the surface (and vice versa at the bottom boundary) owing to non-linearities (Hoskins, 1982).

Ou (1984) found that in the inviscid limit, for sufficiently large initial density gradients, convergence associated with the frontal circulation can produce singularities, drawing surface fluid particles into the interior. In this case, an equilibrium state does not exist. The simulations conducted in chapter 5 revealed that for very sharp fronts, instabilities and shear and strain production generated turbulence along the front. The turbulence and frontal

circulation are associated with strong vertical velocities and provides an ideal setting for studying buoyant particle subduction and accumulation.

Here, we take a similar approach but use large eddy simulations (LES) to model an initially unbalanced front under geostrophic adjustment. LES resolve the large turbulent motions that govern the horizontal and vertical transport of particles, and are less computationally expensive than DNS. Whereas the DNS in chapter 5 solved non-dimensional equations, here we use LES to solve dimensional equations with parameters that match typical conditions in the ocean. Our decision to use dimensional parameters in this study allows us to consider buoyant particles with physically relevant vertical slip velocities. We model buoyant particles using a large number of three-dimensional Lagrangian particles, each with a constant slip velocity (which is equivalent to a constant particle size and density) and focus on a front with a large Rossby number, for which an analytical solution doesn't exist. Although the model is highly idealised, our goal here is to use controlled conditions and improve our understanding of the physical mechanisms at play rather than replicating a completely realistic front.

The aim of this study is to explore how the frontal circulation and the turbulent flow affect the transport and accumulation of buoyant particles. Since the work in chapter 5 analysed the frontogenesis mechanism and energy budget in depth, we focus on the particle distribution. Below, we introduce the specific set up of the LES and Lagrangian particles in section 6.2. We then provide a qualitative and quantitative description of particle transport for a range of buoyant particles in section 6.3. We conclude in section 6.4 with an overview of the results and implications for future studies.

6.2 Setup and numerical methods

Here, we closely follow the setup of chapter 5 and Ou (1984) to model a geostrophically adjusting front in the upper ocean. Specifically, we consider a finite width frontal region initialised with no initial velocity and a horizontal buoyancy gradient with finite lateral extent. Without loss of generality, we take the buoyancy gradient to be aligned with the x-direction,

$$b|_{t=0} = \frac{\Delta b}{2} \tanh\left(\frac{x}{L_0}\right), \quad \mathbf{u}|_{t=0} = \mathbf{0}, \tag{6.1}$$

where $\Delta b = 2M_0^2 L_0$, $M_0^2 = 1.6 \times 10^{-7}$ s^{-2} is the maximum initial horizontal buoyancy gradient, and $L_0 = 100$ m is the initial frontal width. This initial condition is highly idealised but could represent conditions following a storm where buoyancy is well mixed in the vertical and a lateral buoyancy gradient still exists (Ferrari and Rudnick, 2000; Price, 1981). There is

no variation in the initial buoyancy field in the vertical, so the vertical buoyancy gradient is zero, i.e. $N_0^2 \equiv |\partial b/\partial z| = 0$.

We use LES to solve a low-pass filtered version of the non-hydrostatic incompressible Boussinesq Navier-Stokes equations in terms of the filtered velocity $\mathbf{u} = (u, v, w)$, filtered pressure p and fluid buoyancy b,

$$\frac{\partial \mathbf{u}}{\partial t} + \mathbf{u} \cdot \nabla \mathbf{u} + \mathbf{f} \times \mathbf{u} = -\frac{1}{\rho_0} \nabla p + \nu \nabla^2 \mathbf{u} - \nabla \cdot \boldsymbol{\tau} + b\, \widehat{\mathbf{z}}\,, \tag{6.2}$$

$$\nabla \cdot \mathbf{u} = 0\,. \tag{6.3}$$

In the momentum equation (6.2), $\mathbf{f} = (0, 0, f)$ is the Coriolis force, ρ_0 is the reference density, $\widehat{\mathbf{z}}$ is the unit vector in the vertical direction, ν is the molecular viscosity, and $\boldsymbol{\tau}$ is the sub-grid scale stress tensor.

We assume a linear equation of state and treat the fluid buoyancy using a single scalar variable. The total buoyancy field, b is decomposed into a constant background gradient, and departures from this gradient, $b^\dagger$,

$$b(x, y, z, t) = b^\dagger(x, y, z, t) + \frac{\Delta b}{L_x} x. \tag{6.4}$$

where L_x is length of the domain in the x direction. Under this decomposition, the linear equation of state solved by the LES is:

$$\frac{\partial b^\dagger}{\partial t} + \mathbf{u} \cdot \nabla b^\dagger + u \frac{\Delta b}{L_x} = \kappa_b \nabla^2 b^\dagger + \nabla \cdot \boldsymbol{\lambda}. \tag{6.5}$$

In the buoyancy equation (6.5), $\boldsymbol{\lambda}$ is the sub-grid scale scalar flux. Both $\boldsymbol{\tau}$ and $\boldsymbol{\lambda}$ are calculated using the constant Smagorinsky model (Deardorff, 1973, 1970; Lilly, 1967; Smagorinsky, 1963). We apply periodic boundary conditions to $b^\dagger$ in the horizontal directions which ensures that the buoyancy difference across the domain remains constant, i.e. $b(L_x, y, z, t) - b(0, y, z, t) = \Delta b$. We also apply periodic boundary conditions to the velocity field in both horizontal directions. At the top and bottom of the domain, free slip boundary conditions are applied to the velocity field, and no-flux boundary conditions are applied to b. Planetary rotation is included with a Coriolis parameter of $f = 10^{-4}$ s^{-1}. This gives an inertial period of about 18 hours, and we run the simulations for 40 hours to cover two inertial periods. The velocity is seeded with random white noise with an amplitude of 10^{-4} m/s. The molecular viscosity is $\nu = 10^{-6}$ m^2/s, and molecular diffusivity is $\kappa_b = 10^{-6}$ m^2/s, although both are small compared to the sub-grid scale terms and do not directly influence the model results.

The vertical depth of the simulations is 100 m. Although this is deeper than many mixed layers where frontogenesis occurs, it enables us to achieve a small aspect ratio of the front which is crucial for maximising the Rossby number (see below). The computational domain is $L_x = 2000$ m in the cross-front direction, which is large enough to account for frontal slumping (the deformation scale is $L_d = HM^2/f^2 = 1600$ m). In the along-front direction, the domain size is 750 m which allows turbulence to develop along the front. Our focus is limited to particle behaviour at early times, and we do not capture the baroclinic instability that develops later on.

This frontal system can be fully described by four dimensionless parameters (Wienkers et al., 2021a,b),

$$\Gamma_0 \equiv \frac{M_0^2}{f^2}; \quad \delta_0 \equiv \frac{L_0}{H}; \quad Ek \equiv \frac{\nu}{H^2 f}; \quad Pr \equiv \frac{\nu}{\kappa}, \tag{6.6}$$

where a subscript 0 indicates the initial value of an evolving quantity. In terms of these, the balanced Rossby number can be defined as

$$Ro_0 \equiv \frac{\zeta}{f} = \frac{HM_0^2}{f} \cdot \frac{1}{L_0} \cdot \frac{1}{f} = \frac{\Gamma_0}{\delta_0}, \tag{6.7}$$

which characterises the relative importance of the vertical vorticity compared to the planetary vorticity. The critical Rossby number above which a discontinuity forms is $Ro_c = 3.5$ (see chapter 5, Ou (1984)). The dimensional parameters chosen for the LES are such that $\Gamma_0 = 16$, $\delta_0 = 1$ and $Pr = 1$ which coincides with $Ro_0 = 16$ (the largest Ro_0 considered in chapter 5).

The resolved fields are discretised on a grid with 1024 points in the cross-front direction, 384 points in the along-front direction and 65 points in the vertical direction. This gives a horizontal grid spacing of 2.0 m and a variable vertical grid spacing between 0.90 m and 2.04 m with higher resolution near $z = 0$ m. The aspect ratio of the computational grid is about 2:1 at the surface and 1:1 near the bottom which falls in the desirable range for LES (Vreugdenhil and Taylor, 2018).

Derivatives in the horizontal directions are calculated using a pseudospectral method, whilst vertical derivatives are approximated using second-order finite differences. The equations are time-stepped using an implicit Crank–Nicolson method for the viscous and diffusive terms and a third-order Runge–Kutta method for all other terms. Further details of the numerics can be found in Taylor (2008). The sub-grid scale terms are modelled with the constant Smagorinsky model. We also tested the anisotropic minimum dissipation (AMD) model (Abkar et al., 2016; Rozema et al., 2015; Vreugdenhil and Taylor, 2018) but found that large amounts of numerical noise developed in the first inertial period when the front collapsed to a small width. In both cases, the behaviour of particles was qualitatively similar,

and to reduce noise, we choose to use the constant Smagorinsky model. For more details please refer to appendix 6.A.

We model three-dimensional, non-inertial, Lagrangian buoyant particles which evolve according to the Maxey-Riley equations (Maxey and Riley, 1983) with all terms except for flow advection and Brownian motion neglected (Chamecki et al., 2019). The particle equations of motion are

$$\mathbf{x}_p(t+dt) = \mathbf{x}_p(t) + \mathbf{u}(\mathbf{x}_p,t)dt + \mathbf{x}_{sgs}(\mathbf{x}_p,t) + w_s\widehat{\mathbf{z}} \ , \tag{6.8}$$

$$x_{sgs,i} = \frac{\partial \nu_{sgs}}{\partial x_i}(\mathbf{x}_p,t)\,dt + (2(\nu_{sgs}(\mathbf{x}_p,t))_+)^{\frac{1}{2}} d\xi_i \ , \tag{6.9}$$

where $\mathbf{u}$ is the resolved velocity interpolated at the particle position, w_s is the constant slip velocity and $\mathbf{x}_{sgs}$ is the displacement due to sub-grid scale motion. In equation (6.9), the subscript i indicates the spatial dimension, ν_{sgs} is the sub-grid scale viscosity interpolated at the particle position, $d\xi_i$ is Gaussian white noise with variance dt, and $(\cdot)_+ = \max(\,\cdot\,,0)$. The appearance of the sub-grid scale viscosity in equation (6.9) helps account for the influence of unresolved turbulence on particle motion (Liang et al., 2018). We interpolate the velocity onto the particle position using cubic B-splines (Hinsberg et al., 2012) in the horizontal direction and linear interpolation in the vertical direction, and time-step the particle position using the third-order Runge-Kutta method alongside the main LES code. Periodic conditions are applied in the horizontal directions, and particles are prevented from rising above $z = -0.5$ m to stop them becoming trapped on the top/bottom (where $w = 0$ m/s). In reality, we expect missing physical processes such as breaking surface waves to pull buoyant particles off the surface.

Typically, the slip velocity for buoyant particles falls between $w_s = 0.005 - 0.025$ m/s for microplastics (Kukulka et al., 2012), $w_s \simeq 0.008 - 0.3$ m/s for oil droplets (Chor et al., 2018a) and $0.0003 - 0.002$ m/s for phytoplankton (Noh et al., 2006; Tiselius and Kiørboe, 1998). In this study, we consider particles with five different slip velocities which span the observed range, $w_s = 10^{-4}, 10^{-3}, 5\times10^{-3}, 10^{-2}, 10^{-1}$ m/s. For each slip velocity, we simulate 3000 particles that are initially randomly distributed 0.5 m below the surface.

6.3 Results

We begin with a qualitative description of the flow and the vertical and horizontal distribution of particles in the first two inertial periods of our simulation in section 6.3.1. We then analyse particle transport and investigate how particles move between light and dense waters in section 6.3.2. Throughout our analysis, we primarily focus on three particle slip velocities,

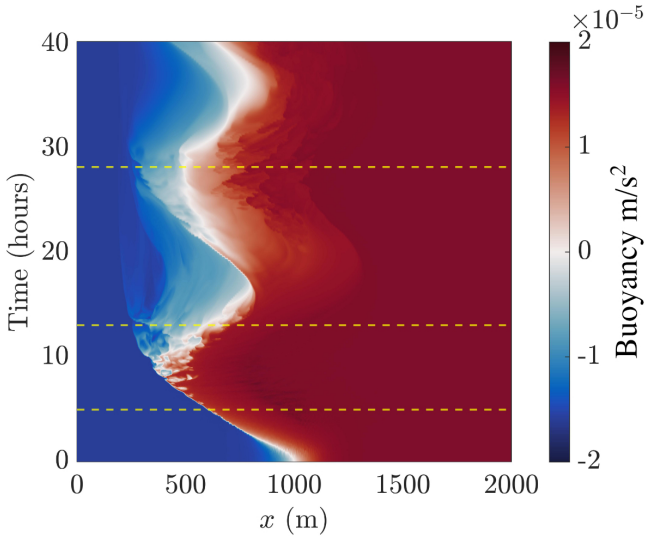

Fig. 6.1 Cross-frontal evolution of the buoyancy field at $y = 0$ m, $z = 0$ m as a function of cross-front distance (x) and time. Dashed yellow lines indicate times used for horizontal and vertical slices below.

$w_s = 10^{-4}$ m/s, $w_s = 10^{-3}$ m/s and $w_s = 10^{-2}$ m/s which we refer to as slow rising, medium rising and fast rising particles, respectively. The other two slip velocities ($w_s = 5 \times 10^{-3}$ m/s and $w_s = 10^{-1}$ m/s) display qualitatively similar behaviour to $w_s = 10^{-2}$ m/s.

6.3.1 Qualitative description of the flow and the distribution of buoyant particles

Figure 6.1 shows the evolution of the surface buoyancy field over time. The front exhibits near-inertial oscillations with a time-scale close to the inertial period (18 hours). The initial front width is 100 m, but as the front slumps within the first few hours, the surface front converges to scales of only a few metres. This steepens the buoyancy gradient resulting in an abrupt buoyancy jump, analogous to the frontal singularity predicted by Ou (1984). In chapter 5, we showed that frontogenesis induces turbulence at the edge of the front, and that the vertical and horizontal shear production and strain production are the main contributors in the energy budget. This is consistent with the turbulence which develops at around $t = 7$ hours in the LES. After half an inertial period, the turbulent front has travelled about 600 m from its starting location (which agrees relatively well with the deformation scale) before the flow reverses. Interestingly, some small regions with sharp density gradients are left behind as the main front retreats, for example at $x = 300$ m.

The second inertial period is characterised by similar dynamics but with buoyancy gradients that are not as steep as in the first inertial period. Again, the front slumps and sharpens, and at $t = 20$ hours, convergence associated with the frontal circulation causes a splitting of the main front into two distinct fronts. Both fronts are associated with instabilities and enhanced turbulence. Interestingly, the front on the light (right) side retreats, sharpens and readjusts, but the front on the dense (left) side weakens and does not return to its initial position. This is significant for particles that accumulate along the dense front, and are then left behind in relatively quiescent waters. Below, we show visualisations of the flow field and particle distribution for three different times in the simulation which are marked in figure 6.1 for reference: $t = 5$ hours (when the front is sharpening), $t = 13$ hours (when the front is retreating in the first inertial period) and $t = 28$ hours (when the front is on the brink of retreating in the second inertial period).

Horizontal cross-sections of the surface buoyancy field (figure 6.2) illustrate the onset of small-scale instabilities and the development of turbulence. At $t = 5$ hours, the front is very sharp and we see small, $\sim$ 1m instabilities along the front. These are similar to the instabilities observed in DNS and described in chapter 5. As the front retreats ($t = 13$ hours), the instabilities are stretched and break apart, which widens the frontal region. As seen in figure 6.1, there is a sharp buoyancy jump left behind on the dense side when the front retreats (at around $x = 250$ m). Finally, when the front sharpens a second time, horizontal convergence causes two distinct fronts to emerge which are visible at $t = 28$ hours. One is located on the dense side at $x = 250$ m, and one is located between light and dense water at $x = 500$ m, with some turbulent structures on the light side of both fronts (between $x = 600$ m and $x = 1000$ m).

Subduction occurs during phases of frontal intensification. If the particle slip velocity is smaller than the magnitude of the local downwards vertical velocity (i.e. $w_s + w < 0$) then the particle will move downwards into the interior. During intensification in the first inertial period, the vertical velocity reaches a minimum of -0.015 m/s at $z = -0.5$ m (where particles are initialised) which is strong enough to submerge the slow, medium and fast rising particles. The extent of subduction and whether particles subsequently rise or stay submerged depends on the slip velocity. This is illustrated in figure 6.3, which shows vertical cross-sections of the vertical velocity and the vertical particle distribution for $t = 5$ hours, $t = 13$ hours and $t = 28$ hours with the buoyancy contours $b = -10^{-5}$ m/s^2, $b = -5 \times 10^{-6}$ m/s^2, $b = 0$ m/s^2, $b = 5 \times 10^{-6}$ m/s^2, and $b = 10^{-5}$ m/s^2 marked in black.

At $t = 5$ hours, strong downwelling occurs on the dense side of the surface front with weak upwelling near the surface on the light side of the front (and similarly at the bottom we have strong upwelling and weak downwelling since our model is symmetric), which

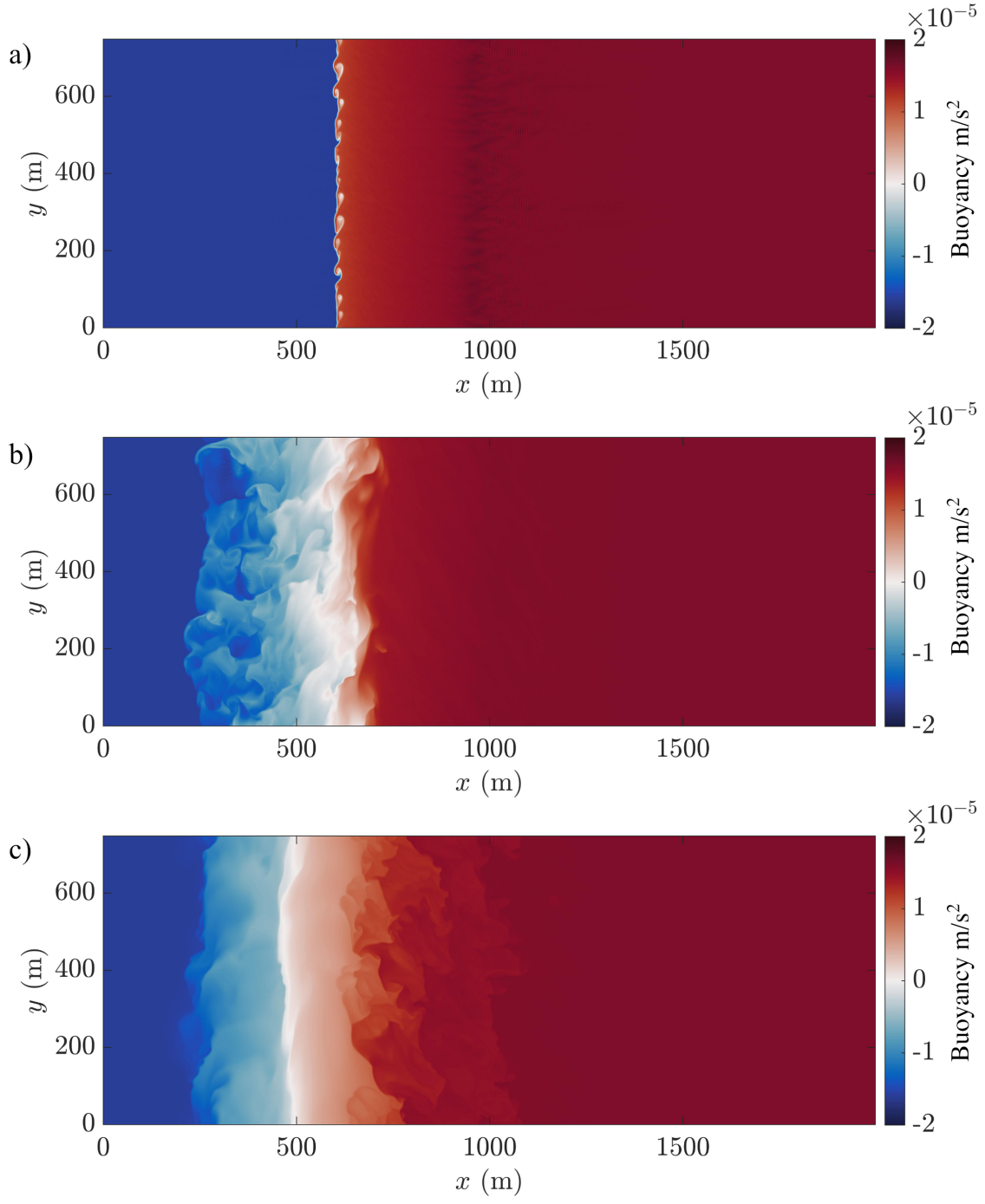

Fig. 6.2 Horizontal slices of the buoyancy field at $z = 0$ m. We show three different times in the simulation: $t = 5$ hours (a), $t = 13$ hours (b) and $t = 28$ hours (c).

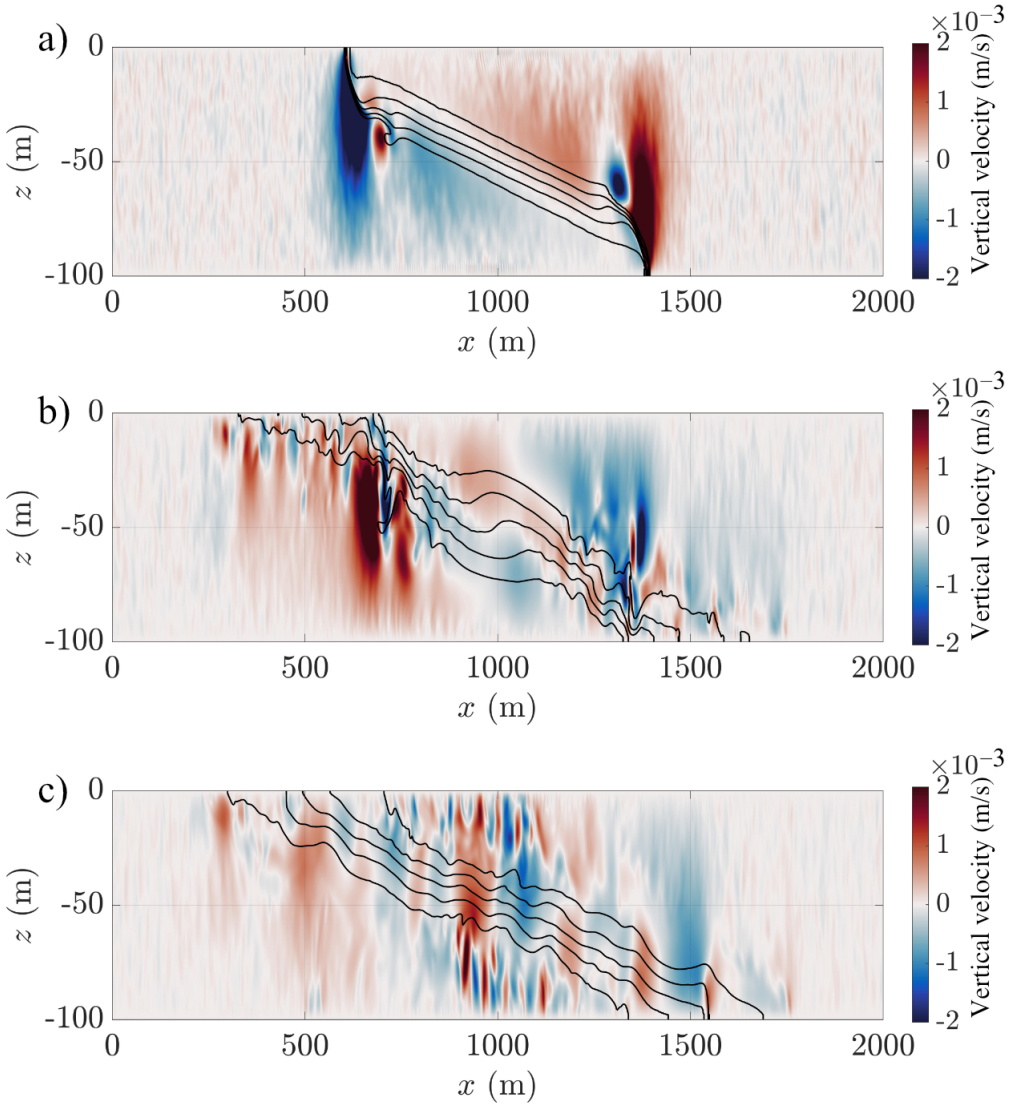

Fig. 6.3 Vertical slices of the vertical velocity field at $y = 0$ m. Buoyancy contours at levels $b = -10^{-5}, -5\times10^{-6}, 0, 5\times10^{-6}, 10^{-5}$ m/s^2 are shown in black. We show three different times in the simulation: $t = 5$ hours (a), $t = 13$ hours (b) and $t = 28$ hours (c).

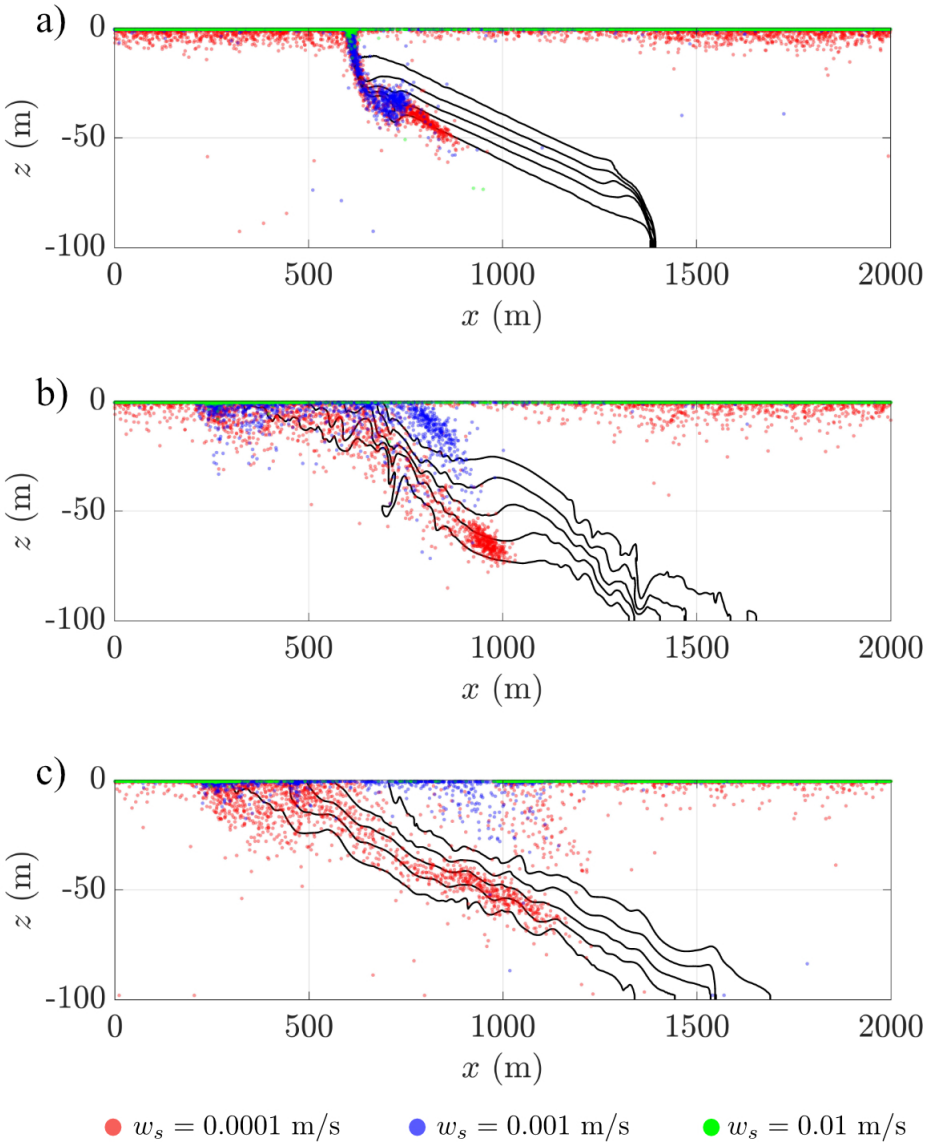

Fig. 6.4 Vertical profiles of particle distribution with $w_s = 10^{-4}$ m/s (red), $w_s = 10^{-3}$ m/s (blue) and $w_s = 10^{-2}$ m/s (green). Buoyancy contours at levels $b = -10^{-5}, -5\times10^{-6}, 0, 5\times10^{-6}, 10^{-5}$ m/s^2 are shown in black. are shown in black. We show three different times in the simulation: $t = 5$ hours (a), $t = 13$ hours (b) and $t = 28$ hours (c).

characterises the frontal circulation. Strong downwelling persists up to depths of -50 m where fluid is weakly stratified, but we see some overturnings developing along the buoyancy contours as the front becomes turbulent. The slow (red) and medium (blue) rising particles are both subducted on the dense side of the front along the bottom-most buoyancy contour where the downwelling is strongest, with slow rising particles populating greater depths (since $w_s + w$ will be comparatively smaller for slow rising particles). Some of the medium rising particles are caught in the small region of upwelling and begin to rise back to the surface, but most slow rising particles are sufficiently subducted to escape the overturning. Although difficult to see, the fast rising particles (green) are subducted down by a few metres at the head of the front. Consistent with the minimum vertical velocity, the particles with a higher slip velocity ($w_s = 10^{-1}$ m/s, not shown) all remain at the surface.

The frontal collapse prompts the development of three-dimensional turbulence along isopycnals, visible as sharp 'kinks' in the buoyancy contours (figure 6.4b). This manifests as regions of positive and negative vertical velocity. At $t = 13$ hours, the vertical velocity fluctuates between positive and negative values with a maximum of 0.015 m/s and a minimum of -0.013 m/s, and a particularly large overturning event can be seen at $x = 700$ m on the dense side. When particles enter a region with $w_s + w > 0$, they begin to rise towards the surface. Areas of downwelling can pull particles back towards the interior, but only if they have not already risen out of the turbulence. The slow rising particles remain subducted in the front, with a large cluster -70 m below the surface, where the flow is still relatively quiescent (here the vertical velocity has a minimum of -0.0005 m/s). In contrast, the medium rising particles are caught up in turbulent overturnings and as a result, have ascended above the 10^{-5} m/s^2 buoyancy contour on the warm side of the front, where they continue to rise towards the surface.

In the second inertial period, the front is less turbulent and vertical velocities are weaker. At $t = 28$ hours, the front is beginning to retreat and the vertical velocity fluctuates between a maximum of 0.003 m/s and a minimum of -0.002 m/s inside the front. At this time, the slow rising particles remain submerged within the front, although they have risen to the -5×10^{-6} m/s^2 buoyancy contour. The strongest vertical motions are located at the surface amongst the turbulent features on the light side of the surface front (figure 6.3b) with a minimum vertical velocity of -0.004 m/s. This is enough to submerge the slow and medium rising particles to depths of -40 m between the 1.4×10^{-5} m/s^2 and 1.5×10^{-5} m/s^2 buoyancy contours (not shown). There is also evidence of subduction of medium rising particles at the edge of the front at $x = 250$ m and the front at $x = 500$ m, where there are signs of downwelling, although only to relatively shallow depths.

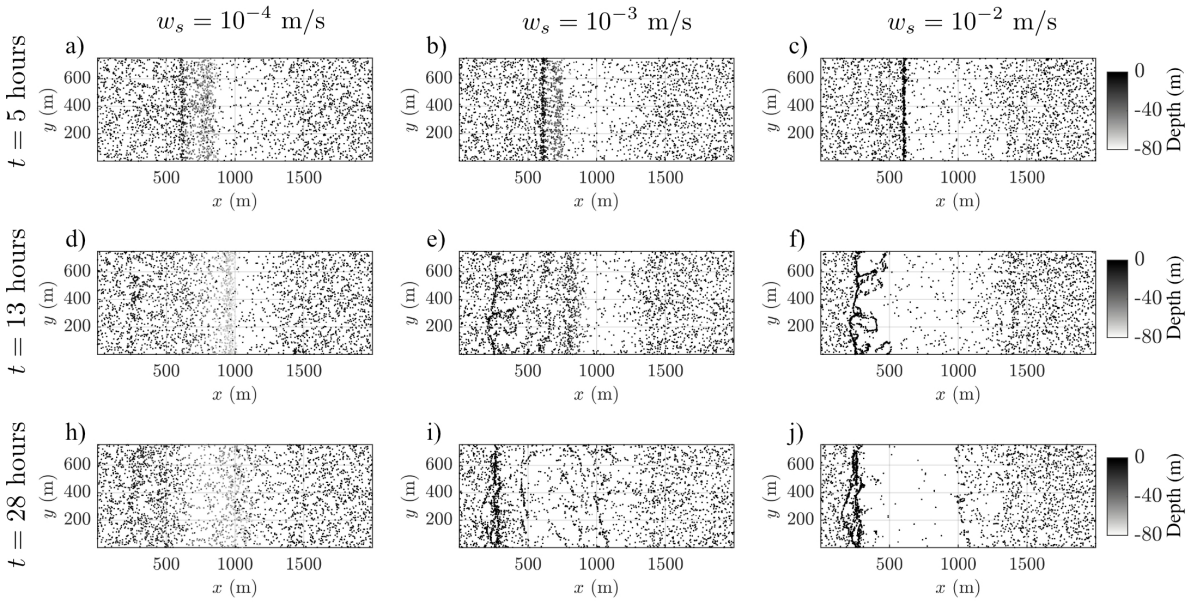

Fig. 6.5 Horizontal particle distribution for $w_s = 10^{-4}$ m/s (a,d,h), $w_s = 10^{-3}$ m/s (b,e,f) and $w_s = 10^{-2}$ m/s (c,f,j) with particles coloured by depth. We show three different times in the simulation: $t = 5$ hours (a,b,c), $t = 13$ hours (d,e,f) and $t = 28$ hours (h,i,j).

The horizontal distribution of particles strongly depends on the particle slip velocity. Figure 6.5, shows horizontal cross sections of the particle position coloured by particle depth. At $t = 5$ hours, convergence drives particles into the sharpening surface front, and the particles move with the front as it slumps to the left. This leads to a narrow line of enhanced particle concentration. Later, we show that the narrow line twists and turns with the small-scale instabilities (figure 6.8) which plays a significant role in transporting particles outside the front. The line of accumulation is more pronounced for the faster rising particles, which are largely confined to the surface and the slow and medium rising particles subduct below the surface (indicated using lighter shades of grey). In all cases, particles are uniformly distributed at the surface outside the front.

As the front retreats ($t = 13$ hours), narrow rows of medium and fast rising particles are pulled away from the front in streaks which are linked to the motions generated by frontal instabilities. For example, the hook-like formation of particles at $y = 200$ m in figure 6.5e,f can be directly matched to a feature of a similar shape in figure 6.2b. A significant number of particles remain in a narrow vertical line, whose location coincides with the large density jump on the left-hand side (figure 6.2b). Again, this behaviour is most prevalent for the fast rising particles which stay at the surface. Surprisingly, very few particles at the surface retreat with the front, and most remain on the dense side of the front, leaving a large void

of particles between $x = 500$ m and $x = 1200$ m. Below, we outline a physical mechanism which allows particles to stay concentrated even as the surface flow reverses, and in section 6.3.2, we qualitatively and quantitatively describe the movement of particles between fluids of different density during frontal adjustment.

Buoyant particles initially accumulate along the interface of the light and dense fluids where the density gradient is sharpest (and convergence is strongest). As the front adjusts, light fluid moves leftwards above dense fluid. Horizontal shear production (see chapter 5) contributes to the formation of small-scale instabilities which distort the front and allows for mixing of pockets of dense, slow-moving water into light, fast-moving water, sometimes carrying particles with them (figure 6.8a). Soon after, vertical shear production prompts a transition into three-dimensional turbulence.

In its fully slumped state, the front is very thin at the surface with a small amount of light water above dense water. Diffusion of the fluid mixes dense and light fluid, but has a greater effect at the surface (where the front is thin) compared to at depth (where there is a larger body of light water). This lowers the fluid density at the location of particles near the surface at the head of the front.

When the front is on the point of retreat, surface flow is directed along the front but the fluid below is comparatively stationary. Diffusion of the fluid acting on the thin front near the surface causes a decrease in momentum, so this part of the front (where particles are located) does not retreat and particles are left behind in dense waters. As the front inertially oscillates, this process continues resulting in a net movement of particles from the front into dense fluid.

In this chapter, we use LES so mixing is parameterised and depends on the sub-grid scale diffusivity. However, simulations comparing the Smagorinsky and AMD models (see appendix 6.A) reveal qualitatively similar particle behaviour where fast rising particles are left behind when the front retreats, and the frontal adjustment is qualitatively similar to the DNS in chapter 5. This suggests that the mechanism is not a numerical artefact of the LES.

Compared to the medium and fast rising particles, the slow rising particles exhibit much less accumulation near the surface. Instead, at $t = 13$ hours, only the subducted particles exhibit significant accumulation, and the particles are relatively uniformly distributed by $t = 28$ hours.

When the front sharpens and slumps in the second inertial period, the line of medium and fast rising particles is pushed further away from the front (to the left). The meandering structures that were visible in the fast rising particles at $t = 13$ hours are largely gone at $t = 28$ hours and the particles get re-aligned parallel to the front. At $t = 28$ hours, the medium rising particles that were subducted during the first inertial oscillation and have returned to

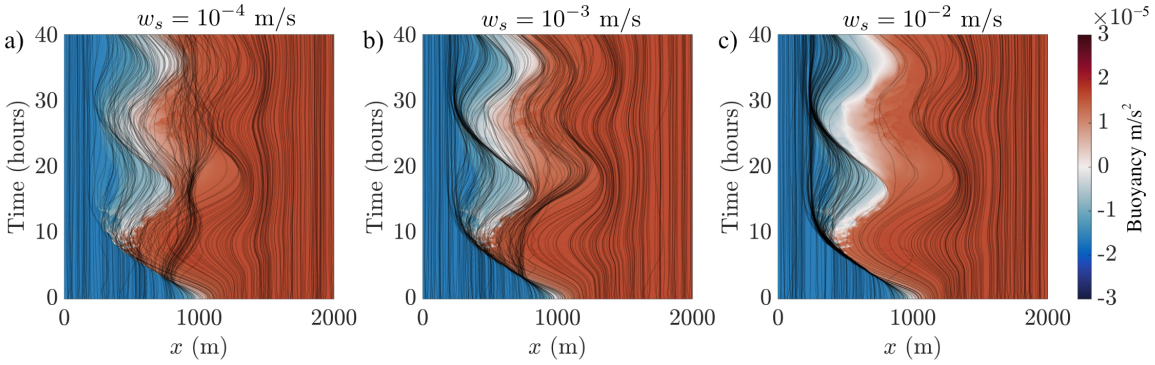

Fig. 6.6 Trajectories of cross-front particle location over time (black) for 300 randomly selected particles in each of $w_s = 10^{-4}$ m/s (a), $w_s = 10^{-3}$ m/s (b) and $w_s = 10^{-2}$ m/s (c). We underlay the surface buoyancy field at $y = 0$ m in colour.

the surface exhibit some aggregation near $x = 500$ m in a region that is devoid of fast rising particles, which instead remain separated into light and dense waters.

6.3.2 Movement of particles between fluid of different densities

The distinct patterns of particle accumulation are determined by a combination of the inertial oscillations, turbulence and the particle buoyancy. We visualise the different particle pathways in figure 6.6, which shows the across-front location of 300 randomly selected particles for each slip velocity as a function of x and t with the surface buoyancy field (at $y = 0$ m) shown in colour for reference. The particles broadly follow the inertial oscillations of the front. Particles inside the front are subject to oscillations of a larger amplitude, and the amplitude of the oscillations decreases further away from the front. There are also times when the oscillations of particles on the light and dense sides of the front are out of phase with one another, which indicates convergent flow (e.g. $t = 28$ hours). This phase difference is ultimately responsible for the generation of the new front observed in figure 6.2c.

The trajectories of slow and medium rising particles branch off from the front at about $t = 4$ hours when these particles are subducted beneath the front. The slow rising particles inertially oscillate at depth in a less coherent manner, while the medium rising particles display some transient behaviour at depth, but settle back into the inertial oscillation of the surface buoyancy field by the second cycle. Recall from figure 6.4 that most medium rising particles are close to the surface at $t = 13$ hours, while most slow rising particles remain subducted. Importantly, some of the medium particles which started in dense waters have now moved into light waters by rising through the stratified waters inside the front.

In contrast, intense accumulation of medium and fast rising particles occurs along the dense side of the front during frontogenesis in the first and second inertial periods. Some

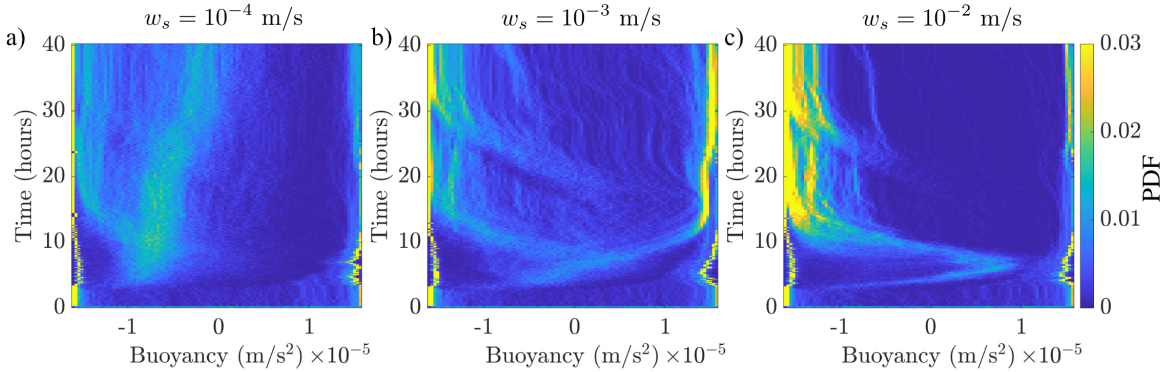

Fig. 6.7 PDF of buoyancy along particle paths against time for particles with $w_s = 10^{-4}$ m/s (a), $w_s = 10^{-3}$ m/s (b) and $w_s = 10^{-2}$ m/s (c).

of the accumulated particles continue to oscillate with the front, but others are left behind in dense waters when the front retreats. Some of the particles that escape the front remain at a nearly fixed cross-front position, leading to a concentrated line of particles which is most prominent for the fast rising particles. When the front retreats a second time, more particles are left behind on the dense side and accumulate. At later times, some accumulation of medium rising particles also occurs within the second front that emerges at $x = 500$ m.

Although an equal number of particles start in light and dense waters, significantly more fast rising particles are located in dense waters by the end of the simulation. This suggests that, on average, the particles have moved into denser water. Recall that we use zero buoyancy flux boundary conditions, so the buoyancy of a fluid parcel can only be changed by mixing two masses of fluid with different buoyancy. Neutrally buoyant particles are advected along fluid parcels, and hence along constant buoyancy contours unless mixing occurs. The particles we consider are positively buoyant, which additionally allows them to move off constant buoyancy contours as they rise towards the surface. The front is generally stably stratified, so rising particles generally move from denser to lighter waters, and movement from light to dense waters is therefore likely due to mixing.

Figure 6.7 shows the probability density function (PDF) of the fluid buoyancy sampled along the paths of slow, medium and fast rising particles during the first two inertial periods. In the discussion that follows, note the distinction between the buoyancy of particles (which determines the slip velocity, w_s), and the fluid buoyancy sampled along particle paths. In all cases, particles initialised in very dense or very light water (at the edges of the domain) remain on the same buoyancy contour throughout the simulation, aside from some mixing between $t = 4 - 10$ hours when the front first collapses. This is because flow remains relatively quiescent outside the front so there is no subduction and no mixing.

Submerged particles rise towards the surface, moving from denser to lighter waters, and the magnitude of the slip velocity affects how quickly particles do this. In the case of slow rising particles, we see a peak in the PDF near $b = -1 \times 10^{-5}$ m/s^2 which gradually shifts towards $b = 0$ m/s^2 (figure 6.7a). In contrast, the medium rising particles rise at a faster speed and reach the light side of the front by the end of the first inertial period where they become trapped. Here, there is less mixing and subduction, so particles tend to remain on a single buoyancy contour.

Interestingly, a large number of the fast rising particles which start in dense waters are transported into light waters near the start of the simulation. At first glance, one may think that this increase is also due to rising of particles, but particles with a higher slip velocity ($w_s = 10^{-1}$ m/s, not shown) display qualitatively and quantitatively similar behaviour even though they remain at the surface throughout the simulation. This suggests that the increase through buoyancy space is due to turbulent mixing rather than rising of particles. When the front is turbulent, overturnings develop along isopycnals and the flow can be unstably stratified (see figure 6.4b). Near the surface where particles are located, these overturnings can advect boils of dense water onto the light side of the front and mix with the surrounding flow, decreasing the buoyancy of the fluid. This creates a pathway for particles to move from light waters to dense waters. Particles can also be suducted into overturning regions, which allows them to sample both positive and negative buoyancy fluid as they rise back towards the surface. Below, we outline the mechanism through which instabilities, turbulent mixing and overturnings cause the fast rising particles to into light water and then back into dense waters as in figure 6.7c.

The mixing of fast rising particles from dense to light waters appears to be caused by motion generated through frontal instabilities (figure 6.2a). Figure 6.8 shows sections of the buoyancy field zoomed into the surface front, along with the position of the fast rising particles. At $t = 3$ hours, small shear instabilities develop along the front with tell-tale 'billows' associated with Kelvin-Helmholtz instability visible along the front. The particles which converge along the front accumulate in the centre of each billow. At $t = 5$ hours, as the front continues to propagate to the left, the billows with $b = 0$ m/s^2 detach from the front and drift to the light side of the front, carrying the particles with them. As the fluid inside the billows mixes with the surrounding fluid, the fluid buoyancy increases. This process is associated with the increase in buoyancy visible in figure 6.7c. At $t = 7$ hours 'boils' of dense fluid appear on the light side of the front due to advection by three-dimensional turbulence. At this time, most of the particles at the front are associated with fluid with $b > 0$ (figure 6.7c at $t = 7$ hours).

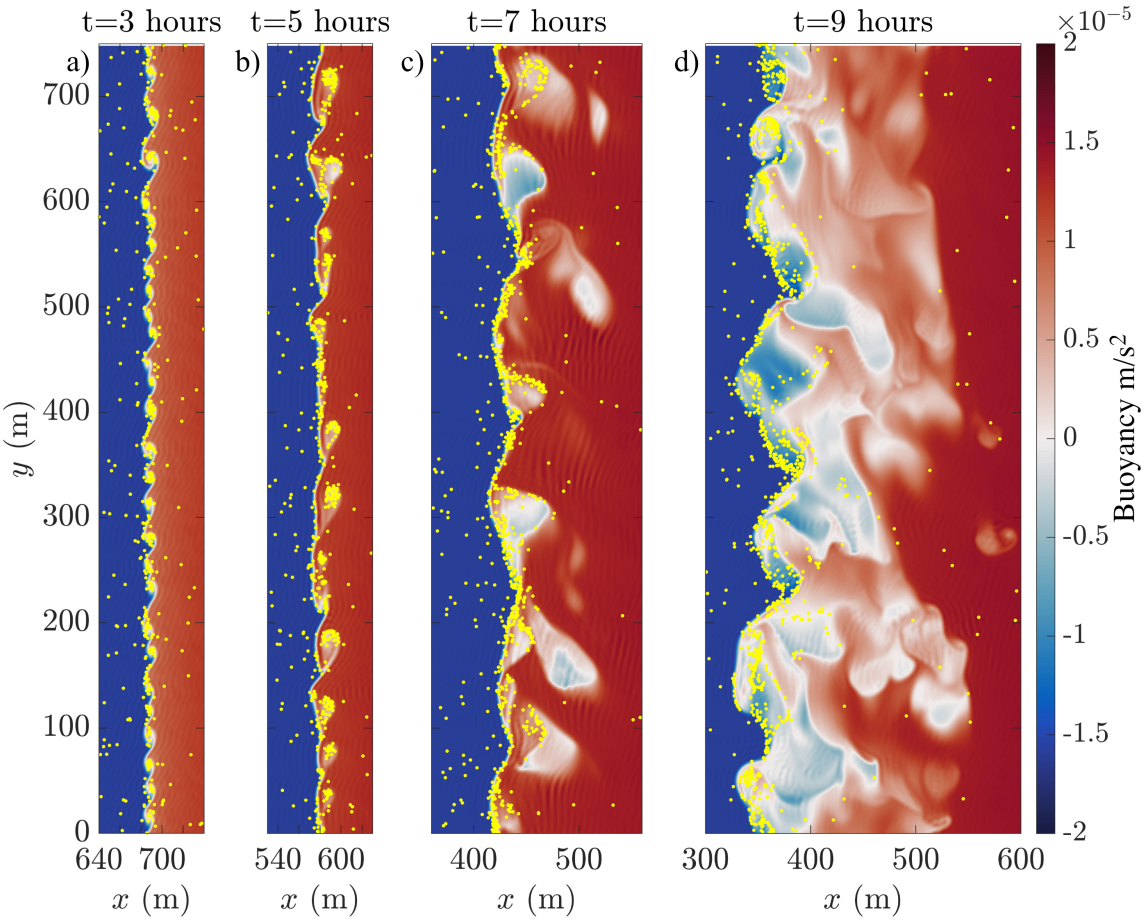

Fig. 6.8 Horizontal slices of the surface buoyancy field zoomed in on the shear instabilities. Particles with $w_s = 10^{-2}$ m/s are shown in yellow.

At $t = 9$ hours, the front begins to retreat. As it does so, more dense fluid is upwelled from the interior onto the light side at the surface. Pockets of dense fluid are stretched as the front retreats and merge with fluid on the dense side, which broadens the front. The mixing of dense water into the front causes the particles to shift back into denser waters. As the front widens, some of these particles are carried outside the front (leading to the high concentration in very dense waters in figure 6.7c), and some accumulate in less dense waters (leading to the multiple streaks in the PDF in figure 6.7c).

As noted earlier (and in chapter 5) turbulence is not as energetic along the front during the second inertial period. As a result, the movement of particles through buoyancy space is not as dramatic as during the first inertial period. Instead, two separate fronts emerge during the second inertial period (see figure 6.2c) which creates an additional barrier between light and dense waters, trapping particles on one side or the other. However, particles still move into more dense waters when the front retreats a second time which gives rise to the second decrease through buoyancy space in figure 6.7b,c, with more particles mixed outside the front. This has the effect of strongly accumulating particles on the dense side, and segregating particles between strong positively and negatively buoyant fluid.

6.4 Conclusions and discussion

Here, we used large eddy simulations (LES) to study buoyant particles in a geostrophically adjusting front whose initial balanced Rossby number is much larger than the critical value. In this regime, frontal collapse generates small-scale instabilities and turbulence which are associated with intense downwelling. As the front adjusts, convergent flow drives new, sharp fronts to develop which also contribute to turbulence and downwelling.

The response of buoyant particles to the adjustment process depends on their slip velocity. Weakly buoyant particles (with $w_s \leq 10^{-3}$ m/s) are subducted by the frontal circulation along isopycnals into the interior when the front first collapses. The most weakly buoyant particles ($w_s = 10^{-4}$ m/s) are carried deeper and further, and rise very slowly towards the surface. Particles with a higher slip velocity ($w_s = 10^{-3}$ m/s) are subducted, but rise back to the surface within the first inertial period, and become trapped on the light side of the front. Turbulence that develops later in the simulation is capable of re-submerging weakly buoyant particles, although to shallower depths than during initial collapse.

In contrast, strongly buoyant particles (with $w_s > 10^{-3}$ m/s) remain close to the surface throughout the simulation where they are subject to inertial oscillations. In this case, mixing associated with shear instabilities and frontogenesis transfers particles between light and dense waters, eventually leading to accumulation of particles on the dense side of the front.

Mixing is strong enough that some particles completely escape the front and are left behind on the dense side of the front when the front retreats. This creates a large void of particles in the central portion of the front and segregates them between light and dense waters. As the front adjusts back, more particles are deposited, leading to large concentrations of particles on the dense side of the front.

In chapter 5, we investigated geostrophic adjustment for several Rossby numbers ranging from $Ro_0 = 0.5 - 16$. A possible extension of this work could be to compare the behaviour of buoyant particles in some of the less turbulent cases. For a smaller Rossby number, we expect weaker downwelling and less turbulence, and more particles would likely remain at the surface. Below the critical Rossby number, the DNS exhibited relatively laminar flow with waves propagating from the front into the surrounding weakly stratified fluid. This could allow new mechanisms which could accumulate or disperse buoyant particles in different ways.

These results have important implications for modelling particles in the ocean. We observe accumulation on very small scales, on the order of tens of metres, which is much too small to be resolved even in high resolution regional ocean models (Kudryavtsev et al., 2012). Typically these models assume particles are transported and dispersed homogeneously at the submesoscale and below (Sebille et al., 2020), and don't account for the very non-homogeneous behaviour observed in this study or others of accumulation in submesoscale flows (D'Asaro et al., 2018; Taylor, 2018). Although it is difficult to assess the impact that accumulation on these scales may have on the large-scale transport of buoyant materials, it may be necessary to include some of these effects in parameterisation schemes in regional and global models.

We find that particles with different buoyancies respond very differently to the same flow field and exhibit distinct behaviour. In particular, weakly buoyant particles accumulate on the light side of the front but strongly buoyant particles do not. Buoyant material such as oil droplets, microplastics or zooplankta are made up of a wide range of particle sizes and buoyancies. This could lead to segregation between different types of material, or segregation between particles of the same material when composed of different slip velocities. This creates challenges in how to best model buoyant materials. Adding to this challenge is the influence of time-dependent particle density. For example, biofouling can cause a microplastic particle to become less buoyant, or cause it to sink (Fazey and Ryan, 2016; Semcesen and Wells, 2021). Likewise, particles can break up by chemical degradation, weathering or abrasion which changes their size and density. This could change or create additional particle pathways, complicating dynamics even more. Such questions remain relatively unexplored and should be addressed in future work.

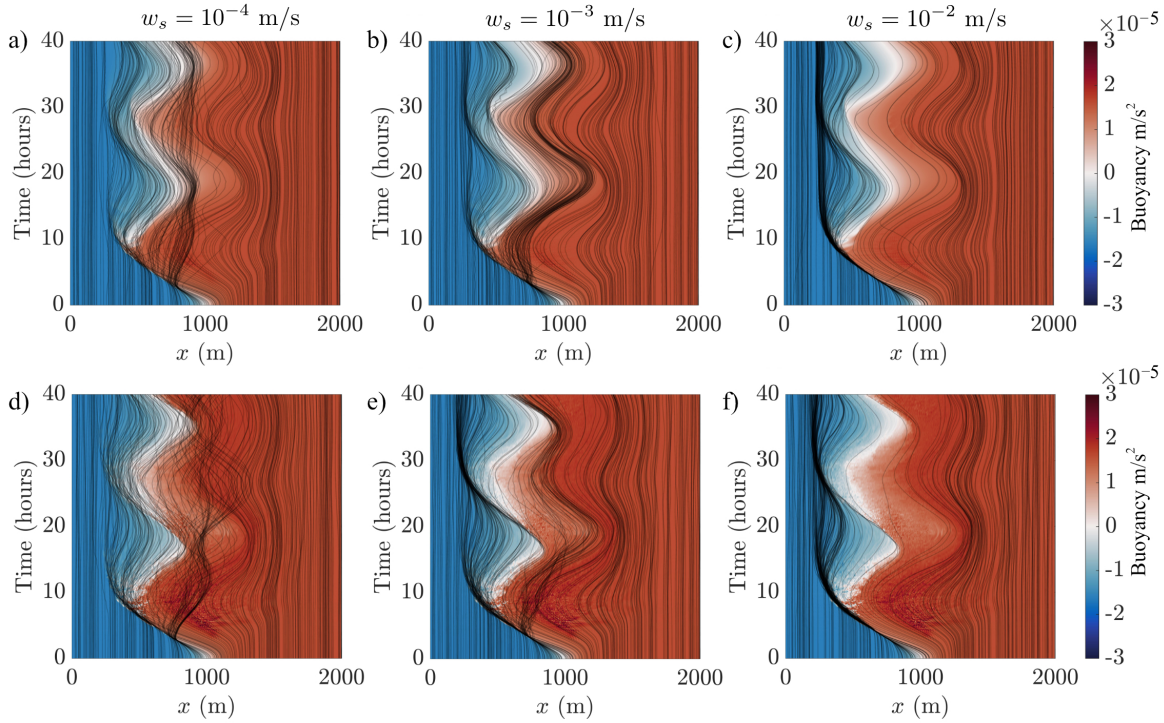

Fig. 6.9 Trajectories of cross-front particle location over time (black) for 300 randomly selected particles in each of $w_s = 10^{-4}$ m/s (a), $w_s = 10^{-3}$ m/s (b) and $w_s = 10^{-2}$ m/s (c). We underlay the surface buoyancy field at $y = 0$ m in colour. The top row (a,b,c) shows a simulation with the constant Smagorinsky model. The bottom row (d,e,f) shows a simulation with the AMD model.

Appendix 6.A

We examine the influence of the sub-grid scale model on the particle dynamics. In developing our simulations, we tested the constant Smagorinsky model (Lilly, 1967; Smagorinsky, 1963) and the anisotropic minimum dissipation (AMD) model (Abkar et al., 2016; Rozema et al., 2015; Vreugdenhil and Taylor, 2018). The AMD model experienced numerical difficulties when the horizontal grid was not square, so here we run two additional simulations with a lower resolution and a square horizontal grid to allow for comparison of the two different SGS models. Specifically, the horizontal domain size is 2000 m in each direction and the horizontal resolution is 3.9 m, which is double that of the simulation used in the study. The vertical resolution and all other parameters are kept the same. The grid aspect ratio of the test simulations is 4 : 1, which is larger than recommended (Vreugdenhil and Taylor, 2018) and motivates the use of the higher resolution, non-square simulations in the main study.

Figure 6.9 shows the SGS model dependence of the transport of particles and the surface buoyancy field. The inertial oscillation of the buoyancy field is similar in amplitude and period both inside and outside the front. However, there is more numerical noise when the front collapses in the AMD model compared to the Smagorinsky model (at around $t = 10$ hours, $x = 1000$ m) which persists until the third inertial period.

The numerical noise has a small impact on particle distribution, and the overall behaviour of particles is very similar for the constant Smagorinsky and AMD models. The medium and fast rising particles accumulate in a narrow line in on the dense side and are segregated between dense and light waters. This is the same as the higher resolution Smagorinsky simulation used in the main text (figure 6.6b,c). The slow and medium rising particles are both subducted at $t = 4$ hours and oscillate at depth, which is again the same as the higher resolution Smagorinksy simulation. The numerical noise in the AMD model means that particles display more variation in particle position and do not oscillate as uniformly. In both models, the slow particles slowly rise towards the surface, but the medium particles rise more quickly and rejoin the inertial oscillations on the light side of the front.

Since the particle dynamics are very similar for the AMD and constant Smagorinsky models, we choose to use the constant Smagorinsky model because there is less numerical noise in the velocity and buoyancy fields. We increase the resolution in the main study to capture smaller-scale turbulence, but this does not significantly affect the transport of particles.

Chapter 7

Conclusions

7.1 Conclusions

In this thesis, we have addressed fundamental fluid dynamical processes in the upper ocean mixed layer and investigated their implications on the transport and accumulation of buoyant particles. This is widely applicable to predicting the transport and distribution of pollutants in the ocean. Motivated to explore a range of scales and behaviours, we focused on two distinct flow configurations: convective turbulence and a geostrophically adjusting front. In each of these, we ran a suite of numerical simulations which uncovered both interesting flow phenomena and particle dynamics. Below, we summarise the key findings from these studies.

To enable the consideration of Lagrangian particles (in addition to Eulerian tracer fields), we developed and implemented a three-dimensional Lagrangian particle tracking model into the existing numerical solver, DIABLO. This allowed us to include Lagrangian particles in any flow field which can be investigated using DIABLO. The particle tracking code includes a parameterisation of sub-grid scale motions for use in large eddy simulations, and was parallelised using MPI. Considerable effort has been taken to ensure that the code is easy to use and modify for different scenarios, for example changing the number of particles, particle buoyancy and initial conditions. We anticipate that the particle tracking code will be useful in a variety of research projects in the future.

In chapter 3, we began our investigation of oceanic convective vortices in a convectively driven flow (Chor et al., 2018a). Using large eddy simulations, we varied the surface wind stress and surface buoyancy fluxes to encompass a wide range of the parameter space. In a purely convective regime, we observed the formation of persistent convective vortices in the nodes between convective cells. When wind forcing was included, there was a transition from convective cells to longitudinal wind rolls with three distinct flow patterns observed under weak, moderate and strong wind forcing. For sufficiently weak winds, convective

vortices were able to survive but under strong wind forcing, convective vortices no longer existed.

We modelled non-inertial buoyant particles using a combination of buoyant tracers and Lagrangian surface particles, which allowed us to a explore a wide range of particle buoyancies. The convective vortices trapped buoyant particles, leading to large concentrations. Under weak wind forcing, the convective vortices were less effective at trapping buoyant material, and under strong wind forcing (when there were no convective vortices), some clustering occurred in regions of high fluid speed associated with longitudinal wind rolls. We quantified the degree of clustering using the Gini coefficient and found that clustering was strongly influenced by the relative size of the friction and convective velocities and the particle buoyancy.

Although convective vortices are small and characterised by a large Rossby number, we found that they exhibit a previously unknown bias towards cyclonic vorticity. Based on an analysis of Lagrangian trajectories at the surface, we found that the average time that a particle spends inside a convective vortex is long enough for planetary vorticity to become important and vortex stretching causes an exponential increase in vorticity.

Motivated by this discovery, we developed a theory to explain the vorticity bias of convective vortices in chapter 4. There has been a long-standing debate on whether terrestrial dust devils exhibit a rotational bias, but the general consensus is that they are largely unbiased. However, our simulations of convective vortices in the ocean presented in chapter 3 uncovered a clear cyclonic bias which re-opened the question of what controls the rotational bias of convective vortices.

To investigate this, we used large eddy simulations of free convection configured for the ocean, but the idealisation of our simulations makes the results more broadly relevant to a wide range of flows. In contrast to chapter 3, we focused on a purely convective regime (removing the influence of wind stress), and independently varied the Coriolis acceleration and surface buoyancy flux, including cases with convective vortices with and without a rotational bias.

The higher resolution in this set of simulations revealed the existence of small convective vortices, in addition to the large convective vortices in chapter 3. While large convective vortices were biased for sufficiently large values of the Coriolis parameter, small convective vortices did not exhibit a clear bias. By tracking the position of Lagrangian surface particles, we found that the large convective vortices develop through the merger of small convective vortices. We proposed a statistical theory to quantitatively predict the cyclonic bias of large convective vortices composed of many small unbiased convective vortices. We tested our theory using simulations of idealised circulation cells initialised with an array of small

vortices with random amplitude and equal probability of cyclonic and anticyclonic rotation. Large vortices, which form through the merger of the small vortices, exhibit a cyclonic rotation bias, and our theory agreed very well with these simulations. Our theory was also able to explain the cyclonic bias found in the full LES of convective turbulence, although there were larger discrepancies between the theory and LES due to the chaotic nature of the flow and the uncertainty in some key parameters (e.g. the number of small vortices that make up each large convective vortex). We then used our theory to explain the bias in typical convective conditions in the ocean (where we found the bias is strong) and the terrestrial and Martian atmospheres (where we found the bias is weak). This prediction is consistent with the lack of bias in observations of terrestrial dust devils and provides some justification.

In chapters 5 and 6, we turned our attention to submesoscale dynamics, broadly motivated by the SUNRISE field campaign where observations revealed strong accumulation of buoyant material (seaweed and bubbles) in distinct patches and streaks. We modelled a highly idealised density front by means of an initially motionless fluid with a lateral density gradient subject to geostrophic adjustment. This is a fundamental geophysical fluid dynamics problem that has been studied in a variety of settings, although until now largely using analytical models or low resolution numerical simulations. In this thesis, we focused on what happens to the density discontinuity predicted in Ou (1984) for very large Rossby numbers in the three-dimensional viscous setup.

First, we analysed the underlying physics of the flow in chapter 5. We examined how the evolution of the front depends on the balanced Rossby number, Ro_0 using direct numerical simulations. In cases when Ro_0 was large enough (exceeding the critical Rossby number, $Ro_c \approx 3.5$), an abrupt density jump formed at the top and bottom boundaries. This is consistent with the analytical solution (Ou, 1984) for the breakdown of the equilibrium state. The density jump was associated with enhanced turbulence and small-scale mixing. We showed that the dominant terms in the energy budget are the vertical and horizontal shear production, which trigger the formation of small-scale shear instabilities, with a secondary contribution from the strain production. In regions of strong turbulence, the mixing efficiency, η, was comparable to the 'canonical' value $\eta \sim 0.2$. However, in simulations associated with less turbulence (i.e. a smaller Ro_0) or in the interior of the front, the mixing efficiency increased to values much higher than the observed $\eta \sim 0.2$. At later times, baroclinic instability developed with the buoyancy flux acting to convert available potential energy into kinetic energy of the growing perturbations.

The turbulence and ageostrophic circulation generated during frontogenesis in chapter 5 was associated with intense subduction. In chapter 6, we investigated the distribution and subduction of buoyant particles in a geostrophically adjusting front. In particular, we ran LES

of the most unstable front examined in chapter 5 (where $Ro_0 = 16$). To investigate buoyant material, we included three-dimensional Lagrangian particles with a wide range of particle buoyancies. The LES and DNS showed very similar frontal dynamics, producing a front rich in instabilities and turbulent features. In the LES, regions of convergence developed within the front due to phase-differences in the inertial oscillation and this did not occur in the DNS. This triggered the generation of multiple fronts which contributed to turbulence and downwelling.

Although all particles were advected by the same velocity field, we found that particle buoyancy had a strong influence on the transport pathways taken by the particles. At early times, strong downwelling associated with the secondary circulation subducted weakly buoyant particles along the sloping isopycnals on the dense side of the front. The submerged particles rose back towards the surface onto the light side of the front. Here, the weakly buoyant particles could be re-submerged by turbulence generated by a secondary front, but did not cross back to the dense side of the front.

The downwelling was not strong enough to submerge strongly buoyant particles, which remained at the surface throughout the simulation. As shown in chapter 5, turbulence is associated with enhanced mixing which moved particles between light and dense waters. We found that mixing preferentially transports strongly buoyant particles onto the light side of the front. As the front becomes more turbulent and begins to the retreat, particles are transported back into dense waters. Surprisingly, the mixing was strong enough to carry some particles on the dense side completely out of the front, and they were left behind when the front retreated. Other particles exhibited inertial oscillations on the dense side of the front, but the second adjustment transported more particles out of the front, leading to large concentrations. This mechanism segregated the particles between light and dense waters, leaving a large void in the centre of the front.

Overall, this thesis has tackled a number of unanswered questions regarding fluid dynamical processes and their effect on the transport of buoyant material at the submesoscale and below. Our studies highlight the importance of small-scale turbulence on transport and accumulation which often lead to highly nonuniform and unpredictable behaviour, and that the particle buoyancy is a crucial parameter in determining where particles accumulate. The hope is that these results will contribute to improving predictions of buoyant material transport in more realistic settings, such as the distribution of microplastics in our oceans, and guide the development of modelling buoyant material in regional and global models.

7.2 Future directions

In addition to being applied to new flow configurations, the Lagrangian particle model developed in this thesis can be extended to tackle a variety of outstanding problems pertaining to the distribution of buoyant, neutral or sinking particles. One such extension could be to account for non-uniform particle density. This thesis has revealed that the extent of clustering strongly depends on particle buoyancy. Over time, particles such as microplastics are subject to processes including fragmentation, degradation and biofouling which have the potential to change the buoyancy of the particles. Taking the example of biofouling, microbes and organic materials which accumulate on the surface of the plastic can make it more dense. If the density of the fouled particle exceeds the density of seawater, the particle begins to sink. This transition between the positively buoyant and negatively buoyant particles remains relatively unexplored, and could be an important mechanism in explaining the 'missing plastic' in the ocean. Our current particle model uses a constant particle buoyancy, but this could be easily modified. Using statistics such as temperature and light sampled along the particle path, we could implement a simple model for the density of a particle over time. For example, Kooi et al. (2016) developed a theoretical model to simulate the effect of biofouling on a microplastic which depends on light, water density, temperature, salinity and viscosity. Incorporating a (perhaps simplified) model such as this in our three-dimensional particle model could further improve its applicability to microplastics (and other buoyant materials) in the ocean.

In our investigation of convective vortices, we mainly focused on the horizontal distribution of buoyant particles. However, questions remain about whether convective vortices are capable of subducting material below the surface. In chapter 3, the averaged convective vortex revealed strong downwelling on the periphery of the vortex encircling an area of weaker vertical velocity in the centre, which is also seen in profiles of dust devils in the atmosphere. Analysis of the higher resolution convective vortices in chapter 4 reveals qualitatively similar profiles of vertical velocity in the instantaneous vortices. Preliminary work investigating the vertical distribution of three-dimensional, positively buoyant Lagrangian particles shows some interesting behaviour. Particles accumulate in the centre of convective vortices, but the weak downwelling here is not strong enough to submerge the particles to significant depths and they become trapped at the surface. However, when vortices interact and merge, particles cross into strong downwelling regions surrounding the vortices, and the particles are more readily subducted. Initial visualisations reveal a sudden downwards 'burst' of particles ejected into the mixed layer. Since vortex merging is frequent, so too are these ejection events. More work is needed to explore specifics of the mechanism and its implications. For

example, could this behaviour contribute to buoyant particles escaping the mixed layer, and how do additional effects such as wind forcing or diurnal heating impact results?

In a similar vein, further verification of the cyclonic bias of convective vortices and the impact of the bias could be explored further. Our prediction in the context of the atmosphere in chapter 4 is based on the free-slip boundary condition applicable to the ocean. In the case of the atmosphere, a no-slip boundary condition might produce significant dissipation, which could increase vorticity fluctuations and inhibit the cyclonic bias. Studies have also shown that convective vortices form more readily when a free-slip boundary condition is applied compared to a no-slip boundary condition (Giersch and Raasch, 2021). It would be straightforward to test this using simulations comparable to those in chapters 3 and 4, but configured with a no-slip boundary condition which would be more directly relevant for the atmospheric boundary layer. This could shed light on the extent of properties shared by atmospheric and oceanic convective vortices. Although challenging, more rigorous observations of dust devils on Earth and Mars are needed to verify our predictions.

Convective vortices remain unobserved in the ocean, and directly measuring them and their influence on buoyant material should be a priority. A challenge in observing convective vortices is their small scale and ephemeral nature. One way of searching for them could be to instead look for areas with high concentrations of buoyant material at the surface (perhaps using inexpensive surface drifters as in the CARTHE experiment). However, dynamics occur on relatively small scales and surface cooling usually occurs at night, which makes purely visual efforts challenging. In reality, we are probably still some time away from verifying the cyclonic bias of convective vortices in the ocean. Finally, this work has opened questions on whether we need to reconsider the effect of planetary vorticity for other small-scale flows, which is usually neglected.

Chapters 5 and 6 analyse a highly-idealised front under geostrophic adjustment, inspired by fronts observed in the SUNRISE campaign. In particular, observations of sargassum and bubbles revealed a distinct offset between the two materials (see figure 1.4d). Although work in chapter 6 revealed one mechanism for segregating buoyant particles, it is unclear whether the same mechanism is responsible for the separation of sargassum and bubbles observed in SUNRISE (which occurs on much smaller scales at the frontal interface). Sargassum and bubbles have different sizes and density, and therefore different particle buoyancies. The accumulated sargassum was centred around 50 cm below the surface while the bubbles were located at the surface. This suggests that the vertical velocity near the surface submerged the sargassum along a sloping front, similar to that modelled in chapters 5 and 6. However, the horizontal resolution of our LES was 2.0 m and the vertical resolution was 0.90 m near the surface, which may not be large enough to capture the offset. To test this, higher

resolution simulations could be run by further restricting the along-front domain length, or using two-dimensional simulations.

In addition, to make our simulations computationally feasible, we had to stray outside the parameter space relevant for fronts in the Gulf of Mexico. In the Gulf of Mexico, Rossby numbers can reach as high as 300, depths are confined to only $10-20$ m and the fronts were very flat with a much larger horizontal length-scale compared to the vertical length-scale. The large aspect ratio needed to capture a front on these scales poses major difficulties for both LES and DNS. However, other progress could be made by adding degrees of realism to the simulations. For example, a no-slip boundary condition could be applied at the bottom (to represent the seafloor) and a buoyancy flux or wind forcing at the top boundary. This is likely to generate more turbulence at both the surface and seafloor which could affect the particle distribution, potentially allowing more subduction of strongly buoyant particles.

The idealisation of our front also limits the applicability of our results to SUNRISE observations. At the ocean submesoscale, fronts are not isolated features but are part of a rich field of eddies. These eddies can deform fronts which adds complications to our idealisation of a straight front. However, fieldwork in the SUNRISE campaign in 2021 took place in regions with relatively straight, tightly packed isobaths, which supported the development of two-dimensional, straight fronts. This confirms that our assumption of an initially straight front is reasonable in some circumstances. In contrast, the field experiment in the summer of 2022 investigated the interaction of submesoscale eddies and fronts in regions with more gradually sloping ocean floors, which allowed energetic three-dimensional eddies to develop. An avenue of further research could be to simulate a less straight, turbulent front within a baroclinic eddy. Challenges arise in how to both capture the large-scale eddy (which requires a large domain size), and resolve the turbulent scales of the front (which requires a high resolution). Analysing particles in such a regime could also be difficult due to the wide range of processes. Without large numbers of particles, accumulation of particles might also be hard to quantify if the particles are spread out over a large region. A good starting point for this could be to run simulations of idealised baroclinic instability under controlled conditions and then combine findings with our high resolution studies of frontogenesis.

It is well-known that a bias towards cyclonic vorticity also exists at the submesoscale where Rossby numbers are $\mathcal{O}(1)$ (Thomas et al., 2008), but the origin of the bias is still relatively unexplored. Lagrangian particles proved a useful tool in understanding the bias of convective vortices in chapters 3 and 4, and a similar approach could be used in the submesoscale problem. Geostrophic adjustment is an example of a simple flow where a cyclonic front develops, but chapters 5 and 6 did not investigate the evolution of vorticity. A further study could involve initialising the front with some additional turbulence (e.g.

convective forcing) and tracking vorticity along particle paths to see how quickly the bias towards cyclonic vorticity develops.

From a broader perspective, our results have implications for parameterisations of buoyant particles in regional and global ocean models where particle motion is not resolved. Currently, most subgrid scale models treat horizontal transport as a diffusive process (Sebille et al., 2020) or a random walk (Haza et al., 2012; Maximenko et al., 2018), where particles spread out as time progresses. Models also neglect the effect of the particle buoyancy, treating all buoyant particles the same. This thesis has rebutted both of these claims, highlighting the anti-diffusive nature of small-scale flows and the strong dependence on particle buoyancy. Such effects need to be integrated into these parameterisations to assess whether behaviour at the submesoscale and below has a significant impact on the large-scale transport of buoyant particles, or on important climate change research such as the global plastic budget.

References

Abkar, M., Bae, H. J., and Moin, P. (2016). Minimum-dissipation scalar transport model for large-eddy simulation of turbulent flows. *Physical Review Fluids*, 1.

Bachman, S. D. and Taylor, J. R. (2016). Numerical simulations of the equilibrium between eddy-induced restratification and vertical mixing. *Journal of Physical Oceanography*, 46(3):919–935.

Baddeley, P. F. H. (1860). *Whirlwinds and dust storms of India*. Bell & Daldy.

Bagheri, G. and Bonadonna, C. (2016). On the drag of freely falling non-spherical particles. *Powder Technology*, 301:526–544.

Balachandar, S. and Eaton, J. K. (2010). Turbulent dispersed multiphase flow. *Annual review of fluid mechanics*, 42:111–133.

Balachandar, S. and Maxey, M. (1989). Methods for evaluating fluid velocities in spectral simulations of turbulence. *Journal of Computational Physics*, 83(1):96–125.

Balkovsky, E., Falkovich, G., and Fouxon, A. (2001). Intermittent distribution of inertial particles in turbulent flows. *Physical Review Letters*, 86:2790–2793.

Balme, M. and Greeley, R. (2006). Dust devils on earth and mars. *Reviews of Geophysics*, 44(3).

Barth, J. (1989). Stability of a coastal upwelling front: 2: Model results and comparison with observations. *Journal of Geophysical Research: Oceans*, 94(C8):10857–10883.

Belcher, S. E., Grant, A. L., Hanley, K. E., Fox-Kemper, B., Van Roekel, L., Sullivan, P. P., Large, W. G., Brown, A., Hines, A., Calvert, D., et al. (2012). A global perspective on langmuir turbulence in the ocean surface boundary layer. *Geophysical Research Letters*, 39(18).

Bewley, T. (2019). *Numerical Renaissance: Simulation, Optimization, and Control*. Renaissance Press.

Blumen, W. and Wu, R. (1995). Geostrophic adjustment: Frontogenesis and energy conversion. *Journal of Physical Oceanography*, 25(3):428–438.

Boccaletti, G., Ferrari, R., and Fox-Kemper, B. (2007). Mixed layer instabilities and restratification. *Journal of Physical Oceanography*, 37(9):2228–2250.

Borrelle, S. B., Ringma, J., Law, K. L., Monnahan, C. C., Lebreton, L., McGivern, A., Murphy, E., Jambeck, J., Leonard, G. H., Hilleary, M. A., et al. (2020). Predicted growth in plastic waste exceeds efforts to mitigate plastic pollution. *Science*, 369(6510):1515–1518.

Bou-Zeid, E., Meneveau, C., and Parlange, M. (2005). A scale-dependent lagrangian dynamic model for large eddy simulation of complex turbulent flows. *Physics of Fluids*, 17(2).

Brainerd, K. and Gregg, M. (1993). Diurnal restratification and turbulence in the oceanic surface mixed layer: 1. observations. *Journal of Geophysical Research: Oceans*, 98(C12):22645–22656.

Brannigan, L., Marshall, D. P., Garabato, A. C. N., Nurser, A. G., and Kaiser, J. (2017). Submesoscale instabilities in mesoscale eddies. *Journal of Physical Oceanography*, 47(12):3061–3085.

Brooks, H. (1960). Shorter contributions: Rotation of dust devils. *Journal of the Atmospheric Sciences*, 17(1):84–86.

Busse, F. (1978). Non-linear properties of thermal convection. *Reports on Progress in Physics*, 41(12):1929.

Caldwell, D. R. and Mourn, J. N. (1995). Turbulence and mixing in the ocean. *Reviews of Geophysics*, 33(S2):1385–1394.

Callies, J. and Ferrari, R. (2018). Note on the rate of restratification in the baroclinic spindown of fronts. *Journal of Physical Oceanography*, 48(7):1543–1553.

Callies, J., Flierl, G., Ferrari, R., and Fox-Kemper, B. (2016). The role of mixed-layer instabilities in submesoscale turbulence. *Journal of Fluid Mechanics*, 788:5–41.

Capet, X., Mcwilliams, J. C., Molemaker, M. J., and Shchepetkin, A. F. (2008). Mesoscale to submesoscale transition in the california current system. part i: Flow structure, eddy flux, and observational tests. *Journal of Physical Oceanography*, 38(1):29–43.

Caughey, S. J. (1982). Observed characteristics of the atmospheric boundary layer. *Atmospheric Turbulence and Air Pollution Modelling: A Course held in The Hague, 21–25 September, 1981*, pages 107–158.

Chamecki, M., Chor, T., Yang, D., and Meneveau, C. (2019). Material transport in the ocean mixed layer: Recent developments enabled by large eddy simulations. *Reviews of Geophysics*, 57:1338–1371.

Chen, R., Fernando, H. J., and Boyer, D. L. (1989). Formation of isolated vortices in a rotating convecting fluid. *Journal of Geophysical Research*, 94.

Chor, T., McWilliams, J. C., and Chamecki, M. (2021). Modifications to the k-profile parameterization with nondiffusive fluxes for langmuir turbulence. *Journal of Physical Oceanography*, 51(5):1503–1521.

Chor, T., Yang, D., Meneveau, C., and Chamecki, M. (2018a). Preferential concentration of noninertial buoyant particles in the ocean mixed layer under free convection. *Physical Review Fluids*, 3(6):064501.

Chor, T., Yang, D., Meneveau, C., and Chamecki, M. (2018b). A turbulence velocity scale for predicting the fate of buoyant materials in the oceanic mixed layer. *Geophysical Research Letters*, 45:11,817–11,826.

Coates, M., Ivey, G., and Taylor, J. (1995). Unsteady, turbulent convection into a rotating, linearly stratified fluid: Modeling deep ocean convection. *Journal of Physical Oceanography*, 25(12):3032–3050.

Cole, M., Lindeque, P., Halsband, C., and Galloway, T. S. (2011). Microplastics as contaminants in the marine environment: A review. *Marine Pollution Bulletin*, 62:2588–2597. Accumulation in gyres.

Compa, M., Alomar, C., Wilcox, C., Sebille, E. V., Lebreton, L., Hardesty, B. D., and Deudero, S. (2019). Risk assessment of plastic pollution on marine diversity in the mediterranean sea. *Science of the Total Environment*, 678:188–196.

Craik, A. D. and Leibovich, S. (1976). A rational model for langmuir circulations. *Journal of Fluid Mechanics*, 73(3):401–426.

Crowe, M. N. and Taylor, J. R. (2018). The evolution of a front in turbulent thermal wind balance. part 1. theory. *Journal of Fluid Mechanics*, 850:179–211.

D'Asaro, E. A. (2003). Performance of autonomous lagrangian floats. *Journal of Atmospheric and Oceanic Technology*, 20(6):896–911.

D'Asaro, E. A. (2014). Turbulence in the upper-ocean mixed layer. *Annual Review of Marine Science*, 6:101–115.

D'Asaro, E. A., Farmer, D. M., Osse, J. T., and Dairiki, G. T. (1996). A lagrangian float. *Journal of Atmospheric and Oceanic Technology*, 13(6):1230–1246.

D'Asaro, E. A., Shcherbina, A. Y., Klymak, J. M., Molemaker, J., Novelli, G., Guigand, C. M., Haza, A. C., Haus, B. K., Ryan, E. H., Jacobs, G. A., Huntley, H. S., Laxague, N. J., Chen, S., Judt, F., McWilliams, J. C., Barkan, R., Kirwan, A. D., Poje, A. C., and Özgökmen, T. M. (2018). Ocean convergence and the dispersion of flotsam. *Proceedings of the National Academy of Sciences of the United States of America*, 115:1162–1167.

Dauhajre, D. P., McWilliams, J. C., and Uchiyama, Y. (2017). Submesoscale coherent structures on the continental shelf. *Journal of Physical Oceanography*, 47(12):2949–2976.

de Lavergne, C., Vic, C., Madec, G., Roquet, F., Waterhouse, A. F., Whalen, C., Cuypers, Y., Bouruet-Aubertot, P., Ferron, B., and Hibiya, T. (2020). A parameterization of local and remote tidal mixing. *Journal of Advances in Modeling Earth Systems*, 12(5):e2020MS002065.

Deardorff, J. (1973). The use of subgrid transport equations in a three-dimensional model of atmospheric turbulence. *Journal of Fluids Engineering*, 95(3):429–438.

Deardorff, J. W. (1970). Convective velocity and temperature scales for the unstable planetary boundary layer and for rayleigh convection. *Journal of the Atmospheric Sciences*, 27:1211–1213.

Deardorff, J. W. (1972). Numerical investigation of neutral and unstable planetary boundary layers. *Journal of Atmospheric Sciences*, 29(1):91–115.

Denman, K. and Gargett, A. (1995). Biological-physical interactions in the upper ocean: the role of vertical and small scale transport processes. *Annual Review of Fluid Mechanics*, 27(1):225–256.

Deser, C., Alexander, M. A., Xie, S.-P., and Phillips, A. S. (2010). Sea surface temperature variability: Patterns and mechanisms. *Annual Review of Marine Science*, 2:115–143.

Dingwall, J., Chor, T., and Taylor, J. R. (2023). Large eddy simulations of the accumulation of buoyant material in oceanic wind-driven and convective turbulence. *Journal of Fluid Mechanics*, 954:A27.

Durward, J. (1931). Rotation of "dust devils". *Nature*, 128(3227):412–413.

D'Asaro, E. A. (2008). Convection and the seeding of the north atlantic bloom. *Journal of Marine Systems*, 69(3-4):233–237.

Eliassen, A. (1962). On the vertical circulation in frontal zones. *Geofys. publ*, 24(4):147–160.

Elipot, S., Lumpkin, R., Perez, R. C., Lilly, J. M., Early, J. J., and Sykulski, A. M. (2016). A global surface drifter data set at hourly resolution. *Journal of Geophysical Research: Oceans*, 121(5):2937–2966.

Ellehoj, M. D., Gunnlaugsson, H. P., Taylor, P., H.Kahanpää, Bean, K. M., Cantor, B. A., Gheynani, B. T., Drube, L., Fisher, D., Harri, A. M., Holstein-Rathlou, C., Lemmon, M. T., Madsen, M. B., Malin, M. C., Polkko, J., Smith, P. H., Tamppari, L. K., Weng, W., and Whiteway, J. (2010). Convective vortices and dust devils at the phoenix mars mission landing site. *Journal of Geophysical Research: Planets*, 115.

Eriksen, M., Thiel, M., and Lebreton, L. (2017). Nature of plastic marine pollution in the subtropical gyres. *Handbook of Environmental Chemistry*, pages 135–162.

Falkowski, P. G., Barber, R. T., and Smetacek, V. (1998). Biogeochemical controls and feedbacks on ocean primary production. *science*, 281(5374):200–206.

Favier, B., Silvers, L. J., and Proctor, M. R. (2014). Inverse cascade and symmetry breaking in rapidly rotating boussinesq convection. *Physics of Fluids*, 26(9).

Fazey, F. M. and Ryan, P. G. (2016). Biofouling on buoyant marine plastics: An experimental study into the effect of size on surface longevity. *Environmental Pollution*, 210:354–360.

Fernando, H. J., Chen, R. R., and Boyer, D. L. (1991). Effects of rotation on convective turbulence. *Journal of Fluid Mechanics*, 228:513–547.

Ferrari, R. (2011). A frontal challenge for climate models. *Science*, 332(6027):316–317.

Ferrari, R. and Rudnick, D. L. (2000). Thermohaline variability in the upper ocean. *Journal of Geophysical Research: Oceans*, 105(C7):16857–16883.

Ferry, J. and Balachandar, S. (2001). A fast eulerian method for disperse two-phase flow. *International Journal of Multiphase Flow*, 27:1199–1226.

Fox-Kemper, B., Ferrari, R., and Hallberg, R. (2008). Parameterization of mixed layer eddies. part i: Theory and diagnosis. *Journal of Physical Oceanography*, 38(6):1145–1165.

Fraga, B. and Stoesser, T. (2016). Influence of bubble size, diffuser width, and flow rate on the integral behavior of bubble plumes. *Journal of Geophysical Research: Oceans*, 121(6):3887–3904.

Frank, D., Landel, J. R., Dalziel, S. B., and Linden, P. F. (2017). Anticyclonic precession of a plume in a rotating environment. *Geophysical Research Letters*, 44:9400–9407.

Frankignoul, C. and Hasselmann, K. (1977). Stochastic climate models, part ii application to sea-surface temperature anomalies and thermocline variability. *Tellus*, 29(4):289–305.

Gargett, A. E. and Wells, J. R. (2007). Langmuir turbulence in shallow water. part 1. observations. *Journal of Fluid Mechanics*, 576:27–61.

Germano, M., Piomelli, U., Moin, P., and Cabot, W. H. (1991). A dynamic subgrid-scale eddy viscosity model. *Physics of Fluids A: Fluid Dynamics*, 3(7):1760–1765.

Geyer, R., Jambeck, J. R., and Law, K. L. (2017). Production, use, and fate of all plastics ever made. *Science Advances*, 3(7):e1700782.

Giersch, S., Brast, M., Hoffmann, F., and Raasch, S. (2019). Toward large-eddy simulations of dust devils of observed intensity: Effects of grid spacing, background wind, and surface heterogeneities. *Journal of Geophysical Research: Atmospheres*, 124:7697–7718.

Giersch, S. and Raasch, S. (2021). Evolution and features of dust devil-like vortices in turbulent rayleigh-bénard convection—a numerical study using direct numerical simulation. *Journal of Geophysical Research: Atmospheres*, 126.

Gill, A. (1976). Adjustment under gravity in a rotating channel. *Journal of Fluid Mechanics*, 77(3):603–621.

Gillette, D. A. and Sinclair, P. C. (1990). Estimation of suspension of alkaline material by dust devils in the united states. *Atmospheric Environment. Part A. General Topics*, 24(5):1135–1142.

Gini, C. (1912). *Variabilità e mutabilità: contributo allo studio delle distribuzioni e delle relazioni statistiche.[Fasc. I.]*. Tipografia P. Cuppini.

Greeley, R., Balme, M. R., Iversen, J. D., Metzger, S., Mickelson, R., Phoreman, J., and White, B. (2003). Martian dust devils: Laboratory simulations of particle threshold. *Journal of Geophysical Research: Planets*, 108(E5).

Gregg, M. (1998). Estimation and geography of diapycnal mixing in the stratified ocean. *Physical Processes in Lakes and Oceans*, 54:305–338.

Gregg, M. C., D'Asaro, E. A., Riley, J. J., and Kunze, E. (2018). Mixing efficiency in the ocean. *Annual Review of Marine Science*, 10:443–473.

Guervilly, C., Hughes, D. W., and Jones, C. A. (2014). Large-scale vortices in rapidly rotating rayleigh–bénard convection. *Journal of Fluid Mechanics*, 758:407–435.

Guseva, K., Daitche, A., Feudel, U., and Tél, T. (2016). History effects in the sedimentation of light aerosols in turbulence: The case of marine snow. *Physical Review Fluids*, 1(7):074203.

Haine, T. W., Gelderloos, R., Jimenez-Urias, M. A., Siddiqui, A. H., Lemson, G., Medvedev, D., Szalay, A., Abernathey, R. P., Almansi, M., and Hill, C. N. (2021). Is computational oceanography coming of age? *Bulletin of the American Meteorological Society*, 102(8):E1481–E1493.

Haine, T. W. and Marshall, J. (1998). Gravitational, symmetric, and baroclinic instability of the ocean mixed layer. *Journal of Physical Oceanography*, 28(4):634–658.

Han, Y., Wang, K., Liu, F., Zhao, T., Yin, Y., Duan, J., and Luan, Z. (2016). The contribution of dust devils and dusty plumes to the aerosol budget in western china. *Atmospheric Environment*, 126:21–27.

Hanawa, K. and Talley, L. D. (2001). Mode waters. In *International Geophysics*, volume 77, pages 373–386. Elsevier.

Harcourt, R. R. and D'Asaro, E. A. (2008). Large-eddy simulation of langmuir turbulence in pure wind seas. *Journal of Physical Oceanography*, 38(7):1542–1562.

Haza, A. C., Özgökmen, T. M., Griffa, A., Garraffo, Z. D., and Piterbarg, L. (2012). Parameterization of particle transport at submesoscales in the gulf stream region using lagrangian subgridscale models. *Ocean Modelling*, 42:31–49.

Heitmann, S. and Backhaus, J. O. (2005). Large-eddy simulations of convective shear flows. *Deep-Sea Research Part II: Topical Studies in Oceanography*, 52:1156–1180.

Hewitt, H., Fox-Kemper, B., Pearson, B., Roberts, M., and Klocke, D. (2022). The small scales of the ocean may hold the key to surprises. *Nature Climate Change*, 12(6):496–499.

Hinsberg, M. A. V., Boonkkamp, J. H. T. T., Tosch, F., and Clercx, H. J. (2012). On the efficiency and accuracy of interpolation methods for spectral codes. *SIAM Journal on Scientific Computing*, 34.

Hoskins, B. J. (1982). The mathematical theory of frontogenesis. *Annual Review of Fluid Mechanics*, 14(1):131–151.

Hussain, F. and Jeong, J. (1995). On the identification of a vortex. *Article in Journal of Fluid Mechanics*, 285:69–94.

Jemmett-Smith, B. C., Marsham, J. H., Knippertz, P., and Gilkeson, C. A. (2015). Quantifying global dust devil occurrence from meteorological analyses. *Geophysical Research Letters*, 42(4):1275–1282.

Jinadasa, S., Lozovatsky, I., Planella-Morató, J., Nash, J. D., MacKinnon, J. A., Lucas, A. J., Wijesekera, H. W., and Fernando, H. J. (2016). Ocean turbulence and mixing around sri lanka and in adjacent waters of the northern bay of bengal. *Oceanography*, 29(2):170–179.

Jones, H. and Marshall, J. (1993). Convection with rotation in a neutral ocean: A study of open-ocean deep convection. *Journal of Physical Oceanography*, 23(6):1009–1039.

Julien, K., Legg, S., McWilliams, J., and Werne, J. (1996). Rapidly rotating turbulent rayleigh-bénard convection. *Journal of Fluid Mechanics*, 322:243–273.

Kahanpää, H., Newman, C., Moores, J., Zorzano, M. P., Martín-Torres, J., Navarro, S., Lepinette, A., Cantor, B., Lemmon, M. T., Valentín-Serrano, P., Ullán, A., and Schmidt, W. (2016). Convective vortices and dust devils at the msl landing site: Annual variability. *Journal of Geophysical Research: Planets*, 121:1514–1549.

Kanak, K. M. (2006). On the numerical simulation of dust devil–like vortices in terrestrial and martian convective boundary layers. *Geophysical Research Letters*, 33(19).

Klein, P., Hua, B. L., Lapeyre, G., Capet, X., Le Gentil, S., and Sasaki, H. (2008). Upper ocean turbulence from high-resolution 3d simulations. *Journal of Physical Oceanography*, 38(8):1748–1763.

Klinger, B. A. and Marshall, J. (1995). Regimes and scaling laws for rotating deep convection in the ocean. *Dynamics of Atmospheres and Oceans*, 21(4):227–256.

Koch, J. and Renno, N. O. (2005). The role of convective plumes and vortices on the global aerosol budget. *Geophysical Research Letters*, 32(18).

Kolmogorov, A. N. (1962). A refinement of previous hypotheses concerning the local structure of turbulence in a viscous incompressible fluid at high reynolds number. *Journal of Fluid Mechanics*, 13(1):82–85.

Kolmogorov, A. N. (1991). The local structure of turbulence in incompressible viscous fluid for very large reynolds numbers. *Proceedings of the Royal Society of London. Series A: Mathematical and Physical Sciences*, 434(1890):9–13.

Kooi, M., Nes, E. H. v., Scheffer, M., and Koelmans, A. A. (2017). Ups and downs in the ocean: effects of biofouling on vertical transport of microplastics. *Environmental science & technology*, 51(14):7963–7971.

Kooi, M., Reisser, J., Slat, B., Ferrari, F. F., Schmid, M. S., Cunsolo, S., Brambini, R., Noble, K., Sirks, L. A., Linders, T. E., Schoeneich-Argent, R. I., and Koelmans, A. A. (2016). The effect of particle properties on the depth profile of buoyant plastics in the ocean. *Scientific Reports*, 6.

Kraus, E. and Turner, J. (1967). A one-dimensional model of the seasonal thermocline ii. the general theory and its consequences. *Tellus*, 19(1):98–106.

Kubota, M. (1994). A mechanism for the accumulation of floating marine debris north of hawaii. *Journal of Physical Oceanography*, 24(5):1059–1064.

Kudryavtsev, V., Myasoedov, A., Chapron, B., Johannessen, J. A., and Collard, F. (2012). Imaging mesoscale upper ocean dynamics using synthetic aperture radar and optical data. *Journal of Geophysical Research: Oceans*, 117(C4).

Kukulka, T. and Brunner, K. (2015). Passive buoyant tracers in the ocean surface boundary layer: 1. influence of equilibrium wind-waves on vertical distributions. *Journal of Geophysical Research: Oceans*, 120:3837–3858.

Kukulka, T., Law, K. L., and Proskurowski, G. (2016). Evidence for the influence of surface heat fluxes on turbulent mixing of microplastic marine debris. *Journal of Physical Oceanography*, 46:809–815.

Kukulka, T., Proskurowski, G., Morét-Ferguson, S., Meyer, D. W., and Law, K. L. (2012). The effect of wind mixing on the vertical distribution of buoyant plastic debris. *Geophysical Research Letters*, 39.

Kukulka, T. and Veron, F. (2019). Lagrangian investigation of wave-driven turbulence in the ocean surface boundary layer. *Journal of Physical Oceanography*, 49(2):409–429.

Lande, R. and Wood, A. M. (1987). Suspension times of particles in the upper ocean. *Deep Sea Research Part A. Oceanographic Research Papers*, 34(1):61–72.

Langmuir, I. (1938). Surface motion of water induced by wind. *Science*, 87(2250):119–123.

Large, W. G., McWilliams, J. C., and Doney, S. C. (1994). Oceanic vertical mixing: A review and a model with a nonlocal boundary layer parameterization. *Reviews of Geophysics*, 32(4):363–403.

Leibovich, S. (1983). The form and dynamics of langmuir circulations. *Annual Review of Fluid Mechanics*, 15(1):391–427.

Lesieur, M. and Metais, O. (1996). New trends in large-eddy simulations of turbulence. *Annual Review of Fluid Mechanics*, 28(1):45–82.

Lévy, M., Ferrari, R., Franks, P. J., Martin, A. P., and Rivière, P. (2012). Bringing physics to life at the submesoscale. *Geophysical Research Letters*, 39(14).

Li, Y., Han, W., and Zhang, L. (2017). Enhanced decadal warming of the southeast indian ocean during the recent global surface warming slowdown. *Geophysical Research Letters*, 44(19):9876–9884.

Liang, J.-H., McWilliams, J. C., Sullivan, P. P., and Baschek, B. (2011). Modeling bubbles and dissolved gases in the ocean. *Journal of Geophysical Research: Oceans*, 116(C3).

Liang, J.-H., McWilliams, J. C., Sullivan, P. P., and Baschek, B. (2012). Large eddy simulation of the bubbly ocean: New insights on subsurface bubble distribution and bubble-mediated gas transfer. *Journal of Geophysical Research: Oceans*, 117(C4).

Liang, J. H., Wan, X., Rose, K. A., Sullivan, P. P., and McWilliams, J. C. (2018). Horizontal dispersion of buoyant materials in the ocean surface boundary layer. *Journal of Physical Oceanography*, 48:2103–2125.

Lilly, D. K. (1967). The representation of small-scale turbulence in numerical simulation experiments. In *Proceedings of the IBM Scientific Computing Symposium on Environmental Sciences*, pages 195–210.

Long, M., Moriceau, B., Gallinari, M., Lambert, C., Huvet, A., Raffray, J., and Soudant, P. (2015). Interactions between microplastics and phytoplankton aggregates: impact on their respective fates. *Marine Chemistry*, 175:39–46.

Lorenz, R. D. (2012). Power law distribution of pressure drops in dust devils: Observation techniques and earth–mars comparison. *Planetary and Space Science*, 60(1):370–375.

Lorenz, R. D. and Myers, M. J. (2005). Local time (hrs) fraction of total dust devil hazard to aviation a review of united states air accident reports. *Journal of Meteorology*, 30.

Loth, E. (2008). Drag of non-spherical solid particles of regular and irregular shape. *Powder Technology*, 182(3):342–353.

Maffioli, A., Brethouwer, G., and Lindborg, E. (2016). Mixing efficiency in stratified turbulence. *Journal of Fluid Mechanics*, 794:R3.

Mahadevan, A., D'asaro, E., Lee, C., and Perry, M. J. (2012). Eddy-driven stratification initiates north atlantic spring phytoplankton blooms. *Science*, 337(6090):54–58.

Mahadevan, A. and Tandon, A. (2006). An analysis of mechanisms for submesoscale vertical motion at ocean fronts. *Ocean Modelling*, 14(3-4):241–256.

Marshall, J. and Schott, F. (1999). Open-ocean convection: Observations, theory, and models. *Reviews of Geophysics*, 37:1–64.

Mason, P. J. (1989). Large-eddy simulation of the convective atmospheric boundary layer. *Journal of Atmospheric Sciences*, 46(11):1492–1516.

Maxey, M. R. and Riley, J. J. (1983). Equation of motion for a small rigid sphere in a nonuniform flow. *Physics of Fluids*, 26:883–889.

Maximenko, N., Hafner, J., Kamachi, M., and MacFadyen, A. (2018). Numerical simulations of debris drift from the great japan tsunami of 2011 and their verification with observational reports. *Marine Pollution Bulletin*, 132:5–25.

Maxworthy, T. and Narimousa, S. (1994). Unsteady, turbulent convection into a homogeneous, rotating fluid, with oceanographic applications. *Journal of Physical Oceanography*, 24(5):865–887.

McWilliams, J. C. (2006). *Fundamentals of Geophysical Fluid Dynamics*. Cambridge University Press.

McWilliams, J. C. (2016). Submesoscale currents in the ocean. *Proceedings of the Royal Society A: Mathematical, Physical and Engineering Sciences*, 472(2189):20160117.

McWilliams, J. C., Molemaker, M. J., and Yavneh, I. (2001). From stirring to mixing of momentum: Cascades from balanced flows to dissipation in the oceanic interior. In *Aha Huliko'a Proceedings*, pages 59–66.

McWilliams, J. C. and Sullivan, P. P. (2000). Vertical mixing by langmuir circulations. *Spill Science & Technology Bulletin*, 6(3-4):225–237.

McWilliams, J. C., Sullivan, P. P., and Moeng, C.-H. (1997). Langmuir turbulence in the ocean. *Journal of Fluid Mechanics*, 334:1–30.

Melville, W. K. (1996). The role of surface-wave breaking in air-sea interaction. *Annual Review of Fluid Mechanics*, 28(1):279–321.

Mendelssohn, I. A., Andersen, G. L., Baltz, D. M., Caffey, R. H., Carman, K. R., Fleeger, J. W., Joye, S. B., Lin, Q., Maltby, E., Overton, E. B., et al. (2012). Oil impacts on coastal wetlands: implications for the mississippi river delta ecosystem after the deepwater horizon oil spill. *BioScience*, 62(6):562–574.

Meneveau, C. and Katz, J. (2000). Scale-invariance and turbulence models for large-eddy simulation. *Annual Review of Fluid Mechanics*, 32(1):1–32.

Mensa, J. A., Özgökmen, T. M., Poje, A. C., and Imberger, J. (2015). Material transport in a convective surface mixed layer under weak wind forcing. *Ocean Modelling*, 96:226–242.

Metzger, S. M., Balme, M. R., Towner, M. C., Bos, B. J., Ringrose, T. J., and Patel, M. R. (2011). In situ measurements of particle load and transport in dust devils. *Icarus*, 214:766–772.

Metzger, S. M., Carr, J. R., Johnson, J. R., Parker, T. J., and Lemmon, M. T. (1999). Dust devil vortices seen by the mars pathfinder camera. *Geophysical Research Letters*, 26(18):2781–2784.

Michaels, T. I. and Rafkin, S. C. (2004). Large eddy simulation of atmospheric convection on mars. *Quarterly Journal of the Royal Meteorological Society*, 130:1251–1274.

Mirocha, J., Kosović, B., and Kirkil, G. (2014). Resolved turbulence characteristics in large-eddy simulations nested within mesoscale simulations using the weather research and forecasting model. *Monthly Weather Review*, 142(2):806–831.

Moeng, C.-H. and Sullivan, P. P. (1994). A comparison of shear- and buoyancy-driven planetary boundary layer flows. *Journal of the Atmospheric Sciences*, 51:999–1022.

Molemaker, M. J., McWilliams, J. C., and Capet, X. (2010). Balanced and unbalanced routes to dissipation in an equilibrated eady flow. *Journal of Fluid Mechanics*, 654:35–63.

Molemaker, M. J., McWilliams, J. C., and Yavneh, I. (2005). Baroclinic instability and loss of balance. *Journal of Physical Oceanography*, 35(9):1505–1517.

Morton, B. t. (1966). Geophysical vortices. *Progress in Aerospace Sciences*, 7:145–194.

Morét-Ferguson, S., Law, K. L., Proskurowski, G., Murphy, E. K., Peacock, E. E., and Reddy, C. M. (2010). The size, mass, and composition of plastic debris in the western north atlantic ocean. *Marine Pollution Bulletin*, 60:1873–1878.

Nishizawa, S., Odaka, M., Takahashi, Y. O., Sugiyama, K.-i., Nakajima, K., Ishiwatari, M., Takehiro, S.-i., Yashiro, H., Sato, Y., Tomita, H., et al. (2016a). Martian dust devil statistics from high-resolution large-eddy simulations. *Geophysical Research Letters*, 43(9):4180–4188.

Nishizawa, S., Odaka, M., Takahashi, Y. O., Sugiyama, K. I., Nakajima, K., Ishiwatari, M., Takehiro, S. I., Yashiro, H., Sato, Y., Tomita, H., and Hayashi, Y. Y. (2016b). Martian dust devil statistics from high-resolution large-eddy simulations. *Geophysical Research Letters*, 43:4180–4188.

Noh, Y., Kang, I., Herold, M., and Raasch, S. (2006). Large eddy simulation of particle settling in the ocean mixed layer. *Physics of Fluids*, 18(8).

Omand, M. M., D'Asaro, E. A., Lee, C. M., Perry, M. J., Briggs, N., Cetinić, I., and Mahadevan, A. (2015). Eddy-driven subduction exports particulate organic carbon from the spring bloom. *Science*, 348(6231):222–225.

Ou, H. W. (1984). Geostrophic adjustment: A mechanism for frontogenesis. *Journal of Physical Oceanography*, 14(6):994–1000.

Pedlosky, J. (1987). Thermocline theories. In *General Circulation of the Ocean*, pages 55–101. Springer.

Plougonven, R. and Zeitlin, V. (2005). Lagrangian approach to geostrophic adjustment of frontal anomalies in a stratified fluid. *Geophysical & Astrophysical Fluid Dynamics*, 99(2):101–135.

Pope, S. B. (2001). Turbulent flows. *Measurement Science and Technology*, 12(11):2020–2021.

Poulain, M., Mercier, M. J., Brach, L., Martignac, M., Routaboul, C., Perez, E., Desjean, M. C., and Ter Halle, A. (2018). Small microplastics as a main contributor to plastic mass balance in the north atlantic subtropical gyre. *Environmental Science & Technology*, 53(3):1157–1164.

Price, J. F. (1981). Upper ocean response to a hurricane. *Journal of Physical Oceanography*, 11(2):153–175.

Raasch, S. and Franke, T. (2011). Structure and formation of dust devil-like vortices in the atmospheric boundary layer: A high-resolution numerical study. *Journal of Geophysical Research Atmospheres*, 116.

Renno, N. O., Abreu, V. J., Koch, J., Smith, P. H., Hartogensis, O. K., De Bruin, H. A., Burose, D., Delory, G. T., Farrell, W. M., Watts, C. J., et al. (2004). Matador 2002: A pilot field experiment on convective plumes and dust devils. *Journal of Geophysical Research: Planets*, 109(E7).

Rossby, C.-G. (1937). On the mutual adjustment of pressure and velocity distributions in certain simple current systems. *Journal of Marine Research*, 1(1).

Rozema, W., Bae, H. J., Moin, P., and Verstappen, R. (2015). Minimum-dissipation models for large-eddy simulation. *Physics of Fluids*, 27.

Ruiz, J. (1996). The role of turbulence in the sedimentation loss of pelagic aggregates from the mixed layer. *Journal of Marine Research*, 54(2):385–406.

Sagaut, P. (2006). Analysis and validation of large-eddy simulation data. *Large Eddy Simulation for Incompressible Flows: An Introduction*, pages 305–322.

Salmon, R. (1980). Baroclinic instability and geostrophic turbulence. *Geophysical & Astrophysical Fluid Dynamics*, 15(1):167–211.

Samelson, R. (1993). Linear instability of a mixed-layer front. *Journal of Geophysical Research: Oceans*, 98(C6):10195–10204.

Samelson, R. and Chapman, D. (1995). Evolution of the instability of a mixed-layer front. *Journal of Geophysical Research: Oceans*, 100(C4):6743–6759.

Schmidt, H. and Schumann, U. (1989). Coherent structure of the convective boundary layer derived from large-eddy simulations. *Journal of Fluid Mechanics*, 200:511–562.

Sebille, E. V., Aliani, S., Law, K. L., Maximenko, N., Alsina, J. M., Bagaev, A., Bergmann, M., Chapron, B., Chubarenko, I., Cózar, A., Delandmeter, P., Egger, M., Fox-Kemper, B., Garaba, S. P., Goddijn-Murphy, L., Hardesty, B. D., Hoffman, M. J., Isobe, A., Jongedijk, C. E., Kaandorp, M. L., Khatmullina, L., Koelmans, A. A., Kukulka, T., Laufkötter, C., Lebreton, L., Lobelle, D., Maes, C., Martinez-Vicente, V., Maqueda, M. A. M., Poulain-Zarcos, M., Rodríguez, E., Ryan, P. G., Shanks, A. L., Shim, W. J., Suaria, G., Thiel, M., Bremer, T. S. V. D., and Wichmann, D. (2020). The physical oceanography of the transport of floating marine debris. *Environmental Research Letters*, 15.

Sebille, E. V., Wilcox, C., Lebreton, L., Maximenko, N., Hardesty, B. D., Franeker, J. A. V., Eriksen, M., Siegel, D., Galgani, F., and Law, K. L. (2015). A global inventory of small floating plastic debris. *Environmental Research Letters*, 10.

Semcesen, P. O. and Wells, M. G. (2021). Biofilm growth on buoyant microplastics leads to changes in settling rates: implications for microplastic retention in the great lakes. *Marine Pollution Bulletin*, 170:112573.

Shakespeare, C. J. and Taylor, J. (2014). The spontaneous generation of inertia–gravity waves during frontogenesis forced by large strain: Theory. *Journal of Fluid Mechanics*, 757:817–853.

Shao, Y., Wyrwoll, K.-H., Chappell, A., Huang, J., Lin, Z., McTainsh, G. H., Mikami, M., Tanaka, T. Y., Wang, X., and Yoon, S. (2011). Dust cycle: An emerging core theme in earth system science. *Aeolian Research*, 2(4):181–204.

Simpson, J. and Linden, P. (1989). Frontogenesis in a fluid with horizontal density gradients. *Journal of Fluid Mechanics*, 202:1–16.

Sinclair, P. C. (1965). On the rotation of dust devils. *Bulletin of the American Meteorological Society*, 46:388–391.

Sinclair, P. C. (1969). General characteristics of dust devils. *Journal of Applied Meteorology and Climatology*, 8(1):32–45.

Sipp, D., Lauga, E., and Jacquin, L. (1999). Vortices in rotating systems: centrifugal, elliptic and hyperbolic type instabilities. *Physics of Fluids*, 11(12):3716–3728.

Skyllingstad, E. D. (2000). Scales of langmuir circulation generated using a large-eddy simulation model. *Spill Science & Technology Bulletin*, 6(3-4):239–246.

Skyllingstad, E. D. and Denbo, D. W. (1995). An ocean large-eddy simulation of langmuir circulations and convection in the surface mixed layer. *Journal of Geophysical Research: Oceans*, 100(C5):8501–8522.

Smagorinsky, J. (1963). General circulation experiments with the primitive equations: I. the basic experiment. *Monthly Weather Review*, 91(3):99–164.

Smith, C. and Metzler, S. (1983). The characteristics of low-speed streaks in the near-wall region of a turbulent boundary layer. *Journal of Fluid Mechanics*, 129:27–54.

Smith, K. M., Hamlington, P. E., and Fox-Kemper, B. (2016). Effects of submesoscale turbulence on ocean tracers. *Journal of Geophysical Research: Oceans*, 121:908–933.

Spiga, A., Barth, E., Gu, Z., Hoffmann, F., Ito, J., Jemmett-Smith, B., Klose, M., Nishizawa, S., Raasch, S., Rafkin, S., et al. (2016). Large-eddy simulations of dust devils and convective vortices. *Space Science Reviews*, 203:245–275.

Stokes, G. G. (1847). On the theory of oscillatory waves. *Transactions of the Cambridge Philosophical Society*, 8:441–455.

Stone, P. H. (1966). On non-geostrophic baroclinic stability. *Journal of the Atmospheric Sciences*, 23(4):390–400.

Stubley, G. and Riopelle, G. (1988). The influence of the earth's rotation on planetary boundary-layer turbulence. *Boundary-layer meteorology*, 45:307–324.

Sullivan, P. P., McWilliams, J. C., and Melville, W. K. (2007). Surface gravity wave effects in the oceanic boundary layer: Large-eddy simulation with vortex force and stochastic breakers. *Journal of Fluid Mechanics*, 593:405–452.

Sutherland, B. R., DiBenedetto, M., Kaminski, A., and Van Den Bremer, T. (2023). Fluid dynamics challenges in predicting plastic pollution transport in the ocean: A perspective. *Physical Review Fluids*, 8(7):070701.

Sutherland, B. R., Ma, Y., Flynn, M. R., Frank, D., Linden, P. F., Lemasquerier, D., Bars, M. L., Pacary, C., Jamin, T., Dauxois, T., and Joubaud, S. (2021). Plumes in rotating fluid and their transformation into tornados. *Journal of Fluid Mechanics*, 924.

Sykes, R. I. and Henn, D. S. (1989). Large-eddy simulation of turbulent sheared convection. *Journal of the Atmospheric Sciences*, 46:1106–1118.

Tandon, A. and Garrett, C. (1994). Mixed layer restratification due to a horizontal density gradient. *Journal of Physical Oceanography*, 24(6):1419–1424.

Tang, Y., Han, Y., and Liu, Z. (2018). Temporal and spatial characteristics of dust devils and their contribution to the aerosol budget in east asia—an analysis using a new parameterization scheme for dust devils. *Atmospheric Environment*, 182:225–233.

Taylor, J. R. (2008). Numerical simulations of the stratified oceanic bottom boundary layer. *PhD thesis, University of California*.

Taylor, J. R. (2016). Turbulent mixing, restratification, and phytoplankton growth at a submesoscale eddy. *Geophysical Research Letters*, 43(11):5784–5792.

Taylor, J. R. (2018). Accumulation and subduction of buoyant material at submesoscale fronts. *Journal of Physical Oceanography*, 48:1233–1241.

Taylor, J. R. and Ferrari, R. (2009). On the equilibration of a symmetrically unstable front via a secondary shear instability. *Journal of Fluid Mechanics*, 622:103–113.

Taylor, J. R. and Ferrari, R. (2010). Buoyancy and wind-driven convection at mixed layer density fronts. *Journal of Physical Oceanography*, 40(6):1222–1242.

Taylor, J. R. and Ferrari, R. (2011). Ocean fronts trigger high latitude phytoplankton blooms. *Geophysical Research Letters*, 38(23).

Taylor, J. R., Smith, K. M., and Vreugdenhil, C. A. (2020). The influence of submesoscales and vertical mixing on the export of sinking tracers in large-eddy simulations. *Journal of Physical Oceanography*, 50:1319–1339.

Taylor, J. R. and Thompson, A. F. (2023). Submesoscale dynamics in the upper ocean. *Annual Review of Fluid Mechanics*, 55:103–127.

Thomas, L. N., Tandon, A., and Mahadevan, A. (2008). Submesoscale processes and dynamics. *Ocean modeling in an Eddying Regime*, 177:17–38.

Thomas, L. N., Taylor, J. R., D'Asaro, E. A., Lee, C. M., Klymak, J. M., and Shcherbina, A. (2016). Symmetric instability, inertial oscillations, and turbulence at the gulf stream front. *Journal of Physical Oceanography*, 46(1):197–217.

Thomas, P. and Gierasch, P. J. (1985). Dust devils on mars. *Science*, 230(4722):175–177.

Thompson, A. F., Lazar, A., Buckingham, C., Garabato, A. C. N., Damerell, G. M., and Heywood, K. J. (2016). Open-ocean submesoscale motions: A full seasonal cycle of mixed layer instabilities from gliders. *Journal of Physical Oceanography*, 46(4):1285 – 1307.

Thomson, J., Gemmrich, J. R., and Jessup, A. T. (2009). Energy dissipation and the spectral distribution of whitecaps. *Geophysical Research Letters*, 36(11).

Thorpe, S. (2004). Langmuir circulation. *Annual Review of Fluid Mechanics*, 36:55–79.

Tiselius, P. and Kiørboe, T. (1998). Colonization of diatom aggregates by the dinoflagellate noctiluca scintillans. *Limnology and Oceanography*, 43(1):154–159.

Toigo, A. D., Richardson, M. I., Ewald, S. P., and Gierasch, P. J. (2003). Numerical simulation of martian dust devils. *Journal of Geophysical Research: Planets*, 108(E6).

Uchiyama, Y., Suzue, Y., and Yamazaki, H. (2017). Eddy-driven nutrient transport and associated upper-ocean primary production along the k uroshio. *Journal of Geophysical Research: Oceans*, 122(6):5046–5062.

Vorobieff, P. and Ecke, R. E. (2002). Turbulent rotating convection: an experimental study. *Journal of Fluid Mechanics*, 458:191–218.

Vreugdenhil, C. A. and Taylor, J. R. (2018). Large-eddy simulations of stratified plane couette flow using the anisotropic minimum-dissipation model. *Physics of Fluids*, 30.

Ward, C. P. and Reddy, C. M. (2020). We need better data about the environmental persistence of plastic goods. *Proceedings of the National Academy of Sciences*, 117(26):14618–14621.

Weil, J. C., Sullivan, P. P., and Moeng, C.-H. (2004). The use of large-eddy simulations in lagrangian particle dispersion models. *Journal of the Atmospheric sSciences*, 61(23):2877–2887.

Weller, R. A. and Price, J. F. (1988). Langmuir circulation within the oceanic mixed layer. *Deep Sea Research Part A. Oceanographic Research Papers*, 35(5):711–747.

Wienkers, A., Thomas, L., and Taylor, J. (2021a). The influence of front strength on the development and equilibration of symmetric instability, part 1: Growth and saturation. *Journal of Fluid Mechanics*, 926:A6.

Wienkers, A., Thomas, L., and Taylor, J. (2021b). The influence of front strength on the development and equilibration of symmetric instability, part 2: Nonlinear evolution. *Journal of Fluid Mechanics*, 926:A7.

Wilcox, C., Sebille, E. V., Hardesty, B. D., and Estes, J. A. (2015). Threat of plastic pollution to seabirds is global, pervasive, and increasing. *Proceedings of the National Academy of Sciences of the United States of America*, 112:11899–11904.

Wilczek, M. and Friedrich, R. (2009). Dynamical origins for non-gaussian vorticity distributions in turbulent flows. *Physical Review E*, 80(1):016316.

Worm, B., Lotze, H. K., Jubinville, I., Wilcox, C., and Jambeck, J. (2017). Plastic as a persistent marine pollutant. *Annual Review of Environment and Resources*, 42:1–26.

Wunsch, C. and Ferrari, R. (2004). Vertical mixing, energy, and the general circulation of the oceans. *Annu. Rev. Fluid Mech.*, 36:281–314.

Yang, D., Chamecki, M., and Meneveau, C. (2014). Inhibition of oil plume dilution in langmuir ocean circulation. *Geophysical Research Letters*, 41:1632–1638.

Yang, D., Chen, B., Chamecki, M., and Meneveau, C. (2015). Oil plumes and dispersion in l angmuir, upper-ocean turbulence: Large-eddy simulations and k-profile parameterization. *Journal of Geophysical Research: Oceans*, 120(7):4729–4759.

Yang, D., Chen, B., Socolofsky, S. A., Chamecki, M., and Meneveau, C. (2016). Large-eddy simulation and parameterization of buoyant plume dynamics in stratified flow. *Journal of Fluid Mechanics*, 794:798–833.

Yeung, P. and Pope, S. (1988). An algorithm for tracking fluid particles in numerical simulations of homogeneous turbulence. *Journal of Computational Physics*, 79(2):373–416.